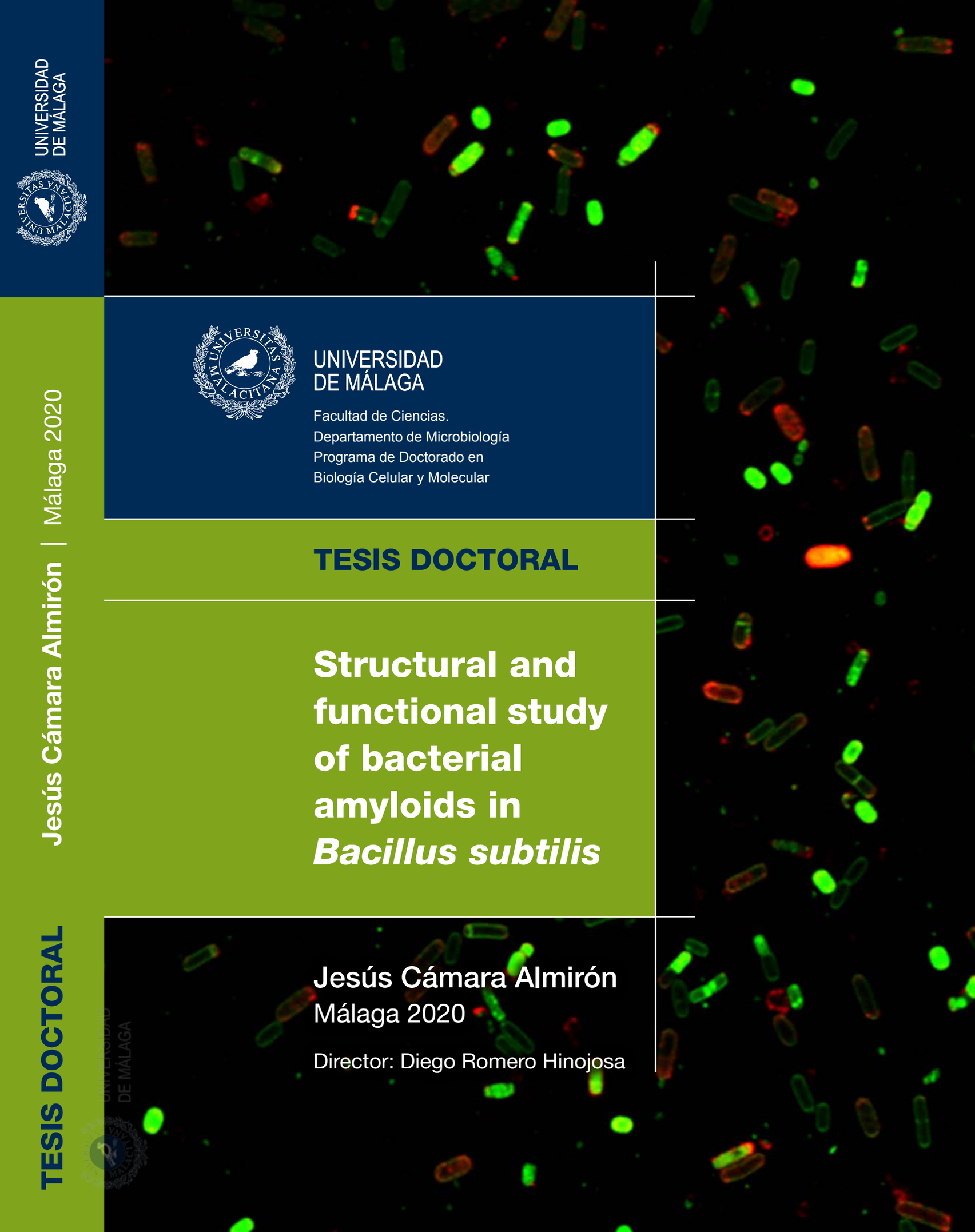

UNIVERSIDAD
DE MÁLAGA

Facultad de Ciencias.
Departamento de Microbiología
Programa de Doctorado en
Biología Celular y Molecular

TESIS DOCTORAL

Structural and functional study of bacterial amyloids in *Bacillus subtilis*

Jesús Cámara Almirón
Málaga 2020

Director: Diego Romero Hinojosa

UNIVERSIDAD DE MÁLAGA
Jesús Cámara Almirón | Málaga 2020
TESIS DOCTORAL

AUTOR: Jesús Cámara Almirón

https://orcid.org/0000-0002-6107-4260

EDITA: Publicaciones y Divulgación Científica. Universidad de Málaga

DECLARACIÓN DE AUTORÍA Y ORIGINALIDAD DE LA TESIS PRESENTADA PARA OBTENER EL TÍTULO DE DOCTOR

D./Dña JESÚS CÁMARA ALMIRÓN
Estudiante del programa de doctorado BIOLOGÍA CELULAR Y MOLECULAR de la Universidad de Málaga, autor/a de la tesis, presentada para la obtención del título de doctor por la Universidad de Málaga, titulada: STRUCTURAL AND FUNCTIONAL STUDY OF BACTERIAL AMYLOIDS IN BACILLUS SUBTILIS

Realizada bajo la tutorización de DIEGO FRANCISCO ROMERO HINOJOSA y dirección de DIEGO FRANCISCO ROMERO HINOJOSA (si tuviera varios directores deberá hacer constar el nombre de todos)

DECLARO QUE:

La tesis presentada es una obra original que no infringe los derechos de propiedad intelectual ni los derechos de propiedad industrial u otros, conforme al ordenamiento jurídico vigente (Real Decreto Legislativo 1/1996, de 12 de abril, por el que se aprueba el texto refundido de la Ley de Propiedad Intelectual, regularizando, aclarando y armonizando las disposiciones legales vigentes sobre la materia), modificado por la Ley 2/2019, de 1 de marzo.

Igualmente asumo, ante a la Universidad de Málaga y ante cualquier otra instancia, la responsabilidad que pudiera derivarse en caso de plagio de contenidos en la tesis presentada, conforme al ordenamiento jurídico vigente.

En Málaga, a 3 de JUNIO de 2020

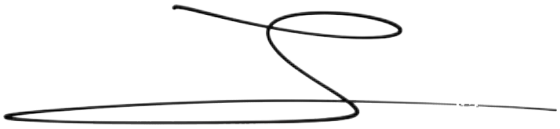

Fdo.: JESÚS CÁMARA ALMIRÓN

Edificio Pabellón de Gobierno. Campus El Ejido. 29071
Tel.: 952 13 10 28 / 952 13 14 61 / 952 13 71 10
E-mail: doctorado@uma.es

UNIVERSIDAD DE MÁLAGA

Departamento de Microbiología

Facultad de Ciencias

Structural and functional study of bacterial amyloids in *Bacillus subtilis*

Memoria presentada por **Jesús Cámara Almirón** para optar al grado de Doctor por la Universidad de Málaga

UNIVERSIDAD DE MÁLAGA

Departamento de Microbiología

Facultad de Ciencias

D. JUAN JOSÉ BORREGO GARCÍA, director del Departamento de Microbiología de la Universidad de Málaga,

INFORMA:

Que **JESÚS CÁMARA ALMIRÓN** ha realizado en los laboratorios de este departamento el trabajo experimental conducente a la elaboración de la presente Memoria de Tesis Doctoral.

Y para que así conste, y tenga los efectos que correspondan, en cumplimiento de la legislación vigente, expido el presente informe.

En Málaga, a 20/05/2020

Fdo: D. Juan José Borrego García

UNIVERSIDAD DE MÁLAGA

Departamento de Microbiología

Facultad de Ciencias

D. DIEGO FRANCISCO ROMERO HINOJOSA, profesor titular del Departamento de Microbiología de la Universidad de Málaga,

INFORMA:

Que **JESÚS CÁMARA ALMIRÓN** ha realizado ha realizado bajo mi dirección el trabajo experimental conducente a la elaboración de la presente Memoria de Tesis Doctoral.

Y para que así conste, y tenga los efectos que correspondan, en cumplimiento de la legislación vigente, expido el presente informe.

En Málaga, a 20/05/2020

Fdo: D. Diego Francisco Romero Hinojosa

UNIVERSIDAD DE MÁLAGA

Departamento de Microbiología

Facultad de Ciencias

Este trabajo ha sido financiado por los proyectos/this work has been funded by the following projects:

MECHANISTIC AND FUNCTIONAL STUDIES OF *Bacillus* BIOFILMS ON PLANTS, AND THEIR IMPACT IN SUSTAINABLE AGRICULTURE AND FOOD SAFETY. ERC637971. European Research Council Executive Agency. Starting Grant (BacBio). Principal investigator: Diego Romero.

ESTUDIO Y MANEJO DE BIOFILMS DE CEPAS DE *Bacillus* RELEVANTES EN CONTROL BIOLÓGICO Y SEGURIDAD ALIMENTARIA SOBRE SUPERFICIES VEGETALES. Ministerio de Economía y Competitividad. Programa Nacional de Proyectos de Investigación Fundamental no Orientada-Retos (AGL2016-78662-R). Investigador principal: Diego Romero

Artículos derivados de esta Tesis Doctoral

- **Jesús Cámara-Almirón**, Joaquín Caro-Astorga, Antonio de Vicente and Diego Romero. Beyond the expected: the structural and functional diversity of bacterial amyloids. *Critical Reviews in Microbiology* 44:6, 653-666 (2018). (Parte de los capítulos I y V).

- **Jesús Cámara-Almirón**, Carlos Molina-Santiago, Antonio de Vicente, Francisco M. Cazorla and Diego Romero. Understanding bacterial physiology for improving full fitness in plants in *Strategies to develop successful Biocontrol Agents*. (2019) Submitted. (Capítulo de libro, parte del capítulo I)

- Nadia El Mammeri, Jesus Hierrezuelo, James Tolchard, **Jesús Cámara-Almirón**, Joaquín Caro-Astorga, Ana Álvarez-Mena, Antoine Dutour, Mélanie Berbon, Jayakrishna Shenoy, Estelle Morvan, Axelle Grélard, Brice Kauffmann, Sophie Lecomte, Antonio de Vicente, Birgit Habenstein, Diego Romero, and Antoine Loquet. Molecular architecture of bacterial amyloids in *Bacillus* biofilms. *The FASEB Journal*. 33:11, 12146-12163 (2019). (Capítulo II).

- **Jesús Cámara-Almirón**, Yurena Navarro, Luis Díaz-Martínez, María Concepción Magno-Pérez-Bryan, Carlos Molina-Santiago, John R. Pearson, Antonio de Vicente, Alejandro Pérez-García, and Diego Romero. Dual functionality of the amyloid protein TasA in *Bacillus* physiology and fitness on the phylloplane. *Nature Communications* 11, 1859 (2020). (Capítulo III y parte del capítulo IV).

- Nitai Steinberg, Alona Keren-Paz, Qihui Hou, Shany Doron, Keren Yanuka-Golub, Tsviya Olender, Rotem Hadar, Gili Rosenberg, Rakeshkumar Jain, **Jesús Cámara-Almirón**, Diego Romero, Sven Van Teeffelen, and Ilana Kolodkin-Gal. The extracellular matrix protein TasA is a developmental cue that maintains a motile subpopulation within *Bacillus subtilis* biofilms. *Science Signaling* 13, eaaw8905, (2020). (discutido en el capítulo V)

Comunicaciones a congresos derivadas de esta Tesis Doctoral

- **Jesús Cámara-Almirón**, Bertrand Morel, Francisco Conejero-Lara, Diego Romero. Caracterización funcional de las proteínas TasA y TapA en la formación de fibras de tipo amiloide en *Bacillus subtilis*. XI Reunión del Grupo Especializado de Microbiología Molecular de la Sociedad Española de Microbiología (2016). Sevilla, España. *Póster.*

- **Jesús Cámara-Almirón**, Mª Luisa Antequera-Gómez, Elena Pedrero-Vega, Alejandro Pérez-García, Antonio de Vicente, Diego Romero. Implicación de la matriz extracelular de biofilms de *Bacillus subtilis* en la interacción beneficiosa con la planta. XVIII Congreso de la Sociedad Española de Fitopatología. (2016). Palencia, España. *Póster*.

- **Jesús Cámara-Almirón**, Bertrand Morel, Francisco Conejero-Lara, Diego Romero. Functional characterization of TasA and TapA in the formation of the amyloid fiber in *Bacillus subtilis*. 19th International Conference in Bacilli and Gram-Positive Bacteria. (2017). Berlín, Alemania. *Póster*.

- **Jesús Cámara-Almirón**, Yurena Navarro, Mª Concepción Magno-Pérez-Bryan, Carlos Molina-Santiago, Antonio de Vicente, Alejandro Pérez-García, Diego Romero. The pivotal functionality of the amyloid protein TasA in *Bacillus* physiology and fitness. 5th Young Microbiologist Symposium on Microbe Signalling, Organisation and Pathogenesis. (2018). Belfast, Reino Unido. *Comunicación oral*.

- **Jesús Cámara-Almirón**, Yurena Navarro, Mª Concepción Magno-Pérez-Bryan, Carlos Molina-Santiago, Antonio de Vicente, Alejandro Pérez-García, Diego Romero. Dual functionality of the amyloid protein TasA in *Bacillus* physiology and fitness. Spanish Portuguese Meeting for Advanced Optical Microscopy. (2018). Granada, España. *Póster.*

- **Jesús Cámara-Almirón**, Yurena Navarro, Mª Concepción Magno-Pérez-Bryan, Carlos Molina-Santiago, Antonio de Vicente, Alejandro Pérez-García, Diego Romero El papel dual del amiloide funcional TasA del biofilm de *Bacillus subtilis* en la fisiología bacteriana y la persistencia sobre la superficie de la planta. VII Reunión del Grupo Especializado de Microbiología de Plantas de la Sociedad Española de Microbiología. (2019). Osuna, Sevilla, España. *Comunicación oral*.

AGRADECIMIENTOS

Aún hoy, todavía me cuesta creer que ya hayan pasado 5 años (¡5 añazos!) desde que llegué a Málaga. Desde que empecé la Licenciatura en Biología allá por el 2008, siempre tuve bastante claro que la investigación era mi camino y muchos de los que leáis estas líneas, probablemente, estaréis de acuerdo conmigo en que, a pesar de las dificultades, es difícil no enamorarse de este trabajo y de los quebraderos de cabeza que nos da. En aquellos momentos antes de venirme, yo nunca había visitado Málaga capital (muchos pensaréis que parecerá mentira que sea cordobés) e incluso me llegué a plantear empezar la carrera investigadora fuera de Andalucía e incluso fuera de España. Sin embargo, no podría estar más contento con la oportunidad que me surgió ya que, gracias a esta, he podido desarrollar un trabajo que me apasiona y he conocido a muchísimas personas geniales que me han acompañado durante este largo camino. Sin embargo, no han sido los únicos, pues afortunadamente, siempre he tenido gente a mi lado que me ha apoyado y que ha estado ahí para los buenos momentos y para los no tan buenos. Estos agradecimientos van dedicados a todos vosotros, a los que ya estabais ahí y a los que entrasteis *de novo* en mi vida, ya que, sin vosotros, todo este trabajo no hubiera sido posible.

Me gustaría empezar estos agradecimientos nombrando a la persona que me dio la oportunidad de que hoy tengáis en vuestras manos (o en vuestras pantallas) esta tesis doctoral, a Diego. Parece que fue ayer cuando entré por primera vez al despacho de La Torre buscándote para hacer la entrevista. Trabajando contigo he podido aprender muchísimo y de cosas tan variadas que nunca imaginé tener que utilizar en mi carrera. Me has transmitido tu pasión por la ciencia y también me has sabido guiar en aquellos momentos en los que la situación me superaba o no encontraba la forma de tirar del hilo. Gracias a ti he aprendido a ser ambicioso, exigente conmigo, crítico, autónomo, a pensar por mí mismo y, en definitiva, a ser científico. Muchísimas gracias por todo, de corazón, y espero que aún nos queden algunos éxitos más que celebrar.

Quiero agradecer también a todos los IPs que forman parte de nuestro grupo de Microbiología y Patología Vegetal: A Alejandro, Lola, Francis y Cayo. Gracias por vuestros comentarios y sugerencias en los seminarios que me han ayudado a ser un mejor comunicador, a pesar de los nervios. Quiero agradecer especialmente a Antonio, por ser una persona siempre dispuesta a ayudar de forma desinteresada, por preocuparse por nosotros y por todas las veces que nos ha abierto la puerta o nos ha cogido el teléfono cuando hemos acudido a él.

También quiero aprovechar para agradecer a todos los compañeros de la Facultad de Ciencias y de La Torre. A France, Sandra, Zaira, Rafa, Guti, Alejandra, Laura, Jesús, Alba, Adri y Carla por los buenos ratos que hemos echado en comidas de grupo. Quiero hacer una mención especial a Irene, por guiarme en mis primeros días en los laboratorios de La Torre cuando acababa de empezar y andaba como pollo sin cabeza, por echarnos un cable siempre que puede y por aguantarnos cada vez que vamos a robarle material. También, por supuesto, quiero hacer darle un agradecimiento especial a Álvaro, por aguantarme con todas las preguntas sobre el depósito de la tesis, por el buen recuerdo que tengo de aquellos días al principio, en los que alguna vez tuvimos que cenar en el labo y, como no, por haberme ayudado a encontrar piso y descubierto la fauna autóctona de Maqueda, ¡mil gracias, vecino!

Todos sabemos que este trabajo tiene luces y sombras y que todo funciona mucho mejor cuando se trabaja en un ambiente bueno y distendido. Por ello, me siento muy afortunado de tener los compañeros de laboratorio que he tenido durante todo este tiempo. Por esta razón quiero dedicar una parte importante de estos agradecimientos a todos mis compañeros del BacBio. A Saray por estar siempre dispuesta a escuchar, por todas las veces que me has ayudado en los días en los que voy de un lado a otro del pasillo como un loco, pero, sobre todo, por tu gran capacidad para hacer MSgg, ¡qué arte! A mi “compañero random de trabajo” Carlos, por ser un gran amigo y una persona a la que admiro. Muchas gracias por todas nuestras charlas de científicas (y no científicas), por leerte mis papers veinte veces y por nuestras sesiones de *brainstorming* que tanto me han estimulado y, a veces, me han ayudado a encontrar el mejor camino. A Ana y Mari, por vuestra energía, vuestras ganas de aprender, porque sin vosotras los eventos sociales del BacBio no hubieran sido iguales y, sobre todo, por vuestra habilidad para timar a la Wendy y sacarle unos eurillos a Amazon. A David, por echarme una mano con las tinciones, la microscopía y la infame PCD ¡y por las barbacoas en tu casa! y a Luis por echarme un cable con las cosas de bioinformática y por aguantarme dando por saco con los datos y las tablas del RNAseq. A Montse, por tu ánimo imbatible en el labo, por nuestros paseos por el barrio durante el confinamiento y porque, aunque hayas llegado de últimas al BacBio, creo que has sabido encajar perfectamente y eso nos ha dejado muy buenos momentos. A Jesús por echarme una mano con las cuestiones químicas y por ayudarme tantísimas veces con el FPLC y a Marisa por estar siempre dispuesta a ayudar. Muchísimas gracias a todos porque todos los años que he pasado trabajando en este grupo van a ser inolvidables y en parte, es gracias a vosotros

Entre la gente que directa o indirectamente ha contribuido a este trabajo están también aquellos que terminaron o continuaron su camino por otras vertientes. Muchas gracias

a Mari Luz, por ser una excelente compañera de poyata y siempre traer la “luz” allá donde ibas (je je). Nuestras escapadas al cine para ver las pelis en VOSE de Marvel eran una buena excusa para desconectar. A Sara, por tu meticulosidad y buen hacer en el laboratorio, de lo que he podido aprender un montón. Muchas gracias a Yurena, por allanar parte del camino que tan buenos frutos nos ha dado. A Conchita, por hacer de “mamá pato” y pasarme protocolos en aquellos primeros días en los que no tenía ni idea ni de cómo transformar un *Bacillus*. A Joaquín, por ser único, por tu inquietud y por todas las veces que me has dado alguna idea en el labo. Muchas gracias a todos.

No puedo terminar sin dedicarle algunas palabras a John y a Juan del servicio de microscopía de Bionand, que tantas veces me han tenido por allí con doscientas muestras y poco tiempo. Muchísimas gracias por haberme hecho huecos *in extremis*, por vuestra ayuda técnica y por vuestra implicación.

Por último, me gustaría dedicarles unas líneas a mis compis del CNB. A Elena, que, aunque no estuviste mucho por Málaga, siempre recordaré con cariño las risas, los dramas y alguna que otra cena en el labo hasta las tantas. Finalmente, a Julia, por ser una de las personas que más me ha ayudado con la tesis. Gracias por nuestras charlas hasta altas horas de la madrugada, por el tiempo que has dedicado a escucharme, cuando he estado a tope y cuando me ha podido el desánimo, por ayudarme a aclarar las ideas, por la infinidad de experimentos que me has sugerido, por hacer el esfuerzo de leerte lo que escribo y darme tu opinión y por haberme enviado cepas. Gracias, de corazón.

Para poder sobrevivir a una tesis doctoral, una de las claves es, a pesar de las ingentes horas de trabajo que dedicamos a esto, saber desconectar de vez en cuando. Por eso estas líneas se las quiero dedicar a todas aquellas personas ajenas a este mundillo que me han acompañado durante siempre y también durante la tesis. Muchas gracias a Víctor, María, Alberto, Marta, Tapia y Diana por todos los momentos que he podido pasar con vosotros durante este tiempo y que me han ayudado a despejar la mente. Ya son muchos años y vosotros sabéis perfectamente lo que significa para mí que estéis ahí. Simplemente, muchas gracias.

A mi familia, en primer lugar, a mi hermana Laura, porque tus visitas me han alegrado enormemente los fines de semana, sobre todo en los días en los que estaba más solo, y nos han permitido conocer Málaga juntos. Y por supuesto, a mis padres, porque yo no estaría hoy donde estoy sin todo el enorme esfuerzo que nos habéis dedicado siempre. Gracias por los valores que nos habéis transmitido, por animarme siempre a seguir adelante y a perseguir aquello que me gusta. Porque siempre habéis encontrado la

forma de salir adelante y darnos lo mejor de vosotros con la mejor de las sonrisas. Mi hermana y yo no podríamos tener más suerte. Gracias.

Por último, es imposible terminar estos agradecimientos sin mencionar a Teresa, una de las personas más importantes de mi vida y que me ha acompañado durante todo este viaje. Todavía me acuerdo de cuando éramos unos pipiolos y nos tirábamos interminables tardes en la biblioteca mientras yo estudiaba bioquímica y tú arte islámico. Teniendo inquietudes tan diferentes, sin duda, hemos sabido complementarnos y hemos podido compartir infinidad de cosas. Me siento muy afortunado de tenerte en mi vida. Muchas gracias por todos los viajes, las visitas al Grüner, por los miles de gatitos que hemos visto, por enseñarme a disfrutar de los museos y, en definitiva, por ayudarme a desconectar un poco de la tesis, pero sobre todo, por haber sabido tirar de mi cuando la frustración me ha superado, por estar ahí siempre, en los mejores y en los peores momentos, por todo lo que hemos construido juntos, por todos los retos que hemos superado y por todos los que superaremos y porque, aunque el futuro sea incierto, la única certeza es que quiero que tú estés en él.

Sin todos vosotros, este trabajo no habría sido posible. De nuevo, gracias.

My work, which I've done for a long time, was not pursued in order to gain the praise I now enjoy, but chiefly from a craving after knowledge, which I notice resides in me more than most other men.

Leeuwenhoek, Letter of 12 June 1716

CONTENTS

FIGURES

SUPPLEMENTARY FIGURES

TABLES

RESUMEN

Bacillus subtilis es una bacteria grampositiva del grupo de los Firmicutes, con bajo contenido en G + C, forma de bastón y catalasa positiva, distribuida de manera ubicua en la Naturaleza[1]. Sin embargo, se encuentra comúnmente en suelos y en asociación con la rizosfera de plantas, en la cual *B. subtilis* puede promover el crecimiento y la salud de las mismas, o en el tracto gastrointestinal (y heces) de varias especies animales, donde se ha demostrado que puede tener un efecto probiótico[2].

B. subtilis es una especie ampliamente conocida y distribuida por los laboratorios de todo el mundo debido a su sencilla manipulación genética, lo que ha contribuido al uso extendido de esta bacteria como punto de referencia en el estudio de la bacteriología, en general, y de las bacterias grampositivas en particular[3]. Esto ha desembocado a lo largo de los años en una enorme colección de datos biológicos y bioquímicos, que incluyen un genoma bien anotado, que fue uno de los primeros genomas bacterianos en ser secuenciado[4]. La cepa 168 de *B. subtilis*, la más estudiada y la más ampliamente distribuida por todo el mundo en laboratorios de investigación y entornos industriales, deriva de la llamada cepa Marburg, ahora depositada en la Colección Americana de Cultivos Tipo con el número de acceso ATCC 6051 y también conocida como NCIB3610 (del código de acceso que figura en la Colección Nacional Británica de Bacterias Industriales)[3].

Esta cepa de *B. subtilis* ha sido extensamente estudiada, entre muchos otros fines, con el objetivo de elucidar las distintas rutas de señalización y los diferentes mecanismos moleculares que gobiernan la formación de biofilm. La formación de biofilm es una habilidad intrínseca de las especies bacterianas y consiste en comunidades bacterianas formadas sobre una superficie, en las que las células bacterianas están embebidas en una matriz extracelular (MEC), autosecretada, que puede ser de naturaleza muy diversa[5]. En los biofilms, la comunicación y la diferenciación funcional son especialmente relevantes ya que, por la propia naturaleza de estas comunidades, tiene lugar la formación de gradientes de nutrientes, productos de desecho, luz, oxígeno u otros que resulta en una respuesta celular diferencial. *B. subtilis* tiene la capacidad de diferenciarse en distintos tipos celulares que desempeñan funciones distintas, como resultado de la activación de diferentes vías de señalización en respuesta a múltiples señales ambientales[6]. La capacidad de las células bacterianas para responder de manera diferente a las distintas señales dependiendo de las condiciones ambientales y el tipo de señal, conduce a diferencias de expresión génica dentro de una misma

población, creando lo que se conoce como heterogeneidad fenotípica[7]. En este sentido, los biofilm son el paradigma de la heterogeneidad y la diferenciación celular en bacterias ya que, debido a la existencia de estos gradientes químicos, tiene lugar una diferenciación espaciotemporal en la que la heterogeneidad fenotípica se traduce en una división del trabajo. En esta situación las células sacrifican su individualidad en beneficio de la comunidad, que a su vez, se adapta mejor a las cambiantes condiciones ambientales, promoviendo la supervivencia del grupo en su conjunto[8].

La formación de biofilm se caracteriza por la síntesis y secreción de la MEC, que mantiene a las células íntimamente unidas entre sí y ejerce una función protectora sobre la población bacteriana. Los elementos que forman la MEC son de naturaleza muy diversa y varían ampliamente entre diferentes especies bacterianas. En *B. subtilis*, la formación de biofilm conlleva la formación de unos pliegues muy característicos en la superficie, dando lugar a unas películas arrugadas en medio líquido y a colonias con una arquitectura tridimensional muy llamativa en medio sólido. La formación de estas características morfológicas requiere al menos tres componentes estructurales. El exopolisacárido (EPS), codificado por el operón *epsA-O*, es el componente principal de la MEC y, entre otras funciones, actúa como un cemento, manteniendo la cohesión de las células[9]. El soporte estructural de la MEC es proporcionado por un andamiaje proteico constituido por las fibras amiloides[10,11], compuestas por dos proteínas: TasA y TapA[12], que son procesadas por la peptidasa señal SipW, codificada en el mismo operón *tapa-sipW-tasA*[13]. Por último, BslA es una hidrofobina que forma una fina capa hidrofóbica que recubre la superficie del biofilm, lo que confiere a la MEC sus principales propiedades hidrofóbicas[14].

Spo0A es el principal regulador implicado en la formación de biofilm, así como en otros procesos fisiológicos de *B. subtilis* como son la esporulación o el canibalismo[5]. De hecho, los niveles de Spo0A~P determinan, en cierta medida, el proceso de toma de decisiones hacia un destino celular específico. Los niveles de este regulador están controlados por una cascada de fosforilación (phosphorelay), consistente en un conjunto de sensores quinasas, fosfotransferasas y fosfatasas que ajustan el flujo de grupos fosfato hacia el regulador maestro Spo0A en respuesta a diversos estímulos[15]. Una vez activado, Spo0A~P participa directamente en la inducción de los operones *epsA-O* y *tapA-sipW-tasA*, y el gen *bslA*[5]. Los operones *eps* y *tapA* son reprimidos de forma constitutiva por el regulador maestro SinR, que se une a las regiones promotoras de estos operones[16]. Niveles intermedios de Spo0A~P determinan la expresión heterogénea de *sinI* únicamente en células productoras de MEC[17]. SinI es un represor de SinR, con la que forma un complejo que impide la unión de SinR al ADN[18] y, por

tanto, actúa como un antirepresor, de manera que en estas células se induce la expresión de los genes responsables de la síntesis de la MEC y, en consecuencia, la formación de biofilm. Junto con Spo0A, diferentes subredes reguladoras participan en el control de la expresión de estos genes a diferentes niveles. La proteína SlrR es un parálogo de SinR y añade un paso más a la regulación de la expresión de los operones *eps* y *tapA*. SinR y AbrB, que es un represor maestro de los genes del estado de transición, normalmente reprimen a SlrR. Sin embargo, al comienzo de la fase estacionaria, cuando se libera la represión mediada por AbrB, se produce la inhibición de SinR provocada por SinI en las células productoras de MEC. En estas células se activa la expresión de *slrR*, que es una proteína que captura a SinR formando un heterodímero que, además de favorecer la expresión de los operones *eps* y *tapA* al prevenir la represión mediada por SinR[19,20], inhibe la motilidad bacteriana mediante la inhibición de la expresión del gen codificante de la flagelina *hag* o de las autolisinas requeridas para la separación después de la división celular[19,21], comprometiendo a las células a la adopción de un estilo de vida sésil de cadenas celulares productoras de MEC.

La formación de la MEC, análoga a un tejido, permite a las bacterias responder de manera eficiente a un entorno en constante cambio. Por ello, se sabe que la formación de biofilm y, en concreto, los distintos componentes de la MEC, son importantes para la interacción de los microorganismos con las plantas, contribuyendo a la interacción beneficiosa (por ejemplo, colonización y persistencia en los diferentes nichos de la planta[22]) o patógena. Además, desde el lado de la planta, las señales bacterianas que modulan la formación de biofilm y desencadenan la producción de la MEC, pueden actuar proporcionando refugio para los microorganismos. Estos, a su vez, benefician o dañan al huésped debido a que los biofilm bacterianos contienen diferentes metabolitos secundarios y muchas otras moléculas que, eventualmente, son capaces de contribuir a la salud o a la enfermedad de la planta, dependiendo de la interacción[23].

TasA es el principal componente proteico de la MEC y la proteína mayoritaria de las fibras amiloides y forma parte de una familia muy diversa de proteínas denominadas amiloides funcionales. Las proteínas amiloides tienen asociada una mala reputación debido a que son los principales agentes causales de enfermedades neurodegenerativas como el Alzheimer o el Parkinson. Sin embargo, se ha demostrado que este tipo de proteínas desempeñan funciones biológicas muy diversas en multitud de sistemas, razón por la cual algunas de ellas se han denominado amiloides funcionales. Aunque las proteínas amiloides carecen de similitudes aparentes en sus secuencias de aminoácidos, presentan un plegamiento y una estructura secundaria y

cuaternaria en común, caracterizada por la formación de fibras enriquecidas en láminas-β en la cual estas láminas se disponen de manera cruzada perpendicularmente al eje de la fibra[24]. Esta estructura confiere a las proteínas amiloides propiedades únicas, con una gran estabilidad y resistencia frente a diversas condiciones fisicoquímicas.

Las fibras amiloides de *B. subtilis* son un ejemplo de los muchos sistemas amiloides bacterianos que existen en la naturaleza, y que, en muchos casos, consisten en entidades macromoleculares compuestas por el amiloide funcional principal junto con sus correspondientes proteínas accesorias, necesarias para la correcta formación y función de estas fibras. En este caso, el sistema de *B. subtilis* está compuesto por dos proteínas: el amiloide principal TasA y la proteína accesoria TapA. TasA se descubrió inicialmente en la capa más externa de las endosporas y, además, esta proteína mostró una actividad antimicrobiana de amplio espectro. Estas dos características llevaron a que esta proteína recibiera su nombre, debido a las siglas en inglés de componente antibacteriano de la espora dependiente de traslocación (**t**ranslocation-dependent **a**ntimicrobial **s**pore component)[25]. Los factores que afectan la polimerización de TasA se han estudiado *in vitro* en una conformación previamente agregada y purificada directamente de la MEC de *B. subtilis*, lo que demuestra que determinadas condiciones ambientales, en este caso, el pH ácido y la presencia de superficies hidrofóbicas[26], son determinantes para desencadenar el proceso de amiloidogénesis de esta proteína. En el sistema amiloide de *B. subtilis*, además de TasA, existen otras dos proteínas, SipW y TapA, que están involucradas en el ensamblaje de la fibra. SipW es una peptidasa señal que se encarga del procesamiento de las formas inmaduras de TasA y TapA, que contienen un péptido señal para su translocación al exterior de la célula, donde se produce la formación de las fibras amiloides[13,25]. TapA es una proteína necesaria para la formación de la fibra de TasA, y su ausencia disminuye la estabilidad de esta proteína en la célula, da lugar a un menor número de fibras y estas carecen de aparente unión a la superficie celular, de ahí el nombre de TapA (**T**asA anchoring and **a**ssembly **p**rotein)[12]. Sus principales funciones son favorecer la polimerización eficiente de TasA, actuando como nucleador[27], y mantener el anclaje de estas fibras a la superficie celular.

Sin embargo, a pesar de la información funcional que actualmente tenemos sobre la fibra amiloide, se necesita una descripción estructural detallada de ambas proteínas, especialmente en su estado fibrilar, para comprender cómo se forman y cómo responde su conformación a los distintos estímulos ambientales en el contexto de la formación de biofilm. En nuestro esfuerzo por llevar a cabo la caracterización estructural de los filamentos de TasA, desarrollamos y optimizamos protocolos para la sobreexpresión y purificación de TasA. La expresión heteróloga en *Escherichia coli* es un requisito previo

necesario para estudiar el proceso de polimerización y las fibras de TasA en ausencia de TapA, ya que ésta está normalmente presente en los filamentos obtenidos desde células de *B. subtilis*[12].

El análisis preliminar de la secuencia de TasA, reveló que esta proteína está bien conservada en todo el género *Bacillus*, pero puede separarse filogenéticamente en dos grupos distintos: en el grupo de *B. subtilis*, que engloba a otras especies no patógenas como *B. amyloliquefaciens* o *B. pumillus*, la proteína es de mayor tamaño, 261 aminoácidos en el caso de *B. subtilis*; y en el grupo de *B. cereus* y otras especies relacionadas, como *B. thuringiensis* o *B. anthracis*, en el que la proteína es significativamente más pequeña y tiene una longitud de unos 170 aminoácidos. La comparación entre TasA de *B. subtilis* y TasA de *B. cereus* mostró que, en ambas cepas, representativas de cada grupo, la proteína comparte un ~35% de homología de secuencia entre las dos especies, ubicadas principalmente en la mitad N-terminal, lo cual, aparentemente, es suficiente para la funcionalidad relacionada con la multicelularidad y la formación de biofilm[28].

Nuestros resultados demostraron que TasA recombinante purificada desde *E. coli* es biológicamente funcional, ya que es capaz de restaurar la formación de biofilm cuando es añadida exógenamente a un mutante en *tasA*. Además, hemos podido ver cómo, *in vitro*, esta proteína es capaz de autoensamblarse formando fibras con una morfología muy característica, recta y uniforme, en la que los protofilamentos (es decir, la entidad fibrilar más pequeña de la arquitectura cuaternaria) se disponen en una organización supramolecular en forma de haces constituidos de protofilamentos apilados y asociados lateralmente. El diámetro de los protofilamentos es de ~5 nm, y su longitud es variable (de hasta varias micras). Curiosamente, se observa una disposición simétrica de repeticiones uniformes (de unos ~ 5 nm) que discurren de forma perpendicular al eje primario del filamento. Este autoensamblaje, coincide con el enriquecimiento progresivo en estructura secundaria de láminas-β, ya que se observa un incremento paulatino en la unión a tioflavina-T, un colorante típico empleado para la detección de amiloides[29]. Por último, demostramos que estos filamentos presentan el canónico patrón de difracción de rayos X de las fibras amiloides, con reflexiones a 4,7 y 10 Å, correspondientes a las distancias entre segmentos-β y láminas-β respectivamente, demostrando la típica arquitectura en β-cruzada.

Así mismo, se llevó a cabo una caracterización de TasA en su forma fibrilar mediante espectroscopía de resonancia magnética nuclear en estado sólido (SSNMR, por sus siglas en inglés). El análisis espectral de la estructura los filamentos de TasA mediante

SSNMR reveló que estas fibras exhiben un alto grado de orden estructural, compuesto por subunidades de TasA bien ordenadas. El análisis de la estructura secundaria de los filamentos muestra un enriquecimiento en el contenido de la láminas-β, aunque se observa una proporción inusual de hélice-α. Además, este análisis demostró la existencia de un núcleo amiloide, rígido y altamente ordenado con disposición en β-cruzada, que no incluye la secuencia correspondiente a toda la proteína. En efecto, vimos que solo una parte, específicamente, la parte N-terminal de la proteína, contribuye a la formación de este núcleo amiloide. Esto se debe a la presencia en esta región de la proteína de varias características propias de la secuencia que contribuyen a la tendencia amiloide de TasA y a la formación de la fibra, como son en este caso, las repeticiones aminoacídicas imperfectas y dos regiones amiloidogénicas dentro de este núcleo amiloide.

Además de esto, también llevamos a cabo el estudio y caracterización estructural de la proteína accesoria TapA. El análisis de esta proteína mostró que, *in vitro*, es capaz de autoensamblarse en agregados amiloides amorfos con un pliegue estructural en β-cruzada, similar al observado para TasA, exhibiendo todas las características típicas de las proteínas amiloides. Un análisis posterior mediante SSNMR demostró que la arquitectura de TapA en su forma ensamblada es muy similar a la de las fibras de TasA. Además, el co-ensamblaje *in vitro* de las dos proteínas no perturba la arquitectura global del filamento de TasA, lo cual resalta la posibilidad de que TapA sea una parte integral de la fibra y sugiere que este co-ensamblaje pueda ocurrir en el contexto celular durante la formación de biofilm.

A parte de ser un modelo para el estudio de la formación de comunidades bacterianas multicelulares, *B. subtilis* es también ampliamente estudiado por su capacidad como agente de biocontrol. Uno de los principales mecanismos por los cuales *B. subtilis* y otros microorganismos de especies filogenéticamente cercanas son buenos candidatos para desarrollar productos para este fin, es la producción de lipopéptidos cíclicos no-ribosomales, algunos de los cuales, presentan actividad antimicrobiana[30]. Curiosamente, uno de estos lipopéptidos, la surfactina, se ha descrito como un autoinductor de la formación de biofilm *in vitro*[31], pero también en la filosfera de melón[32], donde se ha visto que la formación de biofilm es relevante para el antagonismo de ciertas cepas de *Bacillus sp.* frente a distintos patógenos de plantas. Por ello, nos preguntamos cómo de relevantes son los distintos componentes estructurales de la MEC de *B. subtilis* para la interacción de este microorganismo con la planta y cómo contribuyen a su actividad de biocontrol.

Como era de esperar, dadas sus funciones estructurales, todos los mutantes en los distintos componentes de la MEC mostraron una supervivencia reducida; sin embargo, el mutante en *tasA* (Δ*tasA*) mostro una adhesión a hojas de melón significativamente menor que el resto de las cepas estudiadas y, además, su persistencia sobre la superficie vegetal disminuyó de forma continuada y progresiva en el tiempo en comparación con las poblaciones de los mutantes en el EPS o en BslA. Basándonos en la reducida capacidad de estas cepas mutantes para persistir sobre la planta y su incapacidad para ensamblar un biofilm, hipotetizamos que estas cepas podían estar también afectadas sus interacciones antagonistas con *Podosphaera xanthi* (un importante hongo biotrofo fitopatógeno que afecta especialmente a las cucurbitáceas[33]) en la filosfera. Sin embargo, observamos que Δ*tasA* no presentaba diferencias significativas respecto a la cepa silvestre (WT) en cuanto a la actividad antagonista frente a este patógeno. Esto se debe a que, según demostró nuestro análisis de espectrometría de masas, Δ*tasA* produce en las plantas inoculadas en torno a un orden de magnitud más cantidad de fengicina, el principal lipopéptido con capacidad antifúngica producido por *B. subtilis*, que la cepa WT.

Este hallazgo nos llevó a investigar un posible papel de TasA, más allá de su funcionalidad estructural durante el ensamblaje de la MEC. Mediante un análisis transcriptómico, vimos que la deleción de TasA tiene un efecto pleiotrópico en la expresión génica, dando lugar a cambios de expresión en casi un tercio del genoma en algunos momentos del desarrollo de la colonia. Todos los cambios transcripcionales que observados en Δ*tasA*, apuntan hacia un reordenamiento metabólico completo y un exceso de estrés celular, con expresión diferencial de genes relacionados con: síntesis de metabolitos secundarios, respiración anaeróbica y fermentación, estrés general y daño en el ADN entre otras funciones. Un análisis más en profundidad a nivel de colonia reveló que, de hecho, las células Δ*tasA* exhiben una amplia gama de alteraciones y daños celulares. En primer lugar, las células que carecen de TasA muestran una menor tasa respiratoria y una mayor generación de especies reactivas de oxígeno. Esto último, es probablemente la causa de algunas de las diferentes alteraciones citológicas encontradas en las células Δ*tasA*, como son una menor tolerancia a la peroxidación lipídica o la presencia de roturas de cadena en el ADN. Además de esto, las alteraciones metabólicas se traducen en una mayor producción de fengicina por parte de Δ*tasA*, consistente con los resultados obtenidos en planta, y una disminución en el pH intracelular. Las células Δ*tasA*, además, presentan alteraciones del potencial de membrana y un aumento en la fluidez de la membrana plasmática. Esta desestabilización de la membrana celular podría ser, de hecho, la fuente de todos los

cambios observados los cuales, eventualmente, conducen a un aumento de la muerte celular en la colonia Δ*tasA* que es, en promedio, alrededor de un 20% mayor que la observada en las colonias WT.

Este papel de TasA en la prevención de la muerte celular prematura es independiente del papel de esta proteína en la formación de biofilm, ya que demostramos que cepas mutantes afectadas en la formación de biofilm, como son, por ejemplo, un mutante en *tapA* o un mutante en *sinI*, no se ven afectadas en sus niveles de viabilidad en comparación con la cepa WT. Para confirmar estos resultados, construimos una cepa que expresa una versión mutada de TasA, incapaz de ensamblar una MEC completamente estructurada, pero en la que TasA es estable y está presente en la MEC en cantidades similares a las encontradas en la cepa WT. Esta versión mutada de TasA está, presumiblemente, afectada en su capacidad para formar fibras amiloides. Sin embargo, esta proteína mutada es capaz de restaurar a la normalidad todos los fenotipos fisiológicos alterados en Δ*tasA*. Por lo tanto, podemos asignar a TasA una nueva función previamente desconocida, en la prevención de la muerte celular prematura durante el desarrollo de las comunidades bacterianas de *B. subtilis*.

Las alteraciones de membrana que tienen lugar en Δ*tasA* sugieren que el mecanismo molecular por el cual se produce esta nueva función puede estar relacionado con la membrana celular, ya que alteraciones en esta estructura celular crítica, son consistentes con la gran extensión de los cambios observados en Δ*tasA*. Especialmente, el aumento de la fluidez de la membrana en comparación con la cepa WT, apunta hacia cambios específicos relacionados con las flotillinas, que organizan complejos de señalización en la membrana que regulan diversos procesos biológicos al actuar como un andamiaje proteico[34-37]. Las flotilinas se localizan en dominios específicos dentro de la membrana celular, denominados microdominios funcionales de membrana (FMM, por sus siglas en inglés)[35], que se caracterizan por estar enriquecidos en ciertas proteínas y tener una composición lipídica diferente[37,38]. Estas proteínas presentan un patrón de distribución típico en forma de focos que se distribuyen heterogéneamente a lo largo de la membrana celular[35,36]. Al estudiar la localización del flotillina FloT en las células Δ*tasA* mediante una fusión traduccional a YFP, descubrimos que esta proteína se deslocaliza en el mutante y pierde el patrón de distribución típico con su localización focal dentro de la membrana celular. Por ello, decidimos estudiar la localización celular de TasA empleando varias metodologías. Primero, llevamos a cabo un fraccionamiento químico de la membrana celular en función de su solubilidad a detergentes. Este tratamiento divide la membrana en fracciones resistentes o sensibles a los detergentes (DRM o DSM, respectivamente, según sus siglas en inglés)[35,39]. La

DRM, resistente a la acción de los detergentes, contiene la mayoría de las proteínas de membrana que están presentes en los FMM. El análisis de estas fracciones mediante Western blot utilizando un anticuerpo anti-TasA, localizó a la proteína principalmente en la fracción DRM de la membrana y en el citosol. En segundo lugar, el análisis de la localización de TasA por microscopía confocal, utilizando una fusión traduccional a mCherry, reveló que esta proteína aparece distribuida de forma homogénea en la superficie celular y, en ocasiones, se pudieron observar dos pequeños focos en los polos celulares. Curiosamente, esto también se observó cuando se analizaron protoplastos bacterianos, es decir, células que se han sometido a un tratamiento con lisozima para eliminar la pared celular. En general, estos resultados indican que TasA es una proteína unida a la membrana.

Dada la localización de TasA en la membrana y la alteración en el patrón de distribución de FloT en ausencia de TasA, nos preguntamos si la hipotética interacción de FloT y TasA dentro de la membrana celular podría ser una posible explicación para los cambios fenotípicos observados en ausencia de esta proteína. Para probar esta hipótesis, construimos una cepa portadora de fusiones de TasA y FloT a distintos genes reporteros en un fondo genético WT. El análisis de microscopía de fluorescencia de las células bacterianas seleccionadas no mostró una colocalización significativa entre las dos proteínas. Además, nos preguntamos si la pérdida de la distribución de FloT estaba relacionada de alguna manera con el aumento de muerte celular observado en las células Δ*tasA*. El análisis de un mutante doble en las dos flotilinas presentes en el genoma de *B. subtilis* demostró que la ausencia de estas proteínas no tiene un efecto sobre la viabilidad celular y que, por tanto, su alteración en Δ*tasA* es la consecuencia, y no la causa, de los cambios que tienen lugar en esta cepa mutante.

Para estudiar cómo se une y qué efectos tiene TasA sobre la membrana plasmática, analizamos *in vitro* la interacción de esta proteína con lípidos de diferente naturaleza. En primer lugar, se llevó a cabo la purificación de TasA y su encapsulación en vesículas lipídicas multilamelares con la composición lipídica típica de *B. subtilis* con el objetivo de estudiar la estructura lipídica en presencia de TasA mediante SSNMR. Los resultados de este análisis demuestran que las bicapas lipídicas pueden acomodar TasA sin perturbar su integridad o estructura y, de hecho, TasA aumenta la rigidez global de la estructura lipídica. Al mismo tiempo, se estudió la interacción de TasA con membranas *in vitro* mediante vesículas lipídicas unilamelares de distintas composiciones lipídicas, con el objetivo de estudiar el efecto de la proteína sobre las mismas cuando ésta es añadida de forma exógena. Estos experimentos determinaron que la interacción de TasA con los lípidos está determinada por la composición lipídica y que, en estas

interacciones, una secuencia amiloidogénica en la región N-terminal de la proteína, que curiosamente, exhibe un alto grado de hidrofobicidad, es relevante para este proceso.

A modo resumen, los resultados experimentales derivados de esta tesis doctoral nos han permitido obtener las siguientes conclusiones: i) TasA y TapA son proteínas de naturaleza amiloide, capaces de autoensamblarse en entidades moleculares con un pliegue estructural similar, lo que sugiere un posible co-ensamblaje *in vivo* de ambas proteínas; ii) TasA tiene una función dual en *B. subtilis*: por un lado, tiene una función estructural como parte de la MEC y por otro, actúa manteniendo la estabilidad celular previniendo la muerte celular prematura de la población; y iii) TasA es una proteína presente en la membrana celular implicada en el control de la dinámica de la membrana y la estabilidad de esta estructura celular.

REFERENCIAS

1 Willey, J. M., Sherwood, L. M. & Woolverton, C. J. in *Microbiología de Prescott, Harley y Klein* (eds María Álvarez & Cristina Sánchez) Ch. 23, (McGraw and Hill-Interamericana de España, 2008).

2 Earl, A. M., Losick, R. & Kolter, R. Ecology and genomics of *Bacillus subtilis*. *Trends Microbiol.* **16**, 269-275, (2008).

3 Zeigler, D. R. *et al.* The origins of 168, W23, and other *Bacillus subtilis* legacy strains. *J. Bacteriol.* **190**, 6983-6995, (2008).

4 Kunst, F. *et al.* The complete genome sequence of the gram-positive bacterium *Bacillus subtilis*. *Nature* **390**, 249-256, (1997).

5 Vlamakis, H., Chai, Y., Beauregard, P., Losick, R. & Kolter, R. Sticking together: building a biofilm the *Bacillus subtilis* way. *Nat. Rev. Microbiol.* **11**, 157-168, (2013).

6 Lopez, D., Vlamakis, H. & Kolter, R. Generation of multiple cell types in *Bacillus subtilis*. *FEMS Microbiol. Rev.* **33**, 152-163, (2009).

7 Lopez, D. & Kolter, R. Extracellular signals that define distinct and coexisting cell fates in *Bacillus subtilis*. *FEMS Microbiol. Rev.* **34**, 134-149, (2010).

8 van Gestel, J., Vlamakis, H. & Kolter, R. Division of Labor in Biofilms: the Ecology of Cell Differentiation. *Microbiol. Spectr.* **3**, MB-0002-2014, (2015).

9 Marvasi, M., Visscher, P. T. & Casillas Martinez, L. Exopolymeric substances (EPS) from *Bacillus subtilis*: polymers and genes encoding their synthesis. *FEMS Microbiol. Lett.* **313**, 1-9, (2010).

10 Branda, S. S., Chu, F., Kearns, D. B., Losick, R. & Kolter, R. A major protein component of the *Bacillus subtilis* biofilm matrix. *Mol. Microbiol.* **59**, 1229-1238, (2006).

11 Romero, D., Aguilar, C., Losick, R. & Kolter, R. Amyloid fibers provide structural integrity to *Bacillus subtilis* biofilms. *Proc. Natl. Acad. Sci. USA* **107**, 2230-2234, (2010).

12 Romero, D., Vlamakis, H., Losick, R. & Kolter, R. An accessory protein required for anchoring and assembly of amyloid fibres in *B. subtilis* biofilms. *Mol. Microbiol.* **80**, 1155-1168, (2011).

13 Tjalsma, H. *et al.* Conserved serine and histidine residues are critical for activity of the ER-type signal peptidase SipW of *Bacillus subtilis*. *J. Biol. Chem.* **275**, 25102-25108, (2000).

14 Hobley, L. *et al.* BslA is a self-assembling bacterial hydrophobin that coats the *Bacillus subtilis* biofilm. *Proc Natl Acad Sci U S A* **110**, 13600-13605, (2013).

15 Stragier, P. & Losick, R. Molecular genetics of sporulation in *Bacillus subtilis*. *Annu. Rev. Genet.* **30**, 297-241, (1996).

16 Kearns, D. B., Chu, F., Branda, S. S., Kolter, R. & Losick, R. A master regulator for biofilm formation by *Bacillus subtilis*. *Mol. Microbiol.* **55**, 739-749, (2005).

17 Chai, Y., Chu, F., Kolter, R. & Losick, R. Bistability and biofilm formation in *Bacillus subtilis*. *Mol. Microbiol.* **67**, 254-263, (2008).

18 Bai, U., Mandic-Mulec, I. & Smith, I. SinI modulates the activity of SinR, a developmental switch protein of *Bacillus subtilis*, by protein-protein interaction. *Genes Dev.* **7**, 139-148, (1993).

19 Chai, Y., Norman, T., Kolter, R. & Losick, R. An epigenetic switch governing daughter cell separation in *Bacillus subtilis*. *Genes Dev.* **24**, 754-765, (2010).

20 Chai, Y., Kolter, R. & Losick, R. Reversal of an epigenetic switch governing cell chaining in *Bacillus subtilis* by protein instability. *Mol. Microbiol.* **78**, 218-229, (2010).

21 Cozy, L. M. *et al.* SlrA/SinR/SlrR inhibits motility gene expression upstream of a hypersensitive and hysteretic switch at the level of sigma(D) in *Bacillus subtilis*. *Mol. Microbiol.* **83**, 1210-1228, (2012).

22 Danhorn, T. & Fuqua, C. Biofilm formation by plant-associated bacteria. *Annu. Rev. Microbiol.* **61**, 401-422, (2007).

23 Rudrappa, T., Biedrzycki, M. L. & Bais, H. P. Causes and consequences of plant-associated biofilms. *FEMS Microbiol. Ecol.* **64**, 153-166, (2017).

24 Knowles, T. P., Vendruscolo, M. & Dobson, C. M. The amyloid state and its association with protein misfolding diseases. *Nat. Rev. Mol. Cell. Biol.* **15**, 384-396, (2014).

25 Stover, A. G. & Driks, A. Secretion, localization, and antibacterial activity of TasA, a *Bacillus subtilis* spore-associated protein. *J. Bacteriol.* **181**, 1664-1672, (1999).

26 Chai, L. *et al.* Isolation, characterization, and aggregation of a structured bacterial matrix precursor. *J. Biol. Chem.* **288**, 17559-17568, (2013).

27 Romero, D., Vlamakis, H., Losick, R. & Kolter, R. Functional analysis of the accessory protein TapA in *Bacillus subtilis* amyloid fiber assembly. *J. Bacteriol.* **196**, 1505-1513, (2014).

28 Caro-Astorga, J., Perez-Garcia, A., de Vicente, A. & Romero, D. A genomic region involved in the formation of adhesin fibers in Bacillus cereus biofilms. *Front. Microbiol.* **5**, 745, (2014).

29 LeVine, H., 3rd. Thioflavine T interaction with synthetic Alzheimer's disease beta-amyloid peptides: detection of amyloid aggregation in solution. *Protein Sci.* **2**, 404-410, (1993).

30 Ongena, M. & Jacques, P. Bacillus lipopeptides: versatile weapons for plant disease biocontrol. *Trends Microbiol.* **16**, 115-125, (2008).

31 Lopez, D., Vlamakis, H., Losick, R. & Kolter, R. Paracrine signaling in a bacterium. *Genes Dev.* **23**, 1631-1638, (2009).

32 Zeriouh, H., de Vicente, A., Perez-Garcia, A. & Romero, D. Surfactin triggers biofilm formation of *Bacillus subtilis* in melon phylloplane and contributes to the biocontrol activity. *Environ. Microbiol..* **16**, 2196-2211, (2014).

33 Perez-Garcia, A. *et al.* The powdery mildew fungus Podosphaera fusca (synonym Podosphaera xanthii), a constant threat to cucurbits. *Mol. Plant Pathol.* **10**, 153-160, (2009).

34 Bach, J. N. & Bramkamp, M. Flotillins functionally organize the bacterial membrane. *Mol. Microbiol* **88**, 1205-1217, (2013).

35 Lopez, D. & Kolter, R. Functional microdomains in bacterial membranes. *Genes Dev.* **24**, 1893-1902, (2010).

36 Schneider, J. *et al.* Spatio-temporal remodeling of functional membrane microdomains organizes the signaling networks of a bacterium. *PLoS Genet.* **11**, e1005140, (2015).

37 Bramkamp, M. & Lopez, D. Exploring the existence of lipid rafts in bacteria. *Microbiol. Mol. Biol. Rev.* **79**, 81-100, (2015).

38 Lopez, D. & Koch, G. Exploring functional membrane microdomains in bacteria: an overview. *Curr. Opin. Microbiol.* **36**, 76-84, (2017).

39 Donovan, C. & Bramkamp, M. Characterization and subcellular localization of a bacterial flotillin homologue. *Microbiology* **155**, 1786-1799, (2009).

Chapter I

General introduction and objectives

Parts of the content of this chapter have been published in:

Jesús Cámara-Almirón, Joaquín Caro-Astorga, Antonio de Vicente and Diego Romero. Beyond the expected: the structural and functional diversity of bacterial amyloids. *Critical Reviews in Microbiology* **44:6**, 653-666 (2018).

Jesús Cámara-Almirón, Carlos Molina-Santiago, Antonio de Vicente, Francisco M. Cazorla and Diego Romero. Studying bacterial physiology for improving full fitness in *Strategies to develop successful Biocontrol Agents*. Submitted.

MICROBIOLOGY AND THE BIRTH OF BACTERIOLOGY: HISTORICAL BACKGROUND

Since the moment of birth, we are completely covered by bacteria. This microbiological tapestry established inside and outside of our body constitutes what has been denominated as the (human, in this case) microbiome, a term coined for the first time in 1988[1]. However, microorganisms have been studied since much earlier. One of the earliest references to microorganisms in modern times were given during the Renaissance and are the hypothesis of Girolamo Fracastoro. This Italian phyisician, poet and scholar in many other disciplines, speculated, based on his observations, that infectious diseases were transmitted by small entities invisible to the human eye through direct or indirect contact with an infected person or its belongings. In fact, he coined the term *fomites* to refer to inert objects, such as clothes, that could transmit the disease due to the presence of "seeds" of the contagion[2]. The breakthrough came in the 17th century, with Robert Hooke and Antonie Van Leeuwenhoek[3]. Robert Hooke was a natural philosopher and a scholar that published the first description of molds in his book *Micrographia* in 1665, in which he used a microscope composed of two convex lenses to describe the microscopical view of several objects (Fig. 1.1A). Practically at the same time, 8 years later, Antonie Van Leeuwenhoek, a draper and store owner in Holland, observed for the first-time bacteria and other microscopic forms of life using a rudimentary single lens microscope of his own design (Fig. 1.1B).

The birth of bacteriology as a branch of microbiology took place in the 19th century from the hands of Louis Pasteur, Robert Koch and Ferdinand Cohn. Louis Pasteur was known for his works in fermentation, where he also described a method for preventing the growth of microorganisms in food and beverages (pasteurization), which he knew were the cause of contamination. He was also a fervent detractor of the theory of spontaneous generation, which he disproves with a series of simple experiments. In contrast, his later works in disease and vaccination supported the germ theory of disease[4]. In line with this theory, Robert Koch, who developed the modern culture techniques in bacteriology, was able to isolate in the laboratory the causative agents of many illness of the time, such as cholera, anthrax or tuberculosis and based on that, he formulated his famous postulates[5].

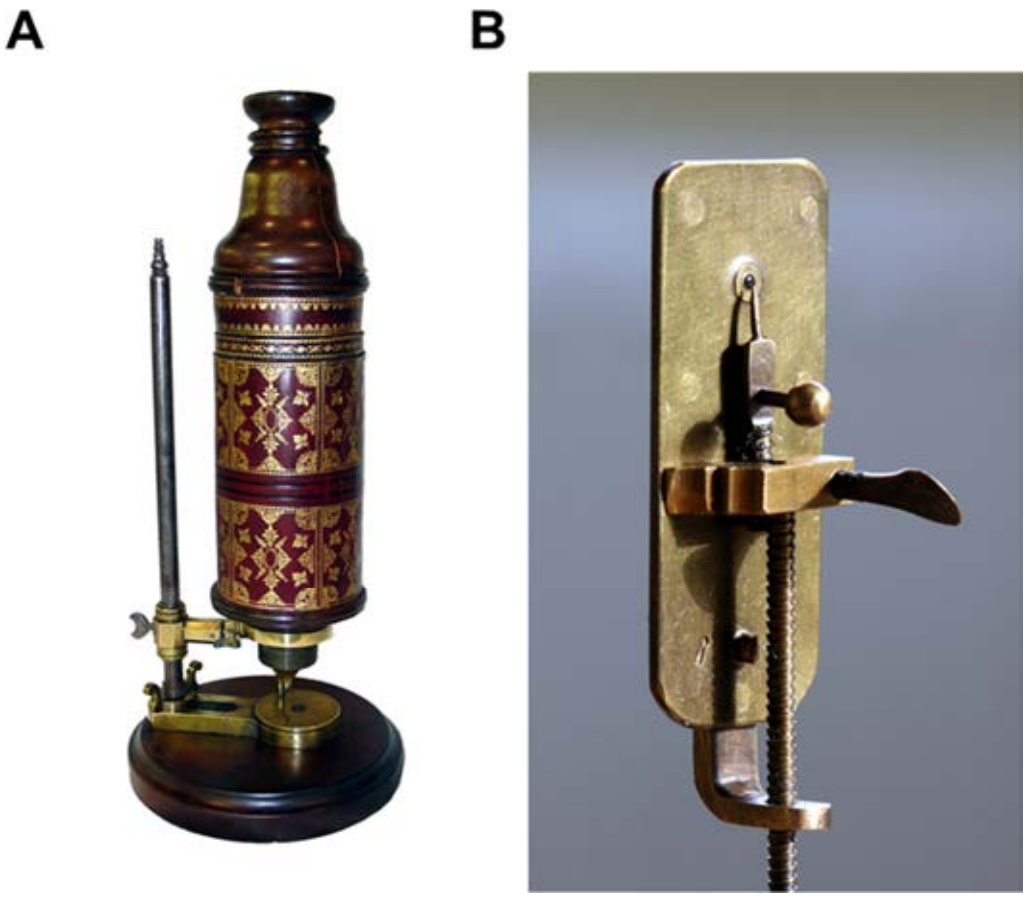

Figure 1.1. Microscopes made by Leeuwenhoek and Hooke. A) Image of Robert Hooke's microscope manufactured by Christopher Cock. From the Billings Microscope Collection of the National Museum of Health and Medicine of the US army, Silver Spring, Maryland, United States. **B)** Replica of the single lens microscope manufactured by Antonie Van Leeuwenhoek. Images have been taken from Wikimedia Commons.

The third name in the list, not as renowned as the other two, is Ferdinand Cohn, contemporary of both Pasteur and Koch. However, his contributions to bacteriology were as relevant, especially for the contents of this thesis. Cohn was mainly a botanist, however, in the study of plant cell biology, he investigated in detail the development of algae, fungi and bacteria with the use of one of the best microscopes at the time. He worked extensively in taxonomy and classification of bacteria. He was one of the first scientists to suggest the classification of bacteria according to shape (being sphere-shaped, rod-like, filamentous and screw-like), a character that is still used at the present day. Interestingly, Cohn studied the heat-resistant bacteria that survived in hay infusion. He studied a form of the bacteria that resisted boiling and contained the germ of the bacterium, from which the thermolabile phase will develop. He described, with outstanding microscopic detail at the time, the complete life cycle of *Bacillus spp.* and how vegetative cells will become endospores upon heating that will then germinate to give rise to a new population[6].

GRAM-POSITIVE BACTERIA AND THE STUDY OF *Bacillus subtilis* AS A MODEL ORGANISM

The formation of the endospore as a form of resistance and the thick peptidoglycan layers are the exclusive traits of gram-positive bacteria. This classification (gram-positive or gram-negative) proposed by Hans Christian Gram, who developed a staining to visualize bacteria under the microscope, is made based on the structure of the cell wall and its differential tinctorial features[7]. As it is widely known today, the bacterial cell wall consists of repeating linear units of N-acetylglucosamine (NAG) and N-acetylmuramic acid (NAM) linked by β-1-4 bonds that are covalently bound at their ends to a peptide stem. Normally, the glycan part is very conserved among the different species, the peptide part, however, can vary between different bacteria and usually contains D-amino acids[8]. The different forms of cross-links that exist to connect the peptides to the peptidoglycans, is one of the main features of the cell wall of gram-positive bacteria. Another one is the major thickness of this layer, ranging from 30 to 100 nm or even thicker, compared to gram-negative bacteria, in which the peptidoglycan is only a few nm thick[8]. Furthermore, the gram-positive cell wall also contains an exclusive component: the teichoic acids. Two different types of teichoic acids are found in the gram-positive cell wall: the cell wall teichoic (WTA) acids and the lipoteichoic acids (LTA). They are negatively charged polymers of glycerol or ribitol phosphate linked to a glycan part via a phosphodiester bond. Both types of molecules are variable in structure depending on the bacterial family, however, LTAs are normally more conserved than WTAs, that possess more variable properties depending on the species[9]. Their functions involve protection against environmental hardships[10], enzymatic control of autolysins and cation concentration in the cell wall[11], pathogenicity[12], biofilm formation (in some cases)[13] or phage infection (acting as receptors)[14,15].

Endospore formation is the other well-defined feature present only in some genera of gram-positive bacteria, specifically in *Bacillus spp.* and *Chlostridium spp*, the most studied, which form endospores through an evolutionary conserved mechanism[16]. Nutrient depletion seems to be the clearest sign to trigger the sporulation pathways, however, there are a myriad of environmental signals that can generate higher levels of sporulation in the laboratory. In *Bacillus subtilis*, the sporulation process is controlled by the phosphorelay (Fig. 1.2), which are a set of sensor kinases, phosphotransferases and phosphatases that tune the phosphorylation of the master regulator Spo0A in response to diverse stimuli[17]. This protein, when it is active in its phosphorylated state (Spo0A~P), controls the expression of the sigma factors required for the expression of the different

sporulation regulons and regulates the genes necessary for size asymmetric division, which is the first step in the complex process of endospore formation (Fig. 1.3).

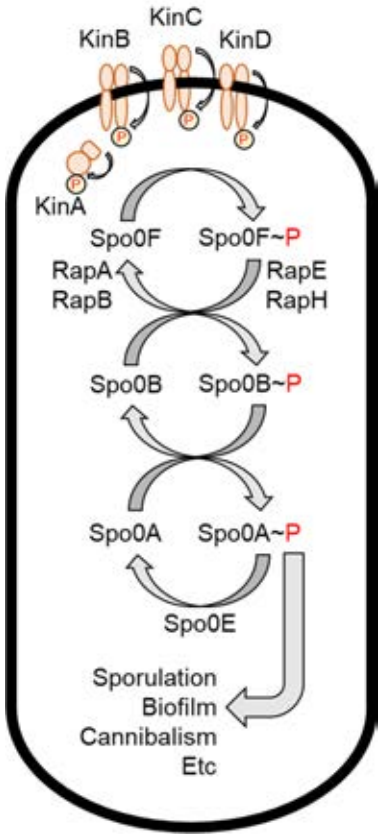

Figure 1.2. Schematic representation of the *B. subtilis* phosphorelay for cell fate determination. The phosphorelay is a signal transduction pathway that is comprised of several modules. The sensor module involves several histidine kinases (KinA, KinB, KinC and KinD) that activate in response to multiple environmental cues. The different kinases undergo autophosphorylation and transfer of this phosphate to the phosphotransferases module (Spo0F and Spo0B), that transfer the signal to the final acceptor, the master transcriptional regulator Spo0A. Different phosphatases (RapA, RapB, RapE and RapH for Spo0F and Spo0E for Spo0A) modulate the signal that reaches Spo0A at different points in the phosphorelay, which will affect the levels of activated Spo0A (Spo0A~P) and therefore, the phenotypic differentiation process.

The irregular division gives rise to the sporangium[16], which is a compartmentalized cell constituted by the forespore of smaller size, and the larger mother cell separated by a septum. After the sporangium is fully formed, the forespore is engulfed by the mother cell, creating a doubled-membrane compartment. At the same time two protective surface structures are formed to cover the final endospore: the peptidoglycan cortex, which is formed between the forespore membrane; and the spore coat, which is a protein-comprised complex structure that constitutes the external layer of the endospore. In the later sporulation stages, the core of the forespore, the inner compartment that contains the genome, is partially dehydrated and most of the water is substituted by dipicolinic acid, which comprises nearly ~10-15% of the dry weight of the endospore. This compound forms a complex with free Ca^{2+} ions, binding water molecules that cause the characteristic dehydration of the spore[16]. Furthermore, dipicolinic acid is able to

intercalate into DNA, which along with other endospore-specific proteins, protects DNA from heat denaturation, conferring the endospore its remarkable heat resistance[18].

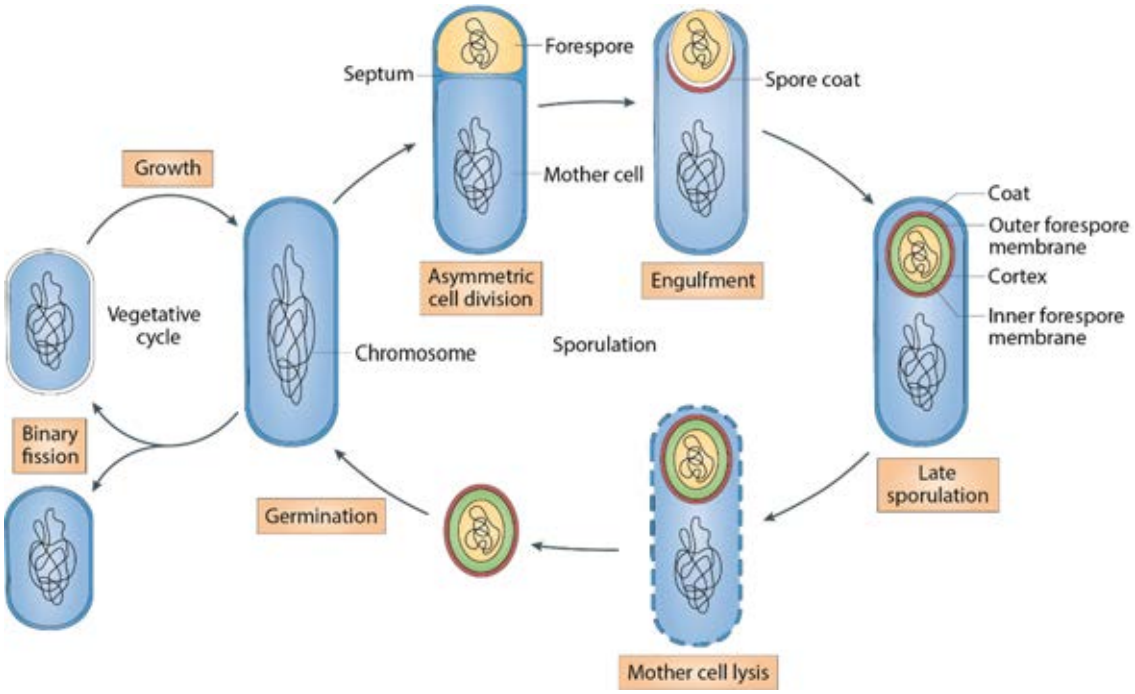

Figure 1.3. Schematic representation of the sporulation process. Under normal environmental conditions, cells grow following the vegetative cycle. Different environmental signals, i. e. nutrient depletion, trigger the sporulation process, which is initiated by an asymmetric cell division, giving rise to a mother cell and a forespore. Next, the forespore is engulfed by the mother cell creating a doubled membrane structure that will mature to become the endospore. The endospore is released to the medium by the lysis of the mother cell. When environmental conditions are more benign, endospores germinate to resume vegetative growth. Adapted from from McKenney, P. T, *et al*. (2013)[16] by permission from Springer Nature Customer Service Centre GmbH (Springer Nature). Nature Reviews Microbiology.

Transversal sections of mature endospores observed by transmission electron microscopy (TEM), exhibit a concentric structure that summarize all the above-mentioned layers that surround the cortex, from innermost to outermost: inner spore membrane, the germ cell wall (a thin layer of the mother cell wall), cortex, outer spore membrane and spore coat[16]. The spore coat is itself a multilayered cover comprised by a lamellar inner coat, a thicker outer coat and the crust. This external cover confers endospores their exceptional stress-resistance properties[19]. For instance, increased resistance to UV radiation is achieved by a spore coat protein (CotA) that is responsible for the synthesis of a pigment similar to melanin, that prevents the generation of reactive oxygen species (ROS)[20]. Some differences in the outermost layer of the endospore exist between different species. Specifically, in the *Bacillus cereus* group, comprising several phylogenetically related species like *Bacillus anthracis* or *Bacillus thuringiensis*, the outermost layer of the spore is modified into an exosporium, which is a crystalline glycoprotein-rich layer separated from the outer coat by an interspace gap[21,22]. This exosporium presents, in some species, filamentous projections[23]. The variability of the

outermost layer of the endospore is not only structural; despite the conservation of many coat proteins across different species (approximately, half of the known *B. subtilis* spore coat proteins have orthologues in other *Bacillus* genera), a significant degree of diversity of these proteins exist, suggesting a functional specialization depending on the ecological niche[24]. In the end, when the endospore is fully formed, it is released from the cell by lysis of the mother cell in a process that is aided by autolysins and other cell wall hydrolases from the mother cell[25].

The formation of the endospore is a successful survival strategy under harsh environmental conditions due to the ability of endospores to germinate into vegetative cells under growth supportive environmental conditions. In the process of germination, the spore coat acts as a sieve, only allowing the entry of small molecules or nutrients that will act as germinants[26]. Several germinant receptors are placed in the inner spore membrane to detect the presence of germinants, that can be very diverse in nature and very different depending on the species. These receptors are clustered together within the membrane forming what it is known as the "germinosome"[26]. Once the germinant is sensed, the signal is transduced, irreversibly triggering the germination process. The process starts with a massive excretion of cations H^+, Na^+ and K^+[27]. At the same time the Ca^{2+}-dipicolinic acid complex is released and water starts to slowly flow into the cell, partially rehydrating the core[28]. The next step is the complete degradation of the cortex by the activation of lytic enzymes, leading to a complete rehydration and expansion of the core, which increases the mobility of lipids and proteins within the inner membrane. Moreover, a local degradation of the spore coat starts. At this point, dipicolinic acid has already been released and the proteins that maintained the DNA protected against heat related stress are degraded, making the spore heat-sensitive and marking the end of dormancy[26]. Next, the spore coat is almost completely degraded by a not fully known mechanism from the inside out resulting in the outgrowth of the new vegetative cell. Many mechanistical questions regarding the germination process, as well as the mechanism by which the germinant signal is transduced to activate this complex process still remain and more research on the subject is required[29].

These traits described in the above paragraphs have been thoroughly investigated in *Bacillus subtilis*, which has been a model organism in the study of gram-positive bacteria since long ago. It was first isolated in 1835 by Christian Gottfried Ehremberg, a German scholar focused on natural sciences. He investigated the microorganisms that survived after hay infusion; thus, he unknowingly was the first person to isolate *B. subtilis* endospores. The first name given to this bacterium by Ehremberg was *Vibrio subtilis*[30], however, it was Cohn who gave it its actual name, *Bacillus subtilis*, after his revision of

bacterial taxonomy (see above). Following the current taxonomical characters, *Bacillus subtilis* is a firmicute, with low G+C content, rod-shaped, catalase-positive, gram-positive bacterium. *B. subtilis* is ubiquitously distributed across the globe and can be isolated from many different environments. However, it is commonly found in natural soils and in association with the plant rhizosphere, in which *B. subtilis* is able to promote plant growth. Alternatively in the gastrointestinal tract (and feces) of several animal species, *B. subtilis* has been proven to retain a probiotic effect[31].

The fact that *B. subtilis* can be genetically manipulated has contributed to the extended use of this bacterium as the landmark in the study of bacteriology and gram-positive bacteria, which has led over the years to a vast collection of biological and biochemical data, including a well-annotated genome, one of the first to be sequenced[32]. *B. subtilis* strain 168 is the most studied and the most widely distributed across research laboratories and industrial settings[33]. This strain derives from the so-called Marburg strain, now deposited in the American Type Culture Collection with the accession number ATCC 6051 and also known as NCIB3610 (from the accession code given in the British National Collection of Industrial Bacteria)[33], when it was UV and X-ray irradiated by researchers at Yale University to generate auxotrophs with the objective of associating these defects to single genes[34]. However, this research was abandoned, and it was John Spizizen who discovered that strain 168 (one tryptophan auxotrophic mutant) along with other mutants that showed similar behavior, acquired natural genetic competence in stationary phase and therefore, could be transformed when exposed to exogenous DNA[35]. He described the methodology and the phenomenon in detail and this strain was quickly disseminated, creating an exponential increase of studies about *B. subtilis*, with the subsequent generation of basic knowledge and many mutant and derivative strains. The next sections will describe some of the different cellular and physiological processes that take place during the development and growth of *B. subtilis*, with particular focus on biofilm formation in this bacterial species. Overall, many different molecular signals are integrated to activate the different pathways that lead to distinct phenotypes, indicative of the complexity of the regulatory networks that tightly control bacterial molecular and cellular processes.

MULTICELLULARITY AND DIVISION OF LABOR IN BIOFILMS

B. subtilis has the ability Distinct cell types (e. g. sporulating, competent, etc) are formed as a result of the activation of different signaling pathways in response to multiple environmental signals. The ability of bacterial cells to respond differently to diverse signals, depending on the environmental conditions and the type of signal, leads to differences in gene expression within the same population, creating a phenotypic heterogeneity[36]. This is normally achieved by the activation of transcriptional regulators that induce their own expression, generating a positive feedback loop, or by a double repressor negative regulatory loop. Indeed, only the cells that reach expression levels of these proteins above a certain threshold will activate the pathways that lead to specific cell fates. This process, by which only a subset of the cells expresses the genes that lead to specific phenotypic characteristics, is called bimodality, as it ends with the differentiation of two distinct subpopulations in individuals with exactly the same genetic background[36-38].

Biofilms are the paradigm of heterogeneity and cellular differentiation of bacterial cells. Biofilm formation is an inherent trait of bacterial species that consists of complex surface-attached bacterial communities in which cells are embedded in a self-secreted extracellular matrix (ECM) that can be very diverse in nature[39]. In these communities, communication and functional differentiation are especially relevant. By the own nature of biofilms, in which cells are adhered to a surface and physically connected between themselves, gradients of nutrients, waste products, light or oxygen among others are formed, resulting in a differential cellular response and indeed, generating a phenotypic heterogeneity[40,41]. These chemical gradients lead to a spatiotemporal differentiation in biofilms in which phenotypic heterogeneity is translated into a division of labor. This occurs when cells sacrifice their individuality, with the consequent individual fitness cost, for the benefit of the community, that in turn becomes better adapted to the different environmental cues, promoting the survival of the group as a whole[38]. In this context, different cell differentiation programs coexist during biofilm formation and thus, bacterial cells specialize in complementary tasks that, in occasions, lead to mutually exclusive phenotypes[37,38] (Fig. 1.4A-E).

Sporulation and genetic competence

Sporulation and genetic competence are processes that occur when cells enter stationary phase, however, cells committed to sporulation do not express the genes required for genetic competence and therefore, spore formation and competence

development do not occur simultaneously in the same cell[36]. The commitment towards one of these specific cell fates has several explanations. High levels of Spo0A~P repress competence development by binding to specific sites at the *comK* promoter[42], which is the ultimate responsible of the transcription of the competence *com* genes that encode the DNA pseudopili uptake machinery[43].

Competent cells inhibit sporulation through the expression of several Rap phosphatases that are induced by ComA~P, a regulator activated by quorum sensing signalling[44], that act on some proteins of the phosphorelay, reducing the flow of phosphoryl groups toward Spo0A and therefore, avoiding the accumulation of Spo0A~P and the entry into sporulation[36,45].

Motility and extracellular matrix production

Many cell types coexist in biofilms, including motile flagellated cells. In contrast, ECM-producing cells are attached to the surface, therefore, it seems logic that both cell fates are mutually exclusive. Indeed, it is well documented that in biofilms formed on solid media, expression of the flagellar genes is spatially compartmentalized within the colony[46,47] (Fig. 1.4A). Motility requires de expression of the *fla-che* operon, encoding the flagellum basal body, the chemotaxis machinery and a sigma factor (SigD) required for the transcription of the genes that form the motility regulon[48,49].

We will go into detail about the regulation of biofilm formation in a later section, however, many of the regulators that are active during biofilm formation contribute to the repression of flagellar motility, although the mechanism and the signals by which this occurs is not fully understood. Briefly, biofilm formation is controlled by SinR and SinI. SinR is a repressor of the genes required for the synthesis of the extracellular matrix, whereas SinI is a repressor of SinR activity. Paralogous to both proteins exist, named SlrR and SlrA, respectively. SlrR functions by capturing SinR, forming a heterodimer, activating the genes required for the synthesis of the ECM[39]. This SlrR-SinR complex is also responsible for the inhibition of the genes required for flagellar motility[50]. Another regulator involved in the control of these cell fates is the two-component system DegU DegS. When the levels of phosphorylated DegU are high, matrix genes are induced[51], causing the repression of the *fla-che* operon by induction of FlgM, an anti-sigma factor that blocks SigD[52]. In contrast, low levels of phosphorylated DegU are required for the activation of flagellar genes and swarming motility[51].

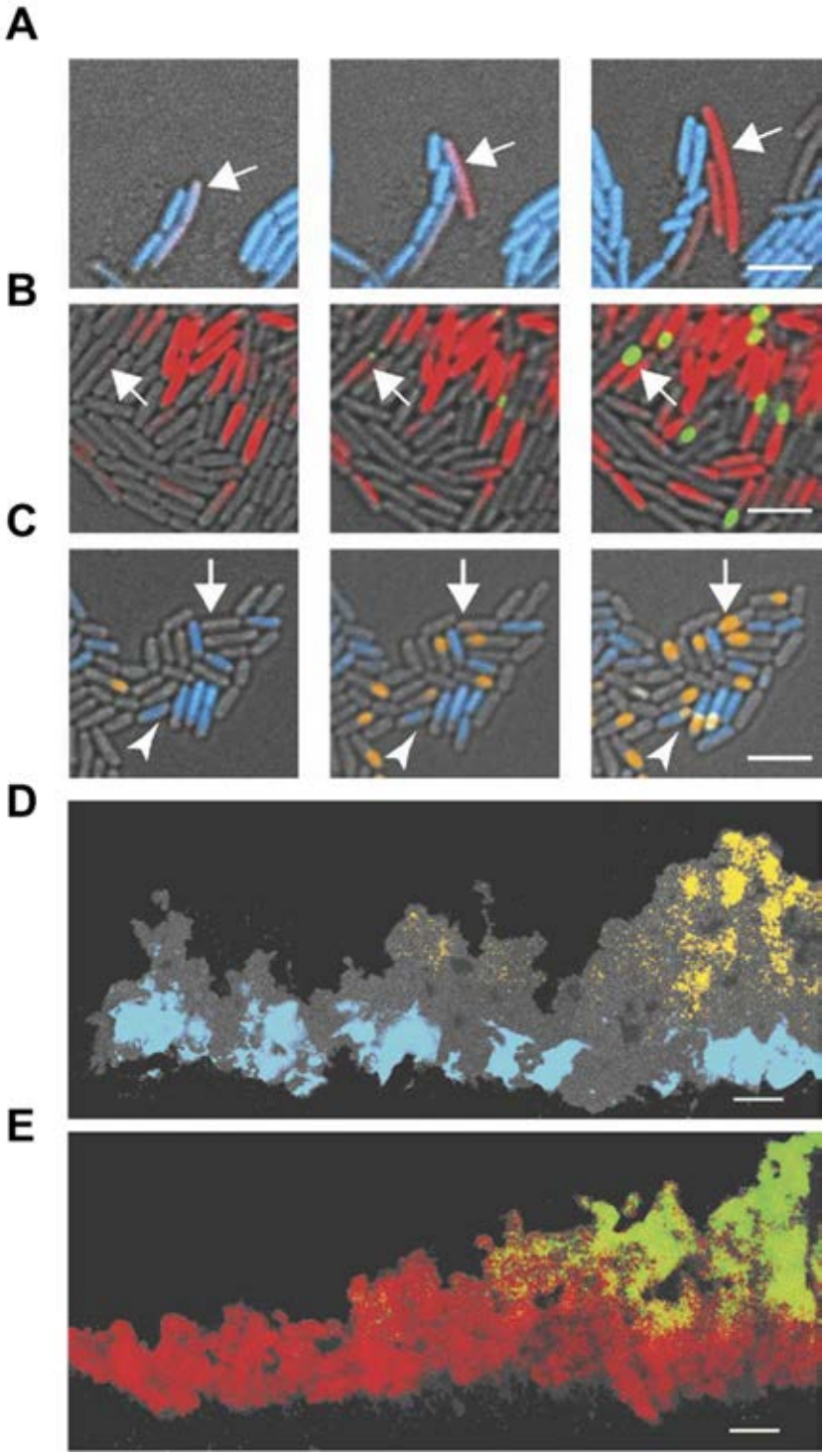

Figure 1.4. Different and mutually exclusive cell fates exist within *B. subtilis* biofilms. **A, B and C.** Time lapse fluorescence microscopy micrographs of *B. subtilis* NCIB3610 carrying a double construct of different promoters fused to reporters. **A)** Images of cells carrying a *Phag-cfp* (motile cells, blue) and a *PtapA-yfp* (matrix-producing cells, red) transcriptional fusion constructs. Arrow indicates a motile cell transitioning to matrix-producing cell. Pictures were taken every 1 hour. **B)** Images of cells harboring a P*tapA*-cfp (matrix-producing cells, red) and a *PsspB-yfp* (sporulating cells, green) transcriptional fusion constructs. Pictures were taken every 2 hours. Arrow points a cell initiating matrix production and then transitioning to sporulation. **C)** Images of cells harboring *Phag-cfp* (motile cells, blue) and *PsspB-yfp* (sporulating cells, orange). Pictures were taken every 2 hours. Most sporulating cells arise from nonmotile cells, indicated by the white arrow. Arrowhead indicates an example of the minority of motile cells that directly initiate sporulation. Scale bars = 5 µm. **D and E.** Thin sections of 48-h colonies from cells labelled with the transcriptional fusion constructs. **D)** Motile cells (blue) appear in distinct regions relative to sporulating cells (orange). **E)** Matrix-producing cells (red) overlap with the region of sporulating cells (green). Scale bars = 50 µm. Figure is reused from Vlamakis, H. *et al.* (2008)[47].

Motility is also repressed in ECM-producing cells in a post-transcriptional manner. The activation of ECM production carries the activation of the genes coding for the machinery required for exopolysaccharides (EPS) synthesis and secretion. It has been demonstrated that one of the proteins of this 15 gene operon, EpsE, has an additional function working as a clutch, arresting flagellar rotation by physically disengaging the flagellar rotor (FliG) from the stator units that allow the flow of protons (MotA and MotB), inhibiting active flagellar rotation without blocking it. Therefore, the induction of EPS and matrix production leads to a direct inhibition of motility[53].

Cannibals and the killing of non-sporulating cells

Cannibalism is the process by which cells that are committed to sporulation eliminate their non-sporulating siblings in order to utilize the nutrients released by these cells and delay the entry into sporulation[54]. This is mediated by the secretion of toxins that are part of the toxin-antitoxin systems, specifically, skf (from spore killing factor) and sdp (from sporulation-delaying protein). The synthesis of these killing factors (and their corresponding defense systems) is also controlled by the intracellular levels of Spo0A~P at a given moment, therefore, giving another example of phenotypic heterogeneity. The cells that produce the ECM and those that are committed to sporulation, i. e. those cells with intracellular levels of SpoA~P above a certain threshold, synthesize the toxins that kill the non-sporulating cells (and therefore, have SpoA~P levels below the threshold) and the corresponding antitoxins that confer immunity[46,54].

ECM production and sporulation

Adverse conditions lead to the formation of endospores as a form of resistance to environmental insults. However, under a broad range of environmental signals and prior to sporulation, bacterial cells constitute biofilms characterized by the assembly of an ECM[36] (Fig. 1.4B). The formation of biofilms and the production of an ECM provide cells protection against desiccation, microbial attacks, antibiotics and other antimicrobials among other ecological advantages[55,56]. The regulons that control the production of the ECM or the entry into sporulation are regulated by Spo0A, that exist in different phosphorylation states. These states are controlled by the phosphorelay[39]. When SpoA~P reach high threshold levels, it activates the expression of SigF, which triggers the process of asymmetric division as the starting point for sporulation[36,46,57]. However, intermediate levels of SpoA~P are sufficient to trigger the synthesis of the ECM[46]. The SinR repressor of the matrix genes is expressed by most of the cells, however, only the cells that are dedicated to matrix production express the anti-repressor SinI that will inactivate SinR. This is achieved when intermediate levels of SpoA~P are reached[39].

The fact that we observe such different cell fates under the control of the same regulator is explained by the affinity of the promoters of the genes that control ECM-production or sporulation for Spo0A~P. Indeed, the genes that regulate biofilm formation have strong binding sites for Spo0A~P, in contrast, the genes that regulate the entry into sporulation show much lower affinity for the activated regulator and thus, higher levels of SpoA~P are required to cause the activation of the expression of these genes[46].

BIOFILM FORMATION

As mentioned earlier, biofilms are bacterial surface-associated communities formed as a result of a developmental program that ends with the formation of a tissue-like structure in which bacterial cells show complex multicellular behaviors such as division of labor. We have previously introduced how different cell fates coexist within biofilms to support the fitness of the community as a whole[36,39,47]. In this context, bacterial cells are hold together by an ECM, that is produced by differentiated cells especially dedicated to this task. However, the differentiation of bacterial cells into ECM-producers is not simple, and there are several pathways that converge to activate the expression of the genes required for ECM production (Fig. 1.5A-B).

Regulation of cell differentiation into ECM producers

Phenotypic differentiation of cells into ECM-producers is not complete, as there seems to be a higher level of division of labor within cells dedicated to the production of this structure. The population of ECM-producing cells are, in turn, subdivided into two different subpopulations. One of these subpopulations are generalists, that express the ECM genes required for the production of the two main structural components, namely, the exopolysaccharide, encoded by the *epsA-O* operon (named EPS hereafter) and the amyloid fibers, encoded by *tapA-sipW-tasA* operon. The other subpopulation of ECM-producing cells expresses only the genes responsible for the synthesis of the EPS and are known as specialists[58].

Nonetheless, Spo0A is the main regulator implicated in biofilm formation, as well as for other physiological processes such as sporulation or cannibalism[39]. Indeed, the levels of Spo0A~P determine, to a certain extent, the decision-making process toward a specific cell fate. As seen before, differentiation into ECM-producing cells requires intermediate levels of Spo0A~P and as biofilm matures, Spo0A~P accumulates in certain cells, triggering the sporulation process in part of the population[39,46]. The levels of Spo0A~P

are controlled by the phosphorelay, in which the starting point are the sensor histidine kinase proteins located in the cell membrane (KinB, KinC, KinD and KinE) or in the cytoplasm (KinA)[59] (Fig. 1.5A). These sensor kinases, although somewhat redundant, respond to different stimuli that are not yet fully known, however, it is has been demonstrated that: (i) KinA is the main kinase involved in sporulation and it has been shown to mostly respond against nutrient depletion[57,60-62]; (ii) KinB senses changes in respiratory activity[63] and potassium (during sliding motility)[64], and also contributes to sensing starvation[65]; (iii) KinC also responds to potassium concentration[66,67] and seems to be directly involved in biofilm formation[66]; (iv) KinD senses the production of the ECM[68] and changes in the osmotic pressure[69] and shows phosphatase or kinase activity depending on these traits[68] and (v) KinE, is probably the most unknown member of this family of sensor kinases and the signals that trigger KinE-dependent signaling or the physiological relevance of this protein are yet to discover. All these kinases feed phosphate groups to Spo0A directly, or through the phosphotransferases present in the phosphorelay Spo0F and Spo0B, and none of them are individually responsible for the triggering of ECM-related genes, but rather contribute to a system that integrates several input signals[39,59]. The phosphorelay is regulated at several levels by the action of specific phosphatases that prevent the accumulation of Spo0A~P through dephosphorylation of Spo0F (RapA, RapB, RapE and RapH) or Spo0A directly (Spo0E, YisI and YndZ) (see Fig. 1.2). Several layers of complexity in this regulatory network exist, for instance, the Rap phosphatases are regulated by the production of cognate Phr peptides that inhibit their activities and that are part of the same tightly regulated *rap-phr* operons[70,71].

Once it is activated, Spo0A~P is directly involved in the induction of the *epsA-O* and *tapA-sipW-tasA* operons, and the protein BslA[39]. We will go into further detail of these components later in this general introduction. The *eps* and *tapA* operons are constitutively repressed by the master regulator SinR, which binds to the promoter regions of these operons[72]. However, the intermediate levels of Spo0A~P determine the heterogeneous expression of *sinI* only in ECM-producing cells[73]. SinI is a repressor of SinR and it works by physically interacting with SinR, rendering it unable to bind to the DNA[74]. Thus, SinI acts as an antirepressor, inducing the expression of the *eps* and *tapA* operons and consequently, biofilm formation. ECM genes are further repressed by a regulator of transition state genes, AbrB, which is inhibited by Spo0A~P when it is accumulated at the beginning of stationary phase (Fig. 1.5A).

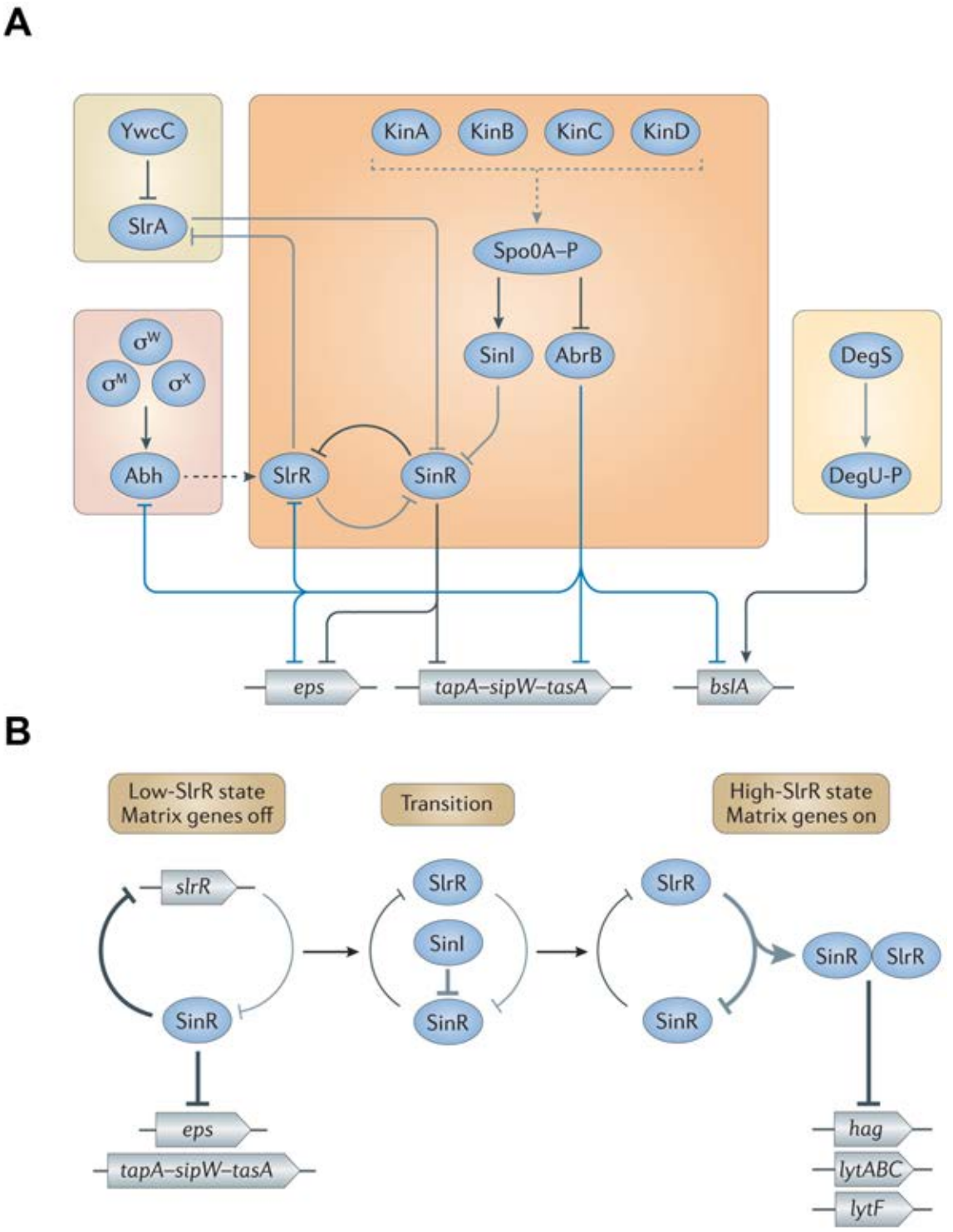

Figure 1.5. Schematic representation of the regulatory pathways that lead to extracellular matrix synthesis and biofilm formation in *B. subtilis*. A) The input from several signaling networks (see main text) are integrated in the activation of the master regulator Spo0A, that activates biofilm formation when intermediate levels of Spo0A ~P are reached. BslA, also required for the formation of a hydrophobic matrix, is regulated by DegU~P. **B)** A double-repressor feedback loop involving *slrR*. The SlrR protein and the master repressor of biofilm formation SinR form a switch to regulate the expression of matrix genes (the *eps* and *tapA–sipW–tasA* operons), autolysin genes (*lytABC* and *lytF*) and the flagellin gene (*hag*). Left. Normally, SinR represses *slrR*, maintaining low expression levels of this gene, therefore, matrix genes are repressed. Center. Under biofilm-inducing conditions, SinR-mediated repression is released due to the activation of the SinI anti-repressor in matrix-producing cells. Expression of *slrR* is activated. Right. When sufficient levels of SlrR are achieved, a heterodimeric complex SinR-SlrR that inhibits SinR is formed, reinforcing the expression of the matrix genes. In addition, SlrR repurposes SinR for the inhibition of flagellar-dependent motility and the genes required for cell separation. Adapted from Vlamakis, H. *et al.* (2013)[39] by permission from Springer Nature Customer Service Centre GmbH (Springer Nature). Nature Reviews Microbiology.

Furthermore, different regulatory subnetworks participate in the control of the expression of these genes at different levels. The protein SlrR is a paralogous of SinR and adds another step to the regulation of the *eps* or *tapA* operons expression (Fig. 1.5B). SlrR is normally repressed by SinR and AbrB, however, at the beginning of stationary phase, when AbrB repression is released and SinI-mediated inhibition of SinR occurs in matrix-producing cells, expression of *slrR* is activated. This protein captures SinR, forming a complex that, in addition to favor the expression of the *eps* and *tapA* operons by preventing SinR-mediated repression[75,76], inhibits motility by repressing *hag*, the flagellin-coding gene, or the autolysins required for cell separation after cell division[75,77], committing the cells to adopt a sessile lifestyle of ECM-producing chains. The SlrR-SinR network constitutes a double negative regulatory feedback switch that reinforces SinR repression once SinI has been activated by Spo0A~P. Independent, but complementary, of the control from Spo0A, SlrR is also under regulation of Abh, a transition-state transcriptional regulator that activates SlrR expression, a process mediated by extracytoplasmic function sigma factors (SigM, SigW or SigX) that respond to different adverse environmental conditions[78-81] (Fig. 1.5A).

Another subset of regulators influence biofilm formation through SinR-SlrR. SlrA is a paralogous of SinI. SlrA is able to inactivate SinR, giving another repression level to this protein, in this case under control of YwcC, which is a transcriptional repressor of *slrA* that is inhibited by an unknown signal. SlrA is produced in most of the cells, contrary to what occurs with SinI, and therefore, it has been suggested that this can be a mechanism to respond quickly to the changing environmental conditions[82] (Fig. 1.5A).

Finally, another pathway involved in the control of biofilm formation is the DegS-DegU system. In this case, phosphorylated DegU activates the expression of *bslA*[83]. Other proteins that affect the transcription of the *eps* or *tapA* operons are RemA and RemB, which also promote the transcription of *slrR*. RemA binds directly to the promoter region of the matrix genes, activating their expression[84,85]. It is believed that this network acts in parallel with SinR, AbrB and DegU in the regulatory control of ECM production

Structural components of the ECM

The elements that form the ECM are very diverse in nature and vary greatly between different bacterial species. In *B. subtills*[39], the formation of the typical wrinkled biofilms (Fig. 1.6) requires at least three structural components. The EPS, which is the major component of the ECM and, among other functions, acts as a cement by maintaining the cohesion of the cells. The structural support of the ECM is provided by a protein scaffold constituted by amyloid fibers, that are comprised of two proteins: TasA and TapA. A

signal peptidase, SipW, encoded in the same operon, is required for processing both proteins. Lastly, BslA is a hydrophobic protein that coats the surface of the biofilm, forming, a thin hydrophobic layer that confer the ECM most of its hydrophobic properties.

Figure 1.6. Biofilm formation by *B. subtilis* NCIB3610. Left. *B. subtilis* NCIB3610 pellicle formed in the interface between the air and the medium. Cells were grown at 30 °C in MOLP (medium optimized for lipopeptide production) medium for 48 hours. **Right.** *B. subtilis* NCIB3610 colonies formed on MSgg (minimal salts + glutamate + glycerol) agar plates. Cells were grown at 30°C for 72 hours.

The exopolysaccharides (EPS)

As mentioned above, the EPS is the major element of the ECM and its synthesis is encoded in the *epsA-O* operon[86], mainly regulated by *sinI-sinR*. The products of this operon, the polymer they synthesize and the whole biosynthetic process itself still remain to be clarified. The two first proteins encoded in the operon, EpsA and EpsB, constitute a sensor tyrosine kinase, in which the membrane bound EpsA acts as the sensor module, and EpsB is the kinase domain. Both proteins participate in a positive auto-regulatory feedback for the synthesis of the EPS. The kinase domain is normally inactive due to phosphorylation by EpsA. In response to the presence of the secreted EPS in the surroundings, phosphorylation of EpsB is inhibited, and this protein participates in the activation of other protein targets important for EPS synthesis, such as the glycosyltransferase EpsE[87]. This protein has been mentioned above for its role in inhibiting flagellar rotation through a clutch-like mechanism. Indeed, this protein is located at the cell membrane and colocalizes with flagellar basal bodies[53]. However, EpsE also present a glycosyl transferase domain that is essential for the synthesis of the EPS and biofilm formation[88]. EpsC, EpsM and EpsN are a dehydratase, an acetyltransferase and an aminotransferase respectively, that seem to constitute the machinery required for the synthesis of N,N'-diacetylbacillosamine[89-91], which in some bacteria acts as the aminosugar link of *N*- and *O*- glycosylated proteins, however, its

precise role in *B. subtilis* is unknown so far[92]. Similarly, EpsHIJK, which are essential genes for biofilm formation, are involved in the synthesis of poly-N-acetylglucosamine, which is a polymeric sugar extensively present in microbial biofilms[93]. The rest of the proteins present in the *epsA-O* operon are not fully characterized and either they have been automatically annotated or their involvement in biofilm formation has been inferred only by mutations that affect pellicle formation. Thus, more research is required to elucidate the role of these proteins and their products and to unravel the nature of the EPS and how its assembly is coordinated.

The functional amyloid fibers: TasA and TapA

These two proteins constitute the amyloid fibers of the *B. subtilis* ECM[94,95]. Amyloid proteins have the inherent ability to aggregate and polymerize in the form of fibers, with a β-sheet enriched quaternary structure that make them remarkably resistant to harsh physicochemical conditions, which is the reason behind the widespread presence of amyloids in nature, especially in bacterial biofilms[96]. Briefly, it is believed that amyloid fibers provide the protein scaffold that support the assembly of the ECM and confer integrity to this structure[94]. The *tapA-sipW-tasA* operon encode the two component of the fibers and a signal-peptidase, SipW, that process both proteins and participate in their secretion outside the cell, where the amyloid fibers will form[97,98]. TasA is the major protein of these fibers, while TapA is present in a minor proportion and aids in the polymerization of TasA[95,99]. A section of this introduction is dedicated to providing further detail of these types of proteins and specially, of TasA and TapA as they are the main subject of this research thesis.

The hydrophobic coat: BslA

BslA is a small secreted hydrophobic protein that coats the surface of the biofilm and confer hydrophobicity to the ECM[100]. This protein is under control of several networks of activators and repressors[101]. BslA is a secreted protein that contains a canonical signal peptide to cellular export through the Sec system. Structurally, BslA is similar to members of the immunoglobulin family of proteins, with a characteristic structure in which α-helices and β-sheets are facing opposite sides within the protein structure, which is appended with a hydrophobic cap comprised of surface-exposed hydrophobic residues that explain the hydrophobic properties of this protein[100]. BslA is involved in the hydrophobicity of the ECM, where it forms a thin layer located at the surface that is very repellent to water, but also confers stiffness and roughness to the biofilms[102]. This layer is formed when the hydrophobic cap, that is normally located in the interior of the protein in aqueous solution, undergo a conformational change when is exposed to the air-liquid

interface, forming a film-like structure similar to a membrane, in which the molecules are tightly packed[103]. In order to reach the interface, dimerization of BslA is essential. This is mediated by the formation of disulfide bonds involving two cysteine residues present in the C-terminal part of the protein. The formation of these dimers relies on the redox state of the cells, which is different depending on the spatial localization within the biofilm due to oxygen gradients that are established when the cells are patterned over the surface[104].

FUNCTIONAL AMYLOIDS: A PARADIGM IN STRUCTURAL AND FUNCTIONAL DIVERSITY

Functional amyloids are a very heterogeneous group of proteins widely distributed in nature, from humans to microbes, and they cover a variety of functions that are fundamentally different from the pathological features of their relative "traditional" amyloids. In bacteria, some physiological processes known to be associated with functional amyloids are: i) bacterial cell attachment and biofilm formation[94,105,106], ii) reproduction[107], iii) control of plasmid replication[108], iv) cytotoxicity[109] and virulence[110]. In eukaryotes, functional amyloids have been found to be dedicated to the following activities: i) cell adhesion in yeasts[111], ii) hyphae compatibility in filamentous fungi[112], iii) antimicrobial activity[113], iv) structural functions[114,115], and v) detoxification in certain physiological processes[116] and hormone storage[117]. These examples are indicative of the versatility of the amyloid state in their contributions to multiple aspects of the biology of living organisms. Apart from their differences in terms of biological significance, there is wide support to the idea that the polymerization process of functional amyloids is tightly controlled in comparison to their pathogenic siblings, as functional amyloids partner with several other proteins for localization, stabilization and function.

Although there are no apparent similarities in their amino acid sequences, amyloids fold into fibers with a common quaternary structure characterized by a cross-β arrangement, in which hydrogen-bonded β-strands run perpendicularly to the axis of the fibril[118]. In the native state, the folding pattern is determined by the intramolecular interactions that occur between the different amino acids, whereas in the amyloid state, intermolecular interactions are favored, resulting in the formation of the distinctive amyloid fiber[119]. Additionally, this β-sheet-enriched structure grants amyloids with tinctorial properties useful for their identification[120,121]. Thus, even though amyloids were firstly studied in the brain tissue deposits of patients suffering from Alzheimer's disease, the pathogenic implications of some amyloids are apparently the exception; new possible and

unpredictable functions are emerging for amyloid proteins traditionally associated with neurodegenerative disorders[122].

There are subtle differences in the fine structures of functional and traditionally pathological amyloids, but similar dynamics of polymerization presumably occur when they are both studied *in vitro*. A noticeable difference, however, appears to be related to the tight regulatory mechanisms that drive the polymerization of functional amyloids in contrast to those that drive the polymerization of pathological amyloids. Several strategies have been found in nature for the proper assembly of amyloid fibrils from monomers with the aim of reducing the accumulation of diffusible toxic oligomeric intermediates[123]. In some groups of bacteria, remarkable complex systems exist to manage the assembly of functional amyloids. In these, so-called, "functional amyloid systems", additional proteins interact with the major protein component of the fiber to enable efficient polymerization.

In *B. subtilis* (and other related *Bacilli*), biofilm formation and proper ECM assembly require the participation of amyloid fibers[124]. TasA fibers are an example of the many bacterial amyloid systems that exist in nature, which consist of macromolecular assemblies that comprise the functional amyloid plus several accessory proteins required for proper formation and function. TasA was initially discovered in the endospore coat and, in addition, showed a broad antibiotic spectrum; these two features led to the protein being called the **T**ranslocation-dependent **a**ntimicrobial **s**pore component[97]. However, it was later found that this protein is also essential for biofilm formation and is able to polymerize into amyloid-like fibrils, both *in vivo* and *in vitro*, with the distinctive features of a functional amyloid that participate in the structuring of the ECM[94]. Factors affecting the polymerization of TasA have been studied *in vitro* in a pre-aggregated conformation purified from the *B. subtilis* extracellular matrix, showing that environmental conditions are determinants in triggering the process of amyloidogenesis. Acidic pH and hydrophobic surfaces seem to be factors that promote complete fibrillation of these pre-formed aggregates[125]. In addition, it has been shown that this protein is affected *in vitro* by the presence of lipids and liposomes simulating bacterial membranes, which influence the polymerization process, giving rise to different oligomeric assemblies[126]. Nonetheless, there are other proteins, SipW and TapA, involved in the assembly of the TasA fiber. These three proteins are part of the *tapA-sipW-tasA* operon, which is transcriptionally regulated by SinI-SinR in response to several factors that also modulate biofilm formation[39]. SipW is a bifunctional signal peptidase in charge of processing premature isoforms of TasA and TapA for their translocation to the exterior of the cell, where the formation of the amyloid fibrils occurs[97,98]. Prior to this SipW-

dependent processing, the three proteins need to be directed to the cell surface through the Sec system. In addition, and independent from its role as a signal peptidase, SipW seems to act as a regulatory element of the expression of the *tapA* and *eps* operons during biofilm formation in solid-surfaces, by a mechanism yet unknown[127]. TapA is a two domain partially disordered protein[128], in which the N-terminal structured region of the protein is required for biofilm and TasA fiber formation, and its absence of both the whole protein or the N-terminal domain, leads to: defects in pellicle formation and colony architecture and a dramatic decrease in the levels of TasA. The remaining TasA produced by this mutant is not able to polymerize efficiently. Indeed, *in vitro*, it has been shown that TapA enhances the speed of polymerization of TasA approximately six-fold[95,99]; therefore, it could act as a nucleator protein, making the polymerization process more efficient. Furthermore, in a *tapA* mutant, TasA fibers lack any apparent attachment to the cell surface. Thus, TapA has been proposed as being necessary for anchoring of the fibers to the cell by a yet unknown mechanism[95]. The C-terminal unstructured domain of this protein is suggested to play this function, by directly or indirectly, interacting with other ECM components or cellular structures[128], however, how this occurs remains to be investigated.

Apart from its function in ECM formation in *B. subtilis*, recent studies have pointed toward a role of TasA in the interaction with other bacterial species. In dual biofilms of *B. subtilis* and *Streptococcus mutans*, TasA mediates initial attachment to *S. mutans* biofilms through an EPS component, a dextran produced by this bacterium[129]. In a different scenario, during the formation of dual species biofilms between *B. subtilis* and *Pantoea agglomerans*, TasA seems to be required for the assembly of a wrinkly pellicle as a result of the interaction between the two species, whereas the rest of the components required for ECM assembly in *B. subtilis* were dispensable[130]. More research is required to understand the contribution of this functional amyloid to interspecies interactions and to gain an insight into other putative biological functions exerted by this protein.

THE ROLE OF ECM COMPONENTS IN THE INTERACTION WITH PLANT HOSTS

The formation of this tissue-like structure allows bacteria to efficiently respond to the constantly changing environment. As such, biofilms and specifically the matrix components are believed to be important for the interaction of microbes and their plant

hosts, contributing to beneficial (e. g. colonization and persistence in the different niches of the plant[131]) or pathogenic interactions. Moreover, from the plant side, the bacterial signals that modulate biofilm formation and trigger ECM production[132], providing shelter for the microbes, in turn benefits or harms the host, since bacterial biofilms contain different secondary metabolites and many other different molecules that, eventually, are able to contribute to the plant health or disease, depending on the interaction.

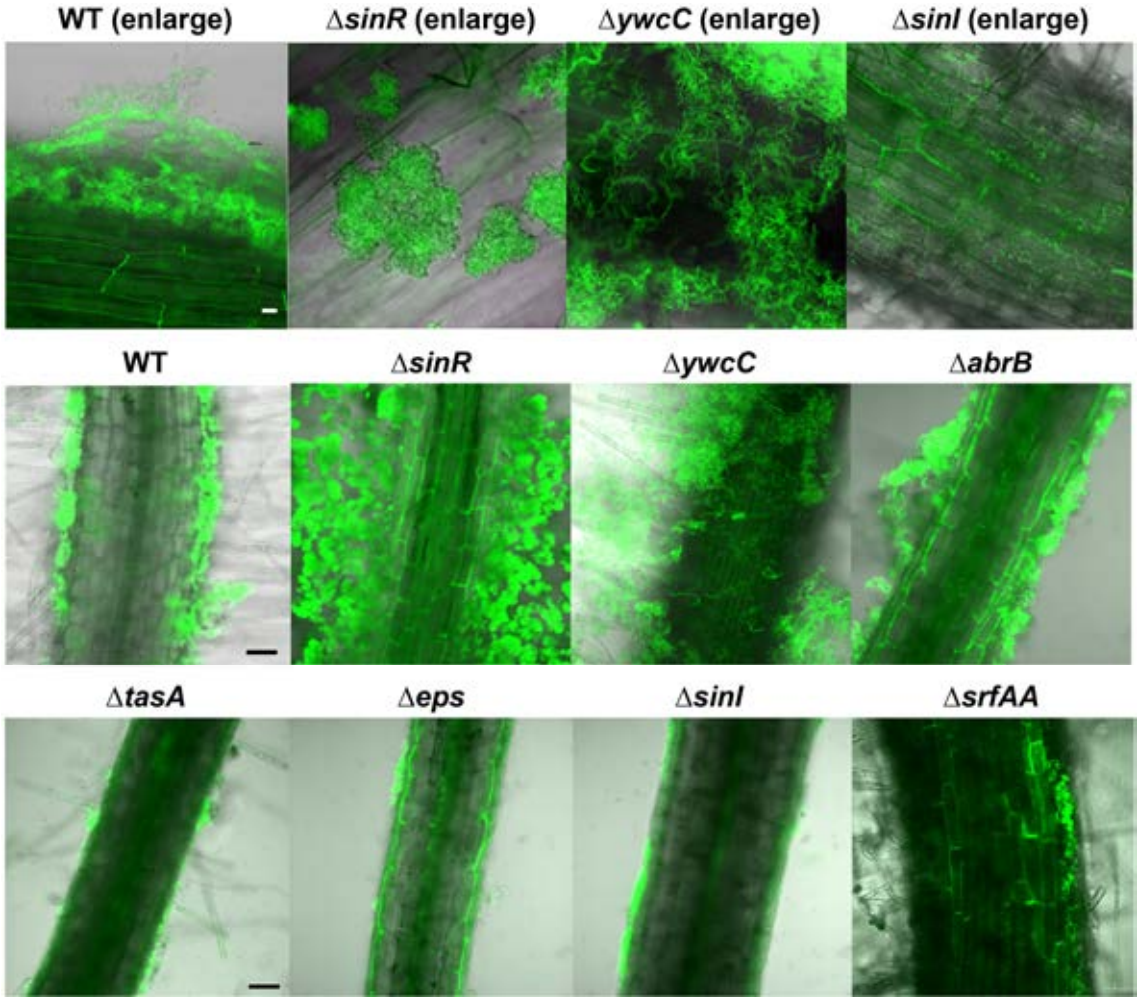

Figure 1.7. Biofilm formation on tomato roots surfaces of different *B. subtilis* mutants in genes related to biofilm formation. Confocal laser scanning microscopy micrographs of *B. subtilis* cells, harboring constitutively expressed *gfp* reporters, present in inoculated tomato roots. Bar in the top panels, 5 mm. Bars in the middle and lower panels, 50 mm. Reused from Chen, Y. *et al.* (2013)[134] by permission from Society for Applied Microbiology and John Wiley & Sons Ltd. Environmental Microbiology. © 2013 Society for Applied Microbiology and John Wiley & Sons Ltd. All rights reserved.

Bacteria from the *Bacillus spp.* genus are broadly known for their contribution to plant health and biocontrol of plant pathogens[133]. Specifically, *B. subtilis* has been extensively used as a model to study biofilm formation and interaction with plants. For instance, it has been demonstrated that biocontrol of *Fusarium oxysporum* in tomato roots by *B. subtilis* relies on a group of conserved genes involved in biofilm formation and ECM production, pointing that the formation of the ECM is essential for colonization and

persistence in the plant root[134] (Fig. 1.7). It was further confirmed that the *B. subtilis tapA* operon was fully activated upon contact with *Arabidopsis thaliana* roots and ECM production was required for colonization[135].

Interestingly, it was shown how plants can influence bacterial biofilm formation on their surface as certain plants polysaccharides were able to induce biofilm formation in several *Bacillus spp.* species[135]. In the melon phyllosphere, it has been demonstrated how the lipopeptide surfactin, that acts as a signal that prompts biofilm formation in *B. subtilis* and related species[136], triggers biofilm and ECM production of *Bacillus amyloliquefaciens* UMAF6639 and becomes necessary for the stability and suppressive activity against several plant pathogens[137]. In a different scenario, it has been shown how the ECM plays a key role in the interaction between *Pseudomonas chlororaphis* PCL1606 and *B. subtilis* NCIB3610 by protecting *B. subtilis* from the invasion of this bacterial competitor. More importantly, the ECM from *B. subtilis* was relevant for the colonization of melon leaves during this interaction, as it has been shown how *Pseudomonas* is able to modulate the interaction and alter the distribution pattern of a *B. subtilis* strain devoid of all the ECM components in the leaf's surface, from which this strain is displaced[138]. For this reason, in this section, we will cover the relevance of different biofilm structural ECM components from various bacterial species in the interaction with the plant hosts.

The EPS and other exopolymeric substances

The exopolymeric substances are defined as the collection of polymers secreted by ECM-producing cells that embed the whole community, acting as a cement that maintain the cohesion of the cells within the biofilm. The best known and the more abundant components are the EPSs, but more in-depth analysis have shown that, in addition to these polymers, there is an intricate mixture of glycoproteins, glycolipids and extracellular DNA[139]. However, the specific composition varies greatly between different bacterial species.

In general, in bacteria-plant interactions over the aerial part of plant, the EPS acts as a defensive barrier for the biofilm, protecting bacteria against desiccation or excess of UV radiation, contributing to the persistence of the community over plant leaves[140]. On the other hand, inoculation of EPS-producing microorganisms in the rhizosphere creates an environment that protects the plant cells from drying, preventing abrupt changes in the water potential, which favors the uptake of nutrients by the plant and therefore, promotes the plant growth. Furthermore, it has been demonstrated that inoculation of EPS producers in the rhizosphere affects soil structure, promoting aggregation and incrementing the root-adhered soil, which benefits nutrients and water intake by the

plant[141]. Additionally, the EPS can protect bacteria against the plant defenses, which are activated by the interaction with both beneficial and pathogenic bacteria. Indeed, in the symbiotic interaction between *Azorhizobium caulinodans* with the roots of *Sesbania rostrata*, the EPS confers protection against H_2O_2, which is produced by the plant during infection, and thus, ensures survival of the bacteria and successful nodulation[142]. Regarding bacterial physiology, one of the main structural function of the EPS in biofilms, along with adhesins, is to mediate cell-to-cell and cell-to-surface adhesion, therefore, ecologically, the EPS contribute to the colonization of the plant tissue for both beneficial microorganisms and pathogens. This is the case for *Pseudomonas fluoescens* CHA0, a non-mucoid well-known biocontrol agent. Mutants of this strain overproducing the expolysaccharide alginate, possess increased adhesion to roots and fungal structures, forming a dense biofilm that favors a more stable interaction[143]. Furthermore, it has been reported how the EPS is critical for biofilm formation and adhesion to surfaces in the vascular pathogen *Xylella fastidiosa*, which absence is translated into a defect in bacterial motility within plants, loss of pathogenicity and propagability[144].

Functional amyloids and other matrix proteins and their role in plant interaction

Several examples are found in nature where functional amyloids are determinant in the beneficial or pathogenic interaction of bacterial species with the plant host. The amyloid protein curli, the paradigm of bacterial amyloid, facilitates the adhesion of bacterial cells of *E. coli* to plant surfaces. Briefly, the curli amyloid fibers of *Escherichia coli* and *Salmonella spp.* are composed mainly of the major protein component CsgA (and its corresponding ortholog in *Salmonella spp.*)[105] and the minor protein CsgB, encoded in the same operon *csgABC,* that acts as a nucleator of curli fiber assembly. CsgB facilitates polymerization of CsgA into fibers upon interaction and seems to be responsible for the attachment of the fibers to the cell surface[145,146]. The expression of the curli-dedicated operons in the K12 strain of *E. coli*, a natural non-producer of curli, restored the ability of the bacterium to form the curli amyloid fibrils and significantly increased the binding of the bacterium to alfalfa sprouts and seed coats[147]. The adhesion of this bacterium to the plant material was comparable to that of several pathogenic strains of *E. coli* that naturally exhibit a slow binding that lasts several days. Interestingly, mutants defective in curli production of some of these diarrheagenic strains of *E. coli* are still able to bind the plant surfaces, which suggests that curli is an important element, although not essential, for plant-bacteria interaction in this species and that several and complementary strategies exist in *E. coli* that ensure their persistence in and colonization of plant tissues[147]. Further transcriptomic analysis of two strains of *E. coli*, K12 and O157:H7, from lettuce or spinach leaves showed that, indeed, the expression of the curli

genes *csgA* and *csgB* is only increased during the first stages of the interaction and decreases rapidly over the course of time[148]. This finding, indicative of the relevance of curli fibers for the initial establishment of the bacteria on the plant surfaces, was confirmed by the lower attachment of *csgA* mutants of O157:H7 to the plant tissue compared to the WT strain during the initial stages of the interaction. Although the mutant in curli reaches adhesion levels similar to those of the wild-type strain, colonization appears to be impaired, which reflects the importance of the curli amyloid fiber in this stage of the interaction with the plant[149].

The pinnacle of functional specialization in the interaction of bacterial amyloids with plant hosts are, probably, the harpins. Briefly, harpins are functional amyloids that can be found in gram-negative plant-pathogenic and consist of a family of glycine-rich proteins present in the bacterial species *Erwinia amylovora*[150], several members of the *Pseudomonas syringae* group[151-153], *Xanthomonas spp*[154] and *Ralstonia solanacearum*[155]. One of the most distinctive features of this family of proteins is their ability to trigger the hypersensitive response (HR) in plants in the absence of bacterial cells[156]. It has been shown that some harpins are intrinsically able to polymerize into fibrils with amyloid properties due to intrinsic properties of their own sequences. This feature has been extensively studied in a harpin called HpaG from *Xanthomonas spp.* in which the rate of fibril formation seems to be influenced by a domain located at the C-terminal half of the protein, whereas the α-helical domain at the amino-terminal half of the protein is essential for the induction of HR in plants[110].They serve a variety of purposes during plant infection: i) participating in the translocation of bacterial effectors into plant cells, ii) as helpers in *hrp* (**h**ypersensitive **r**esponse and **p**athogenesis) type III protein secretion systems and iii), as toxins, forming pores in plant membranes which cause depolarization and further plant cell death[157].

B. subtilis, as seen at the beginning of this introduction, is a soil dwelling bacterium, known to live in association with plants, to which it confers notable beneficial effects: i) defense against microbial diseases, either by direct interaction with the pathogen or indirectly inducing the defense mechanisms of plants, ii) promotion of plant growth or iii) resilience to drought[135,158]. Once established, *B. subtilis* cells trigger the immune system of the plant, a process called ISR (induced systemic resistance), which contributes to the repression of pathogenic infections aboveground. Microbe-associated molecular patterns are the name given to the bacterial factors that activate the plant innate immune system upon recognition[159]. Some of them, such as flagellin, are indistinctly present on pathogenic and beneficial bacteria, while others, such as toxins, are specific to pathogenic bacteria; plants have evolved the ability to differentiate between them. The

studies on the tripartite interaction of *Pseudomonas syringae*, a foliar pathogenic bacterium, with *Arabidopsis* plants and rhizospheric beneficial *B. subtilis* have furthered the understanding of the molecular aspects of this chemical signaling interplay[159]. *P. syringae* applied to the phyllosphere increases the rhizospheric secretions of malic acid, which mediates the recruitment of *B. subtilis* cells to the roots[160]. However, at the same time, *P. syringae* triggers a long-distance defense mechanism in the roots, which could hypothetically antagonize the bacilli recruitment[159]. Two lines of evidence led to the proposal of a hypothetical role for the amyloid-like protein TasA in the way by which *B. subtilis* cells manage these two antagonistic situations in a manner conducive to the efficient colonization of roots. First, by mediating the assembly of biofilms. TasA is a major component of the extracellular matrix and a TasA mutant is found to be arrested in biofilms not only *in vitro* but also on roots[124,135]. Second, and most interestingly, this occurs by repressing the immune response that was initially triggered by the foliar pathogenic *P. syringae* in the roots[159]. These findings expand the view of bacterial amyloids beyond the well-known functionality of adhesion to surfaces or development of multicellularity to mediate communication with the different hosts.

REFERENCES

1 Whipps, J. M., Lewis, K. & Cooke, R. C. in *Fungi in Biological Control Systems* (ed M. N. Burge) Ch. 9, 176 (Manchester University Press, 1988).

2 Fracastoro, G. & WC, W. Hieronymii Fracastorii De Contagione, Libri III, Translation and notes. *New York*, (1930).

3 Gest, H. The discovery of microorganisms by Robert Hooke and Antoni Van Leeuwenhoek, fellows of the Royal Society. *Notes Rec. R. Soc. Lond.* **58**, 187-201, (2004).

4 Schwartz, M. The life and works of Louis Pasteur. *J. Appl. Microbiol.* **91**, 597-601, (2001).

5 Munch, R. Robert Koch. *Microbes Infect.* **5**, 69-74, (2003).

6 Drews, G. The roots of microbiology and the influence of Ferdinand Cohn on microbiology of the 19th century. *FEMS Microbiol. Rev.* **24**, 225-249, (2000).

7 Coico, R. Gram staining. *Curr. Protoc. Microbiol.* **Appendix 3**, Appendix 3C, (2005).

8 Rohde, M. The Gram-Positive Bacterial Cell Wall. *Microbiol Spectr.* **7**, (2019).

9 Brown, S., Santa Maria, J. P., Jr. & Walker, S. Wall teichoic acids of gram-positive bacteria. *Annu. Rev. Microbiol.* **67**, 313-336, (2013).

10 Oku, Y. *et al.* Pleiotropic roles of polyglycerolphosphate synthase of lipoteichoic acid in growth of *Staphylococcus aureus* cells. *J. Bacteriol.* **191**, 141-151, (2009).

11 Fedtke, I. *et al.* A *Staphylococcus aureus ypfP* mutant with strongly reduced lipoteichoic acid (LTA) content: LTA governs bacterial surface properties and autolysin activity. *Mol. Microbiol.* **65**, 1078-1091, (2007).

12 Weidenmaier, C. *et al.* Lack of wall teichoic acids in Staphylococcus aureus leads to reduced interactions with endothelial cells and to attenuated virulence in a rabbit model of endocarditis. *J. Infect. Dis.* **191**, 1771-1777, (2005).

13 Gross, M., Cramton, S. E., Gotz, F. & Peschel, A. Key role of teichoic acid net charge in *Staphylococcus aureus* colonization of artificial surfaces. *Infect Immun* **69**, 3423-3426, (2001).

14 Raisanen, L., Schubert, K., Jaakonsaari, T. & Alatossava, T. Characterization of lipoteichoic acids as *Lactobacillus delbrueckii* phage receptor components. *J. Bacteriol.* **186**, 5529-5532, (2004).

15 Xia, G. *et al.* Wall teichoic Acid-dependent adsorption of staphylococcal siphovirus and myovirus. *J. Bacteriol.* **193**, 4006-4009, (2011).

16 McKenney, P. T., Driks, A. & Eichenberger, P. The *Bacillus subtilis* endospore: assembly and functions of the multilayered coat. *Nat. Rev. Microbiol.* **11**, 33-44, (2013).

17 Stragier, P. & Losick, R. Molecular genetics of sporulation in *Bacillus subtilis*. *Annu. Rev. Genet.* **30**, 297-241, (1996).

18 Setlow, P. I will survive: DNA protection in bacterial spores. *Trends Microbiol* **15**, 172-180, (2007).

19 Setlow, P. Spore Resistance Properties. *Microbiol. Spectr.* **2**, (2014).

20 Hullo, M. F., Moszer, I., Danchin, A. & Martin-Verstraete, I. CotA of *Bacillus subtilis* is a copper-dependent laccase. *J. Bacteriol.* **183**, 5426-5430, (2001).

21 Henriques, A. O. & Moran, C. P., Jr. Structure, assembly, and function of the spore surface layers. *Annu. Rev. Microbiol.* **61**, 555-588, (2007).

22 Maes, E. *et al.* Glycosylation of BclA Glycoprotein from Bacillus cereus and Bacillus anthracis Exosporium Is Domain-specific. *J. Biol. Chem*. **291**, 9666-9677, (2016).

23 Kailas, L. *et al.* Surface architecture of endospores of the Bacillus cereus/anthracis/thuringiensis family at the subnanometer scale. *Proc. Natl. Acad. Sci. USA* **108**, 16014-16019, (2011).

24 Qin, H. & Driks, A. Contrasting evolutionary patterns of spore coat proteins in two Bacillus species groups are linked to a difference in cellular structure. *BMC Evol. Biol.* **13**, 261, (2013).

25 Hosoya, S., Lu, Z., Ozaki, Y., Takeuchi, M. & Sato, T. Cytological analysis of the mother cell death process during sporulation in *Bacillus subtilis*. *J. Bacteriol.* **189**, 2561-2565, (2007).

26 Moir, A. & Cooper, G. Spore Germination. *Microbiol. Spectr.* **3**, (2015).

27 Swerdlow, B. M., Setlow, B. & Setlow, P. Levels of H+ and other monovalent cations in dormant and germinating spores of Bacillus megaterium. *J. Bacteriol.* **148**, 20-29, (1981).

28 Perez-Valdespino, A. *et al.* Function of the SpoVAEa and SpoVAF proteins of *Bacillus subtilis* spores. *J. Bacteriol.* **196**, 2077-2088, (2014).

29 Setlow, P. Germination of spores of Bacillus species: what we know and do not know. *J. Bacteriol.* **196**, 1297-1305, (2014).

30 Ehrenberg, C. Dritter Beitrag zur Erkenntniss grosser Organisation in der Richtung des kleinsten Raumes. *Berlin: Konigl. Akad. d. Wiss.* **1833**, 145-336, (1834).

31 Earl, A. M., Losick, R. & Kolter, R. Ecology and genomics of *Bacillus subtilis*. *Trends Microbiol* **16**, 269-275, (2008).

32 Kunst, F. *et al.* The complete genome sequence of the gram-positive bacterium *Bacillus subtilis*. *Nature* **390**, 249-256, (1997).

33 Zeigler, D. R. *et al.* The origins of 168, W23, and other *Bacillus subtilis* legacy strains. *J. Bacteriol.* **190**, 6983-6995, (2008).

34 Burkholder, P. R. & Giles, N. H., Jr. Induced biochemical mutations in *Bacillus subtilis*. *Am J Bot* **34**, 345-348, (1947).

35 Spizizen, J. Transformation of Biochemically Deficient Strains of *Bacillus subtilis* by Deoxyribonucleate. *Proc. Natl. Acad. Sci. USA* **44**, 1072-1078, (1958).

36 Lopez, D., Vlamakis, H. & Kolter, R. Generation of multiple cell types in *Bacillus subtilis*. *FEMS Microbiol. Rev.* **33**, 152-163, (2009).

37 Lopez, D. & Kolter, R. Extracellular signals that define distinct and coexisting cell fates in *Bacillus subtilis*. *FEMS Microbiol. Rev.* **34**, 134-149, (2010).

38 van Gestel, J., Vlamakis, H. & Kolter, R. Division of Labor in Biofilms: the Ecology of Cell Differentiation. *Microbiol. Spectr.* **3**, MB-0002-2014, (2015).

39 Vlamakis, H., Chai, Y., Beauregard, P., Losick, R. & Kolter, R. Sticking together: building a biofilm the *Bacillus subtilis* way. *Nat. Rev. Microbiol.* **11**, 157-168, (2013).

40 Stewart, P. S. Diffusion in biofilms. *J. Bacteriol.* **185**, 1485-1491, (2003).

41 Stewart, P. S. & Franklin, M. J. Physiological heterogeneity in biofilms. *Nat. Rev. Microbiol.* **6**, 199-210, (2008).

42 Mirouze, N., Desai, Y., Raj, A. & Dubnau, D. Spo0A~P imposes a temporal gate for the bimodal expression of competence in *Bacillus subtilis*. *PLoS Genet.* **8**, e1002586, (2012).

43 Jakobs, M. & Meinhardt, F. What renders Bacilli genetically competent? A gaze beyond the model organism. *Appl. Microbiol. Biotechnol.* **99**, 1557-1570, (2015).

44 Comella, N. & Grossman, A. D. Conservation of genes and processes controlled by the quorum response in bacteria: characterization of genes controlled by the quorum-sensing transcription factor ComA in *Bacillus subtilis*. *Mol. Microbiol.* **57**, 1159-1174, (2005).

45 Mirouze, N. & Dubnau, D. Chance and Necessity in *Bacillus subtilis* Development. *Microbiol. Spectr.* **1**, (2013).

46 Fujita, M., Gonzalez-Pastor, J. E. & Losick, R. High- and low-threshold genes in the Spo0A regulon of *Bacillus subtilis*. *J. Bacteriol.* **187**, 1357-1368, (2005).

47 Vlamakis, H., Aguilar, C., Losick, R. & Kolter, R. Control of cell fate by the formation of an architecturally complex bacterial community. *Genes Dev.* **22**, 945-953, (2008).

48 Marquez-Magana, L. M. & Chamberlin, M. J. Characterization of the *sigD* transcription unit of *Bacillus subtilis*. *J. Bacteriol.* **176**, 2427-2434, (1994).

49 Mukherjee, S. & Kearns, D. B. The structure and regulation of flagella in *Bacillus subtilis*. *Annu. Rev. Genet.* **48**, 319-340, (2014).

50 Piggot, P. Epigenetic switching: bacteria hedge bets about staying or moving. *Curr. Biol.* **20**, R480-482, (2010).

51 Verhamme, D. T., Kiley, T. B. & Stanley-Wall, N. R. DegU co-ordinates multicellular behaviour exhibited by *Bacillus subtilis*. *Mol. Microbiol.* **65**, 554-568, (2007).

52 Hsueh, Y. H. *et al.* DegU-phosphate activates expression of the anti-sigma factor FlgM in *Bacillus subtilis*. *Mol. Microbiol.* **81**, 1092-1108, (2011).

53 Blair, K. M., Turner, L., Winkelman, J. T., Berg, H. C. & Kearns, D. B. A molecular clutch disables flagella in the *Bacillus subtilis* biofilm. *Science* **320**, 1636-1638, (2008).

54 Gonzalez-Pastor, J. E. Cannibalism: a social behavior in sporulating *Bacillus subtilis*. *FEMS Microbiol. Rev.* **35**, 415-424, (2011).

55 Yin, W., Wang, Y., Liu, L. & He, J. Biofilms: The Microbial "Protective Clothing" in Extreme Environments. *Int. J. Mol. Sci.* **20**, (2019).

56 Hall-Stoodley, L., Costerton, J. W. & Stoodley, P. Bacterial biofilms: from the natural environment to infectious diseases. *Nat. Rev. Microbiol.* **2**, 95-108, (2004).

57 Russell, J. R., Cabeen, M. T., Wiggins, P. A., Paulsson, J. & Losick, R. Noise in a phosphorelay drives stochastic entry into sporulation in *Bacillus subtilis*. *EMBO J.* **36**, 2856-2869, (2017).

58 Dragos, A. *et al.* Division of Labor during Biofilm Matrix Production. *Curr. Biol.* **28**, 1903-1913 e1905, (2018).

59 Jiang, M., Shao, W., Perego, M. & Hoch, J. A. Multiple histidine kinases regulate entry into stationary phase and sporulation in *Bacillus subtilis*. *Mol. Microbiol.* **38**, 535-542, (2000).

60 Eswaramoorthy, P. *et al.* The threshold level of the sensor histidine kinase KinA governs entry into sporulation in *Bacillus subtilis*. *J. Bacteriol.* **192**, 3870-3882, (2010).

61 Devi, S. N., Kiehler, B., Haggett, L. & Fujita, M. Evidence that Autophosphorylation of the Major Sporulation Kinase in *Bacillus subtilis* Is Able To Occur in trans. *J. Bacteriol.* **197**, 2675-2684, (2015).

62 Kiehler, B., Haggett, L. & Fujita, M. The PAS domains of the major sporulation kinase in *Bacillus subtilis* play a role in tetramer formation that is essential for the autokinase activity. *Microbiology open* **6**, (2017).

63 Kolodkin-Gal, I. *et al.* Respiration control of multicellularity in *Bacillus subtilis* by a complex of the cytochrome chain with a membrane-embedded histidine kinase. *Genes Dev.* **27**, 887-899, (2013).

64 Grau, R. R. *et al.* A Duo of Potassium-Responsive Histidine Kinases Govern the Multicellular Destiny of *Bacillus subtilis*. *mBio* **6**, e00581, (2015).

65 Liu, W., He, Z., Gao, F., Yan, J. & Huang, X. Sensor kinase KinB and its pathway-associated key factors sense the signal of nutrition starvation in sporulation of *Bacillus subtilis*. *Microbiologyopen* **7**, e00566, (2018).

66 Lopez, D., Fischbach, M. A., Chu, F., Losick, R. & Kolter, R. Structurally diverse natural products that cause potassium leakage trigger multicellularity in *Bacillus subtilis*. *Proc. Natl. Acad. Sci. USA* **106**, 280-285, (2009).

67 Lopez, D., Gontang, E. A. & Kolter, R. Potassium sensing histidine kinase in *Bacillus subtilis*. *Methods Enzymol* **471**, 229-251, (2010).

68 Aguilar, C., Vlamakis, H., Guzman, A., Losick, R. & Kolter, R. KinD is a checkpoint protein linking spore formation to extracellular-matrix production in *Bacillus subtilis* biofilms. *mBio* **1**, (2010).

69 Rubinstein, S. M. *et al.* Osmotic pressure can regulate matrix gene expression in *Bacillus subtilis*. *Mol. Microbiol.* **86**, 426-436, (2012).

70 Jiang, M., Grau, R. & Perego, M. Differential processing of propeptide inhibitors of Rap phosphatases in *Bacillus subtilis*. *J. Bacteriol.* **182**, 303-310, (2000).

71 Smits, W. K. *et al.* Temporal separation of distinct differentiation pathways by a dual specificity Rap-Phr system in *Bacillus subtilis*. *Mol. Microbiol.* **65**, 103-120, (2007).

72 Kearns, D. B., Chu, F., Branda, S. S., Kolter, R. & Losick, R. A master regulator for biofilm formation by *Bacillus subtilis*. *Mol. Microbiol.* **55**, 739-749, (2005).

73 Chai, Y., Chu, F., Kolter, R. & Losick, R. Bistability and biofilm formation in *Bacillus subtilis*. *Mol. Microbiol.* **67**, 254-263, (2008).

74 Bai, U., Mandic-Mulec, I. & Smith, I. SinI modulates the activity of SinR, a developmental switch protein of *Bacillus subtilis*, by protein-protein interaction. *Genes Dev.* **7**, 139-148, (1993).

75 Chai, Y., Norman, T., Kolter, R. & Losick, R. An epigenetic switch governing daughter cell separation in *Bacillus subtilis*. *Genes Dev.* **24**, 754-765, (2010).

76 Chai, Y., Kolter, R. & Losick, R. Reversal of an epigenetic switch governing cell chaining in *Bacillus subtilis* by protein instability. *Mol. Microbiol.* **78**, 218-229, (2010).

77 Cozy, L. M. *et al.* SlrA/SinR/SlrR inhibits motility gene expression upstream of a hypersensitive and hysteretic switch at the level of sigma(D) in *Bacillus subtilis*. *Mol. Microbiol.* **83**, 1210-1228, (2012).

78 Murray, E. J., Strauch, M. A. & Stanley-Wall, N. R. SigmaX is involved in controlling *Bacillus subtilis* biofilm architecture through the AbrB homologue Abh. *J. Bacteriol.* **191**, 6822-6832, (2009).

79 Huang, X., Fredrick, K. L. & Helmann, J. D. Promoter recognition by *Bacillus subtilis* sigmaW: autoregulation and partial overlap with the sigmaX regulon. *J. Bacteriol.* **180**, 3765-3770, (1998).

80 Luo, Y., Asai, K., Sadaie, Y. & Helmann, J. D. Transcriptomic and phenotypic characterization of a *Bacillus subtilis* strain without extracytoplasmic function sigma factors. *J. Bacteriol.* **192**, 5736-5745, (2010).

81 Mascher, T., Hachmann, A. B. & Helmann, J. D. Regulatory overlap and functional redundancy among *Bacillus subtilis* extracytoplasmic function sigma factors. *J. Bacteriol.* **189**, 6919-6927, (2007).

82 Chai, Y., Kolter, R. & Losick, R. Paralogous antirepressors acting on the master regulator for biofilm formation in *Bacillus subtilis*. *Mol. Microbiol.* **74**, 876-887, (2009).

83 Verhamme, D. T., Murray, E. J. & Stanley-Wall, N. R. DegU and Spo0A jointly control transcription of two loci required for complex colony development by *Bacillus subtilis*. *J. Bacteriol.* **191**, 100-108, (2009).

84 Winkelman, J. T., Blair, K. M. & Kearns, D. B. RemA (YlzA) and RemB (YaaB) regulate extracellular matrix operon expression and biofilm formation in *Bacillus subtilis*. *J. Bacteriol.* **191**, 3981-3991, (2009).

85 Winkelman, J. T. *et al.* RemA is a DNA-binding protein that activates biofilm matrix gene expression in *Bacillus subtilis*. *Mol. Microbiol.* **88**, 984-997, (2013).

86 Marvasi, M., Visscher, P. T. & Casillas Martinez, L. Exopolymeric substances (EPS) from *Bacillus subtilis*: polymers and genes encoding their synthesis. *FEMS Microbiol Lett.* **313**, 1-9, (2010).

87 Elsholz, A. K., Wacker, S. A. & Losick, R. Self-regulation of exopolysaccharide production in *Bacillus subtilis* by a tyrosine kinase. *Genes Dev.* **28**, 1710-1720, (2014).

88 Guttenplan, S. B., Blair, K. M. & Kearns, D. B. The EpsE flagellar clutch is bifunctional and synergizes with EPS biosynthesis to promote *Bacillus subtilis* biofilm formation. *PLoS Genet.* **6**, e1001243, (2010).

89 Kaundinya, C. R., Savithri, H. S., Krishnamurthy Rao, K. & Balaji, P. V. In vitro characterization of N-terminal truncated EpsC from *Bacillus subtilis* 168, a UDP-N-acetylglucosamine 4,6-dehydratase. *Arch. Biochem. Biophys.* **657**, 78-88, (2018).

90 Kaundinya, C. R., Savithri, H. S., Rao, K. K. & Balaji, P. V. EpsM from *Bacillus subtilis* 168 has UDP-2,4,6-trideoxy-2-acetamido-4-amino glucose acetyltransferase activity in vitro. *Biochem. Biophys Res. Commun.* **505**, 1057-1062, (2018).

91 Kaundinya, C. R., Savithri, H. S., Rao, K. K. & Balaji, P. V. EpsN from *Bacillus subtilis* 168 has UDP-2,6-dideoxy 2-acetamido 4-keto glucose aminotransferase activity in vitro. *Glycobiology* **28**, 802-812, (2018).

92 Sharon, N. Celebrating the golden anniversary of the discovery of bacillosamine, the diamino sugar of a Bacillus. *Glycobiology* **17**, 1150-1155, (2007).

93 Roux, D. *et al.* Identification of Poly-N-acetylglucosamine as a Major Polysaccharide Component of the *Bacillus subtilis* Biofilm Matrix. *J. Biol. Chem.* **290**, 19261-19272, (2015).

94 Romero, D., Aguilar, C., Losick, R. & Kolter, R. Amyloid fibers provide structural integrity to *Bacillus subtilis* biofilms. *Proc. Natl. Acad. Sci. USA* **107**, 2230-2234, (2010).

95 Romero, D., Vlamakis, H., Losick, R. & Kolter, R. An accessory protein required for anchoring and assembly of amyloid fibres in *B. subtilis* biofilms. *Mol. Microbiol.* **80**, 1155-1168, (2011).

96 Romero, D. & Kolter, R. Functional amyloids in bacteria. *Int. Microbiol.* **17**, 65-73, (2014).

97 Stover, A. G. & Driks, A. Secretion, localization, and antibacterial activity of TasA, a *Bacillus subtilis* spore-associated protein. *J. Bacteriol.* **181**, 1664-1672, (1999).

98 Tjalsma, H. *et al.* Conserved serine and histidine residues are critical for activity of the ER-type signal peptidase SipW of *Bacillus subtilis*. *J. Biol. Chem.* **275**, 25102-25108, (2000).

99 Romero, D., Vlamakis, H., Losick, R. & Kolter, R. Functional analysis of the accessory protein TapA in *Bacillus subtilis* amyloid fiber assembly. *J. Bacteriol.* **196**, 1505-1513, (2014).

100 Hobley, L. *et al.* BslA is a self-assembling bacterial hydrophobin that coats the *Bacillus subtilis* biofilm. *Proc. Natl. Acad. Sci. USA* **110**, 13600-13605, (2013).

101 Arnaouteli, S., MacPhee, C. E. & Stanley-Wall, N. R. Just in case it rains: building a hydrophobic biofilm the *Bacillus subtilis* way. *Curr. Opin. Microbiol.* **34**, 7-12, (2016).

102 Kesel, S. *et al.* Direct Comparison of Physical Properties of *Bacillus subtilis* NCIB 3610 and B-1 Biofilms. *Appl. Environ. Microbiol.* **82**, 2424-2432, (2016).

103 Bromley, K. M. *et al.* Interfacial self-assembly of a bacterial hydrophobin. *Proc. Natl. Acad. Sci. USA* **112**, 5419-5424, (2015).

104 Arnaouteli, S. *et al.* Bifunctionality of a biofilm matrix protein controlled by redox state. *Proc. Natl. Acad. Sci. USA* **114**, E6184-E6191, (2017).

105 Chapman, M. R. *et al.* Role of *Escherichia coli* curli operons in directing amyloid fiber formation. *Science* **295**, 851-855, (2002).

106 Dueholm, M. S. *et al.* Functional amyloid in Pseudomonas. *Mol. Microbiol.* **77**, 1009-1020, (2010).

107 Claessen, D. *et al.* A novel class of secreted hydrophobic proteins is involved in aerial hyphae formation in Streptomyces coelicolor by forming amyloid-like fibrils. *Genes Dev.* **17**, 1714-1726, (2003).

108 Molina-Garcia, L. *et al.* Functional amyloids as inhibitors of plasmid DNA replication. *Sci. Rep.* **6**, 25425, (2016).

109 Hetz, C., Bono, M. R., Barros, L. F. & Lagos, R. Microcin E492, a channel-forming bacteriocin from Klebsiella pneumoniae, induces apoptosis in some human cell lines. *Proc. Natl. Acad. Sci. USA* **99**, 2696-2701, (2002).

110 Oh, J. *et al.* Amyloidogenesis of type III-dependent harpins from plant pathogenic bacteria. *J. Biol. Chem.* **282**, 13601-13609, (2007).

111 Ramsook, C. B. *et al.* Yeast cell adhesion molecules have functional amyloid-forming sequences. *Eukaryot. Cell* **9**, 393-404, (2010).

112 Coustou-Linares, V., Maddelein, M. L., Begueret, J. & Saupe, S. J. In vivo aggregation of the HET-s prion protein of the fungus Podospora anserina. *Mol. Microbiol.* **42**, 1325-1335, (2001).

113 Jang, H. *et al.* Antimicrobial protegrin-1 forms amyloid-like fibrils with rapid kinetics suggesting a functional link. *Biophys. J.* **100**, 1775-1783, (2011).

114 Iconomidou, V. A., Vriend, G. & Hamodrakas, S. J. Amyloids protect the silkmoth oocyte and embryo. *FEBS Lett.* **479**, 141-145, (2000).

115 Kenney, J. M., Knight, D., Wise, M. J. & Vollrath, F. Amyloidogenic nature of spider silk. *Eur. J. Biochem.* **269**, 4159-4163, (2002).

116 Fowler, D. M. *et al.* Functional amyloid formation within mammalian tissue. *PLoS Biol.* **4**, e6, (2006).

117 Maji, S. K. *et al.* Functional amyloids as natural storage of peptide hormones in pituitary secretory granules. *Science* **325**, 328-332, (2009).

118 Knowles, T. P., Vendruscolo, M. & Dobson, C. M. The amyloid state and its association with protein misfolding diseases. *Nat. Rev. Mol. Cell Biol.* **15**, 384-396, (2014).

119 Fitzpatrick, A. W., Vanacore, G. M. & Zewail, A. H. Nanomechanics and intermolecular forces of amyloid revealed by four-dimensional electron microscopy. *Proc. Natl. Acad. Sci. USA* **112**, 3380-3385, (2015).

120 Klunk, W. E., Jacob, R. F. & Mason, R. P. Quantifying amyloid beta-peptide (Abeta) aggregation using the Congo red-Abeta (CR-abeta) spectrophotometric assay. *Anal Biochem.* **266**, 66-76, (1999).

121 LeVine, H., 3rd. Thioflavine T interaction with synthetic Alzheimer's disease beta-amyloid peptides: detection of amyloid aggregation in solution. *Protein Sci.* **2**, 404-410, (1993).

122 Soscia, S. J. *et al.* The Alzheimer's disease-associated amyloid beta-protein is an antimicrobial peptide. *PLoS One* **5**, e9505, (2010).

123 Sengupta, U., Nilson, A. N. & Kayed, R. The Role of Amyloid-beta Oligomers in Toxicity, Propagation, and Immunotherapy. *EBioMedicine* **6**, 42-49, (2016).

124 Branda, S. S., Chu, F., Kearns, D. B., Losick, R. & Kolter, R. A major protein component of the *Bacillus subtilis* biofilm matrix. *Mol. Microbiol.* **59**, 1229-1238, (2006).

125 Chai, L. *et al.* Isolation, characterization, and aggregation of a structured bacterial matrix precursor. *J. Biol. Chem.* **288**, 17559-17568, (2013).

126 Malishev, R., Abbasi, R., Jelinek, R. & Chai, L. Bacterial Model Membranes Reshape Fibrillation of a Functional Amyloid Protein. *Biochemistry* **57**, 5230-5238, (2018).

127 Terra, R., Stanley-Wall, N. R., Cao, G. & Lazazzera, B. A. Identification of *Bacillus subtilis* SipW as a bifunctional signal peptidase that controls surface-adhered biofilm formation. *J. Bacteriol.* **194**, 2781-2790, (2012).

128 Abbasi, R. *et al.* The Bacterial Extracellular Matrix Protein TapA Is a Two-Domain Partially Disordered Protein. *Chembiochem* **20**, 355-359, (2019).

129 Duanis-Assaf, D. *et al.* Cell wall associated protein TasA provides an initial binding component to extracellular polysaccharides in dual-species biofilm. *Sci. Rep.* **8**, 9350, (2018).

130 Yannarell, S. M., Grandchamp, G. M., Chen, S. Y., Daniels, K. E. & Shank, E. A. A Dual-Species Biofilm with Emergent Mechanical and Protective Properties. *J. Bacteriol.* **201**, (2019).

131 Danhorn, T. & Fuqua, C. Biofilm formation by plant-associated bacteria. *Annu. Rev. Microbiol.* **61**, 401-422, (2007).

132 Rudrappa, T., Biedrzycki, M. L. & Bais, H. P. Causes and consequences of plant-associated biofilms. *FEMS Microbiol. Ecol.* **64**, 153-166, (2017).

133 Fira, D., Dimkic, I., Beric, T., Lozo, J. & Stankovic, S. Biological control of plant pathogens by *Bacillus* species. *J. Biotechnol.* **285**, 44-55, (2018).

134 Chen, Y. *et al.* Biocontrol of tomato wilt disease by *Bacillus subtilis* isolates from natural environments depends on conserved genes mediating biofilm formation. *Environ. Microbiol.* **15**, 848-864, (2013).

135 Beauregard, P. B., Chai, Y., Vlamakis, H., Losick, R. & Kolter, R. *Bacillus subtilis* biofilm induction by plant polysaccharides. *Proc. Natl. Acad. Sci. USA* **110**, E1621-1630, (2013).

136 Lopez, D., Vlamakis, H., Losick, R. & Kolter, R. Paracrine signaling in a bacterium. *Genes Dev.* **23**, 1631-1638, (2009).

137 Zeriouh, H., de Vicente, A., Perez-Garcia, A. & Romero, D. Surfactin triggers biofilm formation of *Bacillus subtilis* in melon phylloplane and contributes to the biocontrol activity. *Environ. Microbiol.* **16**, 2196-2211, (2014).

138 Molina-Santiago, C. *et al.* The extracellular matrix protects *Bacillus subtilis* colonies from *Pseudomonas* invasion and modulates plant co-colonization. *Nat. Commun.* **10**, 1919, (2019).

139 Flemming, H. C. EPS-Then and Now. *Microorganisms* **4**, (2016).

140 Whipps, J. M., Hand, P., Pink, D. & Bending, G. D. Phyllosphere microbiology with special reference to diversity and plant genotype. *J Appl Microbiol* **105**, 1744-1755, (2008).

141 Costa, O. Y. A., Raaijmakers, J. M. & Kuramae, E. E. Microbial Extracellular Polymeric Substances: Ecological Function and Impact on Soil Aggregation. *Front Microbiol* **9**, 1636, (2018).

142 D'Haeze, W. & Holsters, M. Surface polysaccharides enable bacteria to evade plant immunity. *Trends Microbiol* **12**, 555-561, (2004).

143 Bianciotto, V., Andreotti, S., Balestrini, R., Bonfante, P. & Perotto, S. Mucoid mutants of the biocontrol strain *Pseudomonas fluorescens* CHA0 show increased ability in biofilm formation on mycorrhizal and nonmycorrhizal carrot roots. *Mol. Plant Microbe. Interact.* **14**, 255-260, (2001).

144 Killiny, N., Martinez, R. H., Dumenyo, C. K., Cooksey, D. A. & Almeida, R. P. The exopolysaccharide of *Xylella fastidiosa* is essential for biofilm formation, plant virulence, and vector transmission. *Mol. Plant Microbe. Interact.* **26**, 1044-1053, (2013).

145 Hammer, N. D., Schmidt, J. C. & Chapman, M. R. The curli nucleator protein, CsgB, contains an amyloidogenic domain that directs CsgA polymerization. *Proc. Natl. Acad. Sci. USA* **104**, 12494-12499, (2007).

146 Shu, Q. *et al.* The *E. coli* CsgB nucleator of curli assembles to beta-sheet oligomers that alter the CsgA fibrillization mechanism. *Proc. Natl. Acad. Sci. USA* **109**, 6502-6507, (2012).

147 Jeter, C. & Matthysse, A. G. Characterization of the binding of diarrheagenic strains of *E. coli* to plant surfaces and the role of curli in the interaction of the bacteria with alfalfa sprouts. *Mol. Plant Microbe. Interact.* **18**, 1235-1242, (2005).

148 Fink, R. C. *et al.* Transcriptional responses of *Escherichia coli* K-12 and O157:H7 associated with lettuce leaves. *Appl. Environ. Microbiol.* **78**, 1752-1764, (2012).

149 Carter, M. Q., Louie, J. W., Feng, D., Zhong, W. & Brandl, M. T. Curli fimbriae are conditionally required in *Escherichia coli* O157:H7 for initial attachment and biofilm formation. *Food Microbiol.* **57**, 81-89, (2016).

150 Barny, M.-A. *Erwinia amylovora hrpN* mutants, blocked in harpin synthesis, express a reduced virulence on host plants and elicit variable hypersensitive reactions on tobacco. *European Journal of Plant Pathology* **101**, 333-340, (1995).

151 Charkowski, A. O. *et al.* The *Pseudomonas syringae pv. tomato* HrpW protein has domains similar to harpins and pectate lyases and can elicit the plant hypersensitive response and bind to pectate. *J. Bacteriol.* **180**, 5211-5217, (1998).

152 Lee, J. *et al.* HrpZ(Psph) from the plant pathogen *Pseudomonas syringae pv. phaseolicola* binds to lipid bilayers and forms an ion-conducting pore in vitro. *Proc. Natl. Acad. Sci. USA* **98**, 289-294, (2001).

153 He, S. Y., Huang, H. C. & Collmer, A. *Pseudomonas syringae pv. syringae* harpinPss: a protein that is secreted via the Hrp pathway and elicits the hypersensitive response in plants. *Cell* **73**, 1255-1266, (1993).

154 Kim, J. G. *et al.* Characterization of the *Xanthomonas axonopodis pv. glycines* Hrp pathogenicity island. *J. Bacteriol.* **185**, 3155-3166, (2003).

155 Li, J. G. *et al.* PopW of *Ralstonia solanacearum*, a new two-domain harpin targeting the plant cell wall. *Mol Plant Pathol* **11**, 371-381, (2010).

156 Wei, Z. M. *et al.* Harpin, elicitor of the hypersensitive response produced by the plant pathogen *Erwinia amylovora*. *Science* **257**, 85-88, (1992).

157 Choi, M. S., Kim, W., Lee, C. & Oh, C. S. Harpins, multifunctional proteins secreted by gram-negative plant-pathogenic bacteria. *Mol. Plant Microbe. Interact.* **26**, 1115-1122, (2013).

158 Chen, Y. *et al.* A *Bacillus subtilis* sensor kinase involved in triggering biofilm formation on the roots of tomato plants. *Mol. Microbiol.* **85**, 418-430, (2012).

159 Lakshmanan, V. *et al.* Microbe-associated molecular patterns-triggered root responses mediate beneficial rhizobacterial recruitment in *Arabidopsis*. *Plant Physiol.* **160**, 1642-1661, (2012).

160 Rudrappa, T., Czymmek, K. J., Pare, P. W. & Bais, H. P. Root-secreted malic acid recruits beneficial soil bacteria. *Plant Physiol.* **148**, 1547-1556, (2008)

Our research aims at understanding the intricate molecular mechanisms underlying the assembly of the extracellular matrix during *B. subtilis* biofilm formation and how this macromolecular structure contributes to the interaction of *B. subtilis* with plants. Previous studies in the laboratory demonstrated that surfactin acts as a self-trigger of biofilm formation in *B. subtilis* on the phylloplane through the induction of the *tapA* operon. This finding and the relevance of the amyloid protein TasA for ECM assembly *in vitro*, led us to hypothesize a prominent role of this protein in the ecology and adaptation of *B. subtilis* to the phyllosphere. The goal of this research is, thus, to study how the two protein components of the *B. subtilis* amyloid system, TasA and TapA, participate in the process of amyloidogenesis, and to evaluate how relevant they are in *B. subtilis* physiology *in vitro* and over a plant host. To achieve this general goal, we have proposed the following individual objectives:

1. To study the contribution of TasA and TapA to the formation of the final tridimensional molecular structure of the amyloid fibers present in the extracellular matrix of *B. subtilis* biofilms.

2. To analyze the contribution of the TasA amyloid fibers to the physiology and survival of *B. subtilis* on plant leaves.

3. To dissect the molecular mechanism by which TasA, the major component of the amyloid fibers, diversifies its biological function at the cellular level.

Chapter II

Molecular characterization and architecture of bacterial amyloids in *B. subtilis* biofilms

Parts of the content of this chapter have been published in:

Nadia El Mammeri, Jesus Hierrezuelo, James Tolchard, **Jesús Cámara-Almirón**, Joaquín Caro-Astorga, Ana Álvarez-Mena, Antoine Dutour, Mélanie Berbon, Jayakrishna Shenoy, Estelle Morvan, Axelle Grélard, Brice Kauffmann, Sophie Lecomte, Antonio de Vicente, Birgit Habenstein, Diego Romero, and Antoine Loquet. Molecular architecture of bacterial amyloids in Bacillus biofilms. *The FASEB Journal*. **33:11**, 12146-12163 (2019).

ABSTRACT

The formation of biofilms provides structural and adaptive bacterial response to the environment. In *Bacillus subtilis*, the biofilm extracellular matrix is composed of exopolysaccharides, hydrophobins, and a functional amyloid called TasA, that requires the accessory protein TapA for efficient polymerization. We report, using multiscale approaches, the molecular architecture of *Bacillus subtilis* functional amyloids. SSNMR data reveal that the major amyloid component TasA, in its fibrillar amyloid form, contains β-sheet and α-helical secondary structure, suggesting a nontypical amyloid architecture. Proteinase K digestion experiments indicate the amyloid moiety is ∼100 amino acids long and is mostly located at the N-terminal half of the protein, which is a conserved region that contains imperfect amino acid repeats and amyloidogenic segments that are important for the assembly of the amyloid fiber and biofilm formation. Structural analysis of the accessory protein TapA revealed its amyloid nature and a common structural architecture, suggesting a co-assembly in the cellular context. Our findings highlight the (nontypical) amyloid behavior of TasA and TapA and underline the importance of the N-terminal domain of TasA for the biological function of this protein during the assembly of the extracellular matrix.

INTRODUCTION

Functional amyloids[1] have emerged as one of the most outstanding protein contributors to bacterial cell physiology and behavior[2-4]. Amyloids functionality[5] can range from purely structural[6] to supporting multicellular bacterial communities[7,8], mediating interaction with surfaces[9], driving the assembly of the extracellular matrix[10,11] and, more recently, a putative role in neurodegeneration[12]. This broad functional versatility along with their remarkable tendency to self-assemble into filaments, robust and resistant to most denaturing environmental conditions[13-15] contribute to their consideration as a molecular Swiss-army knife in the bacterial kingdom.

A fascinating step in the bacterial life cycle is the organization of bacterial communities called biofilms. Biofilms are composed of an insoluble, noncrystalline supramolecular matrix mostly made up of water, proteins, lipids, and polysaccharides. The coordinated expression of a pool of structural elements permits the assembly of this extracellular matrix, a sort of bacterial tissue that provides physical support to the biofilm, protects the cells from external aggressions, mediates interactions with the environment and regulates the flow of nutrients and signaling molecules[16]. Functional amyloids are one of these protein structural components, and successive studies are highlighting their definite contribution to different steps of the biofilm life cycle: adhesion, extracellular matrix construction, and motility[17-19]. *Bacillus subtilis*, a soil-dwelling bacterium, is one of the most-studied microbes that has vastly contributed to our understanding of the genetic regulatory pathways and the structural elements related to biofilms[20]. A previous study of the TasA protein, a major protein component of the extracellular matrix of *B. subtilis* biofilms[21], pointed its amyloid-like nature: TasA forms filaments with thioflavin T (ThT) or Congo red dyes-binding activity and can repolymerize after disaggregation with acid treatments[22]. The double mutant strain *eps sinR* served as a natural overproducer of TasA which could be purified mostly as aggregates and copurified with a small amount of TapA, an accessory protein for TasA fibers formation, and thus essential in biofilm assembly[23].

Bacterial amyloids offer a paradigm to understand how the formation of these well-ordered polymers at the mesoscopic scale can counterbalance potential amyloid-associated deleterious effects. Moreover, although most of the disease-related amyloid systems are found in the intracellular space, the vast majority of bacterial functional amyloids evolved at the bacterial surface and need to sustain variable and heterogeneous external conditions to fulfill their functional roles, as exemplified for the

TasA filaments found in *Bacillus* biofilms. The mechanism by which these specific filaments are formed is still not fully known, nonetheless, it is established that, although the amyloid fold does not fully rely in the primary amino acid sequence, the amino acid composition of certain regions with particular chemical and structural properties -that make them prone to aggregation and polymerization- can influence the assembly mechanism of these amyloid aggregates. Several studies have associated certain amino acids at specific positions within protein or peptide sequences with variable kinetics, structures and mechanisms of amyloidogenesis[24,25]. Furthermore, studies with different bacterial functional amyloids implicated in biofilm formation have demonstrated how the repetition of certain amino acid motifs is significant for the process of polymerization of the amyloid fibers[26,27]. However, a detailed structural description of these functional amyloids in their relevant fibrillar states is required to understand how they are formed and how their conformation responds to environmental stimuli in the context of biofilm formation and evolution.

There are two recent structural studies[28,29] that have focused on TasA in its monomeric and fibrillar state. Monomeric TasA (amino acids 28–261), crystallized at pH 4.6, has revealed a jelly-roll fold[28] composed of α-helical and β-sheet secondary structure, and fibrils with a predominant β-sheet conformation from solid-state NMR (SSNMR) analysis that exhibit a typical cross-β signature by X-ray diffraction. Conversely, another study[29] demonstrated an alternative conformation of TasA fibrils lacking a canonical cross-β signature by X-ray fiber diffraction. Although the ability of TasA to form β-sheet–rich fibrils has been substantiated by our group through the observation of straight unbranched fibrils and its binding to ThT and Congo red dyes[22], only scarce information has been reported on the structural organization of TasA within its fibrillar form. We hereafter aimed at: i) investigating the structural signature of these *B. subtilis* biofilm related TasA fibrils, ii) characterizing the sequence determinants important for the polymerization of TasA fibrils and iii) analyzing the singular accessory protein TapA that participates in the process of TasA fibrillation. Using a combination of cell biology and microscopy techniques, along with a biochemical and biophysical experimental approach, we found that TasA protein, as well as TapA, form amyloid-like fibers exhibiting canonical cross-β organization, although a part of both protein sequences maintain a well-ordered α-helical fold within the filaments. Furthermore, a detailed sequence analysis of this TasA amyloid core identified regions and key amino acids important for the structural functionality of the protein. Finally, we suggest a putative structural co-assembly of TasA and TapA in the context of biofilm formation. In summary, our results uncover the complex interdependent assembly mechanism between TasA and its accessory protein.

RESULTS

Functionality of recombinant TasA expressed in *E. coli*

The TasA protein is well conserved across the *Bacillus* genus but can be phylogenetically separated into 2 distinct groups: in the *B. subtilis* group, which englobes other nonpathogenic species such as *B. amyloliquefaciens* or *B. pumillus*, the protein is ~237 aa long (261 aa for TasA in *B. subtilis*); and the group of *B. cereus* and other related species such as *B. thuringiensis* or *B. anthracis*, in which the protein is ~170 aa long. The comparison between *B. subtilis* TasA and *B. cereus* TasA, the two representative strains of each group, reveals that the protein shares ~35% sequence homology between the two species, mostly located in the N-terminal half (Fig. 2.1), which is, apparently, sufficient for functionality concerning bacterial multicellularity and biofilm formation. In *B. subtilis* NCIB3610, TasA is known to participate in the formation of wrinkly pellicles or colonies at the air-liquid interface or in solid media respectively[21].

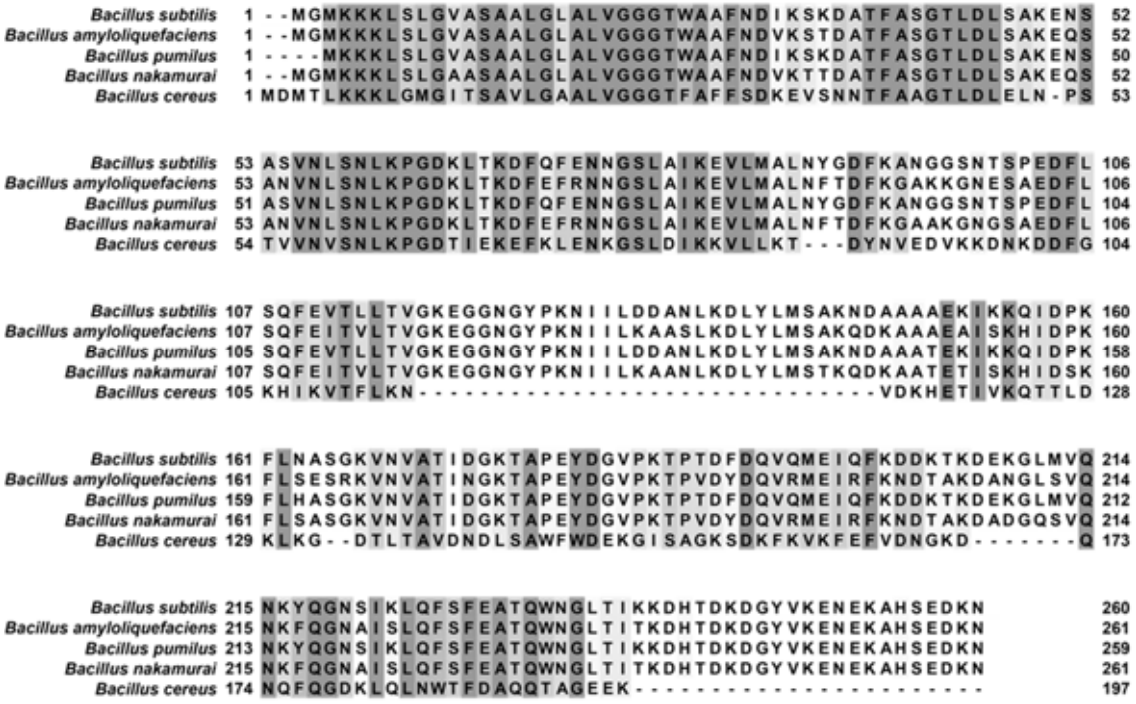

Figure 2.1. Two types of TasA are found across the Bacillus spp. genus. Multiple sequence alignment of TasA orthologues found in different species. The TasA from the *B. subtilis* (and related species) group differ from the TasA found in the *B. cereus* (and related species) group.

In our effort to engage in structural characterization of these filaments, we developed and optimized protocols for the overexpression and purification of TasA. Heterologous TasA expression in *E. coli* was a prerequisite in order to avoid the presence of TapA, an accessory protein involved in TasA fibril polymerization[23]. Therefore, this allowed us to investigate the aggregation and conformation of filaments formed solely by TasA.

Following the overexpression and purification of TasA, samples were kept soluble in acidic buffer at 4°C. In order to demonstrate the biological functionality of the recombinant purified TasA (rTasA), complementation assays were performed as previously described[22] (Fig. 2.2). Since TasA was purified by inducing the formation of inclusion bodies (IBs) and solubilizing them prior to affinity chromatography and refolding, we tested whether these inclusion bodies alone were able to complement the biofilm formation defect observed for a *tasA* mutant. IBs are insoluble and composed of the aggregated and nonfunctional forms of the purified protein. Indeed, 20 µl of the isolated IB suspension (OD_{600} ~ 0.5) were added to 1 ml of the medium in a 24-well microplate and no pellicle restoration was observed (Fig. 2.2A). Conversely, soluble rTasA protomers rescued the formation of a wrinkly pellicle in the Δ*tasA* strain in a concentration-dependent manner (Fig. 2.2A).

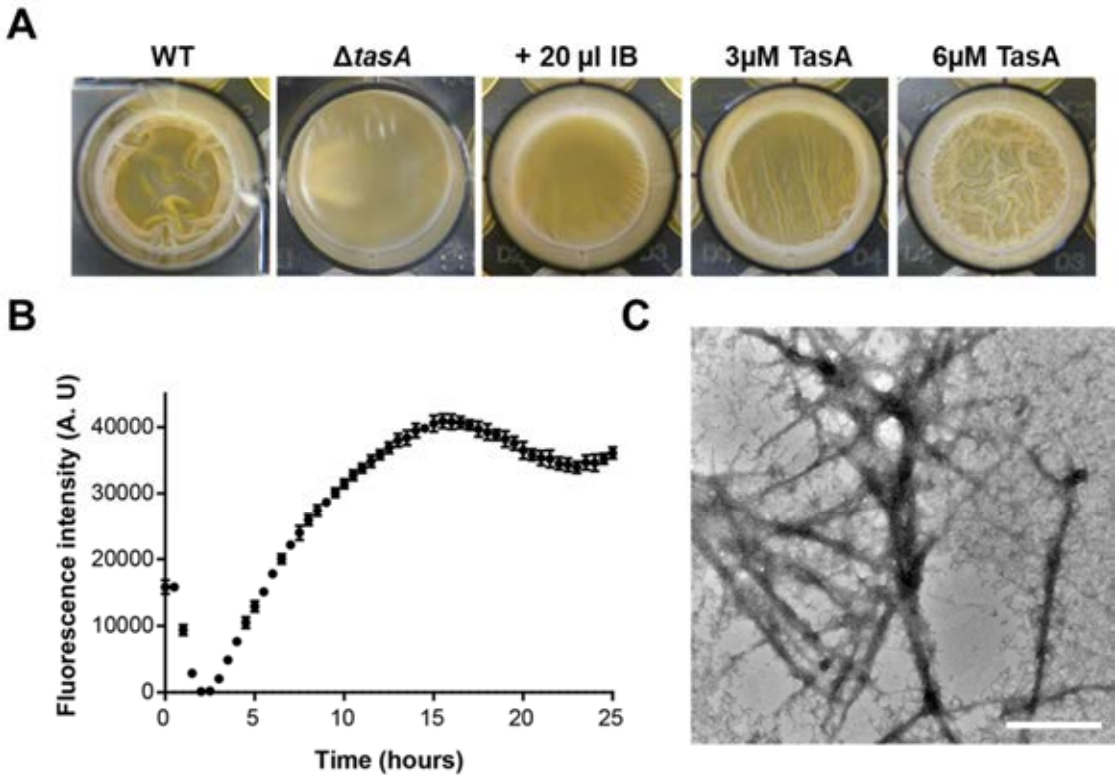

Figure 2.2. Purified recombinant TasA (rTasA) is biologically functional and retains amyloid properties. A) Biofilm assays in MOLP medium of the different strains incubated for 48 h at 30 °C. The Δ*tasA* strain was incubated in the presence or absence of purified rTasA. TasA purified from *E. coli* rescues the phenotype of Δ*tasA* mutant of *B. subtilis* in a concentration-dependent manner. Inclusion bodies (IBs) made of TasA are not functional. WT stands for wild type. **B)** ThT binding kinetics of rTasA at room temperature immediately after buffer exchange to pH 7. 4. Error bars indicate the SEM. **C)** Transmission electron micrograph of negatively strained rTasA filaments formed after 24 h of incubation at room temperature. Scale bar = 500 nm.

Then, in order to see whether this rTasA retains its amyloid properties, we performed two additional experiments. An intrinsic feature of amyloid proteins is their transition from the monomeric to the fibrillar state, concomitant with enrichment in β-sheets, which confer amyloid proteins the ability to bind and react in a very well-defined manner to specific dyes such as Congo red[30] or ThT[31]. We previously demonstrated that acid

disaggregated TasA solutions purified from *B. subtilis* could repolymerize into fibers following a typical amyloid polymerization curve using the ThT fluorescence assay[22,31]. Therefore, we first checked by fluorescence spectroscopy whether the rTasA displayed the typical tinctorial features of amyloid proteins. We took advantage of the fact that freshly purified TasA from *E. coli* could be maintained as monomers in acidic conditions after the purification process. Consistent with its notion as amyloid, after buffer exchanging to physiological pH, the ThT growth curves for rTasA demonstrated that the protein specifically bound ThT and emitted a fluorescent signal at the amyloid-specific 480–484-nm wavelength in a time-dependent manner (Fig. 2.2B), similar to other amyloids proteins[22], which suggests the enrichment of the sample in β-sheet content. Second, the protein *in vitro* was able to polymerize into bodies with fibrillar shape, as shown by transmission electron microscopy (TEM) (Fig. 2.2C).

Taken together, these results validate the use of rTasA for our structural and functional studies as it has been shown that: i) the recombinant protein is biologically active and ii) maintains all the amyloid properties shown for the native protein purified from *B. subtilis*[22].

TasA functional amyloid is able to aggregate into assemblies with various morphologies and characteristic cross-β architecture

rTasA filaments, produced by heterologous expression in *E. coli* and assembled *in vitro* (at a protein concentration of 0.25 mM and pH 7.4), were analyzed in depth using transmission electron microscopy (TEM) (Fig. 2.2C and Fig. 2.3A). rTasA assemblies revealed macroscopic filamentous morphologies following polymerization over 1 week at room temperature. rTasA filaments showed a straight, uniform fibrillar morphology (Fig. 2.3A) in which the protofilaments (i.e., the smallest fibrillar entity of the quaternary architecture) arranged in a supramolecular bundle-like organization made of laterally associated stacked protofilaments. The diameter of the protofilaments was ~5 nm, consistent with previous observations of TasA filaments in biofilm culture[22], and their length was variable (up to several microns). Interestingly, a symmetrical arrangement of uniform repeats perpendicular to the primary axis was observed along the filament. The axial translation per repeat was ~5 nm.

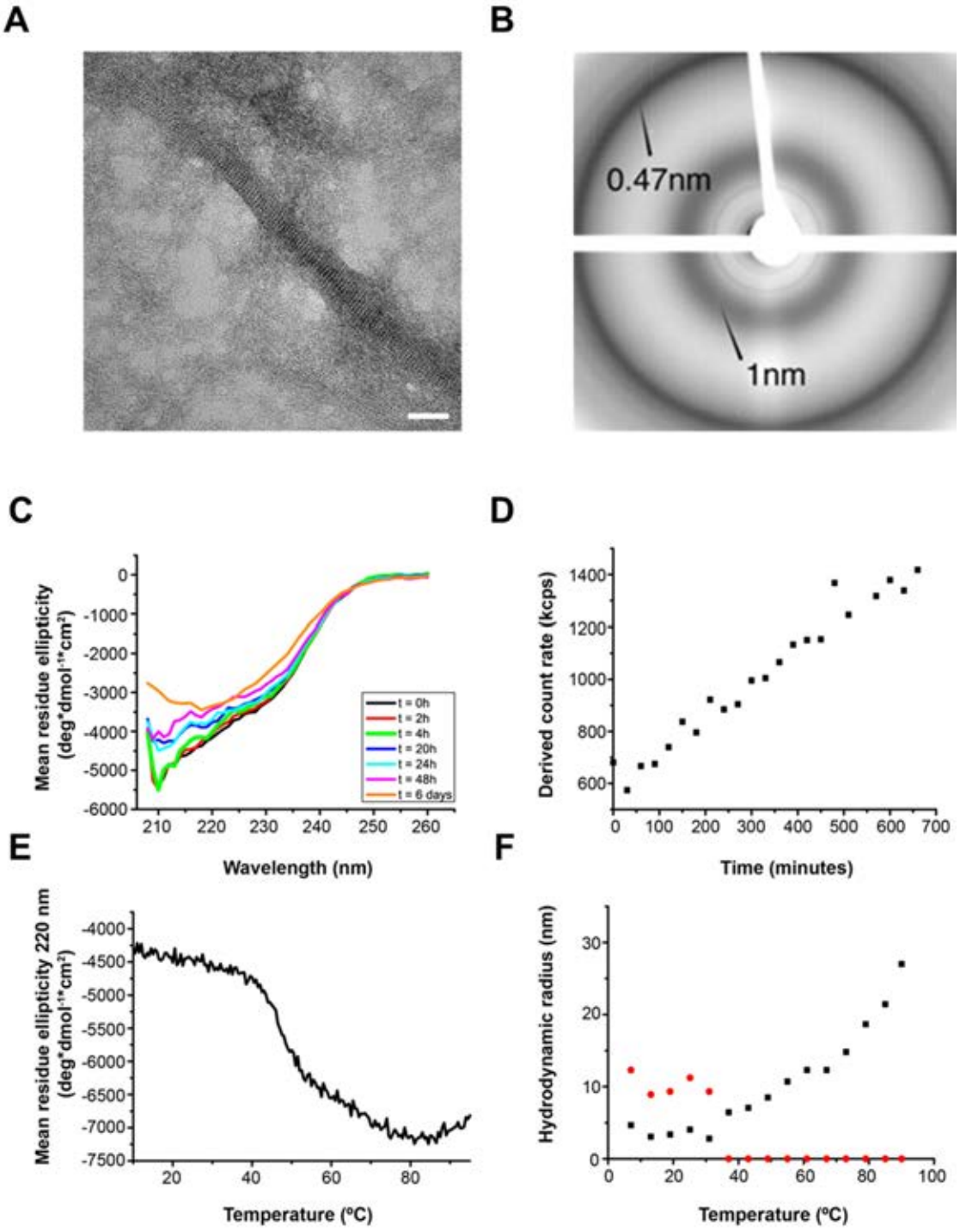

Figure 2.3. rTasA filaments exhibit amyloid properties with a cross-β structure. A) Transmission electron micrographs of negatively strained rTasA filaments after one week of incubation at room temperature. The average filament width was ~5 nm. Scale bar = 50 nm. **B)** X-ray diffraction pattern of rTasA filaments. The arrows indicate reflections at ~4.7 and ~10 Å. **C)** MRE spectra of rTasA recorded over the course of six days. The last time-point recorded shows a minimum at ~216 nm indicative of β-sheet content. **D)** Aggregation kinetics of rTasA followed by DLS. Increasing derived count rate over time indicates aggregation. **E)** Thermal behavior of rTasA studied by CD spectroscopy at 220 nm from 10 to 95 °C. A melting point was found at 50.5 °C. **F)** Thermal behavior of rTasA studied by DLS from 5 to 95 °C. Red dots indicate a larger species (~12nm of hydrodynamic radius) found in the sample. Black squares indicate the expected hydrodynamic radius for monomeric TasA (~3 nm).

A structural hallmark of amyloid protein assemblies is their cross-β arrangement in filaments, a feature reflected in the observation of typical X-ray diffraction patterns, with the signature of interstrand and intersheet repetitive distances at 4.7 and 10 Å, respectively[32]. We have previously demonstrated that filaments of TasA purified from *B. subtilis* can bind ThT and Congo red dyes[22], suggesting that TasA assembles into functional amyloid filaments. Similarly, the results presented in the above section demonstrate the same properties for rTasA; however, detailed structural evidence of the amyloid architecture was missing. X-ray diffraction patterns were recently reported for rTasA fibrils by two independent laboratories[28,29], controversially showing different diffraction rings, encoding[28] or not[29] for a canonical cross-β arrangement. Here, we performed X-ray diffraction experiments on rTasA fibrils to characterize the amyloid nature of our sample preparations. Clear diffraction signals at 4.7 and 10 Å demonstrated the presence of a cross-β structure within TasA filaments (Fig. 2.3B). This was further evidenced by a progressive enrichment in β-sheet secondary structure, as demonstrated by circular dichroism spectroscopy (CD) with the continuous decrease of the mean residue ellipticity (MRE) and the appearance of a minimum around 216 nm, over the course of the experiment (Fig. 2.3C).

The evolution of monomers to insoluble fibers enriched in β-sheet secondary structure implies the formation of intermediate aggregates, which may function as nucleators that further enhance the polymerization process. We characterized the aggregation progression of the starting monomeric protein solutions over the first 12 h by dynamic light scattering assays (DLS). Indeed, the enrichment in β-sheet content was accompanied by exponential aggregation from the very beginning of the experiment, as shown by the increase in kilocounts per second (Fig. 2.3D). Interestingly, these protein aggregates show a high degree of thermostability. A thermal scan experiment performed by measuring the MRE at 222 nm by CD showed that TasA gains secondary structure upon heating (Fig. 2.3E), displaying a thermal behavior that is distinct compared to globular proteins, especially at high temperatures, where heating normally induces protein unfolding and therefore increase of the MRE. However, we observed a decrease in the MRE as a function of temperature, with a melting temperature of 50.5 °C, and instead of reaching a completely unfolded state at high temperatures, for instance at 80 °C, we observed a conformation that still shows high contents of secondary structure, as reported for other amyloid proteins[33,34]. This correlates with the increased hydrodynamic radius observed in a temperature-dependent manner by DLS, indicating a temperature dependent aggregation (Fig. 2.3F). These results also show the presence of larger

species in the sample, that however, disappears after heating when the mean hydrodynamic radius starts to increase.

Altogether, these data allow us to conclude that these filaments exhibit the structural hallmark of amyloid fibers: i) the progressive aggregation and enrichment in β-sheet secondary structure and ii) the polymerization into thermostable fibers that display the canonical cross-β structure and support the amyloid-like nature of the TasA protein in its fibrillar form.

Analysis of the structural signature of TasA amyloid filaments

SSNMR is an exquisite tool to monitor the local structural order and observe the presence of dynamic or static disorder and polymorphism in fibrillar biological samples[35-39]. We overexpressed rTasA in *E. coli* using isotopically [^{13}C]-^{15}N-labeled carbon and nitrogen sources to obtain uniformly [^{13}C]/^{15}N-labeled rTasA filaments. We carried out SSNMR experiments using through-space (i.e., crosspolarization) and through-bond polarization transfers (i.e., INEPT) to respectively detect rigid and mobile protein moieties in the amyloid filamentous state. The 1-dimensional (1D) [^{13}C]–detected SSNMR experiment performed at 278 K (Fig. 2.4A top) revealed well-resolved NMR resonances, indicating a high local structural order of rTasA protein subunit within the filaments. Temperature-dependent experiments performed at room temperature (298 K) and in the frozen state (263 K) show a similar fingerprint (Fig. 2.4A top), indicating that rTasA subunits maintain the same conformation in the filaments at various temperatures, although a significant broadening is observed at −10 °C (263 K) reflecting the presence of multiple local conformations frozen out at low temperatures as already observed by SSNMR for solid proteins[40], including amyloid fibrils[40]. In addition to the previous through-space experiments, through-bond mixing was used to detect mobile protein moieties at different temperatures (Fig. 2.4A bottom). We observed a gradual increase of the signal with the temperature, indicating increasing mobility of rTasA with increasing temperature.

We employed multidimensional ^{1}H-[^{13}C] experiments for rTasA filaments using through-bond mixing to assign SSNMR correlations encoding for mobile residues (Fig. 2.4B). We observed correlations for all amino acid types in a random-coil conformation, clearly indicating the presence of non-assembled TasA molecules within the ultracentrifuged pellet sample. The observation of monomeric TasA in the ultracentrifuged filament sample is consistent with previous observations on other amyloid fibrils such as Tau pair-helical filaments[41] or α-synuclein fibrils[42]. Together with our observation that rTasA form a fibrillar objects, as seen by TEM analysis, these SSNMR data indicated that *B. subtilis*

rTasA filaments are formed by well-ordered TasA subunits, although a fraction of the protein stays in a non-assembled (mobile, unfolded) conformation. Such an observation could suggest the assembly process attains an equilibrium state between the monomeric and the fibrillar (i.e., assembled) TasA state.

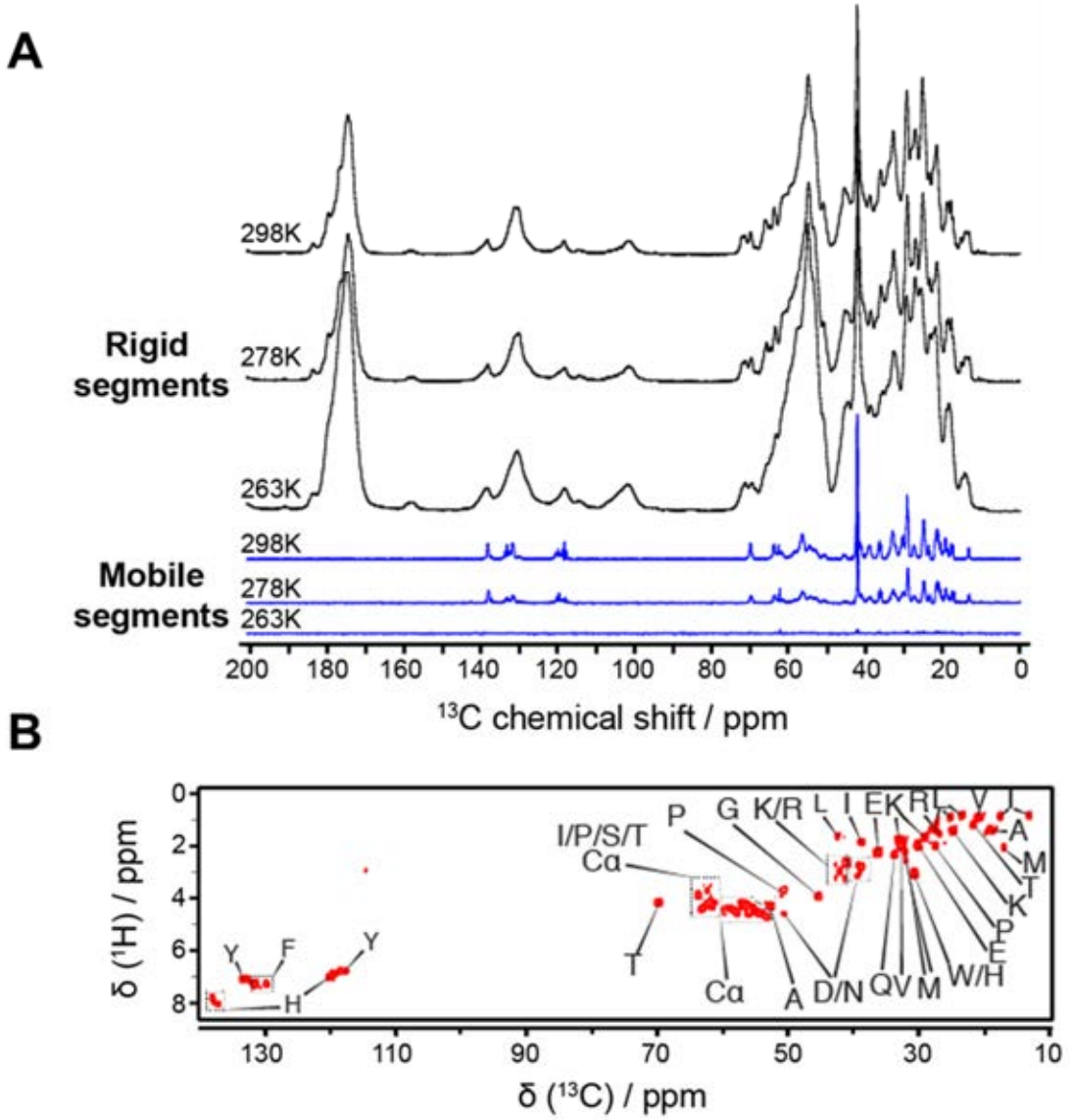

Figure 2.4. SSNMR analysis of the rTasA filament shows an equilibrium between assembled and non-assembled protein. A) Through-space cross-polarization experiments (in black) reveal rigid protein segments in the fibrillar assembly of rTasA. Through-bond INEPT experiments (in blue) reflect mobile segments. **B)** Two-dimensional SSNMR ^{1}H-^{13}C correlation experiment using through-bond mixing (INEPT) to detect the mobile segments of rTasA filaments and their amino acids composition.

To further investigate the structure of the rigid amyloid core in rTasA filaments, we employed multidimensional [^{13}C]-[^{13}C] SSNMR with through-space mixing on uniformly [^{13}C]-labeled rTasA samples (Fig. 2.5A). We observed that the spectral resolution (i.e., [^{13}C] line width) displayed by the rTasA filaments exhibit narrow [^{13}C] line widths (full-width at half-height of ~30–100 Hz), thus accounting for highly ordered local

arrangements of rTasA subunits within the filaments. Interestingly, although TasA in its mature form embodies 233 aa, only ~70 NMR spin systems (i.e., residues) were detected in the rigid core using through-space mixing, suggesting the amyloid rigid core contains only part of the TasA sequence (Supplementary Table 2.1).

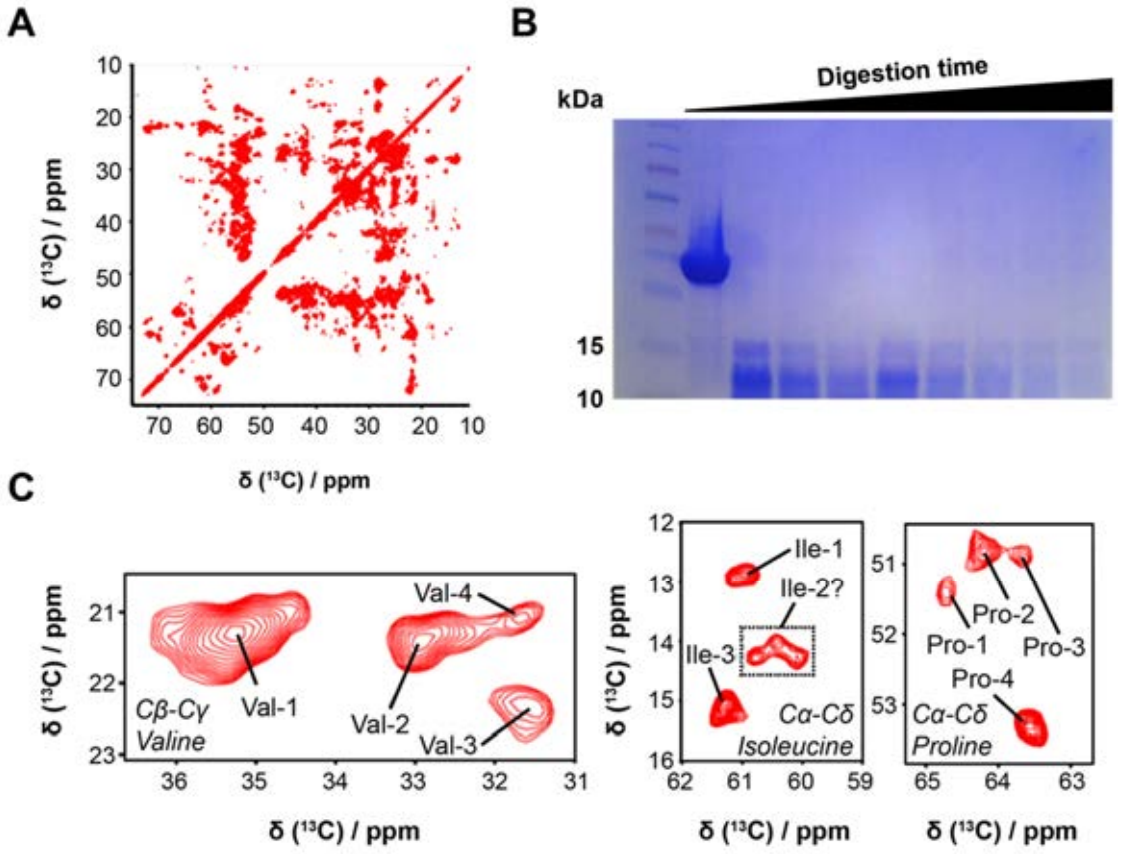

Figure 2.5. SSNMR analysis of rTasA functional amyloids demonstrates the presence of a rigid amyloid core that comprises part of the N-terminal region of TasA. A) 2D [^{13}C]-[^{13}C] SSNMR experiments of rTasA filaments. **B)** SDS-PAGE analysis of rTasA prior and after digestion via proteinase K at different digestion times (lane 2: no digestion; lane 3: 1 minute, lane 4: 5 minutes, lane 5: 15 minutes, lane 6: 20 minutes, lane 7: 30 minutes, lane 8: 45 minutes, lane 9: 1 hour). **C)** Excerpts of the 2D [^{13}C]-[^{13}C] experiment of rTasA fibrils showing chemical shift ranges covering the different Ile Cδ1-Cα, Pro Cδ-Cα, and Val Cγ1-2-Cβ cross-peaks.

In line with the SSNMR results, the use of proteinase K digestion of the mature filaments led to the identification of a 110-aa long resistant segment (K35 to K144). Upon digestion steps at different incubation times, the remaining proteinase-resistant rTasA segments were observed and identified using SDS-PAGE analysis followed by mass spectrometry (Fig. 2.5B). Such observations are in agreement with the 2D [^{13}C]-[^{13}C] SSNMR intraresidual correlation experiments because the number of identified spin systems per residue type (i.e., isoleucine, proline, and valine) match the putative amyloid core amino acid content rather well (Fig. 2.5C). The TasA moiety identified by proteinase K digestion indeed encompasses 3 isoleucines, 3 prolines, and 4 valines (with 10 isoleucines, 7 prolines, and 12 valines, respectively, in the full-length TasA) (Fig. 2.5C, 2.5D and Table S2.1), and interestingly, 2D [^{13}C]-[^{13}C] proton-driven spin-diffusion of rTasA filaments

reveals four crosspeaks in the Cβ-Cγ spectral region of valine 3–4 (depending on potential polymorphism) crosspeaks in the Cα-CΔ region of isoleucines and 4 crosspeaks in the Cα-CΔ region of prolines (Fig. 2.5C).

Secondary structure propensity (SSP) analysis of TasA fibers reveals a rigid β-sheet-enriched amyloid core and a singular proportion of α-helix

Cα and Cβ SSNMR chemical shift values provide reliable data for establishing the secondary structure of TasA in the amyloid state. We engaged in a conformational analysis of the secondary structure extent in rTasA filaments (Fig. 2.6A). For accuracy, we mainly focused on the amino acids alanine, serine, and threonine because their [^{13}C]α -[^{13}C]β correlation signals appear in isolated regions and could be identified unambiguously with respect to other [^{13}C] signal contributions. The mature rTasA construct (233 residues in total) comprises 19 alanines, 15 serines, and 14 threonines. Through the analysis of [^{13}C]α and [^{13}C]β chemical shifts, NMR spectroscopy indeed allows the high accuracy determination of the secondary structural arrangement displayed by any given residue. In other words, depending on the peak position within the spectrum, the secondary structure can be easily inferred. We observed that rTasA amyloid filaments display a pronounced α-helical propensity (Fig. 2.6A). Evaluating peak volume ratios for each residue type, we pursued a more rigorous assessment of secondary structure content. Based on secondary chemical shift analysis[43], we have performed probability-based secondary structure identification. Conformation propensity was assessed using secondary chemical shift [ΔΔCsec = ΔCα − ΔCβ, with ΔCx = Cx(experimental) − Cx(random coil)]. Negative values are considered to be highly indicative of a β-strand conformation. ΔΔCsec values ranging from −1 to 1 were hereafter regarded as random coil-like arrangements because using a less strict segregation would only result in an underestimation of residues arranged in a random coil manner.

For each studied residue type (i.e., alanine, serine, and threonine), the SSNMR peak volumes were used for estimating the percentage of the secondary structure content. rTasA filaments show a considerable tendency to fold in a β-strand–like manner; which is expected considering the typical amyloid X-ray diffraction patterns observed in our study. On average, between alanine, threonine, and serine residues, ∼60% of examined residues are involved in a β-sheet conformation (Fig. 2.6B). However, on average, ∼20% of examined residues in rTasA filaments are involved in a α-helical conformation. Interestingly, amyloid proteins in their fibrillar state are known to contain very high amounts of β-sheet secondary structure[44] and are often uniquely composed of this type of conformation. However, several examples of amyloid fibrils containing a marked

amount of α-helical secondary structure have been reported, including the prion HET-s in its full-length form[45] or full-length Ure2p[46], both comprising a β-sheet–rich amyloid core and a folded or molten globular α-helical moieties. The remarkable presence of α-helical conformation within the TasA amyloid fibrils encoded in SSNMR chemical shifts is proof of its structural singularity.

We next conducted attenuated total reflectance-Fourier transformed infrared spectroscopy experiments (ATR-FTIR) to corroborate the secondary structure elements found for the rTasA amyloids. rTasA filaments have an absorption spectrum with strong amide I and amide II bands at ∼1620 and 1535 cm^{-1}, respectively (Fig. 2.6C). The FTIR spectrum displayed an absorption maximum in the amide I band between 1611–1630 cm^{-1} encoding for β-sheet conformation in amyloid fibrils[47]. We used a deconvolution approach to extract the percentage of secondary structure elements in rTasA filaments; namely, parallel β-sheet (1634 cm−1), antiparallel β-sheet (1620 and 1690 cm−1), α-helix (1658 cm−1), turns (1675 cm−1), and random coil (1646 cm−1), according to well-known assignments[48] (Table 2.1). We observed that the total content of β-sheet secondary structure (including parallel and antiparallel β-sheet) and α-helix is 56 and 21%, respectively, percentages in line with the SSNMR secondary chemical shift analysis.

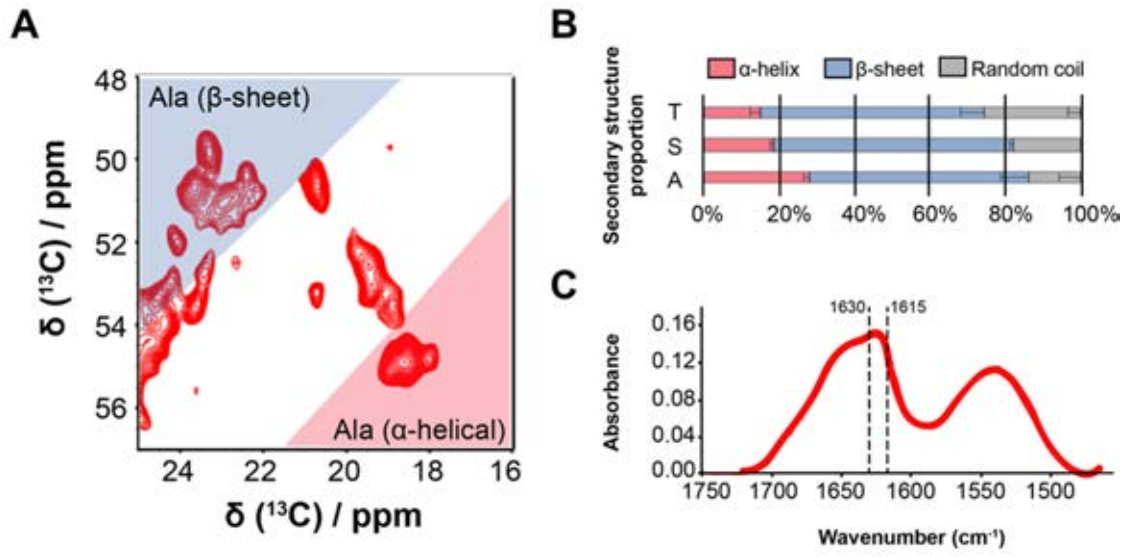

Figure 2.6. Residues in rTasA filaments exhibit a high propensity to β-sheet conformation and a particular proportion of α-helix secondary structure. A) Excerpts of the 2D [^{13}C]-[^{13}C] experiments of rTasA filaments showing a chemical shift range covering the different alanine conformations. Typical expected areas for α-helix and β-sheet conformations are highlighted in light red and light blue, respectively. **B)** SSP of alanine, serine, and threonine as assessed by analyzing secondary chemical shift [^{13}C]-[^{13}C] correlations and using peak volume ratios for quantitative assessment. α-Helix and β-strand conformations are highlighted in light red and light blue, respectively. **C)** ATR-FTIR spectrum of rTasA filaments in the amide I and II range. The dashed lines delineate the position of typical β-sheet contribution.

Table 2.1. SSP of rTasA and TapA resolved by ATR-FTIR analysis.

Secondary structure element	Wave no. (cm^{-1})	Percentage of structural element	
		TasA	**TapA**
β-Sheet antiparallel	1620, 1690	37	20
β-Sheet parallel	1634	19	28
Random coil	1646	14	19
α-Helix	1658	21	24
Turn	1675	9	10

Thus far, our results show that TasA forms amyloid filaments that display the typical features of the amyloid fold, showing a rigid amyloid core resistant to protease activity and enriched in β-sheet content with an atypical proportion of α-helical structure, in line with the observed for other amyloid proteins.

Analysis of TasA amyloid core shows amyloidogenic regions and imperfect amino acid repeats important for filament assembly and biofilm formation

Based on the presence of a rigid amyloid core within rTasA filaments, we decided to investigate in detail the properties of this core in order to find sequences and/or amino acid stretches important for fiber and biofilm formation. We followed two complementary approaches: First, we searched for amino acid repeats within the sequence, which are demonstrated to play a role in the polymerization process of other bacterial functional amyloid proteins[26,27]; second, we looked for amyloidogenic sequences within the core region of TasA (from K35 to K144) using different and specific bioinformatic prediction software.

Analysis of amino acid repeats using RADAR (Rapid Automatic Detection and Alignment of Repeats in protein sequences)[49] showed a region of imperfect amino acid repeats, in which the sequence KDxxFxxxxxxLxxKExxxxxNxxxxKxxxGxxxx is repeated twice and extends from amino acids K35 to S101 (Fig. 2.7A, cyan line). Interestingly, this region comprises the sequence of TasA from the N-terminal region that is mostly conserved between the two groups of TasA found in nature (*B. subtilis* group TasA and *B. cereus* group TasA) and is located within the amyloid core region (amino acids colored in red), which suggests a relevance of this sequence in amyloid fiber assembly and biofilm formation. To explore this hypothesis, we performed an alanine scanning experiment in order to obtain a *tasA* allele encoding a stable version of the protein that shows alterations in colony morphology and biofilm formation. To avoid confounding effects due to expression of the mutated *tasA* gene in the presence of the endogenous operon, we performed this analysis in a strain in which the entire *tapA* operon was deleted and in

which the modified operon, encoding the mutated *tasA* allele, was inserted into the neutral *lacA* locus. Using site-directed mutagenesis, we performed alanine substitutions in some of the amino acids present in the repeated unit (K35 and D36, F72, and K68 and D69) and in some amino acids present in the imperfect region (D64 and G96) (Fig. 2.7A, black arrows).

The strain expressing the native *tasA* gene was unaffected in its ability to form a WT biofilm in solid (Supplementary Fig. S2.1) or in liquid medium (Fig. 2.7B). Strains expressing some of the mutated alleles (K35A, D36A; F72A and G96A) also displayed the characteristic wrinkly morphology of *B. subtilis* biofilm (Fig. 2.7B and Supplementary Fig. S2.1). However, the strains that expressed the D64A and K68A, D69A alleles, failed to fully restore the WT biofilm formation phenotype (Fig. 2.7B and Supplementary Fig. S2.1). We speculated that this partial loss of phenotype could be related to protein instability of the mutated *tasA* alleles due to the alanine substitutions. Biofilm fractionation assay from pellicles followed by immunoblot analysis with anti-TasA antibody (Fig. 2.7C) showed the presence of a very faint anti-TasA reacting band in the cell fraction of the strain bearing the D64A *tasA* allele, contrary to what occurs with the strain expressing the K68A, D69A allele, that exhibits a bands pattern similar to the WT strain, the control or the silent mutants (those expressing the K35A, D36A; F72A and G96A alleles) (Fig. 2.7C, top). However, when the medium fraction was analyzed we observed that TasA D64A was relatively more abundant, reflecting that most of the protein produced by the mutant is secreted to the medium and in a smaller size compared to the WT strain or the native version of TasA. The TasA K68A, D69A allele, also showed a smaller size, however, the intensity of the band was in line with that of the WT or the native TasA (Fig. 2.7C). Finally, very few TasA D64A was present in the extracellular matrix of the strain expressing this allele, showing, in addition, a different immunoreactivity pattern compared to the WT. A similar behavior was observed for TasA K68A, D69A compared to the WT or the native TasA (Fig. 2.7C).

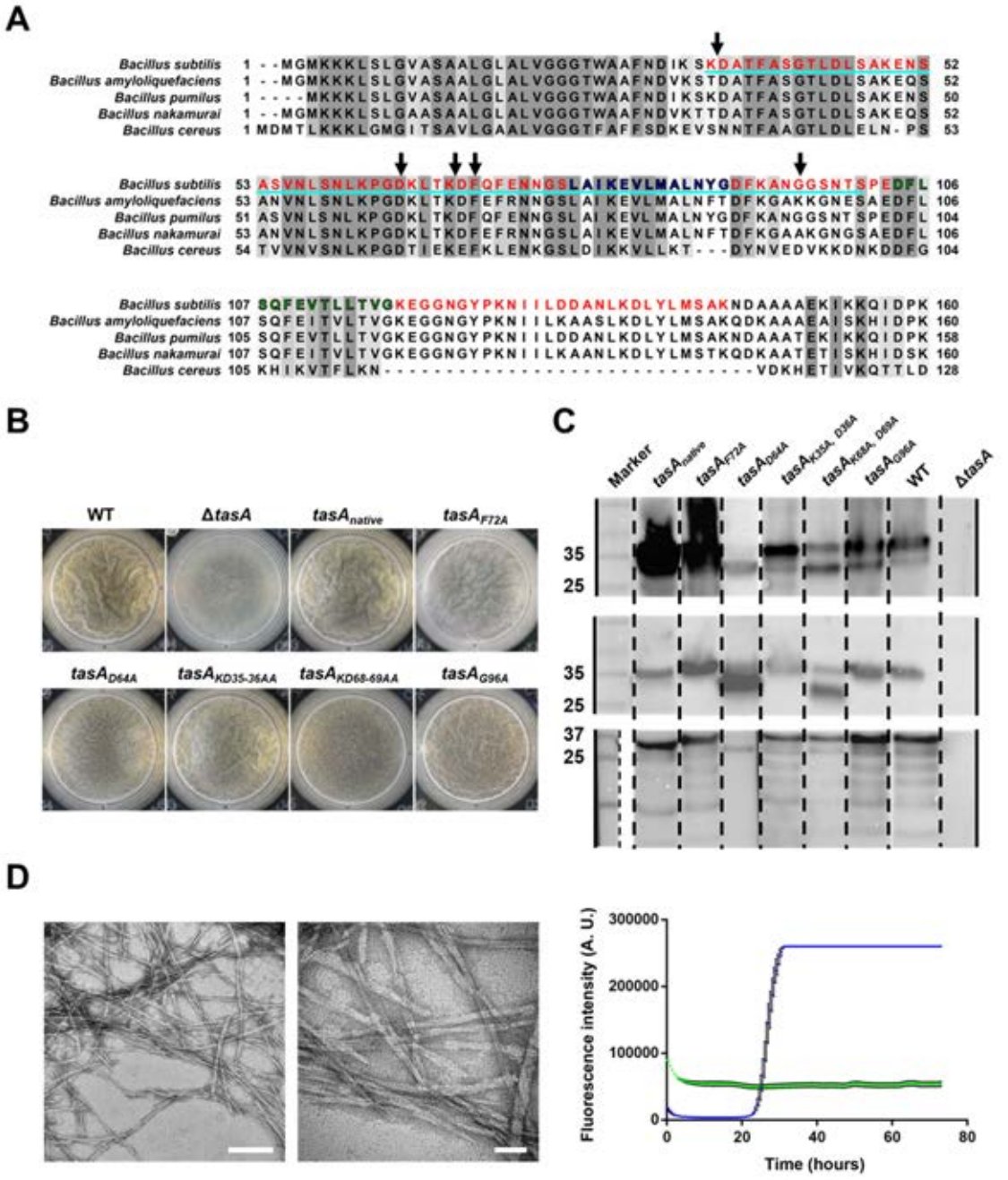

Figure 2.7. Amino acid repeats and amyloidogenic sequences found within the amyloid core regions are relevant for fiber assembly and biofilm formation. A) Multiple sequence alignment of the different TasA orthologues as shown in Figure 2.1, focusing on the N-terminal region of the protein. Amino acids highlighted in red correspond to the amyloid core region. The cyan line delimitates the region of imperfect amino acid repeats. The arrows indicate the amino acids that have been substituted. The sequences in blue (LG-13) or green (DG-14) are the two hypothetical amyloidogenic regions bioinformatically detected within the amyloid core sequence. **B)** Biofilm assays in MSgg medium after 48 h of incubation at 30 °C of the strains expressing the different tasA mutated alleles. The WT and the Δ*tasA* strains were used as controls. **C)** Western blot with anti-TasA antibody corresponding to the cell (top), spent medium (center) or matrix (bottom) fractions respectively of the biofilm formed by the strains bearing the mutated alleles. Immunoblot images have been cropped and spliced for illustrative purposes. All the lines over the immunoblot images delimitate the lanes and the boundaries of the splicing images. **D) Left.** Transmission electron micrographs of negatively stained samples corresponding to the LG-13 peptide after 24 h of incubation at room temperature. Scale bars are 200 nm (left) and 50 nm (right). **Right**. Kinetics of ThT binding of the synthetic peptides corresponding to the amyloidogenic sequences. Blue is LG-13 and green is DG-14. Error bars indicate the SEM.

So far, two alleles showed particular behaviors: i) TasA D64A was mostly secreted out of the cells and was unstable in the matrix, as the majority of the protein was found in the medium and ii) TasA K68A, D69A was produced normally by the cell but somehow processed and secreted differently, as shown by the different pattern observed in the medium fraction compared to the controls, and the unstability in the matrix. These results indicate the inability of these alleles to assemble in the form of amyloid fibers and suggest a relevance of the imperfect repeats, the amyloid core, and these specific amino acids, in the process of filament assembly.

Next, we searched for amyloidogenic stretches within the amyloid core region of TasA. For this purpose, we used several bioinformatic tools (including two meta predictors) that analyze the amyloidogenicity of certain peptides within amino acid sequences[50-54]. The bioinformatic analysis pointed towards two recurrent sequences that were the consensus among all the employed tools: LAIKEVMALNYG, from amino acids 78 to 90 and LSQFEVTLLTV from amino acids 108 to 116 (Fig. 2.7A and Supplementary Fig. S2A). Deletion of each of these sequences through site-directed mutagenesis resulted in non-functional proteins, a fact evidenced by the complete absence of colony architecture or pellicle formation in solid or liquid medium respectively (Supplementary Fig. S2B). However, this loss of function was related to complete loss of protein stability, since no anti-TasA reacting signal was observed in biofilm fractionation followed by immunoblot analysis (Supplementary Fig. S2C). Alternatively, we studied these sequences *in vitro* using synthetic peptides corresponding to those regions. The peptide corresponding to the first region, LAIKEVMALNYG, was designated as LG-13. To improve solubility of the second region, LSQFEVTLLTV, we synthesized the peptide as DFLSQFEVTLLTVG (designated as DG-14). To test the amyloidogenic capacity of these two regions, we first performed a ThT binding analysis by fluorescence spectroscopy. None of the peptides showed ThT binding activity (β-sheet formation) during the first 20 hours of incubation. However, after this time point, the LG-13 peptide exhibited an exponential increase in the fluorescence signal reaching saturation a few hours later (Fig. 2.7D right). To confirm the amyloid nature of the sample, we visualized the LG-13 peptide by TEM after 24 h of incubation (Fig. 2.7D left). TEM analysis revealed abundant fibrillar assemblies consisting of bundles of several protofilaments (~5 nm diameter each) ranging between 6-14 nm diameter, indicative of a molecular organization very similar to that observed for the full length mature TasA assemblies observed *in vitro* (Fig. 2.3A) and verifying the ability of this peptide to adopt a fibrillar conformation.

Altogether, these results demonstrate the importance of the imperfect repeats region and the amyloidogenic sequences, present in the amyloid core of TasA, in the assembly of

the TasA filament and, therefore, in biofilm formation and allow us to define specific regions within the protein sequence that are critical for the structural functions.

The accessory protein TapA self-assemble and adopt the same structural fold as observed for TasA filaments

B. subtilis TapA is an accessory protein present at a molar ratio of ~1/100 (TapA:TasA) in the extracellular matrix and is considered to be a minor biofilm protein. Functional aggregation of TasA in *B. subtilis* and assembly of amyloid filaments requires the *tapA-sipW-tasA* operon[21], and a putative role in cell surface anchoring during TasA aggregation has been proposed for TapA[22,23]. TasA and TapA share 41% of sequence identity (Supplementary Fig. S3), and null TapA mutant induces unstable TasA secretion and polymerization[23], with this effect being localized at the N-terminal half of TapA[55]. The precise role of TapA and its molecular impact on TasA assembly still remains unclear, and several functions of TapA have been proposed[23,56]; namely, a TapA-dependent TasA assembly during biofilm formation and the formation of TapA multimers involved in TasA assembly[23,55]. However, it still remains unclear if TasA and TapA might coassemble in the context of biofilm formation. To gain insights into the molecular structure of TapA, we employed SSNMR and ATR-FTIR to investigate *in vitro* TapA assembly. We observed that recombinant TapA self-assemble at pH 7.4 under the same conditions used for rTasA aggregation. Upon assembly, TapA exhibit a previously unknown ability to form aggregates without the presence of TasA, as demonstrated by the observation of small supramolecular entities using TEM (Fig. 2.8A bottom). The resulting TapA macroscopic entities do not exhibit an unbranched fibrillar shape as observed for rTasA assemblies but rather an amorphous aggregated morphology, with a diameter varying between ~5 and 7 nm, which is comparable to the diameter measured for rTasA filaments. The morphology of TapA assemblies is comparable to small amyloid amorphous aggregates that have been observed for several amyloid proteins depending the experimental conditions during the in vitro aggregation process[57,58]. However, in contrast to the assemblies formed by rTasA, these aggregates are not able to complement the biofilm formation defect observed in a Δ*tasA* strain (Fig. 2.8A top). Nonetheless, these structures exhibit the typical cross-β diffraction pattern, as demonstrated by X-ray diffraction, revealing reflections that are characteristic of cross-β arrangement with strong signals at 4.7 and 10 Å (Fig. 2.8B), implying the amyloid nature of TapA assemblies.

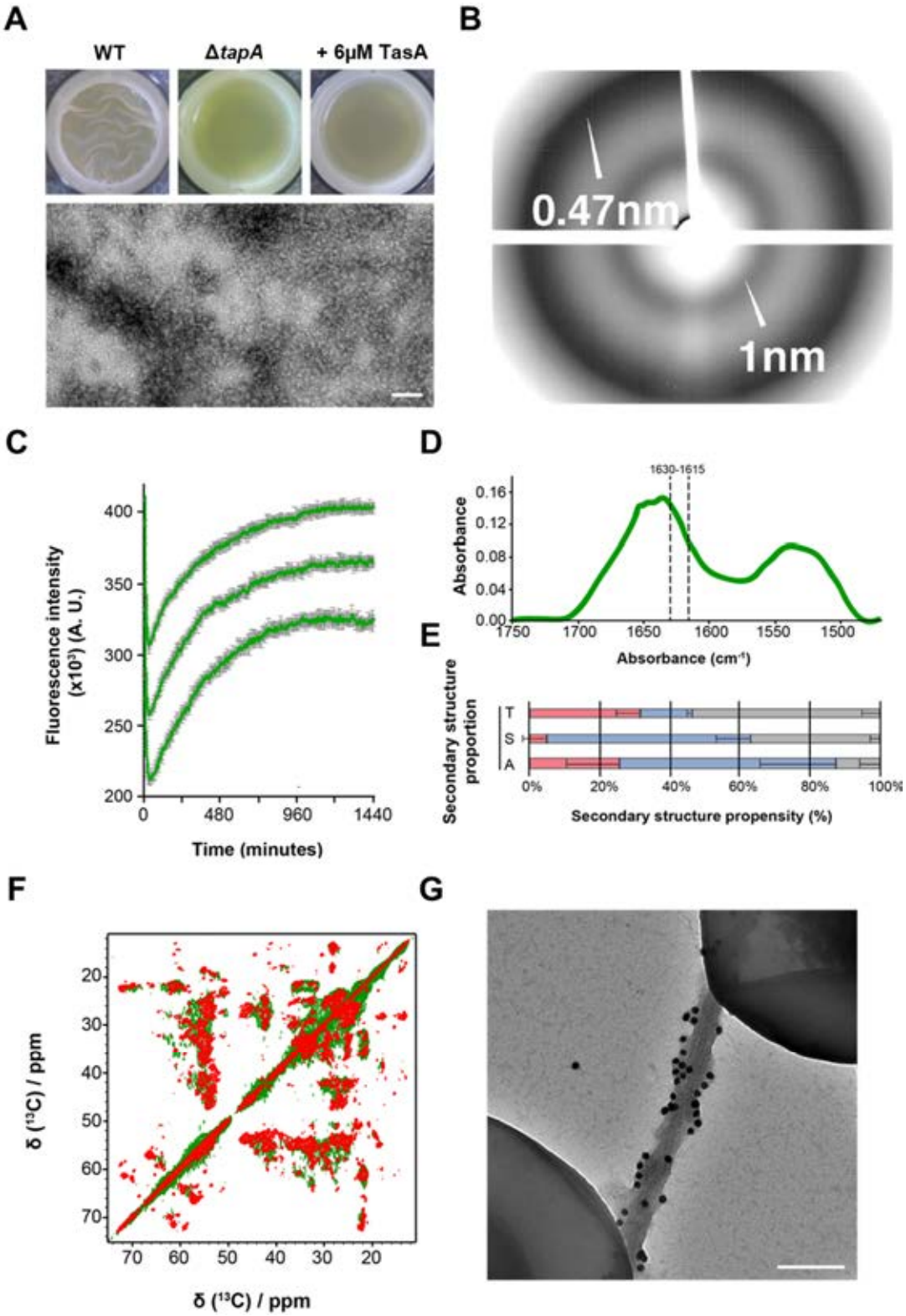

Figure 2.8. TapA self-assemble to form amyloid assemblies. A) Top. Biofilm assays of the WT or Δ*tapA* strains in MOLP medium incubated for 48 h at 30 °C. The Δ*tapA* strain was incubated in the presence or absence of rTasA. Purified rTasA was unable to rescue the WT phenotype in a Δ*tapA* strain. Bottom. Transmission electron micrographs of negatively stained TapA assemblies. Scale bar = 100 nm. **B)** X-ray diffraction pattern of TapA assemblies. **C)** Aggregation kinetics of TapA as followed by ThT binding kinetics assay. **D)** ATR-FTIR spectrum of TapA assemblies; the dashed lines delineate the position of typical β-sheet contribution. **E)** Secondary structure conformational distribution in TapA as analyzed by SSNMR. **F)** Overlay of 2D SSNMR [^{13}C]-[^{13}C] spectra of rTasA (red) and TapA (green) fibrils. **G)** Transmission electron micrograph of Δ*epstasA* double-mutant cells grown under biofilm-inducing conditions and immunolabeled with anti-TapA and 20 nm immunogold-conjugated secondary antibodies.

In order to experimentally validate the amyloid properties of TapA and get an insight into the aggregation process, we studied the ThT binding kinetics of TapA by fluorescence spectroscopy. Interestingly, TapA shows t1/2 values around ~4–5 h (Fig. 2.8C), displaying a clear concentration dependence. We then conducted ATR-FTIR to investigate the secondary structure of mature TapA assemblies. TapA aggregates have an absorption spectrum with a broad amide I band and a maximum at 1630 cm−1, strongly indicating that TapA is, at the molecular level, organized into β-sheet–rich secondary structure elements (Fig. 2.8D). Deconvolution analysis (Table 2.1) suggests that the total amount of β-sheet in TapA is comparable to rTasA (with ~50%), but the proportion of antiparallel β-sheets and parallel β-sheets is different. Interestingly, the content of the α-helical structure is around ~25%, suggesting a similar structural signature between TasA and its accessory protein. Examining by SSNMR the alanine and serine [^{13}C]-[^{13}C] regions encoding for Cβ-Cα correlations, we derived the SSP of TapA assemblies using the same approach as described in a previous section, based on the Cα-Cβ chemical shift patterns for alanine, serine, and threonine. Overall, we observed an SSP for TapA assemblies in line with the obtained in the ATR-FTIR analysis (Fig. 2.8E).

In order to obtain more insights into the structural fingerprint of TapA, we recorded SSNMR [^{13}C]-[^{13}C] spectra and observe a noticeable level of structural polymorphism, reflected in broad lines. When superimposed with the TasA spectrum, the overall 2D [^{13}C]-[^{13}C] patterns observed for TapA and rTasA are comparable, suggesting a common architecture for the accessory protein in the assembled form (Fig. 2.8F). Therefore, we then investigated the putative formation of TapA fibrils *in vivo* in *B. subtilis* biofilms. For this purpose, we used a Δ*tasAeps* strain. This strain shows induction of the extracellular matrix gene expression while lacking both the exopolymeric substances (EPS) and TasA, which are the main components of the extracellular matrix and thus, allowing for a more sensitive and specific detection. We tested the TapA detection in biofilm-inducing conditions in the chemically defined MSgg medium and studied TapA localization in 48 h mature biofilms by TEM and immunogold-conjugated secondary antibodies. We found large concentrations of TapA along the edge of fibrillar assemblies that are not composed of TasA (given the Δ*tasA* background) (Fig. 2.8G), suggesting that, indeed, in agreement to our results obtained *in vitro*, TapA is able to polymerize in fibril-shaped aggregates in the absence of TasA.

These results allow us to conclude that TapA is: i) able to form aggregates with amyloid properties and ii) shows a structural fold very similar to that of rTasA, indicating the integration of TapA within the TasA filament.

In vitro coassembly between TasA and TapA does not perturb the global filament architecture but catalyze its fibrillization

The fact that the SSNMR fingerprints of TasA and TapA proteins in their assembled state show a noticeable level of similarity is an indication that the 3D structure fold of their subunits might have a similar structural arrangement. Therefore, the questions if the accessory protein might influence the kinetics of TasA polymerization and if TasA and its accessory protein could coassemble during biofilm formation arise. The first issue was successfully demonstrated in previous work by the aggregation kinetics of a sample containing TasA from *B. subtilis* and recombinant TapA in different molar ratios. It was then demonstrated that a 3:1 ratio is the most effective to enhance TasA polymerization in *B. subtilis*[55]. Therefore, we questioned the possible perturbation of the TasA fold in the presence of the accessory protein during the assembly process. To address this question, we designed a SSNMR-based coassembly experiment that consists in the coassembly of soluble rTasA and TapA proteins prior to the assembly process (Fig. 2.9).

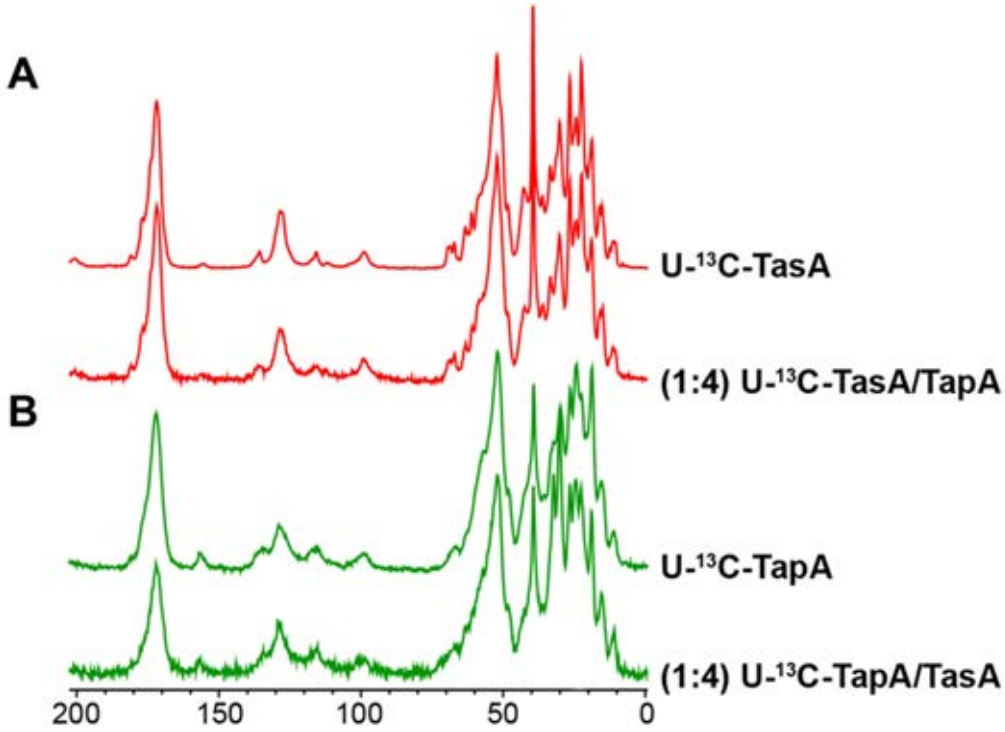

Figure 2.9. In-vitro coassembly of TasA and TapA does not perturb the architecture of the amyloid filament. A) The 1D [^{13}C]-detected experiment of coassembled (1:4) U-[^{13}C] rTasA/TapA. **B)** The 1D [^{13}C]-detected experiment of coassembled (1:4) U-[^{13}C] TapA/rTasA.

Only one of the proteins was chosen to be isotopically labeled with [^{13}C] isotopes, whereas the other protein was at its natural abundance. The coassembled sample was then analyzed by [^{13}C]-detected SSNMR to monitor chemical shift perturbation on the labeled proteins. We prepared 2 samples in total, consisting of [^{13}C]-labeled rTasA or

TapA coassembled with their unlabeled partner (molar ratio of 1:4), ensuring the spectral observation of a single protein and thus spotting some, if any, structural differences using SSNMR (Fig. 2.9A and 2.9B). No drastic changes were observed within the coassembled samples when compared with the assemblies of the single proteins. This hints at the fact that the structural arrangement of mature TasA self-assemblies are not altered by the presence of TapA (Fig. 2.9A and 2.9B) during the polymerization process. A possible explanation could have been that the accessory protein TapA might perfectly accommodate the TasA fold *in vitro* by intercalating between TasA subunits along the amyloid fibril axis, not modifying its structural arrangement. We, however, ruled out this hypothesis based on the observation of similar 1D [^{13}C] signal between U-[^{13}C] TapA and (1:4) (U-[^{13}C] TapA/n.a rTasA) (Fig. 2.9B), indicating that the well-defined (i.e., higher [^{13}C]-spectral resolution) TasA fold could not be propagated to the TapA subunit during its polymerization (i.e., TapA when intercalated with rTasA would display the same [^{13}C]-spectral resolution as rTasA alone).

In conclusion, we have demonstrated that TapA is able to form amyloid assemblies that exhibit a structural signature similar to that of TasA and is able to catalyze the polymerization of TasA *in vitro* without altering the architecture of the filaments. This leads us to propose that a coassembly is conceivable during biofilm formation and would explain why TapA, despite being a minor protein in the extracellular matrix, is essential for biofilm formation.

DISCUSSION

In this work, we describe the structural comparison of TasA functional amyloid fibrils from *B. subtilis* alongside its accessory protein TapA. These results together with previous studies[21-23,28,29,55] allow us to establish a mechanistic picture of TasA assembly.

During the course of this thesis, studies of two independent groups revealed substantial differences regarding the assembly and the structural arrangement of TasA fibrils. Diehl *et al.*[28] reported the high-resolution crystal structure of rTasA in its monomeric form and demonstrated by solution and SSNMR a structural transition between a soluble, globular state to filaments with an unambiguous β-sheet SSNMR signature. Controversially, Erskine *et al*.[29] reported that rTasA may also assemble into a nonamyloid form (as seen by the lack of cross-β reflections in X-ray fiber diffraction experiments) and proposed a supramolecular arrangement made of globular TasA subunits. Our results, although incompatible with Erskine et al., support the observations made by Romero *et al*. and Diehl *et al*.[22,28]. We demonstrate here that rTasA form amyloid filaments upon assembly at pH 7. These fibrils, when analyzed with X-ray diffraction, display typical reflections at 4.7 and 10 Å, which are highly indicative of a canonical cross-β amyloid fold. This suggests that TasA filaments, indeed, adopt a cross-β arrangement within the fibrillar structure, in agreement with previous observations from Diehl *et al.*[28]. Taken together, these data confirm that *B. subtilis* use the greatly stable amyloid arrangement of TasA to ensure its biofilm integrity. Interestingly, as shown by SSNMR, rTasA fibrils exhibit a very high structural order at the molecular level, which indicates a low degree of polymorphism.

Further analysis using SSNMR chemical shift analysis revealed that rTasA in its fibrillar form displays a particular α-helical propensity alongside the expected residues in β-sheet conformation within its rigid core, suggesting the presence of additional structural elements in *B. subtilis* biofilm molecular architectures. The crystal structure[28] uncovered TasA globular monomeric form, which consists of a jelly-roll fold comprising two antiparallel β-sheets surrounded with six short α-helices and several loops. It is tempting to speculate that TasA fibrils might, upon assembly, conserve a part of the TasA globular form while adjusting β-strands in a cross-β stacking manner within its amyloid core. Chemical shift values predicted from the published globular structure have been compared with our experimental results reported here. We superposed predicted peaks over the SSNMR [13C]-[13C] fingerprint spectra of rTasA filaments (Supplementary Fig. S4). This comparison shows a partial overlap, suggesting that a part of the TasA globular

fold may be conserved upon fibril formation, whereas the majority of the secondary structure content would shift to a β-sheet conformation.

Interestingly, the rigid β-sheet enriched amyloid core defined for TasA is one of the most conserved regions in the protein and it contains two imperfect amino acid repeats and two aggregation-prone sequences. Amino acids repeats have many meanings in biological sequences, for instance, the zinc-finger motif involved in interaction with DNA, RNA or proteins[59], or the leucine-rich repeats, typically involved in protein-protein interactions[60]. However, it is surprisingly frequent to find amino acid repeats within the sequences of amyloid proteins, which are, to some extent, involved in the aggregation properties of the sequence[61-63], a feature that is exploited by functional amyloids, specifically in bacteria, for their variety of critical functions[8,26,27]. For this reason, the presence of these imperfect repeats in the core region is in line with what it has been reported for other functional amyloids with similar functions and the in depth study of these regions have allowed us to characterize specific sequences and amino acids that are, most likely, involved in the assembly of the amyloid filaments and the biofilm.

Interestingly, a connection between protein disorder, amino acid repeats and aggregation has been reported in the literature[64,65]. In a previous work, we described the existence of imperfect repeats within the N-terminal sequence of TapA that were essential for the functionality of the protein[55]. In line with what has been mentioned above, the partially disordered conformation for TapA in solution has recently been reported[66]. In this work, we have characterized the accessory protein TapA, associated with TasA filaments in *B. subtilis* biofilms. We have shown the previously unreported ability of TapA to form supramolecular assemblies *in vitro* as observed by TEM analysis. In addition, we have demonstrated that the accessory protein exhibit the typical cross-β X-ray diffraction pattern, which puts into perspective the actual involvement of this auxiliary protein within the biofilm[8,22,23,55]. TapA displays a comparable 2D [13C]-[13C] fingerprint in SSNMR as TasA, and FTIR analysis shows similar behavior with intense signal at 1630 cm^{-1}, as would be expected for β-rich content. Furthermore, both TasA and TapA show comparable SSNMR 2D [13C]-[13C] fingerprints (Fig. 2.8F), thus suggesting a shared structural fold. These results are supported by the notion of the relationship between disorder, repeats and aggregation, which would partly explain the ability of TapA to self-assemble into aggregates with amyloid properties.

Seeding experiments in the mentioned *B. subtilis* proteins indicate that the presence of the accessory protein does not structurally affect TasA fibril formation *in vitro*, at least from a structural point of view. However, kinetics experiments strongly suggest a

catalyzing effect of TapA on TasA fibril formation. Additionally, the observation of *in vivo* TapA filaments in a Δ*tasA* mutant might be indicative of the seeding effect that TapA has over TasA filaments within *B. subtilis* biofilms, in which TapA is, in fact, present within the matrix in a 1:100[23] proportion, inducing the TasA amyloid fold. The observation of heterogeneous aggregates by electron microscopy and the presence of broad SSNMR line widths indicate that TapA lack the ability to self-assemble into homogeneous amyloid fibrils on their own and therefore suggests that the accessory protein is not involved in biofilm integrity but rather assist the TasA protein in the process. Indeed, the biological role of TapA in the *B. subtilis* system might be functionally comparable to the CsgB protein during curli amyloid fiber biogenesis in *E. coli*. In this system, polymerization of the main protein component of the fiber, CsgA, is aided by a minor curli subunit protein CsgB by acting as a nucleator that, additionally, is able to polymerize by itself exhibiting amyloid properties[67]. However, contrary to what occurs for TapA and TasA, CsgB and CsgA do not need to be synthesized in the same cell to assemble a curli fiber and a functioning biofilm[67]. Interestingly, a role in virulence and adhesion of bacterial cells to the host has been reported for CalY, the accessory protein of TasA in *B. cereus*, which is analogous in function to TapA. This amyloid protein is rendered monomeric in early stationary phase and located at the bacterial surface, mediating the initial contact with the host cells. During biofilm formation, however, CalY is secreted and integrated in the matrix amyloid fibers, presumably, favoring TasA polymerization and conferring *B. cereus* biofilms with the versatility needed to colonize the host or interact with abiotic surfaces and maintaining the structural stability of the entire bacterial population[56,68].

Our results contribute to the ongoing investigations of *B. subtilis* biofilm properties and offer a unique view of *B. subtilis* TasA in its fibrillar amyloid form as well as new insights regarding the potential involvement of the accessory protein TapA in biofilm design. More studies of this and other functionally similar systems will tell us how the local differences between the amyloid proteins have been shaped by the evolution to permit efficient interactions with complementary species-specific extracellular matrix components and thus, define the overall chemical features of the biofilm and the effective response to the variety of niches that the bacterial species encounter during their life cycle.

MATERIALS AND METHODS

Bacterial strains and culture conditions

The bacterial strains used in this study are listed in supplementary table 2.2. *Bacillus subtilis* NCIB3610, an undomesticated prototrophic strain from our laboratory collection, and derivative mutant strains were used throughout this study. *Bacillus subtilis* 168, a domesticated laboratory strain, was used for the generation of the mutant strains in *B. subtilis* NCIB3610. For cloning and plasmid replication, *Escherichia coli* DH5α was used. *E. coli* BL21(DE3) pLysS (Merck, Kenilworth, NJ, USA) was used for protein expression and purification. All strains were grown in Luria-Bertani medium: 1% tryptone (Oxoid; Thermo Fisher Scientific, Waltham, MA, USA), 0.5% yeast extract (Oxoid), and 0.5% NaCl. Biofilm assays were performed on MSgg medium: 100 mM morpholinepropane sulphonic acid (MOPS) (pH 7), 0.5% glycerol, 0.5% glutamate, 5 mM potassium phosphate (pH 7), 50 µg/ml tryptophan, 50 µg/ml phenylalanine, 50 µg/ml threonine, 2 mM $MgCl_2$, 700 µM $CaCl_2$, 50 µM $FeCl_3$, 50 µM $MnCl_2$, 2 µM thiamine, 1 µM $ZnCl_2$. Medium optimized for lipopeptide production was used for extracellular complementation assays in experiments performed with the *B. subtilis tasA* or *tapA* mutant strains and was prepared as described[69]. M9 minimal medium [composition for 1 L was 48 mM Na_2HPO_4, 22 mM KH_2PO_4, 8.6 mM NaCl, 1 mM $MgSO_4$, 0.01 mM $ZnCl_2$, 0.001 mM $FeCl_3$, 0.1 mM $CaCl_2$, 18.7 mM NH_4Cl, 0.20% glucose and 10 ml 100× minimum essential medium vitamin solution (sigma)] was used for protein expression for NMR studies. M9 was enriched in$^{15}NH_4Cl$ and [^{13}C] labeled carbon sources [(U-[^{13}C]) d-glucose] in order to produce labeled recombinant proteins. Media were solidified by addition of bacteriological agar (Oxoid) to a final concentration of 1.5%.

The antibiotics used and their final concentrations were 100 µg/ml ampicillin, 10 µg/ml kanamycin, 10 µg/ml tetracycline and 12.5 µg/ml gentamicin. For MLS resistance, 1 µg/ml erythromycin and 25 µg/ml lincomycin were used.

Plasmid and strains construction

All the primers used for this study are listed and described in supplementary table 2.3. Plasmid pDFR6 (pET22b-*tasA*), containing the open reading frame of the *tasA* gene from *B. subtilis* NCIB3610 without the signal peptide or the stop codon, was constructed as previously described by Romero *et al.*[23] and used for TasA expression and purification. Plasmid pJC1 (pDEST17-*tapA*) was constructed using the Gateway Cloning System (Thermo Fisher Scientific). The primers TapA–attb1–forward TapA–attb2–

reverse contain the recognition sites for the BP clonase enzyme and were used to amplify the open reading frame of the *tapA* gene excluding the signal peptide. The insert was then cloned into pDONR207 by a BP recombination reaction (Gateway, Thermo Fisher Scientific). The plasmid pDONR207-*tapA* was purified from the entry clone, and then the insert was cloned into the pDEST17 vector by an LR recombination reaction (Gateway, Thermo Fisher Scientific), creating the final expression vector. The 6his-tag is located at the N-terminal region of the *tapA* sequence.

Strains JC70, JC72, JC75, JC76, JC77, JC78, JC80, JC81 and JC82 were constructed via site-directed mutagenesis (QuickChange Lightning Site Directed Mutagenesis Kit – Agilent Technologies). Briefly, the *tapA* operon (*tapA-sipW-tasA*), including its promoter, was amplified using the primers TasA_1_mutb and YSRI_2, and the resulting product was digested with BamHI and SalI and cloned into the pDR183 vector[70]. Next, the corresponding primers (see supplementary table 2) were used to introduce the alanine substitution mutations into the desired positions of the TasA amino acid sequence. The entire plasmid was amplified from the position of the primers using Pfu DNA polymerase. The native plasmid, which was methylated and lacked the mutations, was digested with DpnI enzyme. The plasmids containing the native version of TasA (JC70) or the mutated versions were transformed into the *B. subtilis* 168 Δ*(tapA-sipW-tasA)* strain replacing the *lacA* neutral locus. Genetic complementation was observed in strain JC70 as a control. Transformants were selected via MLS resistance.

All of the *B. subtilis* strains generated were constructed by transforming *B. subtilis* 168 via its natural competence and then using the positive clones as donors for transferring the constructs into *Bacillus subtilis* NCIB3610 via generalized SPP1 phage transduction[71].

Cell growth and protein expression

A single freshly transformed BL21(DE3) pLysS *E. coli* was picked and cultured in 10 ml of Luria-Bertani medium with 100 µg/ml ampicillin under shaking conditions for 5 h to reach the exponential growth phase. Cells were harvested (1000 G, 10 min) and resuspended in 100 ml of labeled minimal medium [1 g/L $^{15}NH_4Cl$, 2 g/L (U-[^{13}C]) d-glucose] or LB supplemented with antibiotics and grown overnight at 30°C and 200 rpm until the stationary growth phase. A total of 10% (v/v) of the culture was used to inoculate 1 L of LB or labeled minimal medium, supplemented with antibiotics cultured at 37°C and 220 rpm until optical density at 600 nm reached 0.8, and induced with 0.75 mM isopropyl β-D-1-thiogalactopyranoside. TapA was expressed at 18°C for 20 h, and TasA was

expressed at 30°C for 20 h. Cells were harvested (6000 g, 30 min, 4°C, JLA 8.1 rotor; Beckman Coulter, Brea, CA, USA) and frozen at −80°C until purification.

Protein purification

Cells were resuspended in buffer A (50 mM Tris, 150 mM NaCl, pH 8) and sonicated on ice (3 × 45 s, 40%, Bandelin sonopuls VS 70T probe; Bandelin, Germany) and centrifuged (15,000 *g*, 60 min, 4°C, F34-6-38 rotor; Eppendorf, Hamburg, Germany). The supernatant was discarded because proteins were mainly expressed in inclusion bodies (IBs). The pellet was resuspended in buffer A supplemented with 2% Triton X-100, incubated at 37°C under shaking conditions for 20 min, and centrifuged (50,000 *g*, 10 min, 4°C, JA 25.50 rotor; Beckman Coulter). The pellet was extensively washed with buffer A, centrifuged (50,000 *g*, 10 min, 4°C), resuspended in denaturing condition (Tris 50 mM, NaCl 500 mM, guanidine hydrochloride 6 M), and incubated at 60°C overnight until complete solubilization. Lysate was clarified by centrifugation (200,000 *g*, 1 h, 16°C, 50.2 Ti rotor; Beckman Coulter). Solubilized IBs were loaded on a HisTrap HP 5-ml column (GE Healthcare, Waukesha, WI, USA) previously equilibrated in the binding buffer (50 mM Tris, 0.5 M NaCl, 20 mM imidazole, 8 M urea, pH 8). Proteins were eluted from the column with a linear gradient of elution buffer (50 mM Tris, 0.5 M NaCl, 500 mM imidazole, 8 M urea, pH 8). After the affinity chromatography step, proteins were loaded on a HiPrep 26/10 desalting column (GE Healthcare) to exchange buffer for 1% acetic acid at pH 3. Purification fractions were loaded on a 13% Tris-Tricine SDS-PAGE to check purity.

Biofilm formation and extracellular complementation assays

Biofilm experiments of *B. subtilis* NCIB3610 were done by adding 10 µl of a starting culture to 1 ml of MOLP or MSgg medium in 24-well plates[22]. The plates were incubated at 28°C without agitation, and the formation of wrinkly pellicles at the air-liquid interphase was recorded after 48 h of incubation. For biofilm experiments in MSgg plates, 2 µl of starting culture were spotted over the plate and let to dry. Plates were incubated at 28°C for 72 h. A characteristic wrinkly colony morphology is observed in the WT strain at this time-point.

Extracellular complementation experiments were performed by inoculating the *tasA* or *tapA* single mutants of *B. subtilis* in 1 ml of MOLP as described above. A total amount of 80 (3 µM) or 160 µg (6 µM) freshly purified TasA was added to the corresponding culture. Photographs were taken at different time points over the course of 72 h. The same volume of protein buffer (10 mM Tris, 100 mM NaCl) or IBs were additionally included as controls.

Biofilm fractionation

To analyze the presence of TasA in the different strains, biofilms were fractionated into cells and ECM as described elsewhere[21], and both fractions were analyzed separately. Briefly, 48-hour-old pellicles grown under on MSgg were carefully lifted from the wells and resuspended in 10 ml of MS medium (MSgg broth without glycerol and glutamate, which were replaced by water) with a 25 $^{5/8}$ G needle. The spent medium was filtered through a 0.22 µm filter and stored at 4 °C (medium fraction). Next, the samples were subjected to mild sonication in a Branson 450 digital sonifier (4-5 5 seconds pulses at 20% amplitude) to ensure bacterial resuspension. The bacterial suspensions were centrifuged at 9000 g for 20 minutes to separate the cells from the extracellular matrix. The cell fraction was resuspended in 10 ml of MS medium and stored at 4 °C until further processing. The ECM fraction was filtered through a 0.22 µm filter and stored at 4 °C.

For protein precipitation, 2 ml of the cell or ECM fractions were used. The cell fraction was treated with 0.1 mg/ml lysozyme for 30 minutes at 37 °C. Next, both fractions were treated with a 10% final concentration of trichloroacetic acid and incubated in ice for 1 h. Proteins were collected by centrifugation at 13,000 g for 20 minutes, washed twice with ice-cold acetone, and dried in an Eppendorf Concentrator Plus 5305 (Eppendorf).

SDS-PAGE and immunodetection

Precipitated proteins were resuspended in 1x Laemmli sample buffer (BioRad) and heated at 100 °C for 5 minutes. Proteins were separated via SDS-PAGE in 12% acrylamide gels and then transferred onto PVDF membranes using the Trans-Blot Turbo Transfer System (BioRad) and PVDF transfer packs (BioRad). For immunodetection of TasA, the membranes were probed with anti-TasA antibody (rabbit) used at a 1:20,000 dilution in Pierce Protein-Free (TBS) blocking buffer (ThermoFisher). A secondary anti-rabbit IgG antibody conjugated to horseradish peroxidase (BioRad) was used at a 1:3,000 dilution in the same buffer. The membranes were developed using the Pierce ECL Western Blotting Substrate (ThermoFisher).

Assembly of filaments

The concentration of the protein recovered after FPLC purification was measured using the absorbance of aromatic amino acids at 280 nm. The sample was then concentrated in Amicon Ultra-15 (cutoff 3 kDa) centrifugal filter units (MilliporeSigma, Burlington, MA, USA) to 0.25 mM and dialyzed against a 300 mM Tris, 1% acetic acid, 0.02% azide, pH 7.4 solution. Self-assembly was then promoted under agitation for 1 wk. Fibrils were then

extensively washed in water, ultracentrifuged (300,000 *g*, 1 h, 4°C, TLA 120.1 rotor; Beckman Coulter), and transferred to the SSNMR rotor.

ThT measurements

The experiment was initiated by placing the 96-well plate at 37°C and shaking at 100 rpm in a plate reader (Tecan Infinite M1000 Pro; Tecan, Männedorf, Switzerland). The ThT fluorescence was measured through the top of the plate every 1 min (with excitation filter 440 nm and emission filter 480 nm) with continuous shaking at 100 rpm between reads. Every measurement was recorded in triplicate (15 μM ThT and 10, 20, 25, 40, or 50 μM protein homogenate). For coassembly experiments, a protein concentration of 50 μM was used.

Circular dichroism

CD spectra were recorded in a Jasco J-715 spectropolarimeter (Jasco) equipped with Peltier-thermostatic cell holder. Measurements of the far-UV CD spectra (260–200 nm) were made with a 1-mm path length quartz cuvette at a protein concentration of 30 μm in 10mM Tris and 100mM NaCl. Spectra were recorded at a scan rate of 100 nm/min, 1-nm step resolution, 1-s response, and 1-nm bandwidth. The resulting spectra were the result of five accumulations. Each spectrum was corrected by baseline subtraction using the blank spectrum obtained with the buffer. CD signal was normalized as ellipticity units per mole of protein ([θ], in deg. $dmol^{-1}$ cm^2).

Dynamic light scattering experiments

A 50-μM solution of TasA in 1% acetic acid was treated with NaOH 10% to adjust the pH to 7.0 and filtered through a 0.46-μm syringe filter. The size measurements were carried out in a Malvern Zetasizer Nano ZS (Malvern Panalytical, Malvern, United Kingdom) with a 632.8-nm laser wavelength as the excitation source and using a 1-cm pathway polystyrene cuvette as the sample holder. A total of 1 ml of the protein solution was transferred to the cuvette and kept in the system for the whole experiment without stirring. The dynamic light scattering (DLS) signal was monitored at 25°C for each protein at 60-min intervals and a count rate of (2–4) × 103 counts/s for TasA-bs and 30-min intervals and (1–17) × 103 counts/s for TasA-bc. Zetasizer software v.6.34 (Malvern Panalytical) was used in data collection and processing.

Coassembly SSNMR experiments

Soluble [^{13}C]/^{15}N-labeled proteins were mixed with natural abundance (n.a.) proteins in a 4:1 ratio ([^{13}C]-^{15}N TasA:TapA/[^{13}C]-^{15}N TapA:TasA/[^{13}C]-^{15}N) and then concentrated, dialyzed, and assembled as described above.

Proteinase K digestion assay

A 50-µg solution of aggregated TasA protein was treated for 1 h at 37°C with 0.02 mg/ml of proteinase K in 50 mM Tris pH 8 and 150 mM NaCl for various times (1, 5, 15, 20, 30, or 45 min or 1 h). Reactions were stopped by addition of 1 vol. Laemmli buffer and heated at 100°C for 5 min. The resulting samples were separated by SDS-PAGE in 12% acrylamide gels and subsequently stained with Coomassie brilliant blue.

The sequence corresponding to the amyloid core of TasA-bs was identified by tandem mass spectrometry using a nano ion trap system [HPLC–electrospray ionization–tandem mass spectrometry (MS)]. Briefly, the bands obtained after electrophoresis were cut, washed, and destained. Subsequently, disulfide bridges were reduced with DTT, cysteines were alkylated by the use of yodoacetamide, and trypsine digestion was performed in gel to extract the peptides corresponding to the protein samples. This process was carried out automatically using an automatic digester (DigestPro; HB Technologies, Tübingen, Germany). The peptides were then concentrated and desalted using a capture column C18 Zorbax 300SB-C18 (5 × 0.3 mm; Agilent Technologies, Santa Clara, CA, USA) with a 5-µm particle diameter and 300-Å pore size using a gradient of 98% H_2O:2% acetonitrile and 0.1% formic acid (FA) at a flow rate of 20 µl/min for 6 min. The capture column was connected in line with a Zorbax 300SB-C18 analytical column (150 × 0.075 mm; Agilent Technologies), with a 3.5-µm particle diameter and 300-Å pore size through a 6-port valve. Elution of the samples from the capture column was performed in gradient using FA 0.1% in water as mobile phase A and FA 0.1% in acetonitrile 80%/water 20% as mobile phase B. The liquid chromatography system was coupled through a nanospray source (CaptiveSpray; Bruker, Billerica, MA, USA) to a 3D ion trap mass spectrometer (amaZon speed ETD; Bruker) operating in positive mode with a capillary voltage set to 1500 V and a sweep range of *m/z* 300–1500. A data-dependent acquisition was carried out in automatic mode that allowed obtaining sequentially an MS spectrum in full scan (*m/z* 300–1400) followed by an MS spectrum in tandem by collision-induced dissociation of the 8 most abundant ions. For identification, the software ProteinScape 3 (Bruker) coupled to the search engine Mascot 3.1 (Matrix Science, Boston, MA, USA) was used, matching tandem MS data against the databases

Swiss-Prot (https://www.uniprot.org/) and NCBInr (https://www.ncbi.nlm.nih.gov/protein).

X-ray diffraction

Fiber diffraction patterns were measured at 4°C on a Rigaku FR-X rotating anode X-ray generator (Rigaku, Tokyo, Japan) equipped with a Pilatus 200 K hybrid pixel (Dectris, Baden, Switzerland) at the copper wavelength. The concentrated hydrated samples were mounted in a MicroLoops from Mitegen (Ithaca, NY, USA) on a goniometer head under cold nitrogen flow. Each diffraction pattern corresponds to a 360° rotation along the φ axis with an exposure time of 720 s after subtraction of a blank image of the same exposure time with only the loop on the goniometer head.

Solution NMR

Samples were concentrated to ~1 mM and supplemented with 10% D_2O and ~50 μM 4,4-dimethyl-4-silapentane-1-sulfonic acid (DSS) as an internal ^{1}H chemical shift standard. Indirect dimensions were referenced to DSS according to their gyromagnetic ratios and specific nuclear observation frequencies. ^{1}H-^{15}N SOFAST-HMQC spectra were acquired at 700- and 800-MHz ^{1}H Larmor frequency spectrometers (Bruker) at 310 K using a triple-resonance room-temperature probe and a triple-resonance cryoprobe. Backbone assignment was performed using HNCACB, HNCO, HNCA, HNcaCO, HNcoCA, and CBCAcoNH experiments with 20 or 25% nonuniform sampling[72] at 700 MHz at a temperature of 310 K.

SSNMR

Experiments were performed at a magic angle spinning frequency of 11 kHz on triple-resonance 4 and 3.2-mm magic angle spinning probes using 600 and 800 MHz ^{1}H Larmor frequency spectrometers (Bruker). The sample temperature was set to ~278 K, and chemical shifts were calibrated using DSS as an internal reference. A crosspolarization contact time of 1 ms was used for a decoupling strength of 90 kHz using small phase incremental alternation with 64 steps (SPINAL-64). The rigid part of the fibrils was probed using 2-dimensional (2D) [^{13}C]-[^{13}C] correlation spectra using a proton-driven spin-diffusion (PDSD) mixing scheme. Intraresidue correlations were probed using a PDSD mixing time of 50 ms for a total experimental time of ~3 d per sample. The 2D ^{1}H-[^{13}C] insensitive nuclei enhanced polarization transfers (INEPTs) were recorded for a total experimental time of ~18 h per sample.

Secondary structure analysis of fibrils by SSNMR

Conformation propensity assessment was determined using secondary structure assignment calculations *i.e.*, differences of secondary chemical shifts $\Delta\Delta C_{sec} = \Delta C\alpha - \Delta C\beta$, with $\Delta C_x = C_x$(experimental) − C_x[random coil − Biological Magnetic Resonance Bank (BMRB)]. Negative values therefore are considered to be highly indicative of a β-strand–like conformation. For each residue type (*i.e.*, alanines, serines, and threonines), the total peak volume was calculated on Sparky (University of California–San Francisco, San Francisco, CA, USA) using integration tools and used for percentage assessment of α and β conformation for each residue type. Error bars were determined using measurements on both sides of the 2D [^{13}C]-[^{13}C] PDSD diagonal. The theoretical α-β peak distribution on the spectrum is based on crosscalculations between reported secondary structure–based chemical shifts[73] and secondary structure assignment.

Attenuated total reflection FTIR spectroscopy

Attenuated total reflection (ATR)–FTIR spectra were recorded on a Nicolet 6700 FT-IR spectrometer (Thermo Fisher Scientific) equipped with a liquid nitrogen–cooled mercury-cadmium-telluride detector (Thermo Fisher Scientific) with a spectral resolution of 4 cm^{-1} and a 1-level 0 filling. Concentrated and hydrated samples were deposited on a germanium ATR crystal in a 10-µl droplet. The droplet was dried, and the spectrum (200 scans) of the proteins was recorded. To determine the secondary structure element of each protein, spectra were analyzed with an algorithm based on a second-derivative function and a self-deconvolution procedure (GRAMS and OMNIC software; Thermo Fisher Scientific) to determine the number and wavenumber of individual bands within the spectral range of the amide I band (1700–1600 cm^{-1}).

Electron microscopy and immunoelectron microscopy

Negative-staining micrographs were recorded using 1 droplet of 2-fold serial dilutions of TasA and TapA assemblies stained with a 2% uranyl acetate (w/v) solution for 1 min and dried under dark conditions. Samples were observed using a FEI CM120 transmission electron microscope (Field Electron and Ion Co., Hillsboro, OR, USA) at an accelerating voltage of 120 kV under transmission electron microscopy (TEM) low-dose mode at a magnification of ×40,000 for TasA-bs/TasA-bc and 25,000× for TapA/CalY. TEM images were recorded using a Gatan UltraScan1000 2k × 2k camera (Gatan, Pleasanton, CA, USA).

For immunolabeling assays, samples from cells growing under biofilm-inducing conditions for each strain were taken and incubated over copper grids for 2 h. Grids were

washed two times for 30 seconds with ultrapure water and then floated on blocking buffer [1% nonfat dry milk in PBS with 0.1% Tween20 (PBST)] for 30 min. After blocking, the grids were floated on anti-TapA drops at a 1:150 dilution in blocking buffer for 2 h and then washed in PBST. Then, the grids were floated in goat-antirabbit 20-nm immunogold-conjugated secondary antibody (Ted Pella, Redding, CA, USA) at a 1:50 dilution for 1 h, rinsed in PBST and then in ultrapure water four times for 5 min. each. Samples were dried at room temperature and negatively stained with 1% uranyl acetate for 30 s followed by 2 washes in ultrapure water. 20-nm diameter immunogold-conjugated secondary antibodies were used to visualize the signal associated to TapA. Samples were visualized under a FEI Tecnai G2 20 Twin Transmission Electron Microscope at an accelerating voltage of 80 kV. The images were taken using a side-mounted charge-coupled device Olympus Veleta with 2k × 2k Mp (Olympus, Tokyo, Japan).

Bioinformatic analysis of amino acid repeats and amyloidogenic regions

For the detection of amino acid repeats, we used the complete mature sequence of TasA without the signal peptide. We used the tool RADAR[49] for the detection of the repeats.

For the detection of amyloidogenic sequences, we used the sequence corresponding to the amyloid core region from K35 to K110. Then, we used the tools AmylPred 2[50], FoldAmyloid[51], MetAmyl[54], PASTA 2.0[52] and TANGO[53]. The selected amyloidogenic regions were the consensus among all the employed tools.

REFERENCES

1 Loquet, A., Saupe, S. J. & Romero, D. Functional Amyloids in Health and Disease. *J. Mol. Biol.* **430**, 3629-3630, (2018).

2 Van Gerven, N., Van der Verren, S. E., Reiter, D. M. & Remaut, H. The Role of Functional Amyloids in Bacterial Virulence. *J. Mol. Biol.* **430**, 3657-3684, (2018).

3 Deshmukh, M., Evans, M. L. & Chapman, M. R. Amyloid by Design: Intrinsic Regulation of Microbial Amyloid Assembly. *J. Mol. Biol.* **430**, 3631-3641, (2018).

4 Rouse, S. L., Matthews, S. J. & Dueholm, M. S. Ecology and Biogenesis of Functional Amyloids in *Pseudomonas*. *J. Mol. Biol.* **430**, 3685-3695, (2018).

5 Pham, C. L., Kwan, A. H. & Sunde, M. Functional amyloid: widespread in Nature, diverse in purpose. *Essays Biochem.* **56**, 207-219, (2014).

6 Riek, R. & Eisenberg, D. S. The activities of amyloids from a structural perspective. *Nature* **539**, 227-235, (2016).

7 Dragos, A., Kovacs, A. T. & Claessen, D. The Role of Functional Amyloids in Multicellular Growth and Development of Gram-Positive Bacteria. *Biomolecules* **7**, (2017).

8 Camara-Almiron, J., Caro-Astorga, J., de Vicente, A. & Romero, D. Beyond the expected: the structural and functional diversity of bacterial amyloids. *Crit. Rev. Microbiol.* **44**, 653-666, (2018).

9 Zhou, Y., Blanco, L. P., Smith, D. R. & Chapman, M. R. Bacterial amyloids. *Methods Mol. Biol.* **849**, 303-320, (2012).

10 Romero, D. & Kolter, R. Functional amyloids in bacteria. *Int. Microbiol.* **17**, 65-73, (2014).

11 Otzen, D. Functional amyloid: turning swords into plowshares. *Prion* **4**, 256-264, (2010).

12 Friedland, R. P. & Chapman, M. R. The role of microbial amyloid in neurodegeneration. *PLoS Pathog.* **13**, e1006654, (2017).

13 Guijarro, J. I., Sunde, M., Jones, J. A., Campbell, I. D. & Dobson, C. M. Amyloid fibril formation by an SH3 domain. *Proc. Natl. Acad. Sci. USA* **95**, 4224-4228, (1998).

14 Chiti, F. *et al.* Designing conditions for in vitro formation of amyloid protofilaments and fibrils. *Proc. Natl. Acad. Sci. USA* **96**, 3590-3594, (1999).

15 Ramirez-Alvarado, M., Merkel, J. S. & Regan, L. A systematic exploration of the influence of the protein stability on amyloid fibril formation in vitro. *Proc. Natl. Acad. Sci. USA* **97**, 8979-8984, (2000).

16 Dragos, A. & Kovacs, A. T. The Peculiar Functions of the Bacterial Extracellular Matrix. *Trends Microbiol* **25**, 257-266, (2017).

17 Blanco, L. P., Evans, M. L., Smith, D. R., Badtke, M. P. & Chapman, M. R. Diversity, biogenesis and function of microbial amyloids. *Trends Microbiol.* **20**, 66-73, (2012).

18 Taylor, J. D. & Matthews, S. J. New insight into the molecular control of bacterial functional amyloids. *Front. Cell Infect. Microbiol.* **5**, 33, (2015).

19 Van Gerven, N., Klein, R. D., Hultgren, S. J. & Remaut, H. Bacterial amyloid formation: structural insights into curli biogensis. *Trends Microbiol.* **23**, 693-706, (2015).

20 Branda, S. S., Gonzalez-Pastor, J. E., Ben-Yehuda, S., Losick, R. & Kolter, R. Fruiting body formation by *Bacillus subtilis*. *Proc. Natl. Acad. Sci. USA* **98**, 11621-11626, (2001).

21 Branda, S. S., Chu, F., Kearns, D. B., Losick, R. & Kolter, R. A major protein component of the *Bacillus subtilis* biofilm matrix. *Mol. Microbiol.* **59**, 1229-1238, (2006).

22 Romero, D., Aguilar, C., Losick, R. & Kolter, R. Amyloid fibers provide structural integrity to *Bacillus subtilis* biofilms. *Proc. Natl. Acad. Sci. USA* **107**, 2230-2234, (2010).

23 Romero, D., Vlamakis, H., Losick, R. & Kolter, R. An accessory protein required for anchoring and assembly of amyloid fibres in *B. subtilis* biofilms. *Mol. Microbiol.* **80**, 1155-1168, (2011).

24 Sabate, R. *et al.* The role of protein sequence and amino acid composition in amyloid formation: scrambling and backward reading of IAPP amyloid fibrils. *J. Mol. Biol.* **404**, 337-352, (2010).

25 Lopez de la Paz, M. & Serrano, L. Sequence determinants of amyloid fibril formation. *Proc. Natl. Acad. Sci. USA* **101**, 87-92, (2004).

26 Wang, X. & Chapman, M. R. Sequence determinants of bacterial amyloid formation. *J. Mol. Biol.* **380**, 570-580, (2008).

27 Bleem, A. *et al.* Protein Engineering Reveals Mechanisms of Functional Amyloid Formation in Pseudomonas aeruginosa Biofilms. *J. Mol. Biol.* **430**, 3751-3763, (2018).

28 Diehl, A. *et al.* Structural changes of TasA in biofilm formation of *Bacillus subtilis*. *Proc. Natl. Acad. Sci. USA* **115**, 3237-3242, (2018).

29 Erskine, E. *et al.* Formation of functional, non-amyloidogenic fibres by recombinant *Bacillus subtilis* TasA. *Mol. Microbiol.* **110**, 897-913, (2018).

30 Klunk, W. E., Jacob, R. F. & Mason, R. P. Quantifying amyloid beta-peptide (Abeta) aggregation using the Congo red-Abeta (CR-abeta) spectrophotometric assay. *Anal Biochem.* **266**, 66-76, (1999).

31 LeVine, H., 3rd. Quantification of beta-sheet amyloid fibril structures with thioflavin T. *Methods Enzymol.* **309**, 274-284, (1999).

32 Sunde, M. *et al.* Common core structure of amyloid fibrils by synchrotron X-ray diffraction. *J. Mol. Biol.* **273**, 729-739, (1997).

33 Surmacz-Chwedoruk, W., Malka, I., Bozycki, L., Nieznanska, H. & Dzwolak, W. On the heat stability of amyloid-based biological activity: insights from thermal degradation of insulin fibrils. *PLoS One* **9**, e86320, (2014).

34 Fontana, N. A., Fonseca-Maldonado, R., Mendes, L. F. S., Meleiro, L. P. & Costa-Filho, A. J. The yeast GRASP Grh1 displays a high polypeptide backbone mobility along with an amyloidogenic behavior. *Sci. Rep.* **8**, 15690, (2018).

35 Tycko, R. & Wickner, R. B. Molecular structures of amyloid and prion fibrils: consensus versus controversy. *Acc. Chem. Res.* **46**, 1487-1496, (2013).

36 Meier, B. H., Riek, R. & Bockmann, A. Emerging Structural Understanding of Amyloid Fibrils by Solid-State NMR. *Trends. Biochem. Sci.* **42**, 777-787, (2017).

37 van der Wel, P. C. A. Insights into protein misfolding and aggregation enabled by solid-state NMR spectroscopy. *Solid State Nucl. Magn. Reson.* **88**, 1-14, (2017).

38 Linser, R. Solid-state NMR spectroscopic trends for supramolecular assemblies and protein aggregates. *Solid State Nucl. Magn. Reson.* **87**, 45-53, (2017).

39 Loquet, A. *et al.* 3D structure determination of amyloid fibrils using solid-state NMR spectroscopy. *Methods* **138-139**, 26-38, (2018).

40 Linden, A. H. *et al.* Cryogenic temperature effects and resolution upon slow cooling of protein preparations in solid state NMR. *J Biomol. NMR* **51**, 283-292, (2011).

41 Daebel, V. *et al.* beta-Sheet core of tau paired helical filaments revealed by solid-state NMR. *J. Am. Chem. Soc.* **134**, 13982-13989, (2012).

42 Heise, H. *et al.* Molecular-level secondary structure, polymorphism, and dynamics of full-length alpha-synuclein fibrils studied by solid-state NMR. *Proc. Natl. Acad. Sci. USA* **102**, 15871-15876, (2005).

43 Luca, S. *et al.* Secondary chemical shifts in immobilized peptides and proteins: a qualitative basis for structure refinement under magic angle spinning. *J. Biomol. NMR* **20**, 325-331, (2001).

44 Eisenberg, D. S. & Sawaya, M. R. Structural Studies of Amyloid Proteins at the Molecular Level. *Annu. Rev. Biochem.* **86**, 69-95, (2017).

45 Wasmer, C. *et al.* Amyloid fibrils of the HET-s(218-289) prion form a beta solenoid with a triangular hydrophobic core. *Science* **319**, 1523-1526, (2008).

46 Loquet, A. *et al.* Prion fibrils of Ure2p assembled under physiological conditions contain highly ordered, natively folded modules. *J. Mol. Biol.* **394**, 108-118, (2009).

47 Zandomeneghi, G., Krebs, M. R., McCammon, M. G. & Fandrich, M. FTIR reveals structural differences between native beta-sheet proteins and amyloid fibrils. *Protein Sci.* **13**, 3314-3321, (2004).

48 Goormaghtigh, E., Cabiaux, V. & Ruysschaert, J. M. Determination of soluble and membrane protein structure by Fourier transform infrared spectroscopy. III. Secondary structures. *Subcell Biochem.* **23**, 405-450, (1994).

49 Madeira, F. *et al.* The EMBL-EBI search and sequence analysis tools APIs in 2019. *Nucleic Acids Res.* **47**, W636-W641, (2019).

50 Tsolis, A. C., Papandreou, N. C., Iconomidou, V. A. & Hamodrakas, S. J. A consensus method for the prediction of 'aggregation-prone' peptides in globular proteins. *PLoS One* **8**, e54175, (2013).

51 Garbuzynskiy, S. O., Lobanov, M. Y. & Galzitskaya, O. V. FoldAmyloid: a method of prediction of amyloidogenic regions from protein sequence. *Bioinformatics* **26**, 326-332, (2010).

52 Walsh, I., Seno, F., Tosatto, S. C. & Trovato, A. PASTA 2.0: an improved server for protein aggregation prediction. *Nucleic Acids Res.* **42**, W301-307, (2014).

53 Fernandez-Escamilla, A. M., Rousseau, F., Schymkowitz, J. & Serrano, L. Prediction of sequence-dependent and mutational effects on the aggregation of peptides and proteins. *Nat. Biotechnol.* **22**, 1302-1306, (2004).

54 Emily, M., Talvas, A. & Delamarche, C. MetAmyl: a METa-predictor for AMYLoid proteins. *PLoS One* **8**, e79722, (2013).

55 Romero, D., Vlamakis, H., Losick, R. & Kolter, R. Functional analysis of the accessory protein TapA in *Bacillus subtilis* amyloid fiber assembly. *J. Bacteriol.* **196**, 1505-1513, (2014).

56 Caro-Astorga, J., Perez-Garcia, A., de Vicente, A. & Romero, D. A genomic region involved in the formation of adhesin fibers in Bacillus cereus biofilms. *Front Microbiol* **5**, 745, (2014).

57 Yoshimura, Y. *et al.* Distinguishing crystal-like amyloid fibrils and glass-like amorphous aggregates from their kinetics of formation. *Proc. Natl. Acad. Sci. USA* **109**, 14446-14451, (2012).

58 Vetri, V. & Fodera, V. The route to protein aggregate superstructures: Particulates and amyloid-like spherulites. *FEBS Lett.* **589**, 2448-2463, (2015).

59 Cassandri, M. *et al.* Zinc-finger proteins in health and disease. *Cell Death Discov* **3**, 17071, (2017).

60 Bella, J., Hindle, K. L., McEwan, P. A. & Lovell, S. C. The leucine-rich repeat structure. *Cell Mol. Life Sci.* **65**, 2307-2333, (2008).

61 Galzitskaya, O. V. & Lobanov, M. Y. Proteome-scale understanding of relationship between homo-repeat enrichments and protein aggregation properties. *PLoS One* **13**, e0206941, (2018).

62 Harada, R. *et al.* The effect of amino acid substitution in the imperfect repeat sequences of alpha-synuclein on fibrillation. *Biochim. Biophys. Acta* **1792**, 998-1003, (2009).

63 Tank, E. M., Harris, D. A., Desai, A. A. & True, H. L. Prion protein repeat expansion results in increased aggregation and reveals phenotypic variability. *Mol. Cell Biol.* **27**, 5445-5455, (2007).

64 De Simone, A. *et al.* Intrinsic disorder modulates protein self-assembly and aggregation. *Proc. Natl. Acad. Sci. USA* **109**, 6951-6956, (2012).

65 Jorda, J., Xue, B., Uversky, V. N. & Kajava, A. V. Protein tandem repeats - the more perfect, the less structured. *FEBS J.* **277**, 2673-2682, (2010).

66 Abbasi, R. *et al.* The Bacterial Extracellular Matrix Protein TapA Is a Two-Domain Partially Disordered Protein. *Chembiochem* **20**, 355-359, (2019).

67 Hammer, N. D., Schmidt, J. C. & Chapman, M. R. The curli nucleator protein, CsgB, contains an amyloidogenic domain that directs CsgA polymerization. *Proc. Natl. Acad. Sci. USA* **104**, 12494-12499, (2007).

68 Candela, T. *et al.* CalY is a major virulence factor and a biofilm matrix protein. *Mol. Microbiol.* **111**, 1416-1429, (2019).

69 Ahimou, F., Jacques, P. & Deleu, M. Surfactin and iturin A effects on *Bacillus subtilis* surface hydrophobicity. *Enzyme Microb. Technol.* **27**, 749-754, (2000).

70 Doan, T., Marquis, K. A. & Rudner, D. Z. Subcellular localization of a sporulation membrane protein is achieved through a network of interactions along and across the septum. *Mol. Microbiol.* **55**, 1767-1781, (2005).

71 Yasbin, R. E. & Young, F. E. Transduction in *Bacillus subtilis* by bacteriophage SPP1. *J Virol* **14**, 1343-1348 (1974).

72 Hyberts, S. G., Arthanari, H. & Wagner, G. Applications of non-uniform sampling and processing. *Top Curr. Chem.* **316**, 125-148, (2012).

73 Wang, Y. & Jardetzky, O. Probability-based protein secondary structure identification using combined NMR chemical-shift data. *Protein Sci.* **11**, 852-861, (2002).

74 Aguilar, C., Vlamakis, H., Guzman, A., Losick, R. & Kolter, R. KinD is a checkpoint protein linking spore formation to extracellular-matrix production in *Bacillus subtilis* biofilms. *mBio* **1**, (2010).

75 Chu, F., Kearns, D. B., Branda, S. S., Kolter, R. & Losick, R. Targets of the master regulator of biofilm formation in *Bacillus subtilis*. *Mol. Microbiol.* **59**, 1216-1228, (2006).

SUPPLEMENTARY INFORMATION

Supplementary Table 2.1. Amino-acid content of the amyloid core as detected in the 2D 13C-13C solid-state NMR experiments.

Residue	SSNMR	Proteinase K	Sequence
Ala	~13	9	24
Arg	0	0	0
Asn	4	11	20
Asp	4	9	23
Cys	0	0	0
Gln	1	2	10
Glu	2	6	14
Gly	/	10	23
His	0	0	2
Ile	3 or 4	3	10
Leu	2	15	24
Lys	4	11	34
Met	0	2	6
Phe	1	6	12
Pro	3 or 4	3	7
Ser	~15	10	17
Thr	~10	6	15
Trp	0	0	0
Tyr	0	3	6
Val	4	4	12
TOTAL	~68	110	261

Supplementary Table 2.2. Bacterial strains used in this study.

Bacterial strain	Genotype	Source
Bacillus subtilis 168	Prototroph	Laboratory collection
Bacillus subtilis NCIB3610	Wild type. Undomesticated strain	Laboratory collection
CA017	*Bacillus subtilis* NCIB3610 *tasA::km*	(Vlamakis *et al*., 2008)[74]
FC268	*Bacillus subtilis* NCIB3610 *(tapA-sipW-tasA)::spc, amyE::(tapA(13-234)-sipW-tasA) (cm)*	(Chu *et al*., 2006)[75]
SSB149	*Bacillus subtilis* NCIB3610 *(tapA-sipW-tasA)::spc*	(Branda *et al*., 2006)[21]
SSB572	*Bacillus subtilis* NCIB3610 *tasA::km epsA-O::tet*	(Branda *et al.,* 2006)[21]
JC70	*Bacillus subtilis* NCIB3610 *(tapA-sipW-tasA)::spc lacA::(tapA-sipW-tasA$_{native}$)-mls*	This study
JC72	*Bacillus subtilis* NCIB3610 *(tapA-sipW-tasA)::spc lacA::(tapA-sipW-tasA$_{\Delta 82-88}$)-mls*	This study
JC75	*Bacillus subtilis* NCIB3610 *(tapA-sipW-tasA)::spc lacA::(tapA-sipW-tasA$_{\Delta 108-116}$)-mls*	This study
JC76	*Bacillus subtilis* NCIB3610 *(tapA-sipW-tasA)::spc lacA::(tapA-sipW-tasA$_{E82A}$)-mls*	This study
JC77	*Bacillus subtilis* NCIB3610 *(tapA-sipW-tasA)::spc lacA::(tapA-sipW-tasA$_{F72A}$)-mls*	This study
JC78	*Bacillus subtilis* NCIB3610 *(tapA-sipW-tasA)::spc lacA::(tapA-sipW-tasA$_{D64A}$)-mls*	This study
JC80	*Bacillus subtilis* NCIB3610 *(tapA-sipW-tasA)::spc lacA::(tapA-sipW-tasA$_{[K35A, D36A]}$)-mls*	This study
JC81	*Bacillus subtilis* NCIB3610 *(tapA-sipW-tasA)::spc lacA::(tapA-sipW-tasA$_{[K68A, D69A]}$)-mls*	This study
JC82	*Bacillus subtilis* NCIB3610 *(tapA-sipW-tasA)::spc lacA::(tapA-sipW-tasA$_{G96A}$)-mls*	This study

Supplementary Table 2.3. Primers used in this study.

Name	Sequence (5' – 3')	Purpose
TapA–attb1–forward	GGGGACAAGTTTGTACAAAAAAGCAGGCTTGATATGCTTACAATTTTCCGATGAT	Cloning of tapA ORF without the signal peptide into pDEST17
TapA–attb2–reverse	GGGGACCACTTTGTACAAGAAAGCTGGGTCTTACTGATCAGCTTCATTGCT	Cloning of tapA ORF without the signal peptide into pDEST17
TasA_1_mutb	AAAAAGTCGACATTAGATAGTGAATGGGAGAAATTGG	Cloning of (tapA-sipW-tasA) into pDR183
YSRI_2	AAAAAGGATCCGCTATAAGGATCAAATGAAATCG	Cloning of (tapA-sipW-tasA) into pDR183
del82-88-antisense	GTTTGCTTTAAAATCTCCATATTTGATCGCAAGTGATCCGTTATTTTCAAATTG	Site directed mutagenesis: deletion of amino acids 82 to 88 from TasA sequence
del82-88	CAATTTGAAAATAACGGATCACTTGCGATCAAATATGGAGATTTTAAAGCAAAC	Site directed mutagenesis: deletion of amino acids 82 to 88 from TasA sequence
del108-116	CAGAAGATTTCCTCAGCGGAAAAGAGGGCGGCAATG	Site directed mutagenesis: deletion of amino acids 108 to 116 from TasA sequence
del108-116-antisense	CATTGCCGCCCTCTTTTCCGCTGAGGAAATCTTCTG	Site directed mutagenesis: deletion of amino acids 108 to 116 from TasA sequence
KD_AA_35-36	CTGATGCAAAAGTAGCAGCCGCTGATTTAATGTCGTTAAATGCTGCCCATGTTCC	Site directed mutagenesis: substitution of amino acids K35 and D36 by alanines
KD_AA_35-36_antisense	GGAACATGGGCAGCATTTAACGACATTAAATCAGCGGCTGCTACTTTTGCATCAG	Site directed mutagenesis: substitution of amino acids K35 and D36 by alanines
F_A_72	GTGATCCGTTATTTTCAGCTTGGAAATCCTTTGTCAACTTATCTCCCGGC	Site directed mutagenesis: substitution of amino acid F72 by alanine
F_A_72_antisense	GCCGGGAGATAAGTTGACAAAGGATTTCCAAGCTGAAAATAACGGATCAC	Site directed mutagenesis: substitution of amino acid F72 by alanine
G_A_96	GGAGATGTATTGCTGCCGGCGTTTGCTTTAAAATCTC	Site directed mutagenesis: substitution of amino acid G96 by alanine
G_A_96_antisense	GAGATTTTAAAGCAAACGCCGGCAGCAATACATCTCC	Site directed mutagenesis: substitution of amino acid G96 by alanine
D_A_64	GGAAATCCTTTGTCAACTTAGCTCCCGGCTTTAGATTTGAT	Site directed mutagenesis: substitution of amino acid D64 by alanine
D_A_64_antisense	ATCAAATCTAAAGCCGGGAGCTAAGTTGACAAAGGATTTCC	Site directed mutagenesis: substitution of amino acid D64 by alanine

KD_AA_68-70	GATCCGTTATTTTCAAATTGGAAAGCCGCTGTCAACTTATCTCCCGGCTTTAG	Site directed mutagenesis: substitution of amino acids K68 and D69 by alanines
KD_AA_68-70_antisense	CTAAAGCCGGGAGATAAGTTGACAGCGGCTTTCCAATTTGAAAATAACGGATC	Site directed mutagenesis: substitution of amino acids K68 and D69 by alanines

Supplementary figures

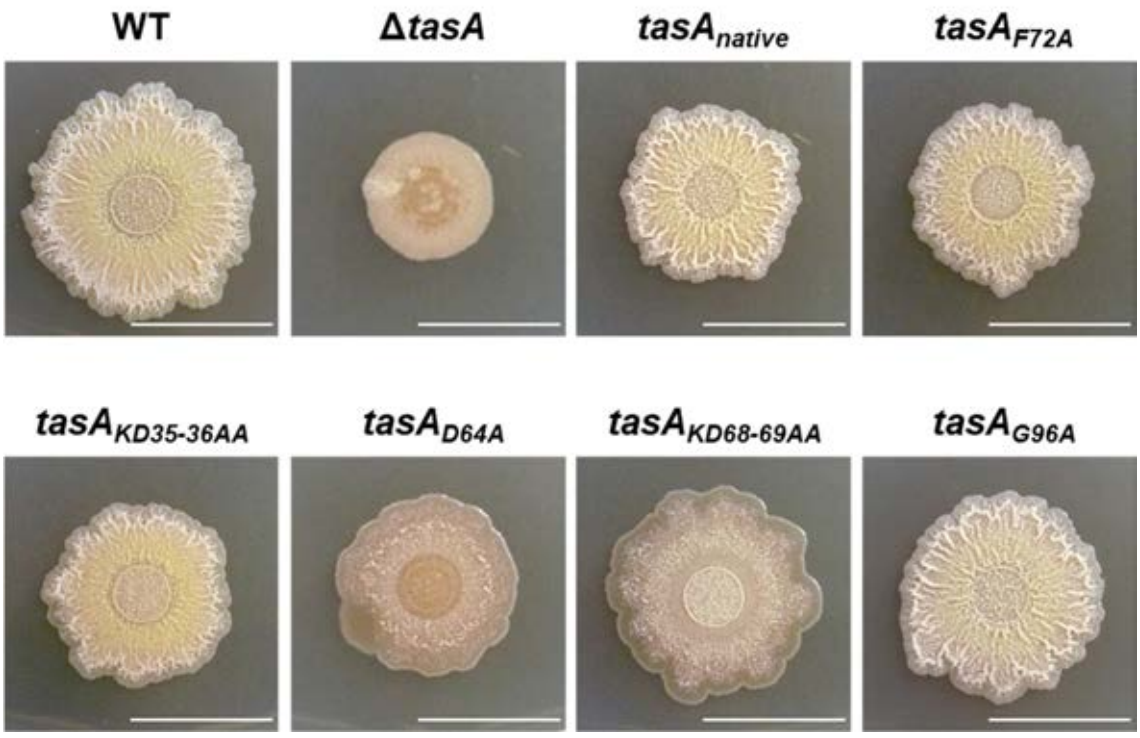

Figure S2.1. Amino acid repeats play a role in filament assembly and biofilm formation. Colony morphologies, after 72 hours of incubation at 30°C in solid MSgg medium, of the strains expressing the ala-substituted alleles.

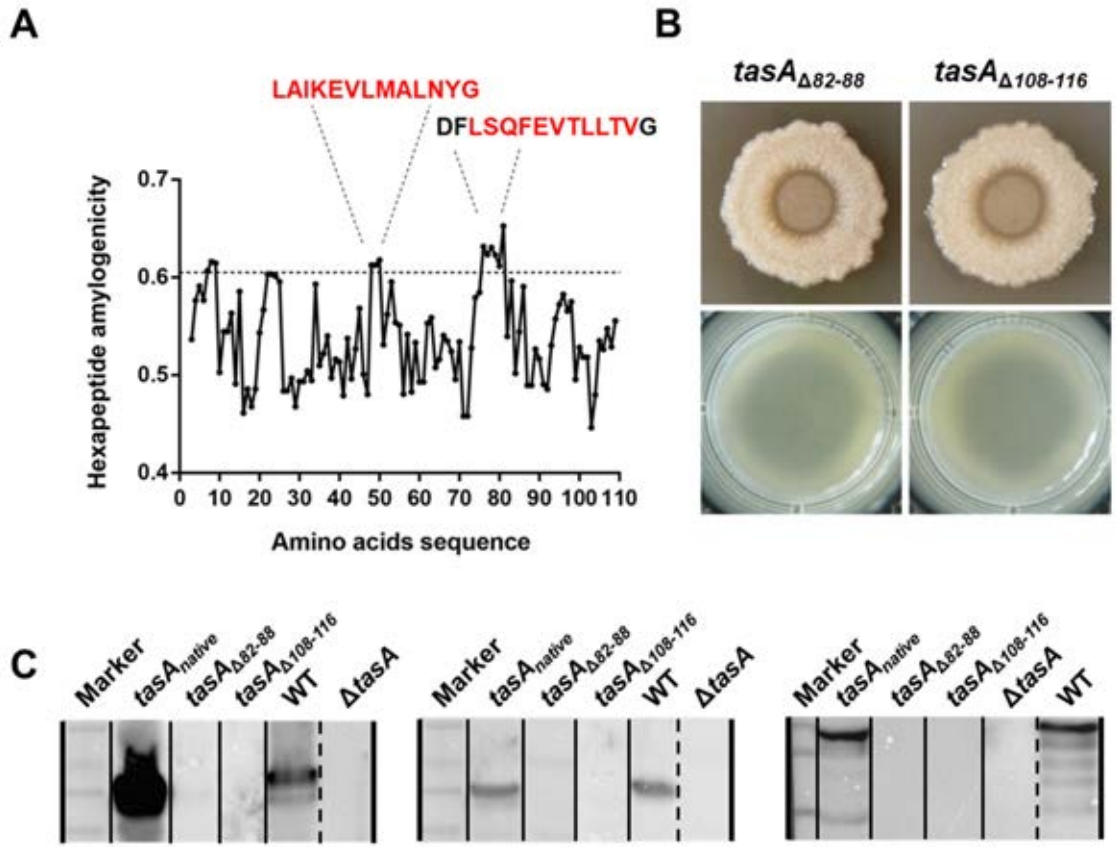

Figure S2.2. The amyloid core region of TasA contains two amyloidogenic sequences. A) Graphical representation of the detection of amyloid-prone regions by MetAmyl. The two selected sequences were the consensus among five different tools. **B)** Top. Colony morphology phenotypes in MSgg-agar at 72 h of the strains expressing the tasA alleles that contain deletions of the amyloidogenic regions. Bottom. Pellicle formation in liquid MSgg medium at 48 h of the strains expressing the tasA alleles that contain deletions of the amyloidogenic regions. **C)** Western blot with anti-TasA antibody corresponding to the cell (left) spent medium (center) or matrix (right) fractions respectively of the biofilm formed by the strains bearing the deletion-mutated alleles. Immunoblot images have been cropped and spliced for illustrative purposes. All the lines over the immunoblot images delimitate the lanes. In addition, the solid lines indicate the boundaries of the splicing images.

Figure S2.3. Sequence alignment of TasA and TapA. Color indicate amino acids with similar properties.

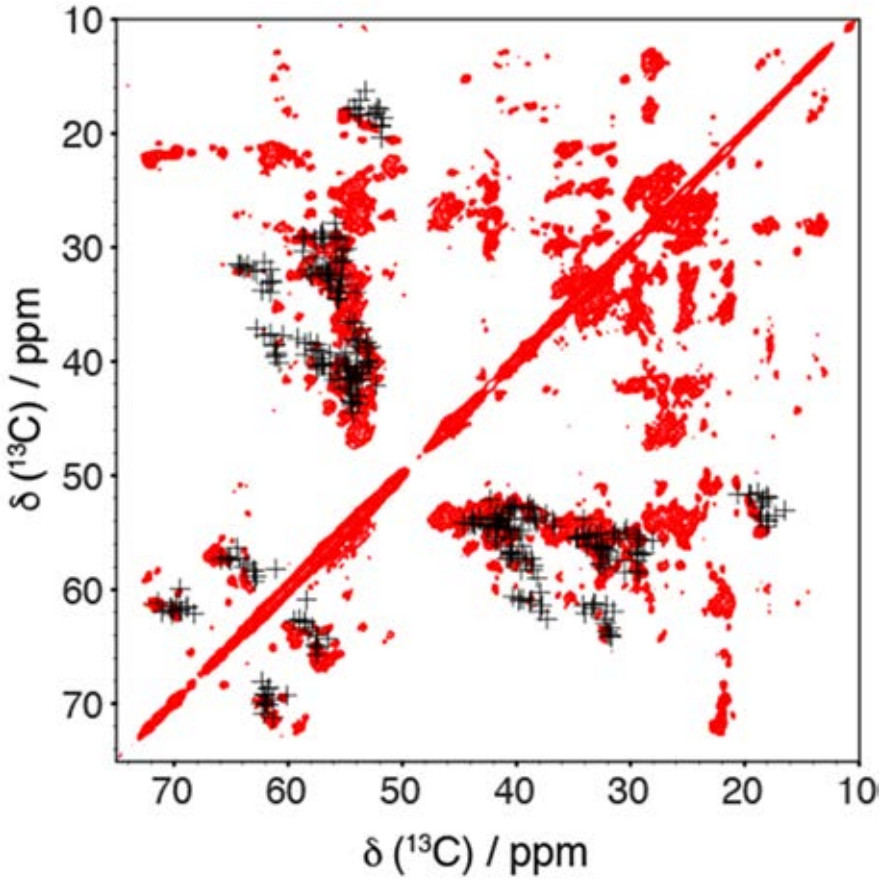

Figure S2.4. TasA globular fold is conserved upon fibril formation. Comparison of solid-state NMR 2D ^{13}C-^{13}C correlation experiment (PDSD, 50 ms mixing time) of rTasA filaments to chemical shift predictions made from the published crystal structure of monomeric TasA.

Chapter III

Dual functionality of the amyloid protein TasA in *Bacillus* physiology and fitness in the phylloplane

Jesús Cámara-Almirón, Yurena Navarro, Luis Díaz-Martínez, María Concepción Magno-Pérez-Bryan, Carlos Molina-Santiago, John R. Pearson, Antonio de Vicente, Alejandro Pérez-García, and Diego Romero. Dual functionality of the amyloid protein TasA in *Bacillus* physiology and fitness on the phylloplane. *Nature Communications* **11,** 1859 (2020).

ABSTRACT

In response to a wide range of environmental factors, bacteria can form biofilms, that consist of multicellular communities embedded in an extracellular matrix (ECM). In *Bacillus subtilis*, the main protein component of the ECM is the functional amyloid TasA. In this study, we demonstrate that beyond their well-known defect in biofilm formation, Δ*tasA* cells also exhibit a range of gene expression changes and cytological symptoms indicative of excessive cellular stress, including DNA damage accumulation, changes in membrane potential, higher susceptibility to oxidative stress, and alterations in membrane dynamics. Collectively, these events lead to increased cell death in the colony. We show that these major physiological changes in Δ*tasA* cells are likely independent from the structural role of TasA during amyloid fiber formation in ECM assembly. We found that a strain expressing a mutated version of TasA was able to restore the physiological conditions and cell viability in a *tasA* null mutant background but was impaired in biofilm formation. Taken together, our results allow the separation of two complementary roles of this functional amyloid protein: i) structural functions during ECM assembly and interactions with plants, and ii) a physiological function in which TasA maintains cell viability preventing premature cell death and supports more effective cellular adaptation to environmental cues.

INTRODUCTION

In response to a wide range of environmental factors[1,2], some bacterial species establish complex communities called biofilms[3]. To do so, planktonic cells initiate a transition into a sedentary lifestyle and trigger a cell differentiation program that leads to: (i) a division of labor, in which different subpopulations of cells are dedicated to covering different processes needed to maintain the viability of the community[4,5], and (ii) the secretion of a battery of molecules that assemble the extracellular matrix (ECM)[3,6]. Like in eukaryotic tissues, the bacterial ECM is a dynamic structure that supports cellular adhesion, regulates the flux of signals to ensure cell differentiation[7,8], provides stability and serves as an interface with the external environment, working as a formidable physicochemical barrier against external assaults[9-11]. In eukaryotic cells, the ECM plays an important role in signaling[12,13] and has been described as a reservoir for the localization and concentration of growth factors, which in turn form gradients that are critical for the establishment of developmental patterning during morphogenesis[14,15,16]. Interestingly, in senescent cells, partial loss of the ECM can influence cell fate, e.g., by activating the apoptotic program[17,18]. In both eukaryotes and prokaryotes, senescence involves global changes in cellular physiology, and in some microbes, this process begins with the entry of the cells into stationary phase[19-21]. This process triggers a response typified by molecular mechanisms evolved to overcome environmental adversities and to ensure survival, including the activation of general stress response genes[22,23], a shift to anaerobic respiration[24], enhanced DNA repair[25], and induction of pathways for the metabolism of alternative nutrient sources or sub-products of primary metabolism[26].

Studies of *Bacillus subtilis* biofilms have contributed to our understanding of the intricate developmental program that underlies biofilm formation[27-30] that ends with the secretion of ECM components. Currently, the *B. subtilis* ECM is known to consist mainly of exopolysaccharide (EPS) and the TasA and BslA proteins[27]. The EPS acts as the adhesive element of the biofilm cells at the cell-to-surface interface, which is important for biofilm attachment[31], and BslA is a hydrophobin that forms a thin external hydrophobic layer and is the main factor that confers hydrophobic properties to biofilms[32]. Both structural factors contribute to maintain the defense function performed by the ECM[11,32]. TasA is a functional amyloid protein that forms fibers resistant to adverse physicochemical conditions that confer biofilms with structural stability[33,34]. Additional proteins are needed for the polymerization of these fibers: TapA appears to favor the transition of TasA into the fiber state, and the signal peptidase SipW processes both proteins into their mature forms[35,36]. The ability of amyloids to transition from monomers

into fibers represents a structural, biochemical and functional versatility that microbes exploit in different contexts and for different purposes[37].

Previous studies have demonstrated that the genetic pathways involved in biofilm formation are active during the interaction of several microbial species with plants[38,39]. In *B. subtilis,* the lipopeptide surfactin acts as a self-trigger of biofilm formation on the melon phylloplane, which is connected with the suppressive activity of *B. subtilis* against phytopathogenic fungi[40]. These findings led us to hypothesize that the ECM makes a major contribution to the ecology of *B. subtilis* in the poorly explored phyllosphere. Our study of the ecology of *B. subtilis* NCIB3610-derived strains carrying single mutations in different ECM components in the phyllosphere highlights the role of TasA in bacteria-plant interactions. Moreover, the increased production of secondary metabolites by a *tasA* mutant strain on plant leaves revealed a complementary role for TasA in the stabilization of the bacterial physiology. In Δ*tasA* cells, gene expression changes and dynamic cytological alterations affect membrane potential, adaptation to oxidative stress and membrane functionality and dynamics, which eventually lead to a premature increase in cell death within the colony. Our results of the ectopic expression of a mutated TasA protein in a *tasA* null mutant background that fails to restore the strain's ability to form biofilms while it does restore the mutant strain's ability to maintain the physiological status of the cells, indicate that these alterations are independent from the structural role of TasA in ECM assembly. All these results indicate that these two complementary roles of TasA, both as part of the ECM and in stabilizing bacterial physiology and preventing cell death, are important to preserve cell viability within the colony and for the ecological fitness of *B. subtilis* in the phylloplane.

RESULTS

TasA contributes to the fitness of *Bacillus* on the phylloplane

Surfactin, a member of a subfamily of lipopeptides produced by *B. subtilis* and related species, contributes to multicellularity in *B. subtilis* biofilms[41]. We previously reported how a mutant strain defective for lipopeptide production showed impaired biofilm assembly on the phylloplane[40]. These observations led us to evaluate the specific contributions made by the ECM structural components TasA and the EPS to *B. subtilis* fitness on melon leaves. Although not directly linked to the surfactin-activated regulatory pathway, we also studied the gene encoding the hydrophobin protein BslA (another

important ECM component). A *tasA* mutant strain (Δ*tasA*) is defective in the initial cell attachment to plant surfaces (4 hours and two days post-inoculation) (Fig. 3.1A, top and Supplementary Fig. S3.1A). As expected, based on their structural functions, all of the matrix mutants showed reduced survival; however, the population of Δ*tasA* cells continuously and steadily decreased over time compared to the populations of *eps* or *bslA* mutant cells (Fig. 3.1B and Supplementary Fig. S3.1B). Examination of plants inoculated with the wild type strain (WT) or with the Δ*tasA* strain via scanning electron microscopy (SEM) revealed variability in the colonization patterns of the strains. WT cells assembled in ordered and compact colonies, with the cells embedded in a network of extracellular material (Fig. 3.1C, top). In contrast, the Δ*tasA* cells were prone to irregular distribution as large masses of cells on the leaves, which also showed collapsed surfaces or lack of surface integrity, suggesting alterations in cellular structures (Fig. 3.1C, bottom). Finally, *eps* and *bslA* mutant cells formed flat colonies (Supplementary Fig. S3.2A) with the same colonization defects observed in the *tasA* mutant cells (Supplementary Fig. S3.1C).

Based on the reduced fitness exhibited by the single ECM component mutant strains and their deficiencies in biofilm formation, we hypothesized that these strains may also be defective in their antagonistic interactions with *Podosphaera xanthi* (an important fungal biotrophic phytopathogen of crops[42]) on plant leaves. Strains with mutations in *eps* and *bslA* partially ameliorated the disease symptoms, although their phenotypes were not significantly different from those of the WT strain (Fig. S3.1D). However, contrary to our expectations, the Δ*tasA* strain retained similar antagonistic activity to that of the WT strain (Fig. 3.1D). The simplest explanation for this finding is that the antifungal activity exhibited by the Δ*tasA* cells is due to higher production of antifungal compounds. *In situ* mass spectrometry analysis revealed a consistently higher relative amount of the antifungal compound plipastatin (also known as fengycin, the primary antifungal compound produced by *B. subtilis*) on leaves treated with Δ*tasA* cells compared to those treated with WT cells (Fig. 3.1E). These observations argue in favor of the relevance of the ECM and specifically TasA in the colonization, survival and antagonistic activity of *B. subtilis* on the phylloplane.

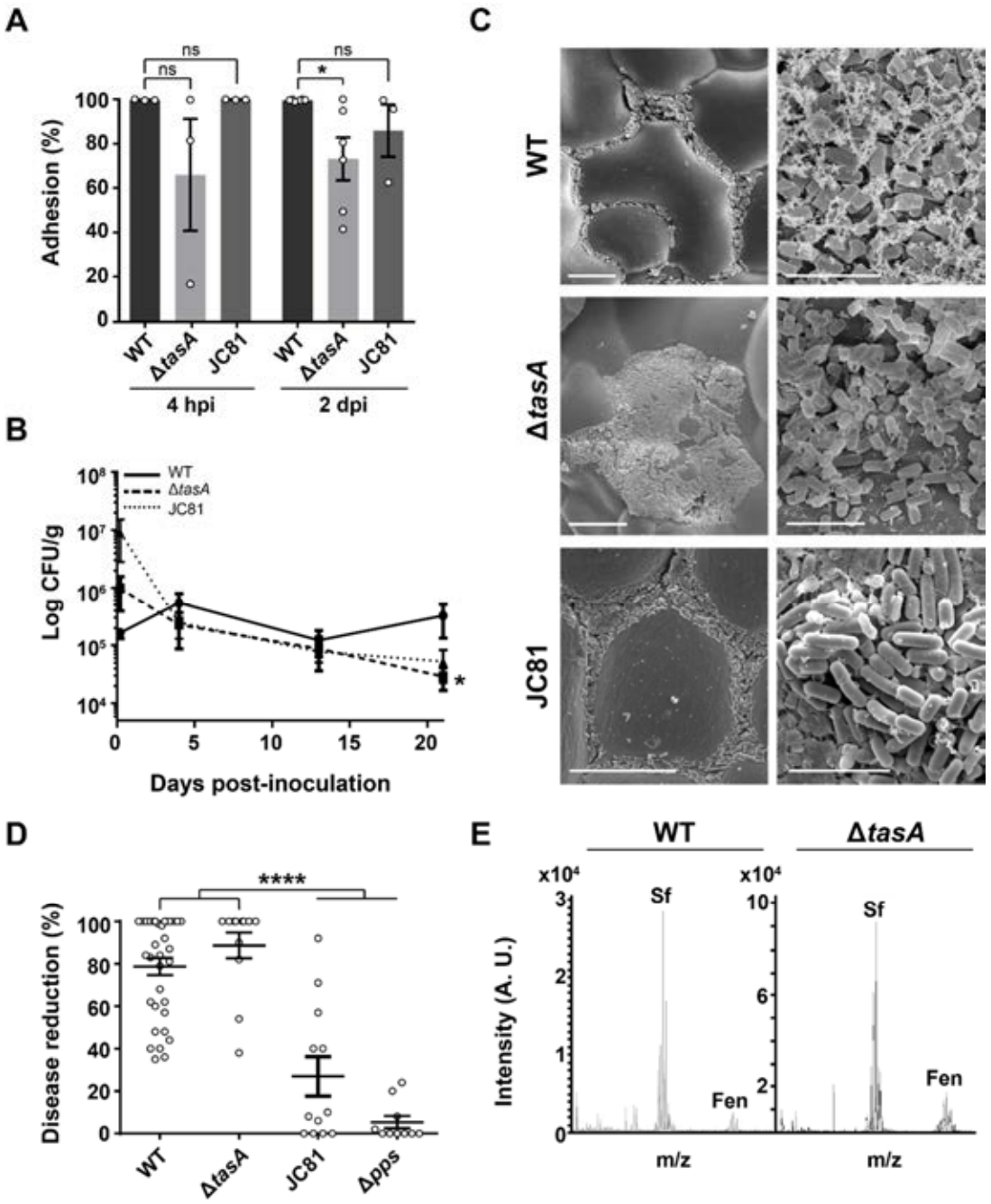

Figure 3.1. TasA is essential for the fitness of Bacillus on the melon phylloplane. A) Adhesion of the WT, Δ*tasA* and JC81 (TasA Lys68Ala, Asp69Ala) strains to melon leaves at 4 h (hpi) and 2 days post-inoculation (dpi). Statistically significant differences between WT and Δ*tasA* were found at 2 dpi. Average values from at least three independent experiments are shown. In each experiment, 10 leaves were analyzed. Error bars represent the SEM. Statistical significance was assessed via two-tailed independent t-tests at each time-point (*p value < 0.05). **B)** The persistence of the Δ*tasA* cells at 21 days was significantly reduced compared with that of the WT cells. The persistence of JC81 cells on melon leaves was reduced compared to that of the WT cells. The first point is taken at 4 hpi. Average values of five biological replicates are shown with error bars representing the SEM. Statistical significance was assessed by two-tailed independent t-test at each time-point (*p value < 0.05). **C)** Representative scanning electron microscopy micrographs of inoculated plants taken 20 days post-inoculation show the WT cells (top) distributed in small groups covered by extracellular material and the Δ*tasA* cells (bottom) in randomly distributed plasters of cells with no visible extracellular matrix. JC81 (TasA Lys68Ala, Asp69Ala) strain shows an intermediate colonization pattern between those of the WT and Δ*tasA* null mutant strains. Scale bars = 25 μm (left panels) and 5 μm (right panels). **D)** The WT and Δ*tasA* strains showed comparable biocontrol activity against the fungal phytopathogen *Podosphaera xanthii*. However, JC81 (TasA Lys68Ala, Asp69Ala) failed to control the disease. Biocontrol activity was measured after 15 days post-inoculation of the pathogen. The points represent the number of plants analyzed over three independent assays. Three leaves per plant were infected and inoculated. Average values are shown with error bars indicating the SEM. The Δ*pps* is a mutant strain in fengycin production and it is used as a negative control. Statistical significance was assessed by two-tailed independent Mann–Whitney tests between each strain and the Δpps mutant (****p < 0.0001). **E)** MALDI-TOF/TOF MS analysis revealed higher fengycin levels on melon leaves treated with ΔtasA (right) cells compared with that on leaves treated with WT cells (left) after 20 days post-inoculation.

Loss of TasA causes a global change in the physiological state of the bacterial cells

The increased fengycin production and the previously reported deregulation of the expression pattern of the *tapA* operon in a Δ*tasA* mutant strain[9] led us to explore whether loss of *tasA* disrupts the genetic circuitry of the cells. We sequenced and analyzed the whole transcriptomes of Δ*tasA* and WT cells grown *in vitro* on MSgg agar plates, a chemically-defined medium specifically formulated to support biofilm. We observed that deletion of *tasA* resulted in pleiotropic effects on the overall gene expression profile of this mutant (Fig. 3.2 and Supplementary Fig. S3.3), with 601, 688 and 333 induced genes and 755, 1077 and 499 repressed genes at 24, 48 and 72 h, respectively (Supplementary Fig. S3.3).

A closer look at the data allowed us to cluster the expression of different genes into groups with similar expression profiles over the time course (Fig. 3.2). In general, four different expression profiles were found in which genes show positive (profiles 1 and 2) or negative (profiles 3 and 4) variations from 24 h to 48 h, and genes with expression levels that remain either stable (profiles 1 and 3) or altered (profiles 2 and 4) from 48 h to 72 h (Fig. 3.2). Profiles 1 and 2 included genes related to the SOS response (profile 1), transcription and replication (profile 1 and 2), purine biosynthetic process (profile 2) and toxin-antitoxin systems (profile 2). Profiles 3 and 4 included genes related to sporulation (profiles 3 and 4), cellular metabolism in general (profile 3) and lipids (profile 3), carbohydrates (profile 3 and 4), monosaccharides (profile 3), polysaccharides (profile 4), or peptidoglycans (profile 3) in particular. These gene expression profiles reflect a general picture that suggests: i) the existence of cellular stress and DNA damage, in which the cells need to fully activate different sets of genes to cope with and compensate for the damage and maintain viability, ii) a decrease in the overall cellular energy metabolism, and iii) strong repression of the sporulation pathway.

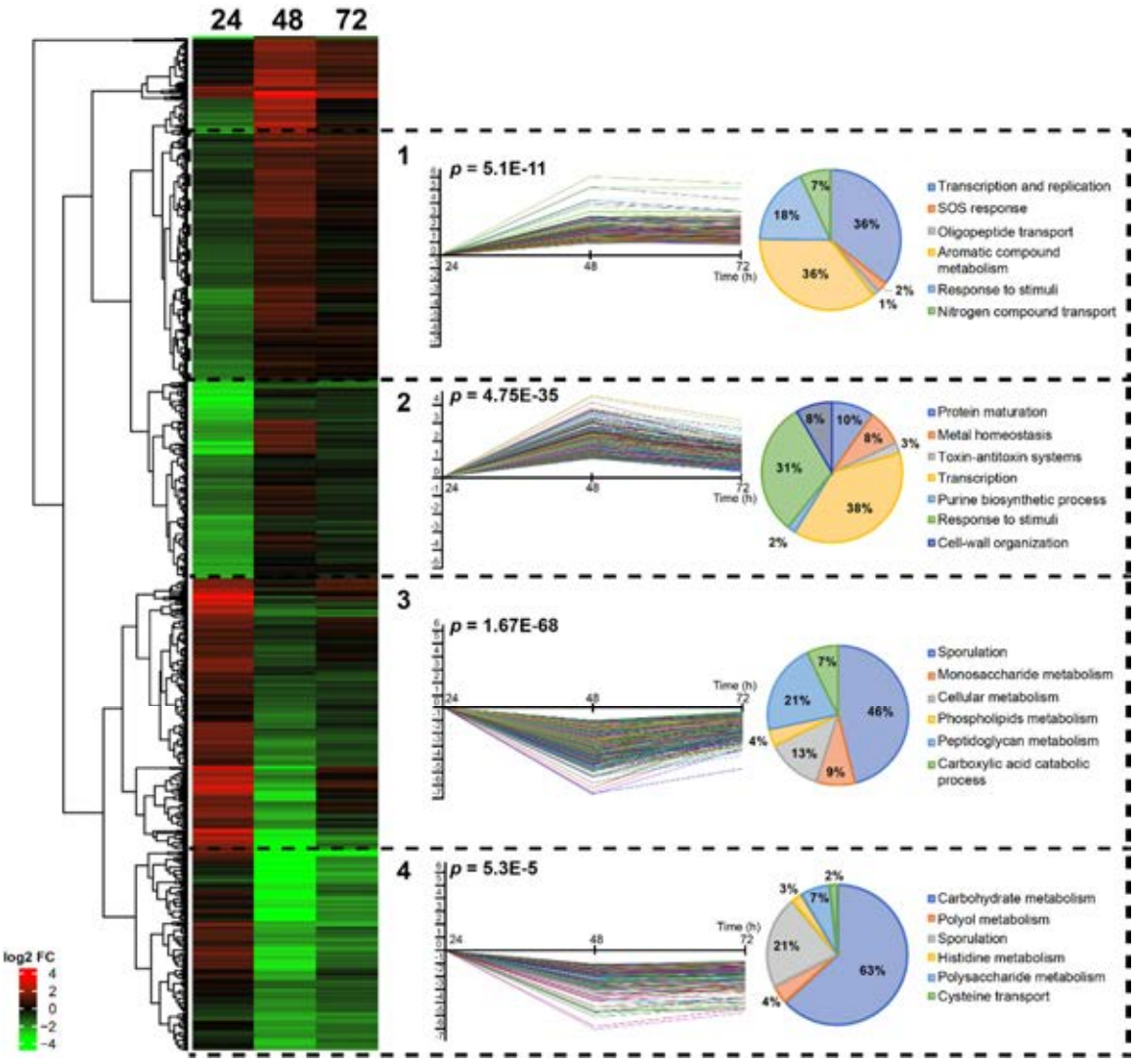

Figure 3.2. The *tasA* mutant display major gene expression changes. Heatmap and gene profiles (1–4) of genes with similar expression patterns. Genes in the same profile are categorized (right) according to their gene ontology (GO) terms. Each gene profile represents statistically significant genes. Statistical significance was assessed by a χ^2 test comparing the number of clustered genes with the expected theoretical number of genes if gene distribution were random. In the heatmap, induced genes are colored in red and repressed genes in green.

To study the observed alterations in gene expression in Δ*tasA* cells, the differentially expressed genes at all the time points were classified into their different regulons. Indeed, the *sigK*, *sigG*, *gerR* and *gerE* regulators (Supplementary Data 3.2 and 3.3), which control the expression of many of the genes related to sporulation, were repressed in the Δ*tasA* cells from 48 h (Fig. 3.3 and Supplementary Fig. S3.5), consistent with the delayed sporulation defect previously reported in ECM mutants[9,30] (Supplementary Fig. S3.6). In contrast, the expression levels of biofilm-related genes, including the *epsA-O*, and *tapA* operons, were higher in the Δ*tasA* cells at all times compared to their expression levels in WT cells (Fig. 3.3, Supplementary Fig. S3.4 and S3.5) (Supplementary Data 3.1 to 3.3). We found repression of *sinR* at 24 h (Supplementary Data Table 1), induction of the *slrR* transcriptional regulator at all times (Supplementary

Data Table 3.1 to 3.3), and repression of the transition state genes transcriptional regulator *abrB* at 24 h and 48 h (Supplementary Data 3.1 and 3.2), which could explain the induction of the ECM-related genes[27].

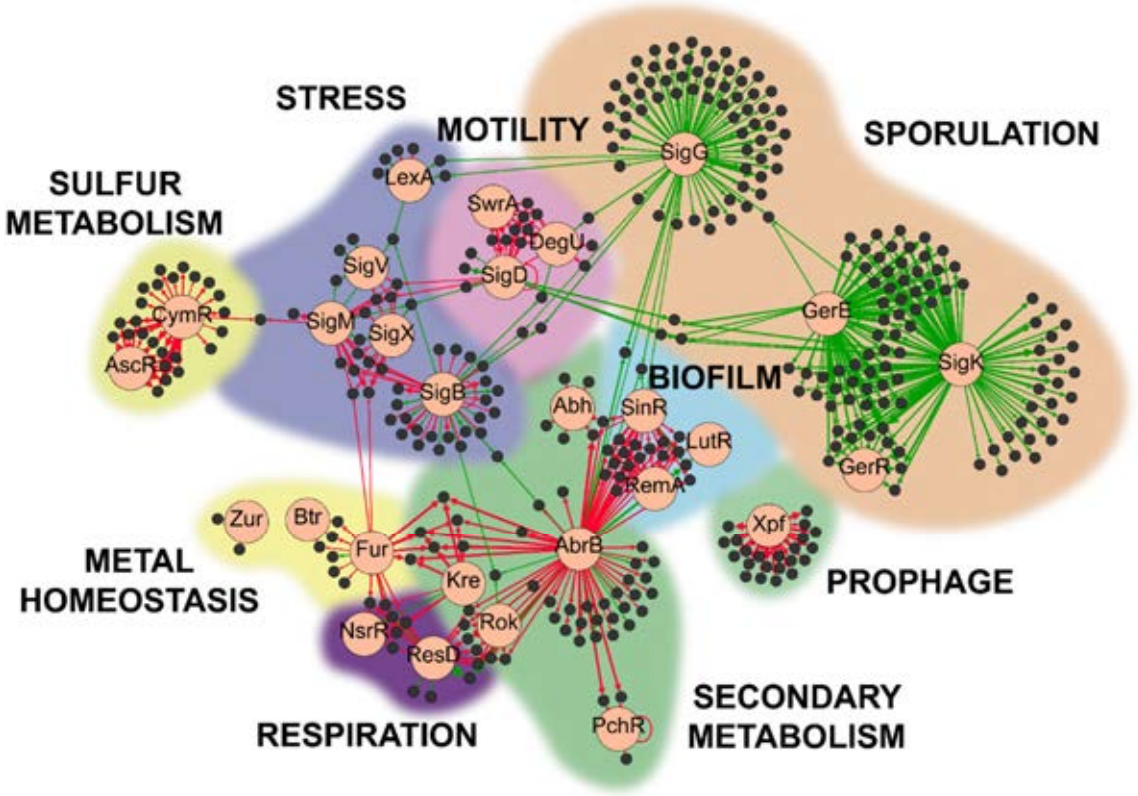

Figure 3.3. Δ*tasA* cells exhibit alterations in many physiological processes. Differentially expressed genes at 72 h clustered into different regulons. The bigger circles indicate de main regulator of that regulon, which is surrounded by arrows pointing to smaller circles that are the differentially expressed genes. The thickness of the arrows indicates expression levels. The color in the arrows indicates induction (red) or repression (green).

The analysis of the transcriptional changes in the *tasA* mutant cells highlighted the broad metabolic rearrangements that take place in Δ*tasA* colonies from 24 h to 72 h, including the expression alteration of genes implicated in energy metabolism, secondary metabolism and general stress, among other categories (Supplementary Data 3.1 to 3.3, Fig. 3.3, Supplementary Fig. S3.4 and Supplementary Fig. S3.5). First, the *alsS* and *alsD* genes, which encode acetolactate synthase and acetolactate decarboxylase, respectively, were clearly induced at all times (suppl. tables 1 to 3). This pathway feeds pyruvate into acetoin synthesis, a small four-carbon molecule that is produced in *B. subtilis* during fermentative and overflow metabolism[43]. Additionally, we found induction of several regulators and genes that are involved in anaerobic respiration and fermentative metabolism. The two-component regulatory system *resD* and *resE,* which senses oxygen limitation, and their target genes[44], were induced in Δ*tasA* cells at 24 h and 48 h (Supplementary Data 3.1 and 3.2 and fig. Supplementary Fig. S3B).

Consistently, induction of the transcriptional regulator *fnr* and the anaerobic related genes *narGHIJK,* which encode the nitrate reductase complex, as well as all of the proteins required for nitrate respiration were induced at 24 h and 48 h (Supplementary Data 3.1 and 3.2 and Supplementary Fig. S3B). Second, we observed induction at all times of the genes involved in fengycin biosynthesis (Supplementary Data 3.1 to 3.3), consistent with the overproduction of this antifungal lipopeptide *in planta* (Fig. 3.1E), genes involved in the biosynthesis of surfactin, subtilosin, bacilysin, and bacillaene (all secondary metabolites with antimicrobial activities[45-48]) (Fig. 3.3, Supplementary Fig. S3.4 and Supplementary Fig. S3.5 and Supplementary Data 3.1 to 3.3), as well as the operon encoding the iron-chelating protein bacillibactin (*dhbACEBF*) (Supplementary Data 3.1 to 3.3). The induction of all of these genes is possibly due to the repression of transcriptional repressors of transition state genes that occurs at 24 h and 48 h, e.g., *abrB* (which controls activation of the genes involved in the synthesis of fengycin, bacilysin, subtilosin and bacillaene) and *abh* (which contributes to the transcriptional control of the genes involved in surfactin production) (Supplementary Data 3.1 and 3.2). The transcriptional changes of other regulators, such as *resD* (for subtilosin) or *comA* (for surfactin), both upregulated at 24 h and 48 h (Supplementary Data 3.1 and 3.2), also contribute to the induction of the genes that participate in the synthesis of all of these secondary metabolites and might explain their overall activation at 72 h (Fig. 3.3). Finally, the gene encoding the regulator AscR was induced at 48 h and 72 h. AscR controls transcription of the *snaA* (*snaAtcyJKLMNcmoOcmoJIrbfKsndAytnM)* and *yxe* (*yxeKsnaByxeMyxeNyxeOsndByxeQ*) operons which are induced at all times (Supplementary Data 3.1 to 3.3). The products of these operons are members of alternative metabolic pathways that process modified versions of the amino acid cysteine. More specifically, the products of the *snaA* operon degrade alkylated forms of cysteine that are produced during normal metabolic reactions due to aging of the molecular machinery[26]. The *yxe* operon is implicated in the detoxification of S-(2-succino)cysteine, a toxic form of cysteine that is produced via spontaneous reactions between fumarate and cellular thiol groups in the presence of excess nutrients, which subsequently leads to increased bacterial stress[49,50].

Additional signs of excess cellular stress in the Δ*tasA* cells were: i) the strong overexpression of the sigma factor SigB (σ^B) at 24 h and 72 h (Fig. 3.3, Supplementary Fig. S3.5 and Supplementary Data 3.1 and 3.3), which controls the transcription of genes related to the general stress response[22], and ii) the repression at 24 h of *lexA* (Supplementary Data 3.1), a transcriptional repressor of the SOS response regulon, as well as the induction of other genes that confer resistance to different types of stress,

i.e., *ahpC* and *ahpF* (induced at all times, Supplementary Data 3.1 to 3.3) against peroxide stress or *liaH* and *liaI* (induced at 48 h, Supplementary Data 3.2), which confer resistance to cell wall antibiotics. Indeed, approximately 41% of the SigB-regulated genes are induced at 24 h (Supplementary Fig. S3.4 and Supplementary Data 3.1), and these genes are involved in multiple and different functions, including protease and chaperone activity, DNA repair or resistance against oxidative stress. At 72 h, around 10% of the genes of the SigB regulon were still upregulated, suggesting the existence of cellular stress during colony development (Fig. 3.3 and Supplementary Data 3.3). Furthermore, the activation of the SOS response points towards the existence of DNA damage in Δ*tasA* cells, another sign of stress, with induction of *uvrA* (at 24 and 72 h, Supplementary Data 3.1 and 3.3) and *uvrB* (at 24 h, Supplementary Data 3.1), both of which are involved in DNA repair. The presence of DNA damage in Δ*tasA* cells is further indicated by the induction of almost all of the genes belonging to the lysogenic bacteriophage PBSX at 72 h, a feature that has been reported to occur in response to mutations as well as to DNA or peptidoglycan damage[51,52] (Fig. 3.3 and Supplementary Data 3.3).

In general, the transcriptional changes observed in the Δ*tasA* cells illustrate an intrinsic major physiological change that progresses over time and suggest the accumulation of excessive cellular stress. These changes result in the early entry of the cells into stationary phase, indicated by the state of the Δ*tasA* colony at 72 h compared to the WT (fig. 2B) and supported by increased expression levels of genes related to: i) biofilm formation ii) synthesis of secondary metabolites (siderophores, antimicrobials, etc.); iii) anaerobic respiration, fermentative metabolic pathways and overflow metabolism; iv) paralogous metabolism and assimilation of modified or toxic metabolic intermediates; v) general stress and DNA damage; and vi) induction of the lysogenic bacteriophage PBSX.

Δ*tasA* cells show impaired respiration and a switch from primary to secondary metabolism

Our transcriptomic analysis suggested that Δ*tasA* cells exhibit a shift from aerobic respiration to fermentation and anaerobic respiration as well as activation of secondary metabolism, physiological features typical of stationary phase cells[24,53]. Based on the higher abundance of fengycin on leaves treated with Δ*tasA* cells and its key role in the antagonistic interaction between *B. subtilis* and fungal pathogens, we further investigated the kinetics of fengycin production *in vitro*. Flow cytometry analysis of cells expressing YFP under the control of the fengycin operon promoter demonstrated the induction of fengycin production in a subpopulation of cells (26.5%) at 48 h in the WT

strain, reminiscent of the expression pattern reported for surfactin[41]. However, more than half of the Δ*tasA* population (67.3%) actively expressed YFP from the fengycin operon promoter at this time point (Fig. 3.4A top). At later stages of growth (72 h), the promoter was still active in the Δ*tasA* cells, and the population of positive cells was consistently higher than that in the WT strain (Fig. 3.4A bottom). Mass spectrometry analysis of cell-free supernatants from WT or Δ*tasA* MOLP (a medium optimized for lipopeptide production) liquid cultures demonstrated that this expression level was sufficient for the *tasA* mutant cells to produce nearly an order of magnitude more fengycin (Fig. 3.4B, bottom spectrum) consistent with our findings in plants (Fig. 3.1E). Additionally, relatively higher levels of fengycin were detected in cells or agar fractions of Δ*tasA* colonies compared to WT colonies grown on solid MSgg, the medium used in all of our experimental settings (Supplementary Fig. S3.8 top and bottom spectra respectively). Similar results were obtained for the lipopeptide surfactin in these fractions (Fig. 3.4B top spectrum, and Supplementary Fig. S3.8), consistent with our RNA-seq analysis (Supplementary Data 3.1 to 3.3). In agreement to these observations, *in vitro* experiments showed that the cell-free supernatants from Δ*tasA* cells exhibited antifungal activity against *P. xanthii* conidia equivalent to that of WT cells, even in highly diluted spent medium (Fig. 3.4C). These results confirm the robust antimicrobial potency of Δ*tasA* cells and imply that primary metabolic intermediates are diverted to different pathways to support the higher secondary metabolite production in the Δ*tasA* mutant cells.

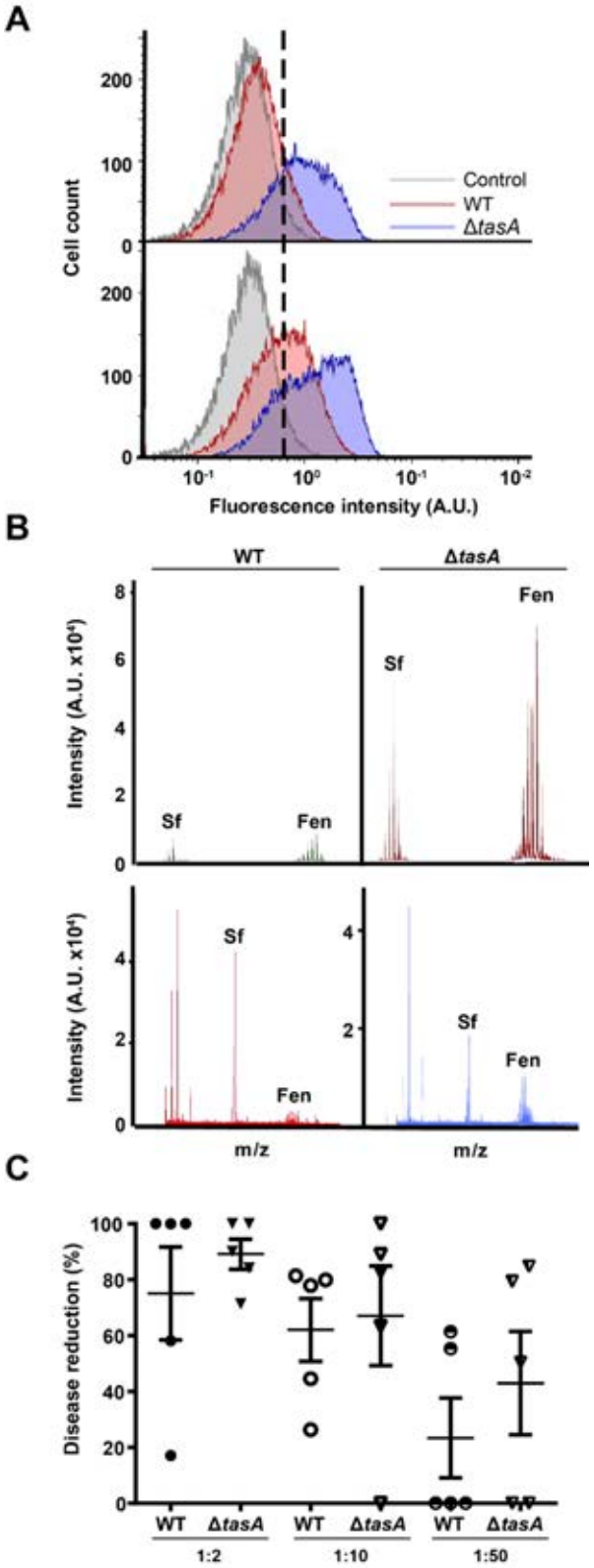

Figure 3.4. Δ*tasA* cells produce larger amounts of fengycin. A) Flow cytometry results of cells encoding the promoter of the fengycin production operon fused to YFP show that a higher percentage of Δ*tasA* cells (blue) expressed YFP compared with the percentage of YFP-expressing WT cells (red) at 48 h (top) and 72 h (bottom). A non-fluorescent negative control corresponding to the unlabeled WT strain at 72 h is shown (gray) in both experiments. **B)** MALDI-TOF/TOF MS analysis of solid MSgg medium (top) or spent MOLP medium after 72 h of growth showed higher fengycin levels in Δ*tasA* cultures (right) compared to that in WT cultures (left). **C)** Serial dilutions of spent medium after 72 h of incubation deposited over infected leaf disks showed that the liquid medium from Δ*tasA* cultures retained as much antifungal activity as the medium from WT cultures. The points indicate the number of independent experiments. In each experiment, three leaf disks were examined. Average values are shown. Error bars represent the SEM.

Consistent with these findings, we observed two complementary results that indicate less efficient metabolic activity in Δ*tasA* cells compared to that in WT cells: first, the induction at 24 h and 48 h of the genes responsible for the synthesis of the anaerobic respiration machinery (Supplementary Data 3.1 and 3.2, Supplementary Fig. S3.4 and Supplementary Fig. S3.5) mentioned above, and second, the differential expression at 72 h of the *nasD* and *nasF* genes (parts of the anaerobic respiration machinery) and the differential expression of genes at all times encoding several terminal oxidases found in the electron transport chain (Supplementary Data 3.1 to 3.3). The analysis of the respiration rates of these strains using the tetrazolium-derived dye 5-cyano-2,3-ditolyl tetrazolium chloride (CTC) and flow cytometry revealed a higher proportion of Δ*tasA* cells with lower respiration rates at 24 h and 72 h compared to the WT proportions (69.10% vs. 43.07% at 24 h and 74.56 vs. 65.11% at 72 h, respectively) (Supplementary Table 3.1 and Fig. 3.5A). Second, the expression levels of the *alsSD* genes, which are responsible for the synthesis of acetoin (a metabolite produced by fermentative pathways) were higher in the Δ*tasA* strain than in the WT strain at all times (Supplementary Data 3.1 to 3.3). Indeed, all of the factors required for acetoin synthesis from pyruvate were overexpressed at 72 h, whereas some key factors involved in the divergent or gluconeogenetic pathways were repressed (Supplementary Data 3.1 to 3.3 and Supplementary Fig. S3.7B). Expression of *alsS* and *alsD* is induced by acetate, low pH and anaerobiosis[43,54,55]. Acetoin, in contrast to acetate, is a neutral metabolite produced to manage the intracellular pH and to ameliorate over-acidification caused by the accumulation of toxic concentrations of acetate or lactate, and its production is favored during bacterial growth under aerobic conditions[56]. Reduced respiration rates typically result in the accumulation of higher cellular proton concentrations, which leads to cytoplasmic acidification. These observations led us to postulate that the activation of the *alsSD* genes and the lower respiration rates observed in Δ*tasA* colonies might also reflect acidification of the intracellular environment, a potential cause of stationary phase-related stress. Measurements of the intracellular pH levels using the fluorescent probe 5-(6)carboxyfluorescein diacetate succinimidyl ester confirmed a significant decrease in the intracellular pH of nearly one unit (-0.92 ± 0.33,) in Δ*tasA* cells at 72 h (Fig. 3.5B) compared to that in WT cells.

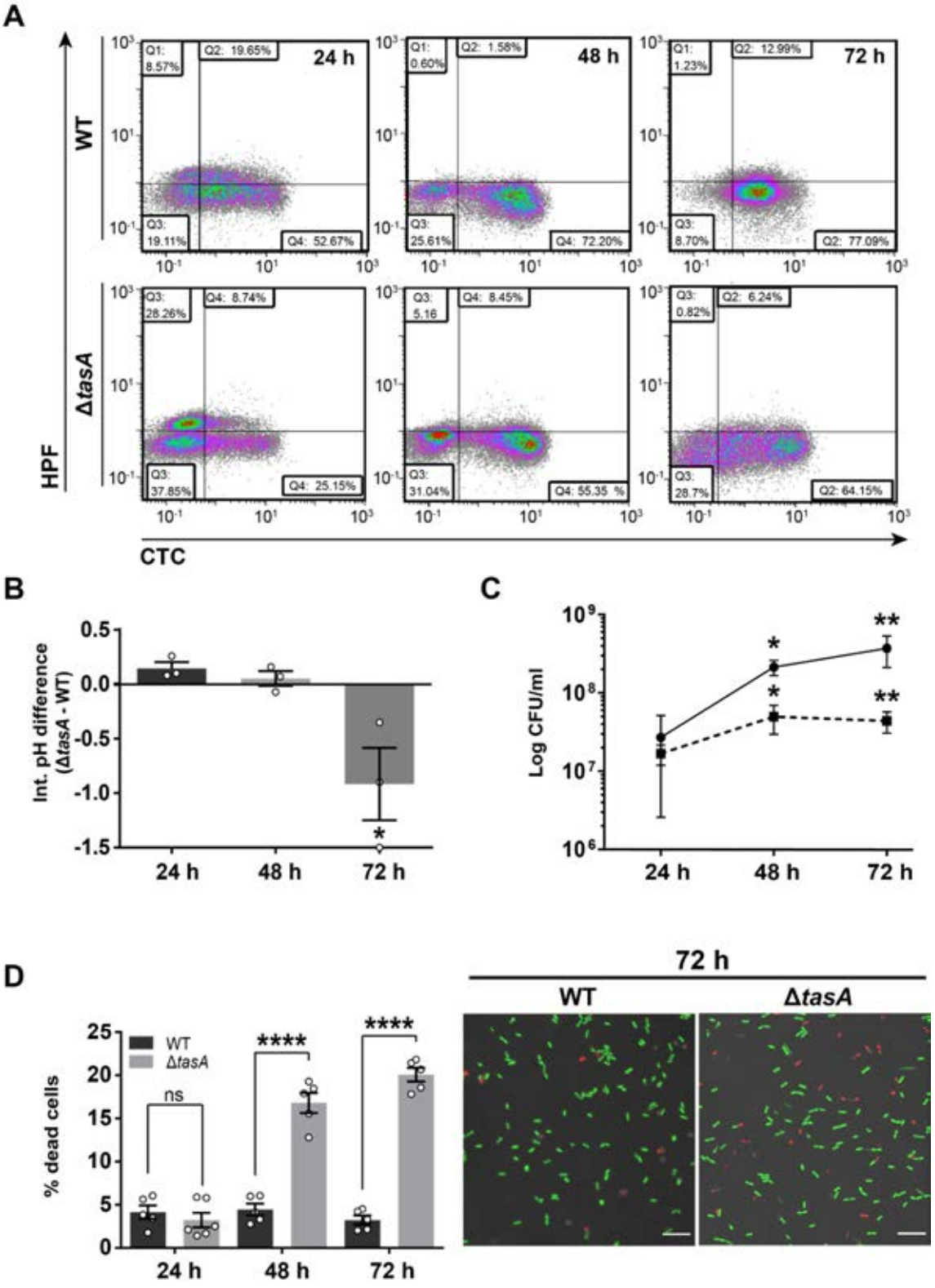

Figure 3.5. Respiration rates and cell viability are compromised in Δ*tasA* cells. A) Flow cytometry density plots of cells double stained with the HPF (Y axis) and CTC (X axis) dyes show that Δ*tasA* cells were metabolically less active (lower proportion of cells reducing CTC) and were under oxidative stress as early as 24 h (higher proportion of HPF-stained cells). **B)** Measurements of intracellular pH show significant cytoplasmic acidification in the Δ*tasA* cells at 72 h. Average values of four biological replicates are shown. Error bars indicate the SEM. Statistical significance was assessed by one-way ANOVA with Tukey multiple comparison test (* p<0.05). **C)** The population dynamics in Δ*tasA* (dashed line) and WT colonies (solid line) grown on MSgg agar at 30 °C showed a difference of nearly one order of magnitude in the Δ*tasA* colony from 48 h. Average values of three biological replicates are shown. Error bars represent the SEM. Statistical significance was assessed by two-sided independent t-tests at each time point (**p value < 0.01 *p value < 0.05). **D)** Left. Quantification of the proportion of dead cells treated with the BacLight LIVE/DEAD viability stain in WT and Δ*tasA* colonies at different time-points reveled a significantly higher population of dead cells at 48 h and 72 h in Δ*tasA* colonies compared to that found in the WT colonies. The points indicate the number of colonies of the corresponding strains examined over three independent experiments. Average values are shown. Error bars represent the SEM. For each experiment and sample, at least three fields-of-view were measured. Statistical significance was assessed via two-tailed independent t-tests at each time-point (****p < 0.0001). Right. Representative confocal microscopy images of fields corresponding to LIVE/DEAD-stained WT or Δ*tasA* samples at 72 h. Scale bars = 10 µm.

Loss of TasA increases membrane fluidity and cell death

The reduction in metabolic activity of Δ*tasA* cells, along with their acidification of the intracellular environment, might be expected to result in reduced bacterial viability. Measurements of the dynamics of viable bacterial cell density, expressed as CFU counts, showed that after 48 h, Δ*tasA* colonies possessed nearly an order of magnitude fewer CFUs than did WT colonies (Fig. 3.5C). These results suggest the hypothesis that Δ*tasA* colonies might exhibit higher rates of cell death than WT colonies. To test this possibility, we analyzed the live and dead sub-populations using the BacLight LIVE/DEAD viability stain and confocal microscopy (Fig. 3.5D right). The proportion of dead cells in Δ*tasA* colonies ranged from between 16.80% (16.80 ± 1.17) and 20.06% (20.06 ± 0.79) compared to 4.45% (4.45 ± 0.67) and 3.24% (3.24 ± 0.51) found in WT colonies at 48 h and 72 h, respectively (Fig. 3.5D left). The significantly higher rate of cell death in Δ*tasA* compared to WT is consistent with the drastically lower bacterial counts found in the Δ*tasA* mutant colonies after 48 hours. To rule out the influence of media composition on the observed phenotype, we performed the same experiments on solid LB medium, on which *B. subtilis* can still form a biofilm, as reflected by the wrinkly phenotype of the colonies (Supplementary Fig. S3.9A). We found that Δ*tasA* colonies exhibited a significantly higher proportion of dead cells at 48 h (17.86 ± 0.92) than did WT colonies (3.88 ± 0.33) (Supplementary Fig. S3.9B). Interestingly, the higher rate of cell death exhibited by the *tasA* mutant was not reproducible when both strains were grown in liquid MSgg with shaking, conditions that promote planktonic growth. WT and Δ*tasA* cultures showed similar growth rates under these conditions (Supplementary Fig. S3.9C), and the proportion of cell death was measured in exponential (Δ*tasA* 0.32 ± 0.03 vs WT 0.78 ± 0.30) or stationary phase cultures (Δ*tasA* 2.31 ± 0.44 vs WT 0.56 ± 0.08) (Supplementary Fig. S3.9D), indicating that the lower viability of Δ*tasA* cells is observable when biofilms form on solid media.

The impaired respiration rates and the acidification of the cellular environment found in the Δ*tasA* cells are causes of cellular stress that can lead to ROS generation[57,58], a well-known trigger of stress-induced cell death[59]. To determine if Δ*tasA* cells possess abnormal ROS levels, we monitored ROS generation using hydroxyphenyl fluorescein (HPF), a fluorescent indicator of the presence of highly reactive hydroxyl radicals. Flow cytometry analysis revealed a larger proportion of HPF-positive cells (which have increased ROS levels) in the Δ*tasA* strain at 24 h compared to the WT proportion (42.38% vs. 28.61%, respectively) (Fig. 3.5A and Supplementary Table 3.1). To test whether this higher ROS production has negative effects on cellular components and functions, we first performed TUNEL assays to fluorescently stain bacterial cells containing DNA strand breaks, a known hallmark of the cell death induced by cellular damage and a frequent outcome of ROS production. At 24 h and 48 h, we found a significantly higher number of fluorescently stained Δ*tasA* cells compared with the number of fluorescently stained WT cells (Fig. 3.6A left and 3.6B left). These results indicated that DNA damage appears to occur not only earlier, but also with a higher frequency, in *tasA* cells than in WT cells. A sizeable number of stained cells was also found at 72 h in the Δ*tasA* colonies, the same time-point at which the TUNEL signal started to increase in the WT colonies (Fig. 3.6A left). The TUNEL signal in the Δ*tasA* cells at this time-point was not significantly different from that of the WT cells (Fig. 3.6B left), probably due to the increased cell death in the Δ*tasA* cells. We next analyzed the existence of caspase-like activity, another hallmark of cell death. Caspases are proteases that participate in apoptotic processes in eukaryotic cells[60]. Functional orthologoues in *Bacillus* are known to regulate general stress response among other processes[61] and interestingly, bacterial CLPs have been reported to regulate also cell death in *E. coli*[62]. The transcriptomics data showed differential expression of genes coding for the caspase-like proteins (CLPs) *clpC* at all times*, clpQ* at 48 and 72 h and *clpY* at 24 h (Supplementary Data 3.1 to 3.3). Bacterial CLPs bind to the same substrates as the eukaryotic caspases involved in apoptosis[62]. Thus, to test the presence of caspase-like activity in *B. subtilis* cells, we used the pan-caspase inhibitor peptide Z-VAD-FMK conjugated to FITC, a general substrate for caspases in eukaryotes that binds to proteins with affinity for these kinds of substrates, increasing the intracellular fluorescence in the presence of caspase activity. Consistent to the RNAseq analysis, a significant increasing proportion of cells that were able to bind the FITC-Z-VAD-FMK substrate was observed in Δ*tasA* at 48 h (14.78 ± 1.53 vs 0.58 ± 0.21) and 72 h (18.60 ± 0.90 vs 0.92 ± 0.19) (Fig. 3.6A right and quantified in 3.6B right), indicating a higher caspase-like activity of the mutant strain at these time-points.

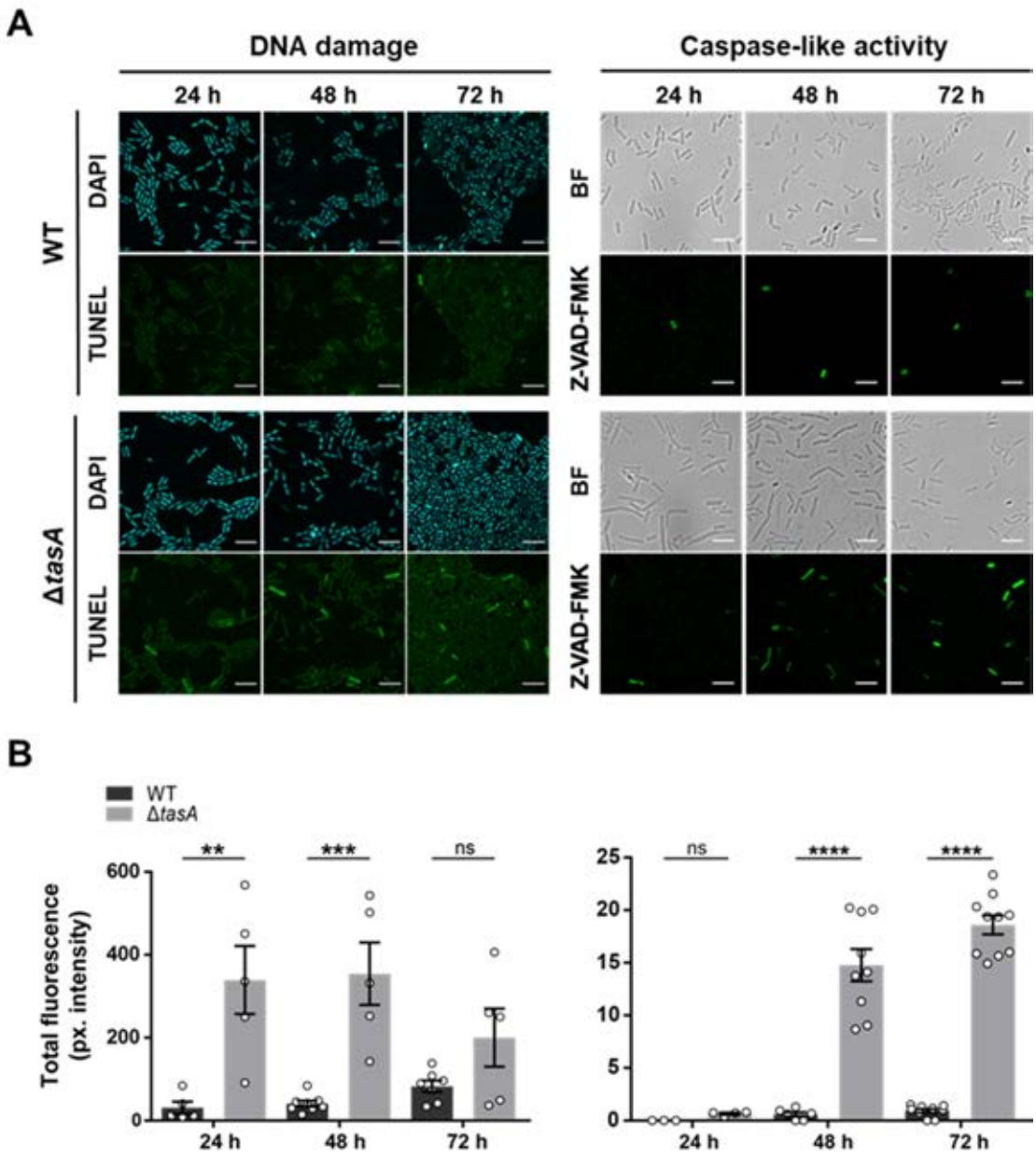

Figure 3.6. The Δ*tasA* cells exhibit higher levels of DNA damage and caspase-like activity. A) Left. CLSM analysis of TUNEL assays revealed significant DNA damage in the Δ*tasA* cells (bottom panels) compared to that in the WT cells (top panels). Cells were counterstained with DAPI DNA stain (top images). Scale bars = 5 µm. **Right**. CLSM analysis of cells stained with the FITC-conjugated caspase substrate inhibitor Z-VAD-FMK indicated significantly higher caspase-like activity in the Δ*tasA* cells (bottom panels) compared to that in the WT cells (top panels) from 48 h. Bright field images (top) are shown for reference. Scale bars = 5 µm. **B) Left**. Quantification of the TUNEL signals in WT and Δ*tasA* colonies. The results showed significant differences in the DNA damage levels between Δ*tasA* and WT cells after 24 and 48 h of growth. The points refer to the number of colonies examined over three independent experiments. For each experiment and sample, at least three fields-of-view were measured. Error bars indicate the SEM. Statistical significance was assessed via two-tailed independent t-tests at each time-point (** p<0.01 *** p<0.001). **Right**. Quantification of cells positive for caspase-like activity (stained with FITC-Z-VAD-FMK). The results showed significant differences in the caspase-like activity levels between Δ*tasA* and WT cells after 48 and 72 h of growth. The points refer to the number of colonies examined over three independent experiments. For each experiment and sample, at least three fields-of-view were measured. Error bars indicate the SEM. Statistical significance was assessed via two-tailed independent t-tests at each time-point (**** p<0.0001).

Then, we examined the cellular membrane potential, another phenotype related to cell death, using the fluorescent indicator tetramethylrhodamine, methyl ester (TMRM). Consistent with all previous analysis, the alterations in the membrane potential of the Δ*tasA* cells were significantly different at all time points compared with the corresponding values for the WT cells (Fig. 3.7A left panel and 3.7B left). As a control, Δ*tasA* cells after 72 h of growth and treated with carbonyl cyanide m-chlorophenyl hydrazine (CCCP), a chemical ionophore that uncouples the proton gradient and can depolarize the membrane, showed a strong decrease in the fluorescence signal (Supplementary Fig. S3.10A and S3.10B). These results indicate that after 48 h (the same time point at which the cell death rate increases and the cell population plateaus in Δ*tasA* colonies) Δ*tasA* cells also exhibit increased membrane hyperpolarization compared with that in the WT cells, a feature that has been linked to mitochondrial-triggered cell death in eukaryotic cells[63-65].

The differences in ROS production, DNA damage level and membrane hyperpolarization between the WT and Δ*tasA* cell populations are consistent with increased cellular stress being the cause of the higher cell death rate observed in Δ*tasA* colonies after 24 h. To test the idea that loss of *tasA* results in increased cellular stress that leads to abnormal cellular physiology and increased cell death, we investigated the level of membrane lipid peroxidation, a chemical modification derived from oxidative stress that subsequently affects cell viability by inducing toxicity and apoptosis in eukaryotic cells[66,67]. Staining with BODIPY 581/591 C11, a fluorescent compound that is sensitive to the lipid oxidation state and localizes to the cell membrane, showed no significant detectable differences in the levels of lipid peroxidation at any time point (Supplementary Fig. S3.17). However, treatment with cumene hydroperoxide (CuHpx), a known inducer of lipid peroxide formation[68], resulted in different responses in the two strains. WT cells showed high reduced/oxidized ratios at 48 and 72 h and, thus, a low level of lipid peroxidation (Fig. 3.7A center panel and Fig. 3.7B center). In contrast, the comparatively lower reduced/oxidized ratios in Δ*tasA* cells at 48 and 72 h indicated increased lipid peroxidation (Fig. 3.7A center panel and Fig. 3.7B center). These results demonstrate that the Δ*tasA* strain is less tolerant to oxidative stress than is the WT strain, and, therefore, is more susceptible to ROS-induced damage.

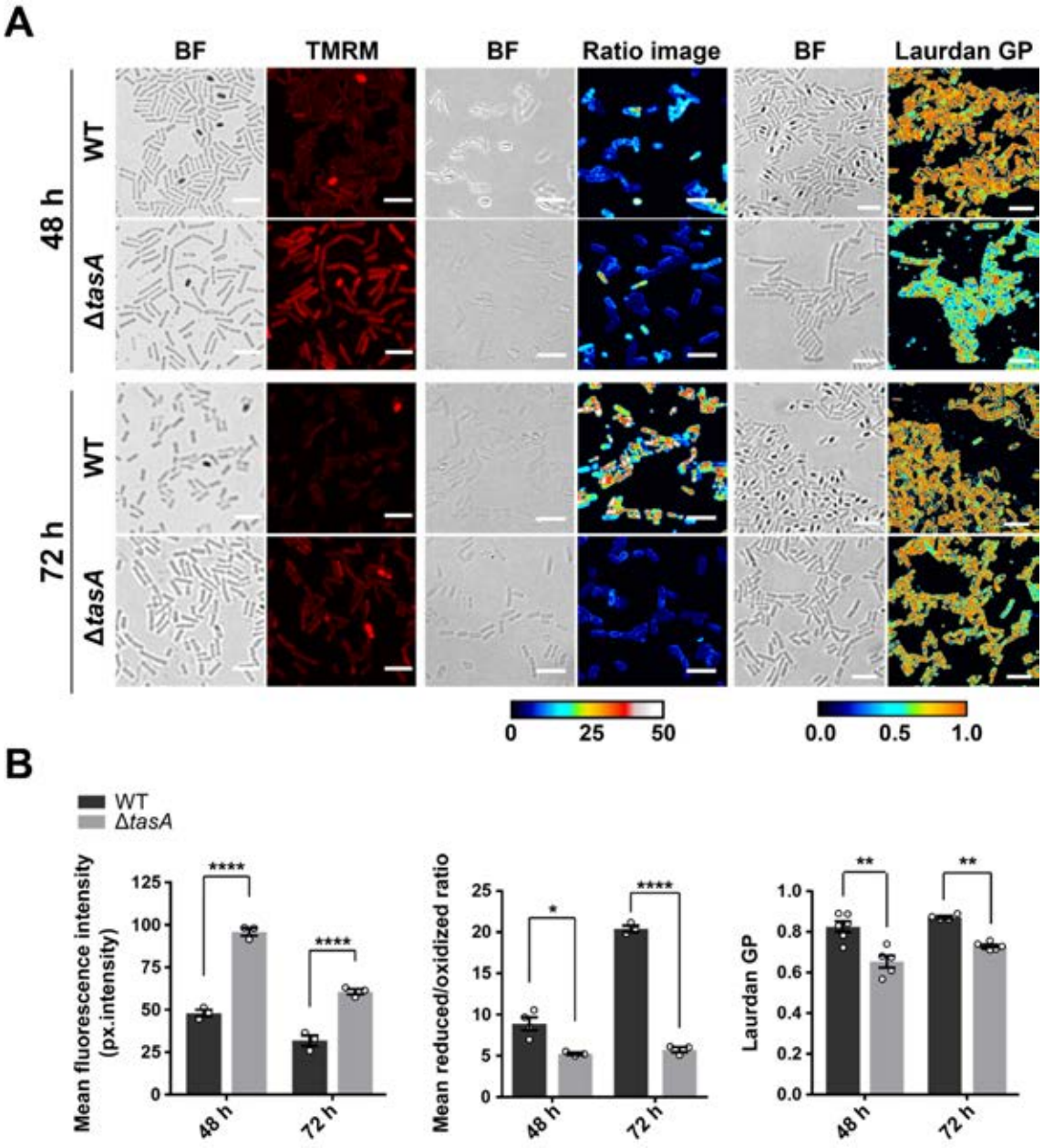

Figure 3.7. Δ*tasA* cells exhibit cytological anomalies. A) Left panel. A TMRM assay of WT and Δ*tasA* cells, located at the top or bottom respectively in each set, showed a decrease in membrane potential in the WT cells, whereas the Δ*tasA* cells exhibited hyperpolarization at 48 and 72 h. **Center panel.** Assessment of the lipid peroxidation levels using BODIPY 581/591 C11 reagent in WT and Δ*tasA* cells after treatment with 5 mM CuHpx and analysis by CLSM. The ratio images represent the ratio between the two states of the lipid peroxidation sensor: reduced channel (590–613 nm emission)/oxidized channel (509–561 nm emission). The ratio images were pseudo-colored depending on the reduced/oxidized ratio values. A calibration bar (from 0 to 50) is located at the bottom of the panel. Confocal microscopy images show that CuHpx treatment was ineffective in the WT strain at 72 h, whereas the mutant strain showed symptoms of lipid peroxidation. **Right panel.** Laurdan GP analyzed via fluorescence microscopy. The images were taken at two different emission wavelengths (gel phase, 432–482 nm and liquid phase, 509–547 nm) that correspond to the two possible states of the Laurdan reagent depending on the lipid environment. The Laurdan GP images represent the Laurdan GP value of each pixel (see Methods section). The Laurdan GP images were pseudo-colored depending on the laurdan GP values. A calibration bar (from 0 to 1) is located at the bottom of the set. The Laurdan GP images show an increase in membrane fluidity (lower Laurdan GP values) in the *tasA* mutant cells at 48 and 72 h. All scale bars are equal to 5 µm. **B) Left.** Quantification of the TMRM signal. **Center.** Quantification of lipid peroxidation. **Right.** Quantification of laurdan GP values. The points represent the number of colonies examined over three independent experiments. Average values are shown. Error bars represent the SEM. For each experiment and sample, at least three fields-of-view were measured. Statistical significance in the TMRM experiments was assessed via two-tailed independent t-tests at each time-point (****$p < 0.0001$). Statistical significance in the lipid peroxidation experiments was assessed via two-tailed independent t-tests at each time-point (****$p < 0.0001$, *p value < 0.05). Statistical significance in the laurdan GP experiments was assessed via two-tailed independent Mann–Whitney tests at each time-point (**p value <0.01).

This finding along with the increased ROS production in Δ*tasA* cells, led us to study the integrity and functionality of the plasma membrane. First, no clear differences in the integrity, shape or thickness of the cell membrane or cell wall were observed via transmission electron microscopy (TEM) of negatively stained thin sections of embedded ΔtasA or WT cells at 24 h and 72 h under our experimental conditions (Supplementary Fig. S3.11). Next, we examined membrane fluidity, an important functional feature of biological membranes that affects their permeability and binding of membrane-associated proteins, by measuring the Laurdan generalized polarization (Laurdan GP)[66,69]. Our results show that the Laurdan GP values were significantly lower at 48 h and 72 h in Δ*tasA* cells compared with the values in WT cells (0.65 ± 0.03 or 0.82 ± 0.03 respectively, at 48 h, and 0.87 ± 0.006 or 0.73 ± 0.007 respectively, at 72 h) (Fig. 3.7A right panel and 3.7B right). These results indicate incremental changes in membrane fluidity, comparable to that resulting from treatment of cells with benzyl alcohol, a known membrane fluidifier (Supplementary Fig. S3.12A top and center panels and Supplementary Fig. S3.12B). Membrane fluidity has been associated with higher ion, small molecule and proton permeability[70,71], which might contribute to the higher concentration of fengycin found in the in cell-free supernatants of Δ*tasA* cultures (Fig. 3.4B). These effects could also explain why Δ*tasA* cells are impaired in energy homeostasis as well as the subsequent effects on the intracellular pH and membrane potential that eventually contribute to cell death.

Mature TasA is required to maintain viable bacterial physiology

TasA is a secreted protein located in the ECM and reaching this specific cellular destination requires the aid of secretion-dedicated chaperones, the translocase machinery and the membrane-bound signal peptidase SipW[72]. It is known that TasA processing is required for assembly of the amyloid fibrils and biofilm formation[35,73]. However, formation of the mature amyloid fibril requires the accessory protein TapA, which is also secreted via the same pathway[36], is present in the mature amyloid fibers and is found on the cell surface[73]. Considering these points, we first wondered whether TapA is involved in the increased cell death observed in the Δ*tasA* mutant. By applying the BacLight LIVE/DEAD viability stain to a Δ*tapA* colony, we found a similar proportion of live to dead cells as that found in the WT colony at 72 h (Fig. 3.8A and 3.8D), suggesting that the *tapA* mutant does not exhibit the cytological alterations and cellular damage that occurs in Δ*tasA* cells.

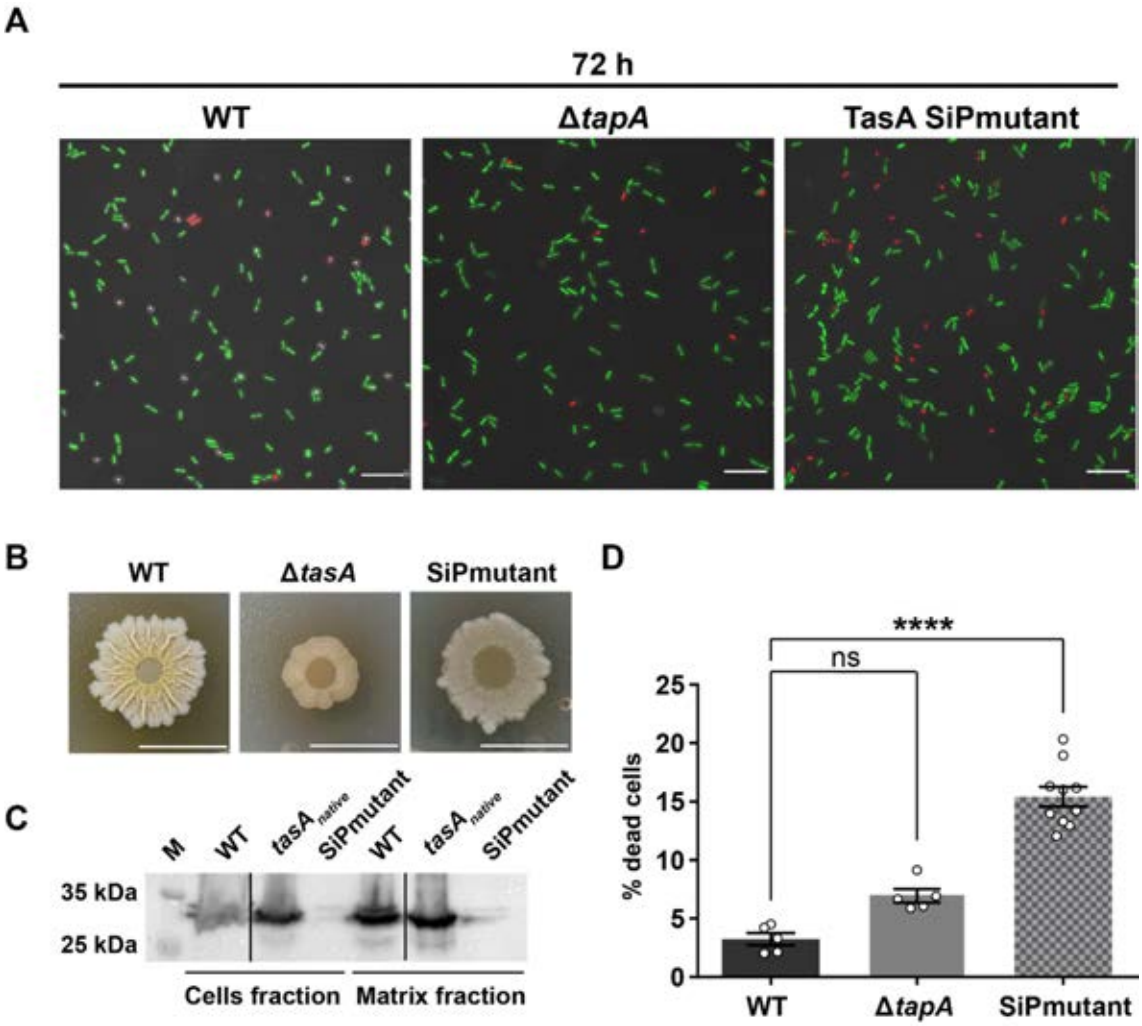

Figure 3.8. Mature TasA is required to stabilize cell viability within the colony. **A)** Representative confocal microscopy images of fields corresponding to LIVE/DEAD-stained WT, Δ*tapA* or signal peptide mutant (SiPmutant, Lys4Ala, Lys5Ala, Lys6Ala) cells at 72 h. Scale bars = 10 µm. **B)** Colony phenotypes of WT, Δ*tasA* and the SiPmutant strains on MSgg agar at 72 h. Scale bars = 1 cm. **C)** Western blot of the cell and matrix fractions of the three strains at 72 h exposed to an anti-TasA antibody. Immunoblot images have been cropped and spliced for illustrative purposes. Black lines over the blot images delineate boundaries of immunoblot splicing. **D)** Quantification of the proportion of dead cells in WT, Δ*tapA*, or SiPmutant colonies at 72 h. The points represent the number of colonies examined over three independent experiments. Error bars represent the SEM. For each experiment and sample, at least three fields-of-view were measured. Statistical significance was assessed via two-tailed independent t-tests at each time-point (****$p < 0.0001$).

Δ*tapA* cells produce a much lower number of TasA fibers but still expose TasA in their surfaces[73]; thus we reasoned that mature TasA is necessary for preserving the cell viability levels observed in the WT strain. To test this possibility, we constructed a strain bearing a mutation in the part of the *tasA* gene that encodes the TasA signal peptide[74]. To generate these constructs, we used the same genetic background and strategy as described in the previous chapter. The strain carrying this construct was designated as "TasA SiPmutant" (for **Si**gnal **P**eptide mutant) and included three amino acid substitutions from the initial lysines of the signal peptide. Specifically, the introduced mutations were Lys4Ala, Lys5Ala, Lys6Ala. The endogenous version of TasA

successfully restored biofilm formation (Supplementary Fig. S3.13A), while the phenotype of SiP mutant on MSgg medium at 72 h was different from those of both the WT and *tasA* mutant strains (Fig. 3.8B and Supplementary Fig. S3.2B). Immunodetection analysis of TasA in fractionated biofilms confirmed the presence of TasA in the cells and ECM fractions from the WT strain and the strain expressing the endogenous version of *tasA* (Fig. 3.8C lanes 1 and 2 and 4 and 5 respectively). However, a faint anti-TasA reactive signal was observed in both fractions of the SiP mutant (Fig. 3.8C). This result indicates that TasA is not efficiently processed in the SiP mutant and, thus, the protein levels in the ECM were drastically lower. The faint signal detected in the cell fraction might be due to the fact that the pre-processed protein is unstable in the cytoplasm and is eventually degraded over time[74]. Consistent with our hypothesis, the levels of cell death in the SiP mutant were significantly different from those of the WT strain (Fig. 3.8A and 3.8D). Taken together, these results rest relevance to TapA to the increase cell death observed in the absence of TasA and indicate that TasA must be processed to preserve the level of cell viability found in WT colonies.

Cells expressing a TasA variant have restored physiological status but impaired biofilm formation

The fact that the Δ*tapA* strain forms altered and fewer TasA fibers but does have normal cell death rates, as well as all the physiological changes associated to the absence of TasA, led us ask whether all these changes might be unrelated the role of TasA in preserving the structural functionality of the biofilm. To test this hypothesis, we performed experiments using one of the strains generated in the results section from the previous chapter. The strain JC81, which expresses the TasA (Lys68Ala, Asp69Ala) variant protein, failed to fully restore the WT biofilm formation phenotype and colony morphology (Fig. 3.9A, Supplementary Fig. S3.2B and Supplementary Fig. S3.13A). Immunodetection analysis of TasA in fractionated biofilms confirmed the presence of the mutated protein in the cells and in the ECM (Fig. 3.9B lanes 1-4, Supplementary Fig. S3.13B left and right, lane 3). Tandem mass spectrometry analysis revealed that the mutated protein found in the ECM corresponded to the mature form of TasA (Supplementary Fig. S3.14A, left, lane 6 and Supplementary Fig. S3.14A right), indicating exclusively a malfunction in the protein's structural role in proper ECM assembly. Electron microscopy coupled to immunodetection with anti-TasA and immunogold-conjugated secondary antibodies showed the presence of a dense mass of extracellular material in JC81 cells with an absence of well-defined TasA fibers, as opposed to WT cells, in which we also observed a higher number of gold particles, indicative of the higher reactivity of the sample (Supplementary Fig. S3.14B left and

center panels). Accordingly, JC81 was reverted to a physiological status comparable to that of the WT strain. This feature was demonstrated by similar expression levels of genes encoding factors involved in the production of secondary metabolites (i.e., *ppsD*, *albE*, *bacB*, *srfAA*) or acetoin (*alsS*), indicating comparable metabolic activities between the two strains (Fig. 3.9C). Further evidence confirmed the restoration of the metabolic status in JC81. First, similar proportions of WT and JC81 cells expressing YFP from the fengycin operon promoter were detected after 72 h of growth via flow cytometry analysis (Fig. 3.9D, green curve). In agreement with these findings, there were no differences in the proportions of cells respiring or accumulating ROS or in the intracellular pH values between the JC81 and WT strains (Fig. 3.9E and Fig. 3.9F). Consistently, the population dynamics of JC81 resembled that of the WT strain (Fig. 3.9G), and, as expected, its level of cell death was comparable to that of the WT strain (Fig. 3.9H). Finally, there were no differences in any of the examined parameters related to oxidative damage and stress-induced cell death (i.e., DNA damage and caspase-like activity, Supplementary Fig. S3.15; membrane potential, susceptibility to lipid peroxidation and membrane fluidity, Supplementary Fig. S3.16) between JC81 and WT cells, and the mutated allele complemented the sporulation defect observed in the ECM mutants (Supplementary Fig. S3.6). To further confirm these results, we performed a viability assay in a mixed Δ*tasA* and Δ*eps* colony co-inoculated at a 1:1 ratio, and we found that, despite the ability of the mixed colony to rescue the wrinkly phenotype typical of a WT colony (Supplementary Fig. S3.18A, top), the proportion of cell death is significantly higher than that observed in WT cells at 48 h (10.39 ± 1.20) and 72 h (14.04 ± 0.72) (Supplementary Fig. S3.18B). In addition, exogenous TasA did not revert the colony morphology phenotype of Δ*tasA* cells on solid MSgg (Supplementary Fig. S3.19A) or the increased cell death rate observed in the Δ*tasA* strain (Supplementary Fig. S3.19B). These results show that the extracellular TasA provided by the Δ*eps* strain is sufficient to complement the ECM assembly and biofilm formation defects but not to prevent cell death, similar to the effects of exogenous TasA supplementation. Thus, TasA must be produced by the cells to exert the physiological function and prevent premature cell death. Interestingly, a Δ*sinI* strain, which is mutant for the *sinI* anti-repressor that inhibits *sinR*, and therefore, has strong repression of ECM genes and is unable to assemble biofilms (Supplementary Fig. S3.20A, bottom), showed similar levels of cell death as the WT strain at all times (1.53 ± 0.25 at 48 h and 2.51 ± 0.50 at 72 h) (Supplementary Fig. S3.18B). This effect might reflect that even a basal amount of TasA[75] in the cell membrane is sufficient to prevent cell death is insufficient to assemble a proper ECM, confirming that indeed, cells lacking a structured ECM do not exhibit the physiological changes observed in cells lacking TasA.

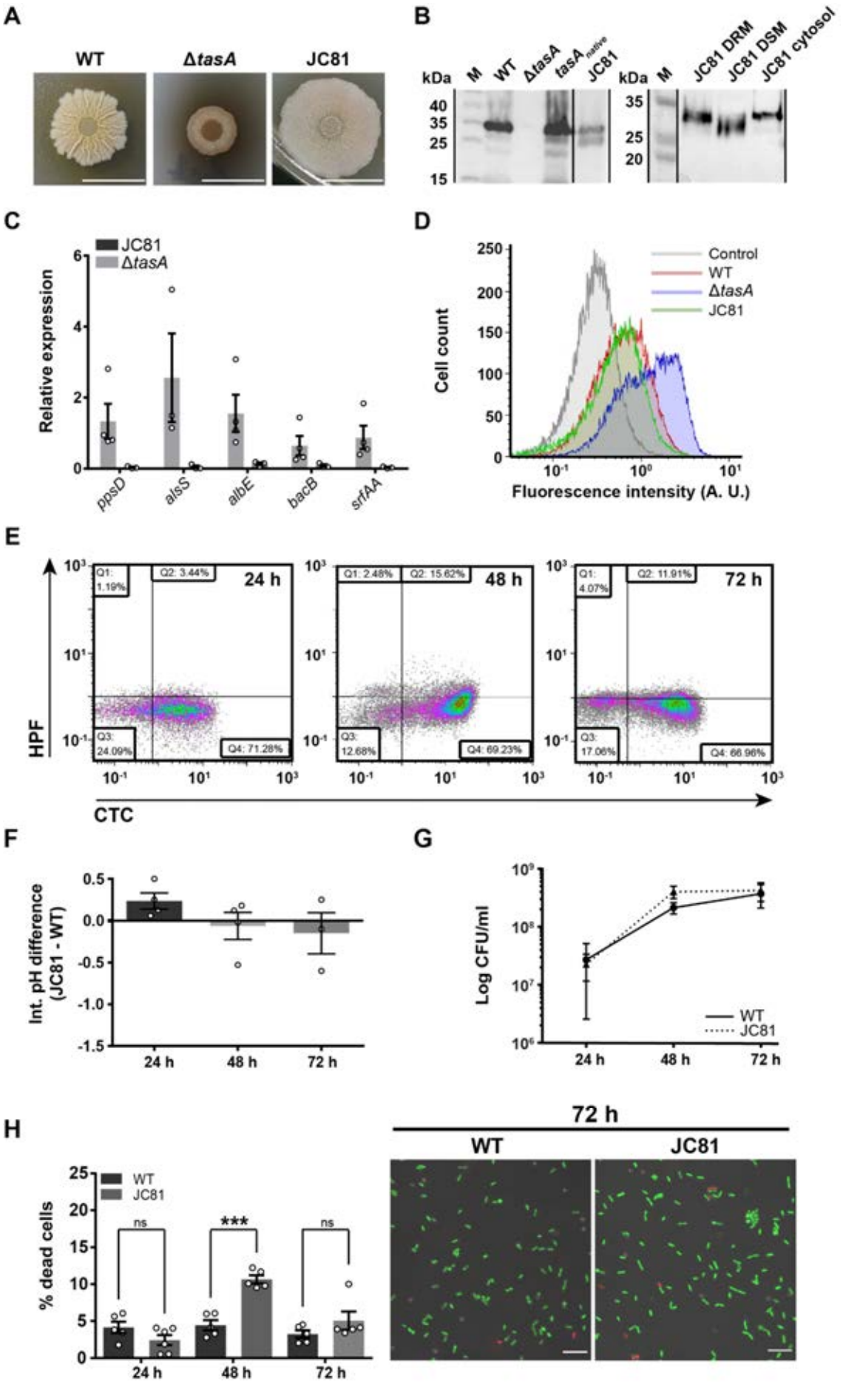

Figure 3.9. A TasA variant fails to restore biofilm formation in *tasA*-deleted cells but rescues their physiological status. A) Colony phenotypes of the three strains on MSgg agar at 72 h. Scale bars = 1 cm. **B)** A western blot of the cell (left) and membrane fractions (right) at 72 h exposed to an anti-TasA antibody. Immunoblot images have been cropped and spliced for illustrative purposes. Black lines over the blot images delineate boundaries of immunoblot splicing. **C)** Relative expression levels of *ppsD*, *alsS*, *albE*, *bacB*, and *srfAA* genes in JC81 compared to the WT strain. Average values of at least three biological replicates are shown with error bars representing the SEM. **D)** Flow cytometry analysis of cells expressing the promoter of the fengyncin production operon in the WT, Δ*tasA* and JC81 strains at 72 h. A non-fluorescent negative control corresponding to the unlabeled WT strain at 72 h is shown (gray). **E)** Density plots of cells double stained with the HPF (Y axis) and CTC (X axis) dyes show that JC81 behaved similarly to the WT strain. **F)** Intracellular pH measurements of the WT and JC81 strains. Average values of four biological replicates are shown. Error bars represent the SEM. **G)** Population dynamics (CFU counts) in WT and JC81 colonies. Average values of four biological replicates are shown. Error bars represent the SEM. **H)** Left. Quantification of the proportion of dead cells in WT and JC81 colonies. The points correspond to the number of colonies of the corresponding strains examined over three independent experiments. Average values are shown. Error bars represent the SEM. For each experiment and sample, at least three fields-of-view were measured. Statistical significance was assessed via two-tailed independent t-tests at each time-point (***p value < 0.001). Right. Representative confocal microscopy images of fields corresponding to LIVE/DEAD-stained WT or JC81 cells at 72 hours. Scale bars = 10 µm.

Taken together, these findings assign TasA complementary functions related to the stabilization of the cellular physiology during normal colony development that prevent premature cell death, a role beyond the well-known structural function of amyloid proteins in biofilm ECMs.

The TasA variant impairs *B. subtilis* survival and fitness on the phylloplane

Our analysis of the intrinsic physiological changes in Δ*tasA* cells showed how the absence of TasA leads to the accumulation of canonical signs of cellular damage and stress-induced cell death, a physiological condition typical of stationary phase cells. These observations help to reconcile two *a priori* contradictory features of *B. subtilis* ecology on plant leaves: the reduced persistence of the Δ*tasA* mutant on the melon phylloplane versus its ability to efficiently exert biocontrol against the fungus *P. xanthii*, which occurs via overproduction of fengycin and other antimicrobial molecules. Following this line of thought, we predicted that the JC81 strain, which expresses a version of TasA that is unable to restore biofilm formation but preserves the physiological status of the cells, would show overall signs of reduced fitness on melon leaves. The JC81 cells retained their initial ability to adhere to melon leaves (Fig. 3.1A); however, their persistence decreased (Fig. 3.1B) and their colonization showed a pattern somewhat intermediate between those of the WT and Δ*tasA* strains (Fig. 3.1C). In agreement with our prediction, the reduced fitness of this strain resulted in a failure to manage *P. xanthii* infection (Fig. 3.1D). Thus, we conclude that the ECM, by means of the amyloid protein TasA, is required for normal colonization and persistence of *B. subtilis* on the phyllosphere. These ecological features depend on at least two complementary roles of TasA: one role related to ECM assembly and a new proposed role in the preservation of the physiological status of cells and the prevention of premature cell death.

DISCUSSION

The ECM provides cells with a myriad of advantages, such as robustness, colony cohesiveness, and protection against external environmental stressors[9,10,27]. Studies of *B. subtilis* biofilms have revealed that the ECM is mainly composed of polysaccharides[31] and the proteins TasA and BslA[27,32]. TasA is a confirmed functional amyloid that provides structural support to the biofilm in the form of robust fibers[33]. A recent study demonstrated that there is heterogeneity in the secondary structure of TasA; however, in biofilms, its predominant conformation is in the form of stable fibers enriched in β-sheets[34]. In this study, we demonstrate that in addition to its structural role in ECM assembly, TasA is also required for normal colony development – both of which are functions that contribute to the full fitness of *Bacillus* cells on the phylloplane.

The physiological alterations observed in a Δ*tasA* null strain reflect a process of progressive cellular deterioration characteristic of senescence[76-78], including early activation of secondary metabolism, low energy metabolic activity, and accumulation of damaged molecular machinery that is required for vital functions. Indeed, it has been previously demonstrated that such metabolic changes can trigger cell death in other bacterial species, in which over-acidification of the cytoplasm eventually leads to the activation of cell death pathways[55]. Interestingly, cytoplasmic acidification due to the production of acetic acid has been linked to higher ROS generation and accelerated aging in eukaryotes[79]. As mentioned throughout this study, ROS generation leads to ongoing DNA damage accumulation, phospholipid oxidation, and changes in cell membrane potential and functionality, all of which are major physiological changes that eventually lead to declines in cellular fitness and, ultimately, to cell death[80,81,82]. The fact that we could restore the physiological status of *tasA* null mutant cells by ectopically expressing a mutated TasA protein incapable of rescuing biofilm formation permitted us to separate two roles of TasA: i) its structural function, necessary for ECM assembly; and ii) its cytological functions involved in stabilizing cellular physiology and preventing premature cell death. This finding led us to predict that this new function might be related to the presence of TasA on the cell surface, rather than to that in the fibers, and this prediction is supported by further evidence. First, TasA can preferentially interact with model bacterial membranes, which impacts fiber assembly[83]. Second, TasA fibers are located and attached to the cell surface via a proposed interaction with TapA, which forms foci that seem to be present in the cell wall[73]. Interestingly, TapA has been recently characterized as a two-domain, partially disordered protein[84]. Disordered domains can be flexible enough to interact with multiple partners[85,86], suggesting a similar mechanism

for TapA: the N-terminal domain might be involved in the interaction with other protein partners, whereas the C-terminal disordered domain might anchor the protein to the cell surface. All of these observations lead us to speculate that TasA may drive the stabilization of domains on the cell surface either by directly interacting with certain phospholipids or with the peptidoglycan, or indirectly via interactions with additional proteins. This alteration at the surface level might cause, given the differences in the expression levels of many genes involved in the respiratory process (Supplementary Data 1 to 3), the impaired respiration observed in Δ*tasA* cells, which could lead to increased ROS generation, leading to the full range of transcriptional and cytological alterations found in the *tasA* mutant over the course of time.

The physiological alterations observed in the Δ*tasA* strain have ecological implications. The intrinsic stress affecting the mutant cells reduced their ability to survive in natural environments; however, paradoxically, their higher induction of secondary metabolism seemed to indirectly and efficiently target fungal pathogens. This could explain why Δ*tasA* cells, which show clear signs of stress, display efficient biocontrol properties against *P. xanthii*. However, the sharp time-dependent decrease in the Δ*tasA* population on leaves suggests that its antifungal production could be beneficial during short-term interactions, but insufficient to support long-term antagonism unless there is efficient colonization and persistence on the plant surface. In this scenario, the deletion of *tasA* has a strong negative effect on bacterial cells, as we have demonstrated how a Δ*tasA* strain is more susceptible to ROS-induced damage (Fig. 3.7A center panel and 3.7B center graph), especially in the phyllosphere, where microbial cells are continuously subjected to different type of stresses, including oxidative stress[87]. We previously speculated that biofilm formation and antifungal production were two complementary tools used by *Bacillus* cells to efficiently combat fungi. Our current study supports this concept, but also enhances our understanding of the roles of the different ECM components. More specifically, we demonstrated that the amyloid protein TasA is one of the most important bacterial factors during the initial attachment and further colonization of the plant host, as it is necessary for the establishment of the bacterial cells over the plant leaves and for the maintenance of the normal cellular structure. The fact that the naturally occurring overexpression of the *eps* genes in the Δ*tasA* is unable to revert the adhesion defect of this strain downplay the importance of the EPS during the early establishment of physical contact. These observations are more consistent with a role for the EPS, along with BslA, in providing biofilms with protection against external stressors[31,88]. A similar role for a functional amyloid protein in bacterial attachment to plant surfaces was found for the *Escherichia coli* curli protein. Transcriptomic studies

showed induction of curli expression during the earlier stages of attachment after the cells came into contact with the plant surface, and a curli mutant strain was defective in this interaction[89,90]. The distinct morphological and biochemical variations typical of amyloids make them perfect candidates for modulating cellular ecology. The observation that Δ*tasA* cells are incapable of colonization in the rhizosphere[91] clearly indicates the need for more in-depth investigation into these two distinctive ecological niches to understand the true roles of specific bacterial components. In addition to demonstrating enhanced production of antifungal compounds, our study revealed additional features that might contribute to the potency of stressed *Bacillus* cells in arresting fungal growth, in particular the overproduction of acetoin via increased expression of the *alsS* and *alsD* genes. Acetoin is a volatile compound produced via fermentative and overflow metabolism, and it has been demonstrated to mediate communication between beneficial bacteria and plants by activating plant defense mechanisms either locally or over long distances in a phenomenon known as induced systemic resistance (ISR)[92,93].

In summary, we have proven that the amyloid protein TasA participates in the proper maturation of *Bacillus* colonies, a function that, along with its previously reported role in ECM assembly, contributes to long-term survival, efficient colonization of the phylloplane, and a competitive advantage mediated by antifungal production. The absence of TasA leads to a series of physiological changes, including an arrest of cell differentiation[9] that paradoxically increases the competitiveness of the mutant cells during short-term interactions via their ability to adapt to stress and their cellular response to early maturation. However, lack of TasA reduces cell fitness during mid- to long-term interactions via increased intrinsic cellular stress and the absence of a structured ECM, both of which limit the adaptability of the cells to the stressful phylloplane.

MATERIAL AND METHODS

Bacterial strains and culture conditions

The bacterial strains used in this study are listed in supplementary table 3.2. Bacterial cultures were grown at 37 ºC from frozen stocks on Luria-Bertani (LB: 1% tryptone (Oxoid), 0.5% yeast extract (Oxoid) and 0.5% NaCl) plates. Isolated bacteria were inoculated in the appropriate medium. The biotrophic fungus *Podosphaera xanthii* was grown at 25 ºC from a frozen stock on cucumber cotyledons and maintained on them until inoculum preparation. Biofilm assays were performed on MSgg medium: 100 mM morpholinepropane sulphonic acid (MOPS) (pH 7), 0.5% glycerol, 0.5% glutamate, 5 mM potassium phosphate (pH 7), 50 µg/ml tryptophan, 50 µg/ml phenylalanine, 50 µg/ml threonine, 2 mM $MgCl_2$, 700 µM $CaCl_2$, 50 µM $FeCl_3$, 50 µM $MnCl_2$, 2 µM thiamine, 1 µM $ZnCl_2$. For the *in vitro* lipopeptide detection and assays with cell-free supernatants, medium optimized for lipopeptide production (MOLP) was used and prepared as previously described[94]. For cloning and plasmid replication, *Escherichia coli* DH5α was used. *Escherichia coli* BL21(DE3) was used for protein purification. *Bacillus subtilis* 168 is a domesticated strain used to transform the different constructs into *Bacillus subtilis* NCIB3610. The antibiotic final concentrations for *B. subtilis* were: MLS (1 µg/ml erythromycin, 25 µg/ml lincomycin); spectinomycin (100 µg/ml); tetracycline (10 µg/ml); chloramphenicol (5 µg/ml); kanamycin (10 µg/ml).

Strain construction

All of the primers used to generate the different strains are listed in Supplementary table 3.3. To build the strain YNG001, the promoter of the fengycin operon was amplified with the Ppps-ecoRI.F and Ppps-HindIII.R primer pair. The PCR product was digested with EcoRI and HindIII and cloned into the pKM003 vector cut with the same enzymes. The resulting plasmid was transformed by natural competence into *B. subtilis* 168 replacing the *amyE* neutral locus. Transformants were selected via spectinomycin resistance. The same plasmid was used to build the strain YNG002 by transforming a Δ*tasA* strain of *B. subtilis* 168. The plasmid was transformed into the WT (DR8) and Δ*tasA* (DR9) *B. subtilis* 168 strains.

Strain YNG003 was constructed using the primers amyEUP-Fw, amyEUP-Rv, Ppps-Fw, Ppps-Rv, Yfp-Fw, Yfp-Rv, Cat-Fw. Cat-Rv, amyEDOWN-Fw, amyEDOWN-Rv to separately amplify the relevant fragments. The fragments were then joined using the NEB builder HiFi DNA Assembly Master Mix (New England Biolabs). The construct was

made using pUC19 digested with BamHI as the vector backbone. The final plasmid was then transformed into *B. subtilis* 168 replacing *amyE,* and transformants were selected via chloramphenicol resistance.

Strain JC97 was generated using the primers bslAUP-Fw, bslAUP-Rv, Spc-Fw, Spc-Rv, bslADOWN-Fw and bslADOWN-Rv and XbaI-digested pUC19 as the vector backbone. The fragments were assembled using NEB Builder HiFi DNA Assembly Master Mix. Strains JC70, JC81 and JC149 were constructed via site-directed mutagenesis (QuickChange Lightning Site Directed Mutagenesis Kit – Agilent Technologies). Briefly, the *tapA* operon (*tapA-sipW-tasA*), including its promoter, was amplified using the primers TasA_1_mutb and YSRI_2, and the resulting product was digested with BamHI and SalI and cloned into the pDR183 vector[95]. Next, the corresponding primers (see suppl. Table 6A) were used to introduce the alanine substitution mutations into the desired positions of the TasA amino acid sequence. The entire plasmid was amplified from the position of the primers using Pfu DNA polymerase. The native plasmid, which was methylated and lacked the mutations, was digested with DpnI enzyme. The plasmids containing the native version of TasA (JC70) or the mutated versions (JC81 and JC149) were transformed into the *B. subtilis* 168 Δ*(tapA-sipW-tasA)* strain replacing the *lacA* neutral locus. Genetic complementation was observed in strain JC70 as a control. Transformants were selected via MLS resistance.

Plasmid pDFR6 (pET22b-*tasA*), which contains the open reading frame of the *tasA* gene from *B. subtilis* NCIB3610 without the signal peptide or the stop codon, was constructed as previously described[73]

All of the *B. subtilis* strains generated were constructed by transforming *B. subtilis* 168 via its natural competence and then using the positive clones as donors for transferring the constructs into *Bacillus subtilis* NCIB3610 via generalized SPP1 phage transduction[96].

Biofilm assays

To analyze colony morphology under biofilm-inducing conditions, we used a method described elsewhere[97]. Briefly, the bacterial strains were grown on LB plates overnight at 37 °C, and the resulting colonies were resuspended in sterile distilled water at an OD_{600} of 1. Next, 2-µl drops of the different bacterial suspensions were spotted on MSgg or LB agar (depending on the assay) agar plates and incubated at 30 °C. Colonies were removed at the appropriate time points (24, 48 and 72 h) for the different analyses.

For the Δ*eps*-Δ*tasA* co-inoculation assay, colonies were resuspended in sterile distilled water and mixed at a final OD_{600} of 1. Next, the bacterial suspension was inoculated onto MSgg agar plates and incubated as described above. For the external complementation assay using purified TasA, a drop containing 80 µg of protein was spotted onto MSgg agar plates and allowed to dry. Next, Δ*tasA* cells were inoculated on top of the dried drop and incubated as described above.

For the CFU counts of the colonies from the different strains, 24-, 48- and 72-hour-old colonies grown on MSgg agar plates were removed, resuspended in 1 ml of sterile distilled water, and subjected to mild sonication (three rounds of 20 second pulses at 20% amplitude). The resulting suspensions were serially diluted and plated to calculate the CFUs per colony (total CFU). To estimate the CFUs corresponding to sporulated cells (CFU endospores), the same dilutions were heated at 80 °C for 10 minutes and plated. The sporulation percentage was calculated as (CFU endospores/total CFU)*100.

Biofilm fractionation

To analyze the presence of TasA in the different strains, biofilms were fractionated into cells and ECM as described elsewhere[97], and both fractions were analyzed separately. Briefly, 72-hour-old colonies grown under biofilm-inducing conditions on MSgg-agar plates were carefully lifted from the plates and resuspended in 10 ml of MS medium (MSgg broth without glycerol and glutamate, which were replaced by water) with a 25 $^{5/8}$ G needle. Next, the samples were subjected to mild sonication in a Branson 450 digital sonifier (4-5 5 seconds pulses at 20% amplitude) to ensure bacterial resuspension. The bacterial suspensions were centrifuged at 9000 g for 20 minutes to separate the cells from the extracellular matrix. The cell fraction was resuspended in 10 ml of MS medium and stored at 4 °C until further processing. The ECM fraction was filtered through a 0.22 µm filter and stored at 4 °C.

For protein precipitation, 2 ml of the cell or ECM fractions were used. The cell fraction was treated with 0.1 mg/ml lysozyme for 30 minutes at 37 °C. Next, both fractions were treated with a 10% final concentration of trichloroacetic acid and incubated in ice for 1 h. Proteins were collected by centrifugation at 13,000 g for 20 minutes, washed twice with ice-cold acetone, and dried in an Eppendorf Concentrator Plus 5305 (Eppendorf).

Protein expression and purification

Protein was expressed and purified as previously described[98] with some changes. Briefly, freshly transformed BL21(DE3) *E. coli* colonies were picked, resuspended in 10 mL of liquid LB with 100 µg/mL of ampicillin and incubated O/N at 37 °C with shaking.

The next day, the pre-inoculum was used to inoculate 500 mL of LB supplemented with ampicillin, and the culture was incubated at 37 °C until an OD_{600} of 0.7-0.8 was reached. Next, the culture was induced with 1 mM isopropyl β-D-1-thiogalactopyranoside (IPTG) and incubated O/N at 30 °C with shaking to induce the formation of inclusion bodies. The next day, cells were harvested via centrifugation (5000 G, 15 minutes, 4 °C) resuspended in buffer A (Tris 50mM, 150mM NaCl, pH8), and then centrifuged again. The pellets were kept at -80 °C until purification or processed after 15 minutes. After thawing, cells were resuspended in buffer A, sonicated on ice (3x45 sec, 60% amplitude) and centrifuged (15000 G, 60 min., 4 °C). The supernatant was discarded, as proteins were mainly expressed in inclusion bodies. The pellet was resuspended in buffer A supplemented with 2 % Triton X-100, incubated at 37 °C with shaking for 20 minutes and centrifuged (15000 G, 10 min., 4 °C). The pellet was extensively washed with buffer A, centrifuged (15000 G for 10 min, 4 °C), resuspended in denaturing buffer (Tris 50 mM NaCl 500 mM, 6 M GuHCl) and incubated at 60 °C overnight until complete solubilization occured. Lysates were clarified via sonication on ice (3x45sec, 60% amplitude) and centrifugation (15000 G, 1h, 16 °C) and were then passed through a 0.45-µm filter prior to affinity chromatography. Protein was purified using an AKTA Start FPLC system (GE Healthcare). Soluble inclusion bodies were loaded into a HisTrap HP 5 mL column (GE Healthcare) previously equilibrated with binding buffer (50 mM Tris, 0.5 M NaCl, 20 mM imidazole, 8 M urea, pH 8). Protein was eluted from the column with elution buffer (50 mM Tris, 0.5 M NaCl, 500 mM imidazole, 8 M urea, pH 8). After the affinity chromatography step, the purified protein was loaded into a HiPrep 26/10 desalting column (GE Healthcare), and the buffer was exchanged to Tris 20 mM, NaCl 50 mM to perform the corresponding experiments.

SDS-PAGE and immunodetection

Precipitated proteins were resuspended in 1x Laemmli sample buffer (BioRad) and heated at 100 °C for 5 minutes. Proteins were separated via SDS-PAGE in 12% acrylamide gels and then transferred onto PVDF membranes using the Trans-Blot Turbo Transfer System (BioRad) and PVDF transfer packs (BioRad). For immunodetection of TasA, the membranes were probed with anti-TasA antibody (rabbit) used at a 1:20,000 dilution in Pierce Protein-Free (TBS) blocking buffer (ThermoFisher). A secondary anti-rabbit IgG antibody conjugated to horseradish peroxidase (BioRad) was used at a 1:3,000 dilution in the same buffer. The membranes were developed using the Pierce ECL Western Blotting Substrate (ThermoFisher).

Mass spectrometry analysis of protein bands

The sequence corresponding to the band of the ECM fraction of JC81 (fig. S14A) was identified via tandem mass spectrometry using a “nano” ion trap system (HPLC-ESI-MS/MS). Briefly, the bands obtained after electrophoresis were cut out, washed and destained. Subsequently, the disulfide bridges were reduced with DTT, cysteines were alkylated via the use of iodoacetamide, and in-gel trypsin digestion was performed to extract the peptides corresponding to the protein samples. This entire process was carried out automatically using an automatic digester (DigestPro, Intavis Bioanalytical Instruments). The peptides were then concentrated and desalted using a capture column C18 ZORBAX 300SB-C18 (Agilent Technologies, Germany), 5x0.3 mm, with 5-µm particle diameter and 300-Å pore size, using a gradient of 98% H2O:2% acetonitrile (ACN)/0.1% formic acid (FA) with a flow rate of 20 µL/min for 6 min. The capture column was connected in line to a ZORBAX 300SB-C18 analytical column (Agilent Technologies), 150x0.075 mm, with a 3.5-µm particle diameter and 300-Å pore size, through a 6-port valve. Elution of the samples from the capture column was performed over a gradient using FA 0.1% in water as the mobile phase A and FA 0.1% in ACN 80%/water 20% as the mobile phase B. The LC system was coupled through a nanospray source (CaptiveSpray, Bruker Daltonics) to a 3D ion trap mass spectrometer (amaZon speed ETD, Bruker Daltonics) operating in positive mode with a capillary voltage set to 1500 V and a sweep range: m/z 300-1,500. "Data-dependent" acquisition was carried out in automatic mode, which allowed the sequential collection of an MS spectrum in "full scan" (m / z 300_1400) followed by an MS spectrum in tandem via CID of the eight most abundant ions. For identification, the software ProteinScape 3 (Bruker Daltonics) coupled to the search engine Mascot 3.1 (Matrix Science) was used, matching the MS/MS data against the Swiss-Prot and NCBInr databases.

Bioassays on melon leaves

Bacterial strains were grown in liquid LB at 30 ºC overnight. The cells in the cultures were washed twice with sterile distilled water. The bacterial cell suspensions were adjusted to the same OD_{600} and sprayed onto leaves of 4- to 5-week-old melon plants. Two hours later, a suspension of *P. xanthii* conidia was sprayed onto each leaf at a concentration of $4–10x10^4$ spores/ml. The plants were placed in a greenhouse or in a growth chamber at 25 °C with a 16 h photoperiod, 3800 lux and 85% RH. The severity of the symptoms was evaluated as the percentage of leaf covered by powdery mildew, as previously described[99]. Briefly, the entire leaf area and the powdery mildew damage area were

measured using FiJi[100], and the ratio of infection was calculated using the formula [(damage area/leaf area)*100].

The persistence of bacterial strains on plant leaves was calculated via CFU counts performed over the twenty-one days following inoculation. Three different leaves from three different plants were individually placed into sterile plastic stomacher bags and homogenized in a lab blender (Colworth Stomacher-400, Seward, London, UK) for 3 min in 10 ml of sterile distilled water. The leaf extracts were serially diluted and plated to calculate the CFUs at each time point. The plates were incubated at 37 °C for 24 h before counting.

The adhesion of bacterial cells to melon leaves was estimated by comparing the number of cells released from the leaf versus the cells attached to the surface. The surfaces of individual leaves were placed in contact with 100 ml of sterile distilled water in glass beakers and, after 10 minutes of stirring (300 rpm), the water and leaf were plated separately. The leaves were processed as described above. Adhesion was calculated as the ratio: (water CFU/total CFU)*100. The data from all of the different strains were normalized to the result of the WT strain (100% adhesion).

Antifungal activity of cell-free supernatant against Podosphaera xanthii

B. subtilis strains were grown for 72 h at 30 ºC in MOLP medium, and the supernatant was centrifuged and filtered (0.22 µm). One-week-old cotyledons were disinfected with 20% commercial bleach for 30 seconds and then submerged two times in sterile distilled water for 2 minutes and then air dried. 10-mm discs were excised with a sterilized cork borer, incubated with cell-free supernatants for 2 h, and then left to dry. Finally, the discs were inoculated with *P. xanthii* conidia as previously described[101].

Lipopeptides production analysis

For the *in vitro* lipopeptide detection, bacteria were grown in MOLP for 72 h. The cultures were centrifuged, and the supernatants were filtered (0.22 µm) prior to analysis via MALDI-TOF/TOF.

For the analysis of lipopeptide production in colonies, WT or Δ*tasA* colonies were grown on MSgg plates for 72 h at 30 °C. For the cell fractions, whole colonies were resuspended as described above in 1 mL of sterile distilled water and centrifuged at 5000 G for 5 minutes. The pellets were then resuspended in 1 ml of methanol and sonicated in a bath for 10 minutes. Cells were harvested via centrifugation at 5000 G for 5 minutes, and the supernatant containing the solubilized lipopeptides was filtered through a 0.22-µm filter and stored at 4 °C prior to analysis. For the agar fraction, after the colonies were

removed, a piece of agar of approximately the same surface was sliced out and introduced into a 2-mL Eppendorf tube containing glass beads. 1 mL of methanol was added, and then the tube was vigorously vortexed until the agar was broken down. Finally, the mixture was sonicated in a bath for 10 minutes and centrifuged at 5000 G for 5 minutes. The supernatant was filtered through a 0.22-µm filter and stored at 4 °C prior to analysis by MALDI-TOF/TOF.

For *in situ* lipopeptide detection on inoculated leaves, leaf discs were taken 21 days post-inoculation with a sterile cork borer and then placed directly on an UltrafleXtreme MALDI plate. A matrix consisting of a combination of CHCA (α-cyano-4-hydroxycinnamic acid) and DHB (2,5-dihydroxybenzoic acid) was deposited over the discs or the supernatants (for the *in vitro* cultures or the colonies' analysis), and the plates were inserted into an UltrafleXtreme MALDI-TOF/TOF mass spectrometer. The mass spectra were acquired using the Bruker Daltonics FlexControl software and were processed using Bruker Daltonics FlexAnalysis.

Electron microscopy analysis

For the scanning electron microscopy analysis, leaf discs were taken 21 days post-inoculation as previously described and fixed in 0.1 M sodium cacodylate and 2% glutaraldehyde overnight at 4 ºC. Three washes were performed with 0.1 M sodium cacodylate and 0.1 M sucrose followed by ethanol dehydration in a series of ethanol solutions from 50% to 100%. A final drying with hexamethyldisilazane was performed as indicated[102]. The dried samples were coated with a thin layer of iridium using an Emitech K575x turbo sputtering coater before viewing in a Helios Nanolab 650 Scanning Electron Microscope and Focus Ion Beam (SEM-FIB) with a Schottky-type field emission electron gun.

For the transmission electron microscopy analysis, bacterial colonies grown on MSgg agar for the appropriate times were fixed directly using a 2% paraformaldehyde-2.5% glutaraldehyde-0.2 M sucrose mix in phosphate buffer 0.1 M (PB) overnight at 4 ºC. After three washes in PB, portions were excised from each colony and then post-fixed with 1% osmium tetroxide solution in PB for 90 minutes at room temperature, followed by PB washes, and 15 minutes of stepwise dehydration in an ethanol series (30%, 50%, 70%, 90%, and 100% twice). Between the 50% and 70% steps, colonies were incubated *in-bloc* in 2% uranyl acetate solution in 50% ethanol at 4 ºC, overnight. Following dehydration, the samples were gradually embedded in low-viscosity Spurr's resin: resin:ethanol, 1:1, 4 hours; resin:ethanol, 3:1, 4 hours; and pure resin, overnight. The sample blocks were embedded in capsule molds containing pure resin for 72 h at 70 ºC.

For the immunolabeling assays, samples from the corresponding strains were grown under biofilm-inducing conditions at 30 °C. After 48 h of incubation, carbon-coated copper grids were deposited into the wells over the pellicles formed at the interface between the medium and the air (in the case of mutants unable to form a pellicle, copper grids were deposited in the interface) and incubated with the samples at 28 °C for 2 h. After incubation, the grids were washed in PSB for 5 min, and then the samples were fixed with a solution of 2% paraformaldehyde for 10 min, washed in PBS and blocked with Pierce Protein-Free (TBS) blocking buffer (ThermoFisher) for 30 min. Anti-TasA primary antibody was used at a 1:150 dilution in blocking buffer, and grids were deposited over drops of the antibody solution and incubated for 1 h at room temperature. Samples were washed three times with TBS -T (50 mM Tris-HCl, 150 mM NaCl, pH 7.5 - Tween20 0.1%) for 5 min and then exposed to 10-nm diameter immunogold-conjugated secondary antibody (Ted Pella) for 1 h at a 1:50 dilution. The samples were then washed twice with TBS-T and once with water for 5 min each. Finally, the grids were treated with glutaraldehyde (2%) for 10 min, washed in water for 5 min, negatively stained with uranyl acetate (1%) for 20 seconds and, lastly, washed once with water for 30 seconds.

The samples were left to dry and were visualized under a FEI Tecnai G^2 20 TWIN Transmission Electron Microscope at an accelerating voltage of 80 KV. The images were taken using a side-mounted CCD Olympus Veleta with 2k x 2k Mp.

Whole-transcriptome analysis and qRT-PCR

Biofilms were grown on MSgg agar as described above. 24-, 48-. and 72-h colonies of the corresponding strains (WT or ΔtasA) were recovered and stored at -80 ºC. All of the assays were performed in duplicate. The collected cells were resuspended and homogenized via passage through a 25 $^{5/8}$ G needle in BirnBoim A^{103} buffer (20% sucrose, 10 mM Tris-HCl pH 8, 10 mM EDTA and 50 mM NaCl). Lysozyme (10 mg/ml) was added, and the mixture was incubated for 30 minutes at 37 ºC. After disruption, the suspensions were centrifuged, and the pellets were resuspended in Trizol reagent (Invitrogen). Total RNA extraction was performed as instructed by the manufacturer. DNA removal was carried out via in-column treatment with the rDNAse included in the Nucleo-Spin RNA Plant Kit (Macherey-Nagel) following the instructions of the manufacturer. The integrity and quality of the total RNA was assessed with an Agilent 2100 Bioanalyzer (Agilent Technologies) and by gel electrophoresis.

To perform the RNA sequencing analysis, rRNA removal was performed using the RiboZero rRNA removal (bacteria) Kit from Illumina, and 100-bp single-end read libraries were prepared using the TruSeq Stranded Total RNA Kit (Illumina). The libraries were

sequenced using a NextSeq550 instrument (Illumina). The raw reads were pre-processed with SeqTrimNext[104] using the specific NGS technology configuration parameters. This pre-processing removes low quality, ambiguous and low complexity stretches, linkers, adaptors, vector fragments, and contaminated sequences while keeping the longest informative parts of the reads. SeqTrimNext also discarded sequences below 25 bp. Subsequently, clean reads were aligned and annotated using the *Bacillus subtilis subsp. subtilis str. 168* genome (NC_000964.3) as the reference with Bowtie2[105] in BAM files, which were then sorted and indexed using SAMtools v1.484[106]. Uniquely localized reads were used to calculate the read number value for each gene via Sam2counts (https://github.com/vsbuffalo/sam2counts). Differentially expressed genes (DEGs) between WT and Δ*tasA* were analyzed via DEgenes Hunter[107], which provides a combined P-value from edgeR and DEseq2 that allowed differentially expressed gene ranking. For each gene, P-value < 0.05 and log2-fold change > 1 or < -1 were considered as the significance threshold. Heatmap and DEGs clusterization was performed using ComplexHeatmap[108] in Rstudio. STEM[109] was used to model temporal expression profiles independent of the data. Only profiles with a pvalue > 0.05 were considered in this study. The DEGs annotated with the *Bacillus subtilis subsp. subtilis str. 168* genome were used to identify the Gene Ontology functional categories using sma3s[110] and TopGo Software[111]. Gephi software (https://gephi.org) was used to generate the DEG networks, and the regulon list was downloaded from subtiwiki (http://subtiwiki.uni-goettingen.de). The data were deposited in the GEO database (GEO accession GSE124307).

Quantitative real-time (qRT)-PCR was performed using the iCycler-iQ system and the iQ SYBR Green Supermix Kit from Bio-Rad. The primer pairs used to amplify the target genes were designed using the Primer3 software (http://bioinfo.ut.ee/primer3/) and Beacon designer (http://www.premierbiosoft.com/qOligo/Oligo.jsp?PID=1), maintaining the parameters described elsewhere[112]. For the qRT-PCR assays, the RNA concentration was adjusted to 100 ng/µl. Next, 1 µg of DNA-free total RNA was retro-transcribed into cDNA using the SuperScript III reverse transcriptase (Invitrogen) and random hexamers in a final reaction volume of 20 µl according to the instructions provided by the manufacturer. The qRT-PCR cycle was: 95 ºC for 3 min, followed by PCR amplification using a 40-cycle amplification program (95 ºC for 20 sec, 56 ºC for 30 sec, and 72 ºC for 30 sec), followed by a third step of 95 ºC for 30 sec. To evaluate the melting curve, 40 additional cycles of 15 sec each starting at 75 ºC with stepwise temperature increases of 0.5 ºC per cycle were performed. To normalize the data, the *rpsJ* gene, encoding the 30S ribosomal protein S10, was used as a reference gene[113].

The target genes *fenD*, encoding fengycin synthetase D, *alsS*, encoding acetolactate synthase, *albE*, encoding bacteriocin subtilosin biosynthesis protein AlbE, *bacB*, encoding the bacilysin biosynthesis protein BacB, and *srfAA* encoding surfactin synthetase A, were amplified using the primer pairs given in supplementary Table 3.3, resulting in the generation of fragments of 147 bp, 82 bp, 185 bp, 160 bp and 94 bp, respectively. The primer efficiency tests and confirmation of the specificity of the amplification reactions were performed as previously described[114]. The relative transcript abundance was estimated using the ΔΔ cyclethreshold (Ct) method[115]. Transcriptional data of the target genes was normalized to the *rpsJ* gene and shown as the fold-changes in the expression levels of the target genes in each *B. subtilis* mutant strain compared to those in the WT strain. The relative expression ratios were calculated as the difference between the qPCR threshold cycles (Ct) of the target gene and the Ct of the *rpsJ* gene ($\Delta Ct = Ct_{gene\ of\ interest} - Ct_{rpsJ}$). Fold-change values were calculated as $2^{-\Delta\Delta Ct}$, assuming that one PCR cycle represents a two-fold difference in template abundance[116,117]. The qRT-PCR analyses were performed three times (technical replicates) using three independent RNA isolations (biological replicates).

Flow cytometry assays

Cells were grown on MSgg agar at 30 ºC. At different time points, colonies were recovered in 500 µL of PBS and resuspended with a 25 $^{5/8}$ G needle. For the promoter expression assays, colonies were gently sonicated as described above to ensure complete resuspension, and the cells were fixed in 4% paraformaldehyde in PBS and washed three times in PBS. To evaluate the physiological status of the different *B. subtilis* strains, cells were stained without fixation for 30 minutes with 5 mM 5-cyano-2,3-ditolyltetrazolium chloride (CTC) and 15 µM 3-(p-hydroxyphenyl) fluorescein (HPF).

The flow cytometry runs were performed with 200 µl of cell suspensions in 800 µL of GTE buffer (50 mM glucose, 10 mM EDTA, 20 mM Tris-HCl; pH 8), and the cells were measured on a Beckman Coulter Gallios™ flow cytometer using 488 nm excitation. YFP and HPF fluorescence were detected with 550 SP or 525/40 BP filters. CTC fluorescence was detected with 730 SP and 695/30BP filters. The data were collected using Gallios™ Software v1.2 and further analyzed using Kaluza Analysis v1.3.

Intracellular pH analysis

Intracellular pH was measured as previously described[55]. Briefly, colonies of the different strains grown on MSgg agar at 30 ºC were taken at different time points and recovered in potassium phosphate buffer (PPB) pH 7 and gently sonicated as described above. Next, the cells were incubated in 10 µl of 1 mM 5-(6)carboxyfluorescein diacetate

succinimidyl (CFDA) for 15 minutes at 30 ºC. PPB supplemented with glucose (10 mM) was added to the cells for 15 minutes at 30 ºC to remove the excess dye. After two washes with the same buffer, the cells were resuspended in 50 mM PPB (pH 4.5).

Fluorescence was measured in a FLUOstar Omega (BMG labtech) microplate spectrofluorometer using 490nm/525nm as the excitation and emission wavelengths, respectively. Conversion from the fluorescence arbitrary units into pH units was performed using a standard calibration curve.

Confocal laser scanning microscopy (CLSM)

Cell death in the bacterial colonies was evaluated using the LIVE/DEAD BacLight Bacterial Viability Kit (Invitrogen). Equal volumes of both components included in the kit were mixed, and 2 µl of this solution was used to stain 1 ml of the corresponding bacterial suspension. Sequential acquisitions were configured to visualize the live or dead bacteria in the samples. Acquisitions with excitation at 488 nm and emission recorded from 499 to 554 nm were used to capture the images from live bacteria, followed by a second acquisition with excitation at 561 nm and emission recorded from 592 to 688 nm for dead bacteria.

For the microscopic analysis and quantification of lipid peroxidation in live bacterial samples, we used the image-iT Lipid Peroxidation Kit (Invitrogen) following the manufacturer's instructions with some slight modifications. Briefly, colonies of the different strains were grown on MSgg plates at 30 °C, isolated at different time points, and resuspended in 1 ml of liquid MSgg medium as described in the previous sections. 5 mM cumene hydroperoxide (CuHpx)-treated cell suspensions of the different strains at the corresponding times were used as controls. The cell suspensions were then incubated at 30 °C for 2 h and then stained with a 10 µM solution of the imageIT lipid peroxidation sensor for 30 minutes. Finally, the cells were washed three times with PBS, mounted, and visualized immediately. Images of the stained bacteria were acquired sequentially to obtain images from the oxidized to the reduced states of the dye. The first image (oxidized channel) was acquired by exciting the sensor at 488 nm and recording the emissions from 509 to 561 nm, followed by a second acquisition (reduced channel) with excitement at 561 nm and recording of the emissions from 590 to 613 nm.

Membrane potential was evaluated using the image-iT TMRM (tetramethylrhodamine, methyl ester) reagent (Invitrogen) following the manufacturer's instructions. Colonies grown at 30 °C on MSgg solid medium were isolated at different time points and resuspended as described above. Samples treated prior to staining with 20 µM carbonyl cyanide m-chlorophenyl hydrazine (CCCP), a known protonophore and uncoupler of

bacterial oxidative phosphorylation, were used as controls (Fig. S11). The TMRM reagent was added to the bacterial suspensions to a final concentration of 100 nM, and the mixtures were incubated at 37 °C for 30 minutes. After incubation, the cells were immediately visualized by CLSM with excitation at 561 nm and emission detection between 576 and 683 nm.

The amounts of DNA damage in the *B. subtilis* strains at the different time points were evaluated via terminal deoxynucleotidyl transferase (TdT) dUTP Nick-End Labeling (TUNEL) using the *In-Situ* Cell Death Detection Kit with fluorescein (Roche) according to the manufacturer's instructions. *B. subtilis* colonies were resuspended in PBS and processed as described above. The cells were centrifuged and resuspended in 1% paraformaldehyde in PBS and fixed at room temperature for one hour on a rolling shaker. The cells were then washed twice in PBS and permeabilized in 0.1% Triton X-100 and 0.1% sodium citrate for 30 minutes at room temperature with shaking. After permeabilization, the cells were washed twice with PBS and the pellets were resuspended in 50 µl of the TUNEL reaction mixture (45 µl label solution + 5 µl enzyme solution), and the reactions were incubated for one hour at 37°C in the dark with shaking. Finally, the cells were washed twice in PBS, counterstained with DAPI (final concentration 500 nM), mounted, and visualized by CLSM with excitation at 488 nm and emission detection between 497 and 584 nm.

Membrane fluidity was evaluated via Laurdan generalized polarization (GP) as described previously[118] with some modifications. Colonies of the different *B. subtilis* strains were grown and processed as described above. The colonies were resuspended in 50 mM Tris pH 7.4 with 0.5% NaCl. Laurdan reagent (6-dodecanoyl-N,N-dimethyl-2-naphthylamine) was purchased from Sigma-Aldrich (Merck) and dissolved in N,N-dimethylformamide (DMF). Samples treated prior to staining with 2% benzyl alcohol, a substance known to increase lipid fluidity[119], were used as positive controls (Supplementary Fig. S3.12). Laurdan was added to the bacterial suspensions to a final concentration of 100 µM. The cells were incubated at room temperature for 10 minutes, mounted, and then visualized immediately using two-photon excitation with a Spectraphysics MaiTai Pulsed Laser tuned to 720 nm (roughly equivalent to 360 nm single photon excitation), attached to a Leica SP5 microscope. Emissions between 432 and 482 nm (gel phase) and between 509 to 547 nm (liquid phase) were recorded using the internal PMT detectors.

The caspase-like activity was detected using the FITC-conjugated pan caspase inhibitor Z-VAD-FMK (CaspACE FITC-VAD-FMK In Situ Marker, Promega). Colonies of the

different *B. subtilis* strains were grown and processed at each time point as described above. The colonies were resuspended in PBS. The FITC-Z-VAD-FMK reagent was added at a final concentration of 20 μM and the bacterial suspensions were incubated at 37 °C for 30 minutes before visualization. Samples were mounted and visualized immediately after incubation by CLSM with excitation at 488 nm and emission detection between 497 and 572 nm.

All images were obtained by visualizing the samples using an inverted Leica SP5 system with a 63x NA 1.4 HCX PL APO oil-immersion objective. For each experiment, the laser settings, scan speed, PMT or HyD detector gain, and pinhole aperture were kept constant for all of the acquired images.

Image analysis

Image processing was performed using Leica LAS AF (LCS Lite, Leica Microsystems) and FIJI/ImageJ software.

Images of live and dead bacteria from viability experiments were processed automatically, counting the number of live (green) or dead (red) bacteria in their corresponding channels. The percentage of dead cells was calculated dividing the number of dead cells by the total number of bacteria found on a field.

For processing the lipid peroxidation images, images corresponding to the reduced and oxidized channels were smoothed and a value of 3 was then subtracted from the two channels to eliminate the background. The ratio image was calculated by dividing the processed reduced channel by the oxidized channel using the FiJi image calculator tool. The ratio images were pseudo-colored using a color intensity look-up table (LUT), and intensity values of min. 0 and max. 50 were selected. All of the images were batch processed with a custom imageJ macro, in which the same processing options were applied to all of the acquired images. Quantification of the lipid peroxidation was performed in Imaris v7.4 (Bitplane) by quantifying the pixel intensity of the ratio images with the Imaris “spots” tool.

The Laurdan GP acquisitions were processed similarly. Images corresponding to the gel phase channel and the liquid phase channel were smoothed and a value of 10 was subtracted to eliminate the background. The Laurdan GP image was then calculated by applying the following formula (1):

$$(1) \quad \frac{(\text{gel phase channel} - \text{liquid phase channel})}{(\text{gel phase channel} + \text{liquid phase channel})}$$

The calculation was performed step by step using the FiJi image calculator tool. Pixels with high Laurdan GP values, typically caused by residual background noise, were eliminated with the “Remove outliers” option using a radius of 4 and a threshold of 5. Finally, the Laurdan GP images were pseudo-colored using a color intensity LUT, and intensity values of min. 0 and max. 1.5 were selected. This processing was applied to all of the acquisitions for this experiment. To quantify the Laurdan GP, bright field images were used for thresholding and counting to create counts masks that were applied to the Laurdan GP images to measure the mean Laurdan GP value for each bacterium.

TUNEL images were analyzed by subtracting a value of 10 in the TUNEL channel to eliminate the background. The DAPI channel was then used for thresholding and counting as described above to quantify the TUNEL signal. The same parameters were used to batch process and quantify all of the images.

To quantify the membrane potential, the TMRM assay images were analyzed as described above using the bright field channel of each image for thresholding and counting to calculate the mean fluorescence intensity in each bacterium. Endospores, which exhibited a bright fluorescent signal upon TMRM staining, were excluded from the analysis. This processing was applied to all of the acquisitions for this experiment.

Images from the caspase-like activity assay were analyzed by subtracting a value of 10 in the FITC-Z-VAD-FML channel to eliminate the background. The bright field channel of each image was used for thresholding and counting to select the positively stained bacteria. Bacteria with a signal over a value of 3 were considered as positive. Endospores exhibited a bright fluorescent signal upon staining with this reagent, therefore, were filtered out and only vegetative cells were analyzed.

Statistical analysis

All of the data are representative of at least three independent experiments with at least three technical replicates. The results are expressed as the mean ± standard error of the mean (SEM). Statistical significance was assessed by performing the appropriate tests (see the figure legends). All analyses were performed using GraphPad Prism version 6. P-values <0.05 were considered significant. Asterisks indicate the level of statistical significance: * = $p < 0.05$, ** = $p < 0.01$, *** = $p < 0.001$, and **** = $p < 0.0001$.

REFERENCES

1 Toyofuku, M. *et al.* Environmental factors that shape biofilm formation. *Biosci Biotechnol. Biochem.* **80**, 7-12, (2016).

2 Wenbo, Z. *et al.* Nutrient depletion in *Bacillus subtilis* biofilms triggers matrix production. *New Journal of Physics* **16**, 015028 (2014).

3 Flemming, H. C. *et al.* Biofilms: an emergent form of bacterial life. *Nat. Rev. Microbiol.* **14**, 563-575, (2016).

4 van Gestel, J., Vlamakis, H. & Kolter, R. Division of Labor in Biofilms: the Ecology of Cell Differentiation. *Microbiol. Spectr.* **3**, MB-0002-2014, (2015).

5 Dragos, A. *et al.* Division of Labor during Biofilm Matrix Production. *Curr. Biol.* **28**, 1903-1913 e1905, (2018).

6 Branda, S. S., Vik, S., Friedman, L. & Kolter, R. Biofilms: the matrix revisited. *Trends Microbiol.* **13**, 20-26, (2005).

7 Shank, E. A. & Kolter, R. Extracellular signaling and multicellularity in *Bacillus subtilis*. *Curr. Opin. Microbiol.* **14**, 741-747, (2011).

8 Steinberg, N. & Kolodkin-Gal, I. The Matrix Reloaded: Probing the Extracellular Matrix Synchronizes Bacterial Communities. *J. Bacteriol.*, (2015).

9 Vlamakis, H., Aguilar, C., Losick, R. & Kolter, R. Control of cell fate by the formation of an architecturally complex bacterial community. *Genes Dev.* **22**, 945-953, (2008).

10 Lopez, D., Vlamakis, H. & Kolter, R. Biofilms. *Cold Spring Harb. Perspect. Biol.* **2**, a000398, (2010).

11 Molina-Santiago, C. *et al.* The extracellular matrix protects *Bacillus subtilis* colonies from Pseudomonas invasion and modulates plant co-colonization. *Nat. Commun.* **10**, 1919, (2019).

12 Juliano, R. L. & Haskill, S. Signal transduction from the extracellular matrix. *J. Cell Biol.* **120**, 577-585 (1993).

13 Aharoni, D., Meiri, I., Atzmon, R., Vlodavsky, I. & Amsterdam, A. Differential effect of components of the extracellular matrix on differentiation and apoptosis. *Curr. Biol.* **7**, 43-51 (1997).

14 Kim, S. H., Turnbull, J. & Guimond, S. Extracellular matrix and cell signalling: the dynamic cooperation of integrin, proteoglycan and growth factor receptor. *J. Endocrinol.* **209**, 139-151, (2011).

15 Cheresh, D. A. & Stupack, D. G. Regulation of angiogenesis: apoptotic cues from the ECM. *Oncogene* **27**, 6285-6298, (2008).

16 Kular, J. K., Basu, S. & Sharma, R. I. The extracellular matrix: Structure, composition, age-related differences, tools for analysis and applications for tissue engineering. *J. Tissue. Eng.* **5**, 2041731414557112, (2014).

17 Shi, Y. B., Li, Q., Damjanovski, S., Amano, T. & Ishizuya-Oka, A. Regulation of apoptosis during development: input from the extracellular matrix (review). *Int. J. Mol. Med.* **2**, 273-282 (1998).

18 Frisch, S. M. & Francis, H. Disruption of epithelial cell-matrix interactions induces apoptosis. *J. Cell Biol.* **124**, 619-626 (1994).

19 Gonidakis, S. & Longo, V. D. Assessing chronological aging in bacteria. *Methods Mol. Biol.* **965**, 421-437, (2013).

20 Kolter, R., Siegele, D. A. & Tormo, A. The stationary phase of the bacterial life cycle. *Annu. Rev. Microbiol.* **47**, 855-874, (1993).

21 Dukan, S. & Nystrom, T. Bacterial senescence: stasis results in increased and differential oxidation of cytoplasmic proteins leading to developmental induction of the heat shock regulon. *Genes Dev.* **12**, 3431-3441 (1998).

22 Hecker, M., Pane-Farre, J. & Volker, U. SigB-dependent general stress response in *Bacillus subtilis* and related gram-positive bacteria. *Annu. Rev. Microbiol.* **61**, 215-236, (2007).

23 Reder, A., Hoper, D., Gerth, U. & Hecker, M. Contributions of individual sigmaB-dependent general stress genes to oxidative stress resistance of *Bacillus subtilis*. *J. Bacteriol.* **194**, 3601-3610, (2012).

24 Navarro Llorens, J. M., Tormo, A. & Martinez-Garcia, E. Stationary phase in gram-negative bacteria. *FEMS Microbiol. Rev.* **34**, 476-495, (2010).

25 Gomez-Marroquin, M. *et al.* Role of *Bacillus subtilis* DNA Glycosylase MutM in Counteracting Oxidatively Induced DNA Damage and in Stationary-Phase-Associated Mutagenesis. *J. Bacteriol.* **197**, 1963-1971, (2015).

26 Chan, C. M., Danchin, A., Marliere, P. & Sekowska, A. Paralogous metabolism: S-alkyl-cysteine degradation in *Bacillus subtilis*. *Environ. Microbiol.* **16**, 101-117, (2014).

27 Vlamakis, H., Chai, Y., Beauregard, P., Losick, R. & Kolter, R. Sticking together: building a biofilm the *Bacillus subtilis* way. *Nat. Rev. Microbiol.* **11**, 157-168, (2013).

28 Kearns, D. B., Chu, F., Branda, S. S., Kolter, R. & Losick, R. A master regulator for biofilm formation by *Bacillus subtilis*. *Mol. Microbiol.* **55**, 739-749, (2005).

29 Chu, F., Kearns, D. B., Branda, S. S., Kolter, R. & Losick, R. Targets of the master regulator of biofilm formation in *Bacillus subtilis*. *Mol. Microbiol.* **59**, 1216-1228, (2006).

30 Aguilar, C., Vlamakis, H., Guzman, A., Losick, R. & Kolter, R. KinD is a checkpoint protein linking spore formation to extracellular-matrix production in *Bacillus subtilis* biofilms. *MBio* **1**, (2010).

31 Marvasi, M., Visscher, P. T. & Casillas Martinez, L. Exopolymeric substances (EPS) from *Bacillus subtilis*: polymers and genes encoding their synthesis. *FEMS Microbiol Lett.* **313**, 1-9, (2010).

32 Hobley, L. *et al.* BslA is a self-assembling bacterial hydrophobin that coats the *Bacillus subtilis* biofilm. *Proc. Natl. Acad. Sci. USA* **110**, 13600-13605, (2013).

33 Romero, D., Aguilar, C., Losick, R. & Kolter, R. Amyloid fibers provide structural integrity to *Bacillus subtilis* biofilms. *Proc. Natl. Acad. Sci. USA* **107**, 2230-2234, (2010).

34 Diehl, A. *et al.* Structural changes of TasA in biofilm formation of *Bacillus subtilis*. *Proc. Natl. Acad. Sci. USA* **115**, 3237-3242, (2018).

35 Stover, A. G. & Driks, A. Secretion, localization, and antibacterial activity of TasA, a *Bacillus subtilis* spore-associated protein. *J. Bacteriol.* **181**, 1664-1672 (1999).

36 Stover, A. G. & Driks, A. Control of synthesis and secretion of the *Bacillus subtilis* protein YqxM. *J. Bacteriol.* **181**, 7065-7069 (1999).

37 Camara-Almiron, J., Caro-Astorga, J., de Vicente, A. & Romero, D. Beyond the expected: the structural and functional diversity of bacterial amyloids. *Crit. Rev. Microbiol.*, (2018).

38 Danhorn, T. & Fuqua, C. Biofilm formation by plant-associated bacteria. *Annu. Rev. Microbiol.* **61**, 401-422, (2007).

39 Castiblanco, L. F. & Sundin, G. W. New insights on molecular regulation of biofilm formation in plant-associated bacteria. *J. Integr. Plant Biol.* **58**, 362-372, (2016).

40 Zeriouh, H., de Vicente, A., Perez-Garcia, A. & Romero, D. Surfactin triggers biofilm formation of *Bacillus subtilis* in melon phylloplane and contributes to the biocontrol activity. *Environ. Microbiol.* **16**, 2196-2211, (2014).

41 Lopez, D., Vlamakis, H., Losick, R. & Kolter, R. Paracrine signaling in a bacterium. *Genes Dev.* **23**, 1631-1638, (2009).

42 Perez-Garcia, A. *et al.* The powdery mildew fungus *Podosphaera fusca* (synonym *Podosphaera xanthii*), a constant threat to cucurbits. *Mol. Plant Pathol.* **10**, 153-160, (2009).

43 Nakano, M. M., Dailly, Y. P., Zuber, P. & Clark, D. P. Characterization of anaerobic fermentative growth of *Bacillus subtilis*: identification of fermentation end products and genes required for growth. *J. Bacteriol.* **179**, 6749-6755 (1997).

44 Hartig, E. & Jahn, D. Regulation of the anaerobic metabolism in *Bacillus subtilis*. *Adv. Microb. Physiol.* **61**, 195-216, (2012).

45 Ongena, M. & Jacques, P. *Bacillus* lipopeptides: versatile weapons for plant disease biocontrol. *Trends Microbiol.* **16**, 115-125, (2008).

46 Shelburne, C. E. *et al.* The spectrum of antimicrobial activity of the bacteriocin subtilosin A. *J. Antimicrob. Chemother.* **59**, 297-300, (2007).

47 Rajavel, M., Mitra, A. & Gopal, B. Role of *Bacillus subtilis* BacB in the synthesis of bacilysin. *J. Biol. Chem.* **284**, 31882-31892, (2009).

48 Patel, P. S. *et al.* Bacillaene, a novel inhibitor of procaryotic protein synthesis produced by *Bacillus subtilis*: production, taxonomy, isolation, physico-chemical characterization and biological activity. *J. Antibiot. (Tokyo)* **48**, 997-1003 (1995).

49 Niehaus, T. D. *et al.* Identification of a metabolic disposal route for the oncometabolite S-(2-succino)cysteine in *Bacillus subtilis*. *J. Biol. Chem.* **293**, 8255-8263, (2018).

50 Thomas, S. A., Storey, K. B., Baynes, J. W. & Frizzell, N. Tissue distribution of S-(2-succino)cysteine (2SC), a biomarker of mitochondrial stress in obesity and diabetes. *Obesity (Silver Spring)* **20**, 263-269, (2012).

51 McDonnell, G. E., Wood, H., Devine, K. M. & McConnell, D. J. Genetic control of bacterial suicide: regulation of the induction of PBSX in *Bacillus subtilis*. *J. Bacteriol.* **176**, 5820-5830 (1994).

52 Toyofuku, M. *et al.* Prophage-triggered membrane vesicle formation through peptidoglycan damage in *Bacillus subtilis*. *Nat. Commun.* **8**, 481, (2017).

53 Nystrom, T. Stationary-phase physiology. *Annu. Rev. Microbiol.* **58**, 161-181, (2004).

54 Chen, Y., Gozzi, K., Yan, F. & Chai, Y. Acetic Acid Acts as a Volatile Signal To Stimulate Bacterial Biofilm Formation. *MBio* **6**, e00392, (2015).

55 Thomas, V. C. *et al.* A central role for carbon-overflow pathways in the modulation of bacterial cell death. *PLoS Pathog.* **10**, e1004205, (2014).

56 Xiao, Z. & Xu, P. Acetoin metabolism in bacteria. *Crit. Rev. Microbiol.* **33**, 127-140, (2007).

57 Larosa, V. & Remacle, C. Insights into the respiratory chain and oxidative stress. *BioSci. Rep.* **38**, (2018).

58 Teixeira, J. *et al.* Extracellular acidification induces ROS- and mPTP-mediated death in HEK293 cells. *Redox Biol.* **15**, 394-404, (2018).

59 Redza-Dutordoir, M. & Averill-Bates, D. A. Activation of apoptosis signalling pathways by reactive oxygen species. *Biochim. Biophys. Acta* **1863**, 2977-2992, (2016).

60 McIlwain, D. R., Berger, T. & Mak, T. W. Caspase functions in cell death and disease. *Cold Spring Harb. Perspect. Biol.* **5**, a008656, (2013).

61 Moliere, N. & Turgay, K. General and regulatory proteolysis in *Bacillus subtilis*. *Subcell Biochem* **66**, 73-103, (2013).

62 Dwyer, D. J., Camacho, D. M., Kohanski, M. A., Callura, J. M. & Collins, J. J. Antibiotic-induced bacterial cell death exhibits physiological and biochemical hallmarks of apoptosis. *Mol. Cell* **46**, 561-572, (2012).

63 Gross, A. *et al.* Biochemical and genetic analysis of the mitochondrial response of yeast to BAX and BCL-X(L). *Mol. Cell Biol.* **20**, 3125-3136 (2000).

64 Giovannini, C. *et al.* Mitochondria hyperpolarization is an early event in oxidized low-density lipoprotein-induced apoptosis in Caco-2 intestinal cells. *FEBS Lett.* **523**, 200-206 (2002).

65 Perry, S. W. *et al.* HIV-1 transactivator of transcription protein induces mitochondrial hyperpolarization and synaptic stress leading to apoptosis. *J. Immunol.* **174**, 4333-4344 (2005).

66 Gaschler, M. M. & Stockwell, B. R. Lipid peroxidation in cell death. *Biochem. Biophys. Res. Commun.* **482**, 419-425, (2017).

67 Wong-Ekkabut, J. *et al.* Effect of lipid peroxidation on the properties of lipid bilayers: a molecular dynamics study. *Biophys. J.* **93**, 4225-4236, (2007).

68 Bindoli, A., Cavallini, L. & Jocelyn, P. Mitochondrial lipid peroxidation by cumene hydroperoxide and its prevention by succinate. *Biochim. Biophys. Acta* **681**, 496-503 (1982).

69 Heimburg, T. & Marsh, D. in *Biological Membranes* (eds Kenneth M. MerzJr & Benoît Roux) (Birkhäuser Boston, 1996).

70 van de Vossenberg, J. L., Driessen, A. J., da Costa, M. S. & Konings, W. N. Homeostasis of the membrane proton permeability in *Bacillus subtilis* grown at different temperatures. *Biochim. Biophys. Acta* **1419**, 97-104 (1999).

71 Rossignol, M., Thomas, P. & Grignon, C. Proton permeability of liposomes from natural phospholipid mixtures. *Biochim. Biophys. Acta* **684**, 195-199 (1982).

72 Tjalsma, H., Bolhuis, A., Jongbloed, J. D., Bron, S. & van Dijl, J. M. Signal peptide-dependent protein transport in *Bacillus subtilis*: a genome-based survey of the secretome. *Microbiol. Mol Biol. Rev.* **64**, 515-547 (2000).

73 Romero, D., Vlamakis, H., Losick, R. & Kolter, R. An accessory protein required for anchoring and assembly of amyloid fibres in *B. subtilis* biofilms. *Mol. Microbiol.* **80**, 1155-1168, (2011).

74 Tjalsma, H. *et al.* Conserved serine and histidine residues are critical for activity of the ER-type signal peptidase SipW of *Bacillus subtilis*. *J. Biol. Chem.* **275**, 25102-25108, (2000).

75 Chai, Y., Chu, F., Kolter, R. & Losick, R. Bistability and biofilm formation in *Bacillus subtilis*. *Mol. Microbiol.* **67**, 254-263, (2008).

76 Lewis, K. Programmed death in bacteria. *Microbiol. Mol. Biol. Rev.* **64**, 503-514 (2000).

77 Bayles, K. W. Bacterial programmed cell death: making sense of a paradox. *Nat. Rev. Microbiol.* **12**, 63-69, (2014).

78 Peeters, S. H. & de Jonge, M. I. For the greater good: Programmed cell death in bacterial communities. *Microbiol. Res.* **207**, 161-169, (2018).

79 Murakami, C. *et al.* pH neutralization protects against reduction in replicative lifespan following chronological aging in yeast. *Cell Cycle* **11**, 3087-3096, (2012).

80 Wang, C. & Youle, R. J. The role of mitochondria in apoptosis*. *Annu. Rev. Genet.* **43**, 95-118, (2009).

81 Cao, J. *et al.* Curcumin induces apoptosis through mitochondrial hyperpolarization and mtDNA damage in human hepatoma G2 cells. *Free Radic. Biol. Med.* **43**, 968-975, (2007).

82 Shi, C. *et al.* Antimicrobial Activity and Possible Mechanism of Action of Citral against Cronobacter sakazakii. *PLoS One* **11**, e0159006, (2016).

83 Malishev, R., Abbasi, R., Jelinek, R. & Chai, L. Bacterial Model Membranes Reshape Fibrillation of a Functional Amyloid Protein. *Biochemistry* **57**, 5230-5238, (2018).

84 Chai, L. *et al.* The bacterial extracellular matrix protein TapA is a two-domain partially disordered protein. *Chembiochem*, (2018).

85 Wright, P. E. & Dyson, H. J. Intrinsically disordered proteins in cellular signalling and regulation. *Nat. Rev. Mol. Cell Biol.* **16**, 18-29, (2015).

86 Dunker, A. K., Cortese, M. S., Romero, P., Iakoucheva, L. M. & Uversky, V. N. Flexible nets. The roles of intrinsic disorder in protein interaction networks. *FEBS J* **272**, 5129-5148, (2005).

87 Vorholt, J. A. Microbial life in the phyllosphere. *Nat. Rev. Microbiol.* **10**, 828-840, (2012).

88 Arnaouteli, S., MacPhee, C. E. & Stanley-Wall, N. R. Just in case it rains: building a hydrophobic biofilm the *Bacillus subtilis* way. *Curr. Opin. Microbiol.* **34**, 7-12, (2016).

89 Fink, R. C. *et al.* Transcriptional responses of *Escherichia coli* K-12 and O157:H7 associated with lettuce leaves. *Appl. Environ. Microbiol.* **78**, 1752-1764, (2012).

90 Carter, M. Q., Louie, J. W., Feng, D., Zhong, W. & Brandl, M. T. Curli fimbriae are conditionally required in *Escherichia coli* O157:H7 for initial attachment and biofilm formation. *Food Microbiol* **57**, 81-89, (2016).

91 Lakshmanan, V. *et al.* Microbe-associated molecular patterns-triggered root responses mediate beneficial rhizobacterial recruitment in Arabidopsis. *Plant Physiol.* **160**, 1642-1661, (2012).

92 Choudhary, D. K. & Johri, B. N. Interactions of Bacillus spp. and plants--with special reference to induced systemic resistance (ISR). *Microbiol. Res.* **164**, 493-513, (2009).

93 Ping, L. & Boland, W. Signals from the underground: bacterial volatiles promote growth in Arabidopsis. *Trends Plant Sci.* **9**, 263-266, (2004).

94 Ahimou, F., Jacques, P. & Deleu, M. Surfactin and iturin A effects on *Bacillus subtilis* surface hydrophobicity. *Enzyme Microb. Technol*. **27**, 749-754 (2000).

95 Doan, T., Marquis, K. A. & Rudner, D. Z. Subcellular localization of a sporulation membrane protein is achieved through a network of interactions along and across the septum. *Mol. Microbiol.* **55**, 1767-1781, (2005).

96 Yasbin, R. E. & Young, F. E. Transduction in *Bacillus subtilis* by bacteriophage SPP1. *J Virol* **14**, 1343-1348 (1974).

97 Branda, S. S., Chu, F., Kearns, D. B., Losick, R. & Kolter, R. A major protein component of the *Bacillus subtilis* biofilm matrix. *Mol. Microbiol.* **59**, 1229-1238, (2006).

98 El Mammeri, N. *et al.* Molecular architecture of bacterial amyloids in Bacillus biofilms. *FASEB J.* **33**, 12146-12163, (2019).

99 Romero, D., Rivera, M. E., Cazorla, F. M., de Vicente, A. & Perez-Garcia, A. Effect of mycoparasitic fungi on the development of *Sphaerotheca fusca* in melon leaves. *Mycol Res* **107**, 64-71 (2003).

100 Schindelin, J. *et al.* Fiji: an open-source platform for biological-image analysis. *Nat. Methods* **9**, 676-682, (2012).

101 Bellon-Gomez, D., Vela-Corcia, D., Perez-Garcia, A. & Tores, J. A. Sensitivity of *Podosphaera xanthii* populations to anti-powdery-mildew fungicides in Spain. *Pest. Manag. Sci.* **71**, 1407-1413, (2015).

102 Fischer, E. R., Hansen, B. T., Nair, V., Hoyt, F. H. & Dorward, D. W. Scanning electron microscopy. *Curr. Protoc. Microbiol.* **Chapter 2**, Unit 2B 2, (2012).

103 Birnboim, H. C. & Doly, J. A rapid alkaline extraction procedure for screening recombinant plasmid DNA. *Nucleic Acids Res.* **7**, 1513-1523 (1979).

104 Falgueras, J. *et al.* SeqTrim: a high-throughput pipeline for pre-processing any type of sequence read. *BMC Bioinformatics* **11**, 38, (2010).

105 Langmead, B. & Salzberg, S. L. Fast gapped-read alignment with Bowtie 2. *Nat. Methods* **9**, 357-359, (2012).

106 Li, H. *et al.* The Sequence Alignment/Map format and SAMtools. *Bioinformatics* **25**, 2078-2079, (2009).

107 González Gayte, I., Bautista Moreno, R., Seoane Zonjic, P. & Claros, M. G. DEgenes Hunter - A Flexible R Pipeline for Automated RNA-seq Studies in Organisms without Reference Genome. *Genomics and Computational Biology; Vol 3 No 3 (2017)DO - 10.18547/gcb.2017.vol3.iss3.e31* (2017).

108 Gu, Z., Eils, R. & Schlesner, M. Complex heatmaps reveal patterns and correlations in multidimensional genomic data. *Bioinformatics* **32**, 2847-2849, (2016).

109 Ernst, J. & Bar-Joseph, Z. STEM: a tool for the analysis of short time series gene expression data. *BMC Bioinformatics* **7**, 191, (2006).

110 Casimiro-Soriguer, C. S., Munoz-Merida, A. & Perez-Pulido, A. J. Sma3s: A universal tool for easy functional annotation of proteomes and transcriptomes. *Proteomics* **17**, (2017).

111 Alexa, A. & Rahnenfuhrer, J. Gene set enrichment analysis with topGO. (2007).

112 Thornton, B. & Basu, C. Real-time PCR (qPCR) primer design using free online software. *Biochemistry and Molecular Biology Education* **39**, 145-154, (2011).

113 Leães, F. L. *et al.* Expression of essential genes for biosynthesis of antimicrobial peptides of *Bacillus* is modulated by inactivated cells of target microorganisms. *Research in Microbiology* **167**, 83-89, (2016).

114 Vargas, P., Felipe, A., Michan, C. & Gallegos, M. T. Induction of *Pseudomonas syringae pv. tomato* DC3000 MexAB-OprM multidrug efflux pump by flavonoids is mediated by the repressor PmeR. *Mol. Plant Microbe. Interact.* **24**, 1207-1219, (2011).

115 Livak, K. J. & Schmittgen, T. D. Analysis of relative gene expression data using real-time quantitative PCR and the 2−ΔΔCT method. *Methods* **25**, 402-408, (2001).

116 Pfaffl, M. W. A new mathematical model for relative quantification in real-time RT-PCR. *Nucleic Acids Res.* **29**, e45 (2001).

117 Rotenberg, D., Thompson, T. S., German, T. L. & Willis, D. K. Methods for effective real-time RT-PCR analysis of virus-induced gene silencing. *J. Virol. Methods* **138**, 49-59, (2006).

118 Strahl, H., Burmann, F. & Hamoen, L. W. The actin homologue MreB organizes the bacterial cell membrane. *Nat. Commun.* **5**, 3442, (2014).

119 Friedlander, G., Le Grimellec, C., Giocondi, M. C. & Amiel, C. Benzyl alcohol increases membrane fluidity and modulates cyclic AMP synthesis in intact renal epithelial cells. *Biochim. Biophys. Acta* **903**, 341-348 (1987).

120 Straight, P. D., Fischbach, M. A., Walsh, C. T., Rudner, D. Z. & Kolter, R. A singular enzymatic megacomplex from *Bacillus subtilis*. *Proc. Natl. Acad. Sci. USA* **104**, 305-310, (2007).

SUPPLEMENTARY INFORMATION

Supplementary data

Supplementary data 3.1, 3.2 and 3.3, containing a list of the differentially expressed genes in the Δ*tasA* strain compared to the WT strain at 24, 48 and 72 hours respectively are available at GEO database with the accession number GSE124307 (https://www.ncbi.nlm.nih.gov/geo/query/acc.cgi?acc=GSE124307). The files containing the tables are the following:

GSE124307_tasA_vs_WT_24h.xlsx

GSE124307_tasA_vs_WT_48h.xlsx

GSE124307_tasA_vs_WT_72h.xlsx

Supplementary Table 3.1. Flow cytometry – Quadrant statistics.

Time	Sample	HPF (Quad. 1)	HPF + CTC (Quad. 2)	Unstained (Quad. 3)	CTC (Quad. 4)
24h	WT	10.79 ± 2.22	17.83 ± 1.83	20.12 ± 1.01	51.27 ± 1.98
	Δ*tasA*	27.70 ± 0.79	14.68 ± 5.94	29.24 ± 8.62	28.40 ± 3.24
	JC81	4.16 ± 1.68	15.58 ± 0.04	20.68 ± 8.00	59.59 ± 9.64
48h	WT	0.45 ± 0.16	2.06 ± 0.48	22.38 ± 3.24	75.12 ± 2.92
	Δ*tasA*	2.72 ± 2.44	4.84 ± 3.62	23.51 ± 7.53	68.93 ± 13.58
	JC81	3.39 ± 0.68	11.24 ± 0.67	21.97 ± 4.91	70.64 ± 5.20
72h	WT	8.44 ± 6.43	51.10 ± 9.51	6.02 ± 4.77	34.44 ± 1.69
	Δ*tasA*	1.40 ± 0.85	4.65 ± 0.80	33.43 ± 12.24	60.46 ± 12.89
	JC81	1.53 ± 0.34	3.98 ± 0.54	26.25 ± 2.16	68.25 ± 3.03

Supplementary Table 3.2. Bacterial strains used in this study.

Bacterial strain	Genotype	Source
Bacillus subtilis 168	Prototroph	Laboratory collection
Bacillus subtilis NCIB3610	Wild type. Undomesticated strain	Laboratory collection
CA017	*Bacillus subtilis* NCIB3610 *tasA::km*	(Vlamakis *et al*., 2008)[9]
FC268	*Bacillus subtilis* NCIB3610 *(tapA-sipW-tasA)::spc, amyE::(tapA(13-234)-sipW-tasA) (cm)*	(Chu *et al*., 2006)[29]
SSB488	*Bacillus subtilis* NCIB3610 *epsA-O::tet*	(Branda *et al*., 2006)[97]
SSB149	*Bacillus subtilis* NCIB3610 *(tapA-sipW-tasA)::spc*	(Branda *et al*., 2006)[97]
PSK0156	*Bacillus subtilis* 168 *ppsB* ΩTn*10 (spc)*	(Straight *et al*., 2007)[120]
DL811	*Bacillus subtilis* NCIB 3610 *sinI::spc* *lacA::P_{srfAA}-lacZ*	Kindly provided by Dr. Daniel López
JC97	*Bacillus subtilis* NCIB3610 *bslA::spc*	This study
YNG001	*Bacillus subtilis* NCIB3610 *amyE::P_{pps}-yfp (spc)*	This study
YNG002	*Bacillus subtilis* NCIB3610 *tasA::km* *amyE::P_{pps}-yfp (spc)*	This study
YNG003	*Bacillus subtilis* NCIB3610 *(tapA-sipW-tasA)::spc* *lacA::(tapA-sipW-tasA$_{(Lys68Ala, Asp69Ala)}$) (mls)* *amyE::P_{pps}-yfp (cm)*	This study
YNG004	*Bacillus subtilis* NCIB3610 *ppsB* ΩTn*10 (spc)*	This study
JC81	*Bacillus subtilis* NCIB3610 *(tapA-sipW-tasA)::spc* *lacA::(tapA-sipW-tasA$_{(Lys68Ala, Asp69Ala)}$) (mls)*	This study
JC149	*Bacillus subtilis* NCIB3610 *(tapA-sipW-tasA)::spc* *lacA::(tapA-sipW-tasA$_{(Lys4Ala, Lys5Ala, Lys6Ala)}$) (mls)*	This study
JC70	*Bacillus subtilis* NCIB3610 *(tapA-sipW-tasA)::spc* *lacA::(tapA-sipW-tasA$_{native}$) (mls)*	This study
JC189	*Bacillus subtilis* NCIB3610 *sinI::spc*	This study

Supplementary table 3.3. Primers used in this study.

Name	Sequence (5' – 3')	Purpose
Ppps-ecoRI.F	AAAAAAGAATTCTCACTTTATATCCGGAAATTTGA	Cloning P_{pps} into pKM003
Ppps-HindIII.R	AAAAAAAAGCTTAACGGATTCCCTCCAGTTCT	Cloning P_{pps} into pKM003
KD_AA_68-70	GATCCGTTATTTTCAAATTGGAAAGCCGCTGTCAACTTATCTCCCGGCTTTAG	Site-directed mutagenesis of residues 68 and 69 in TasA aminoacid sequence
KD_AA_68-70_as	CTAAAGCCGGGAGATAAGTTGACAGCGGCTTTCCAATTTGAAAATAACGGATC	Site-directed mutagenesis of residues 68 and 69 in TasA aminoacid sequence
KKK4-5-6AAA	TCAATAAAAGGGGAGCTTACCATGGGTATGGCAGCGGCATTGAGTTTAGGAGTTGCTTCTGCAGCACT	Site-directed mutagenesis of residues 4, 5 and 6 in TasA aminoacid sequence
KKK4-5-6AAA_as	AGTGCTGCAGAAGCAACTCCTAAACTCAATGCCGCTGCCATACCCATGGTAAGCTCCCCTTTTATTGA	Site-directed mutagenesis of residues 4, 5 and 6 in TasA aminoacid sequence
TasA_1_mutb	AAAAAGTCGACATTAGATAGTGAATGGGAGAAATTGG	Cloning of (*tapA-sipW-tasA*) into pDR183
YSRI_2	AAAAAGGATCCGCTATAAGGATCAAATGAAATCG	Cloning of (*tapA-sipW-tasA*) into pDR183
bslAUP-Fw	TTCGAGCTCGGTACCCGGGGATCCTTAAAGACTTTGATTGTCGTCAG	Construction of *bslA* mutant.
bslAUP-Rv	CGTTACGTTATTAAACAAAATTCCCCCTAAAAAATG	Construction of *bslA* mutant.
Spc-Fw	GGGGAATTTTGTTTAATAACGTAACGTGACTGG	Construction of *bslA* mutant.
Spc-Rv	ATCCGGCTTGTACGCAAGGGTTTATTGTTTTC	Construction of *bslA* mutant.
bslaDOWN-Fw	AATAAACCCTTGCGTACAAGCCGGATGGATAAAATG	Construction of *bslA* mutant.
bslADOWN-Rv	AAGCTTGCATGCCTGCAGGTCGACTTGTAAAAGACCGGTTAACGC	Construction of *bslA* mutant.
amyEUP-Fw	AGTGAATTCGAGCTCGGTACCCGGGGCCGTTTACCGTTCGCCATAAG	Construction of strain YNG004
amyEUP-Rv	GGATATAAAGTGATCTTGACACTCCTTATTTGATTTTTTGAAG	Construction of strain YNG004
Ppps-Fw	AGGAGTGTCAAGATCACTTTATATCCGGAAATTTG	Construction of strain YNG004
Ppps-Rv	TGACGAAGCATGGAACGGATTCCCTCCAGTTC	Construction of strain YNG004
Yfp-Fw	GAGGGAATCCGTTCCATGCTTCGTCAATGTATATG	Construction of strain YNG004

Yfp-Rv	AATATATATTTTATTATTTGTATAGTTCATCCATGC	Construction of strain YNG004
Cat-Fw	ACTATACAAATAATAAAATATATATTTATGTTACAGTAATATTGAC	Construction of strain YNG004
Cat-Rv	TGCCGGCATTTCGTTATAAAAGCCAGTCATTAGG	Construction of strain YNG004
amyEDOWN-Fw	CTGGCTTTTATAACGAAATGCCGGCAATGCTG	Construction of strain YNG004
amyEDOWN-Rv	GCATGCCTGCAGGTCGACTCTAGAGGGGCAAGGCTAGACGGGAC	Construction of strain YNG004

Primers specifically designed for qRT-PCR assays.

Primers pairs	**Primers**	**Sequence (5'-3')**	**Gene**	**Amplicon (bp)**
1	fenD-for fenD-rev	ATGATGGACGGTTGGTGC CTGCTCTTTGTCTTGCTC	*fenD*	147
2	alsS-for alsS-rev	AGTGGTTTCTGTCTCTGGTG AATTGGTGCTTTTAGTCG	*alsS*	82
3	albE-for albE-rev	ACTTGTCTTTCCCTTCTTCTC CGCCTTTATCCTGTCTCTCC	*albE*	185
4	bacB-for bacB-rev	GCAAGAAACGACACAGACCA CTACCCAATCCTCAACAAAGAAC	*bacB*	160
5	srfAA-for srfAA-rev	TGGTGATGCTTTCCGCTTAC GAGTGATTTCTGCCCGCT	*srfAA*	94
6	rpsJ-for rpsJ-rev	TCTGGTCCGATTCCGTTGCC CAGTTTGTGGTGTTGGGTTCA	*rpsJ*	142

Supplementary figures

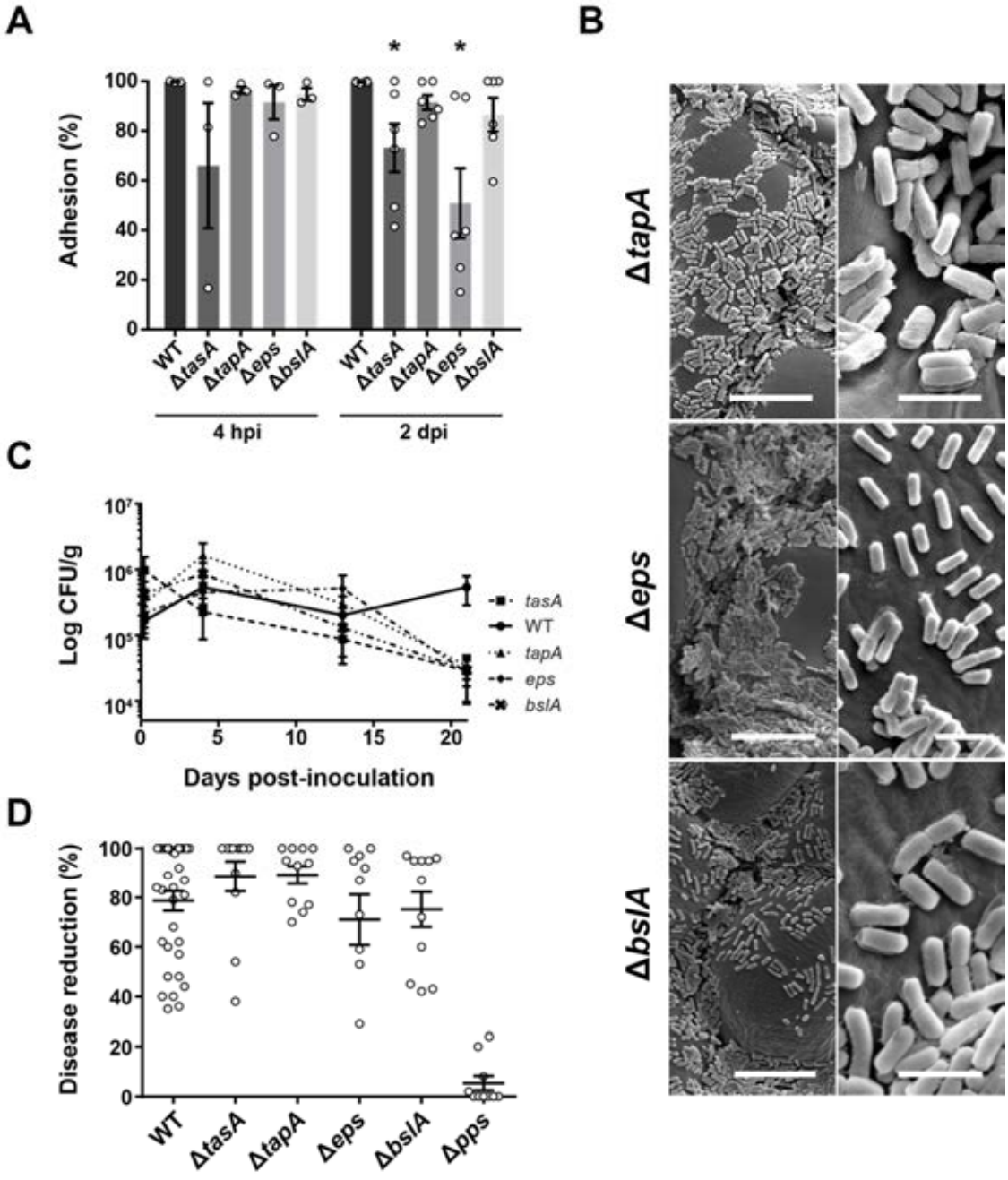

Figure S3.1. Interaction of *Bacillus subtilis* strains with single mutations in ECM components with melon leaves. **A)** Adhesion of the ECM single mutants to melon leaves 4 h and 2 days post-inoculation (hpi and dpi, respectively). The *tasA* and *eps* mutants were the only matrix single mutant strains whose adhesion to melon leaves was significantly affected 2 days post-inoculation (dpi). The points refer to the number independent experiments. In each experiment, 10 leaves were analyzed. Average values are shown. Error bars represent the SEM. Statistical significance was assessed via Kruskal-Wallis test with Dunnet multiple comparisons test (* $p<0.05$). **B)** The Δ*eps*, Δ*bslA* and Δ*tapA* strains showed a colonization pattern in which the cells. were distributed randomly over the leaf surface with no connection between the cells or extracellular material. Scale bars = 12.5 µm (left) or 2.5 µm (right). **C)** All of the matrix single mutants showed decreased persistence on plant leaves. The first point is taken at 4 hpi. Average values of 5 biological replicates are shown with error bars representing the SEM. **D)** Strains with *tapA* mutations (i.e., fewer amyloid fibers) showed as much biocontrol activity as that of the WT strain. The *eps* and *bslA* mutant strains showed reduced antagonistic activity compared to that of the WT strain. The points refer to the number of plants analyzed over three independent assays. Three leaves per plant were infected and inoculated. Average values are shown with error bars indicating the SEM.

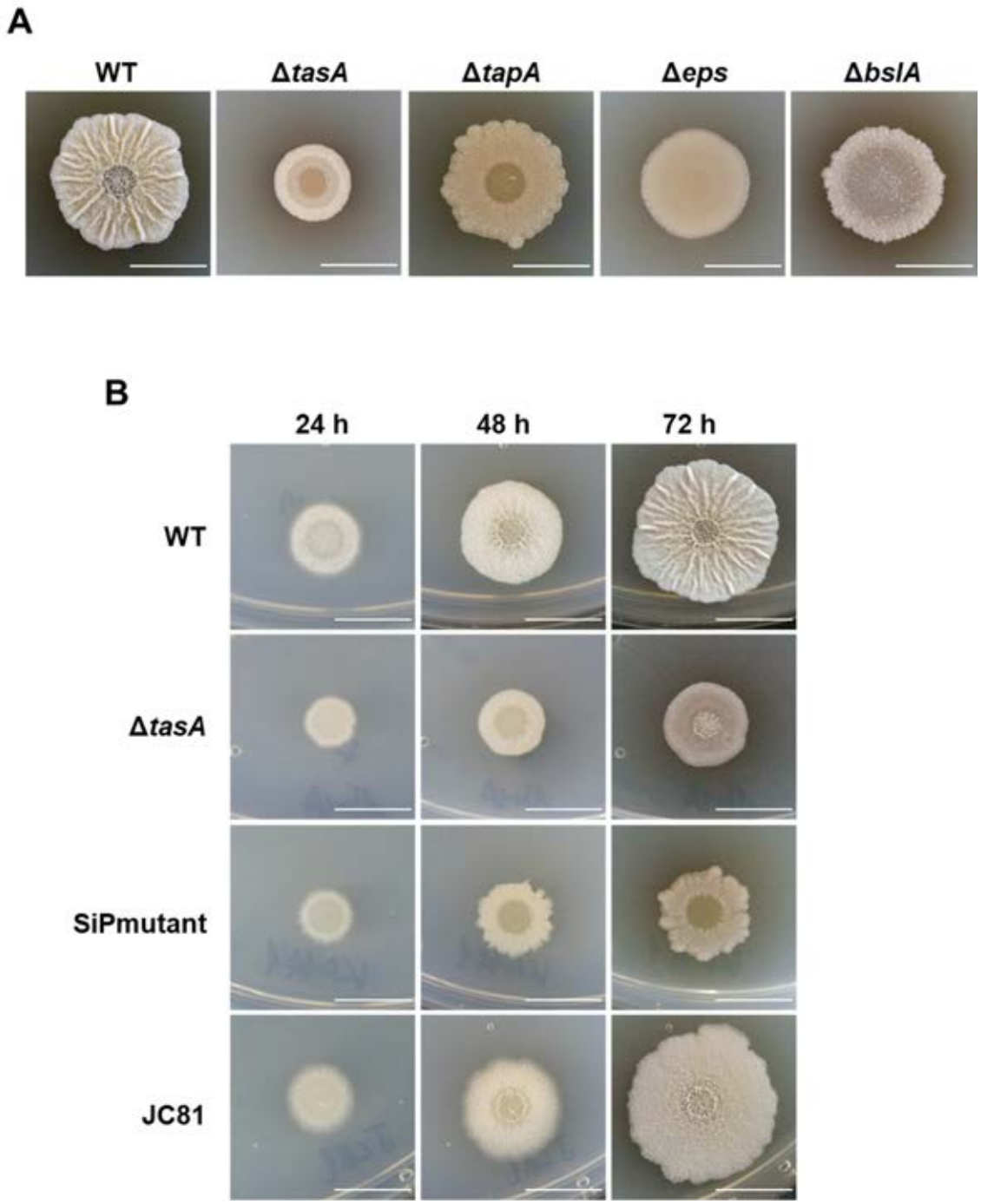

Figure S3.2. Morphology of the *Bacillus subtilis* matrix mutants grown under biofilm-inducing conditions. A) Colony morphologies of the ECM single mutant strains after 72 h of growth on MSgg agar plates. **B)** Time course of the colony morphologies of the WT, ΔtasA, SiPmutant (Lys4Ala, Lys5Ala, Lys6Ala) and JC81 (Lys68Ala, Asp69Ala) strains. Scale bars = 1 cm.

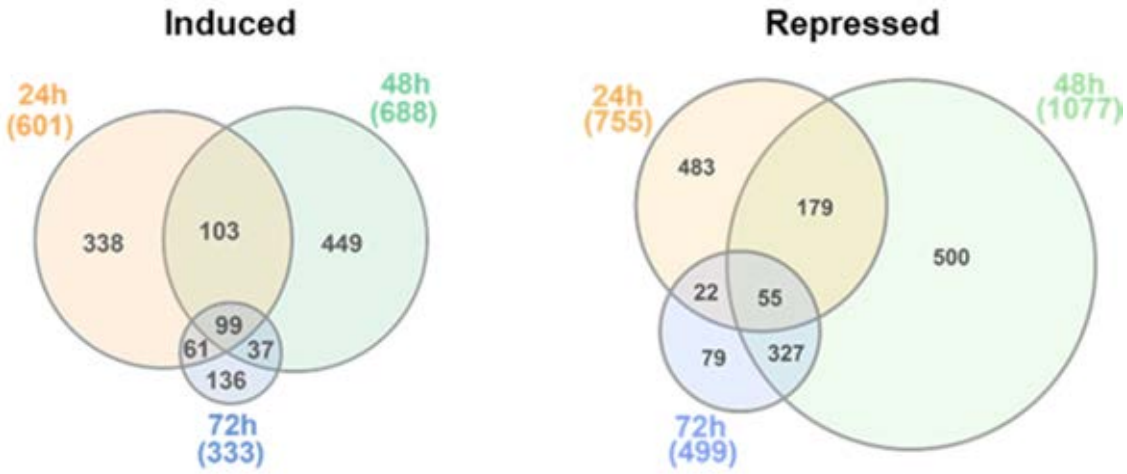

Figure S3.3. Deletion of *tasA* has pleiotropic effects on gene expression. Venn diagrams showing the differentially expressed genes at 24 h, 48 h and 72 h in Δ*tasA* compared to the WT.

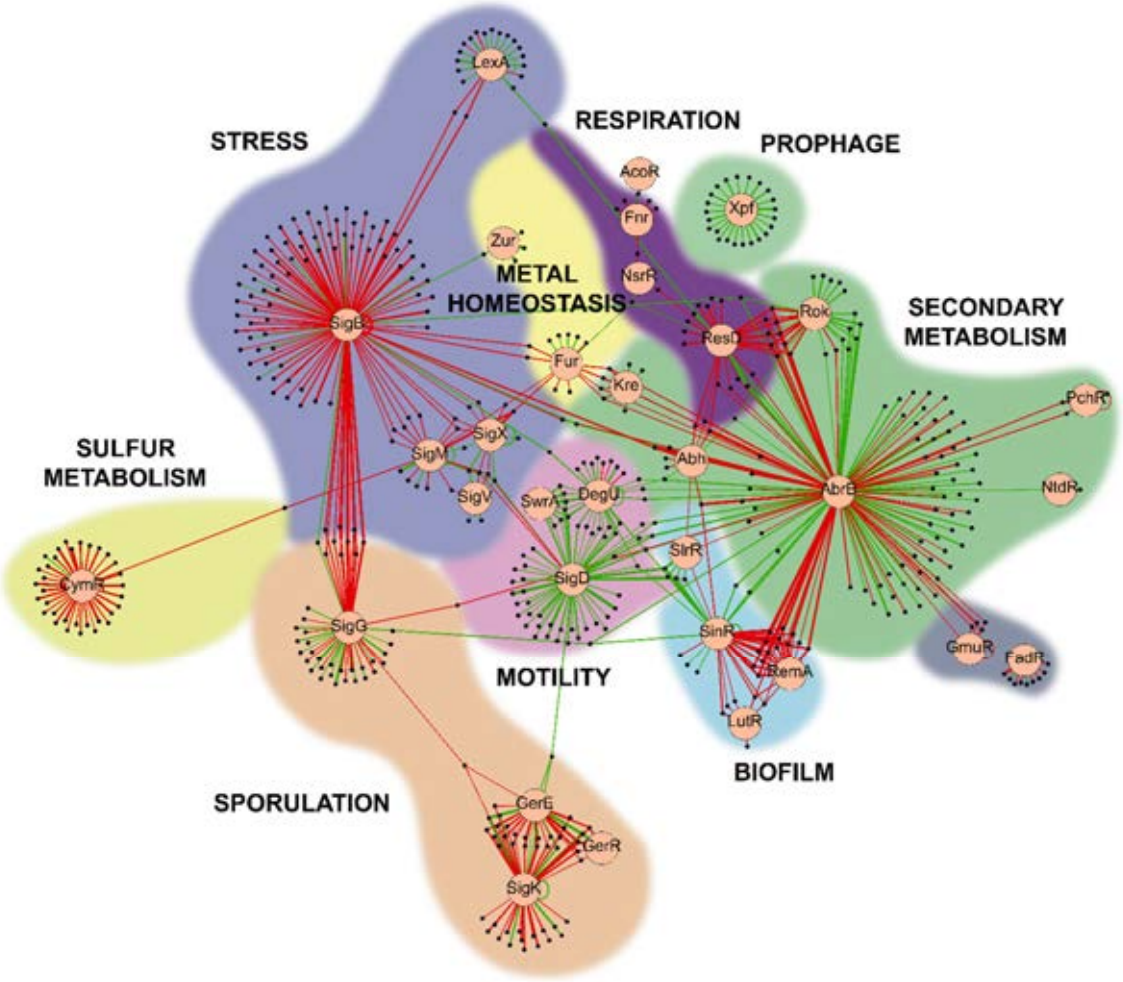

Figure S3.4. Regulation networks affected in a *tasA* mutant at 24 h. Regulation networks of the differentially expressed genes in Δ*tasA* compared to the WT at 24 h. The bigger circles indicate de main regulator of that regulon, which is surrounded by arrows pointing to smaller circles that are the differentially expressed genes. The thickness of the arrows indicates expression levels. The color in the arrows indicates induction (red) or repression (green).

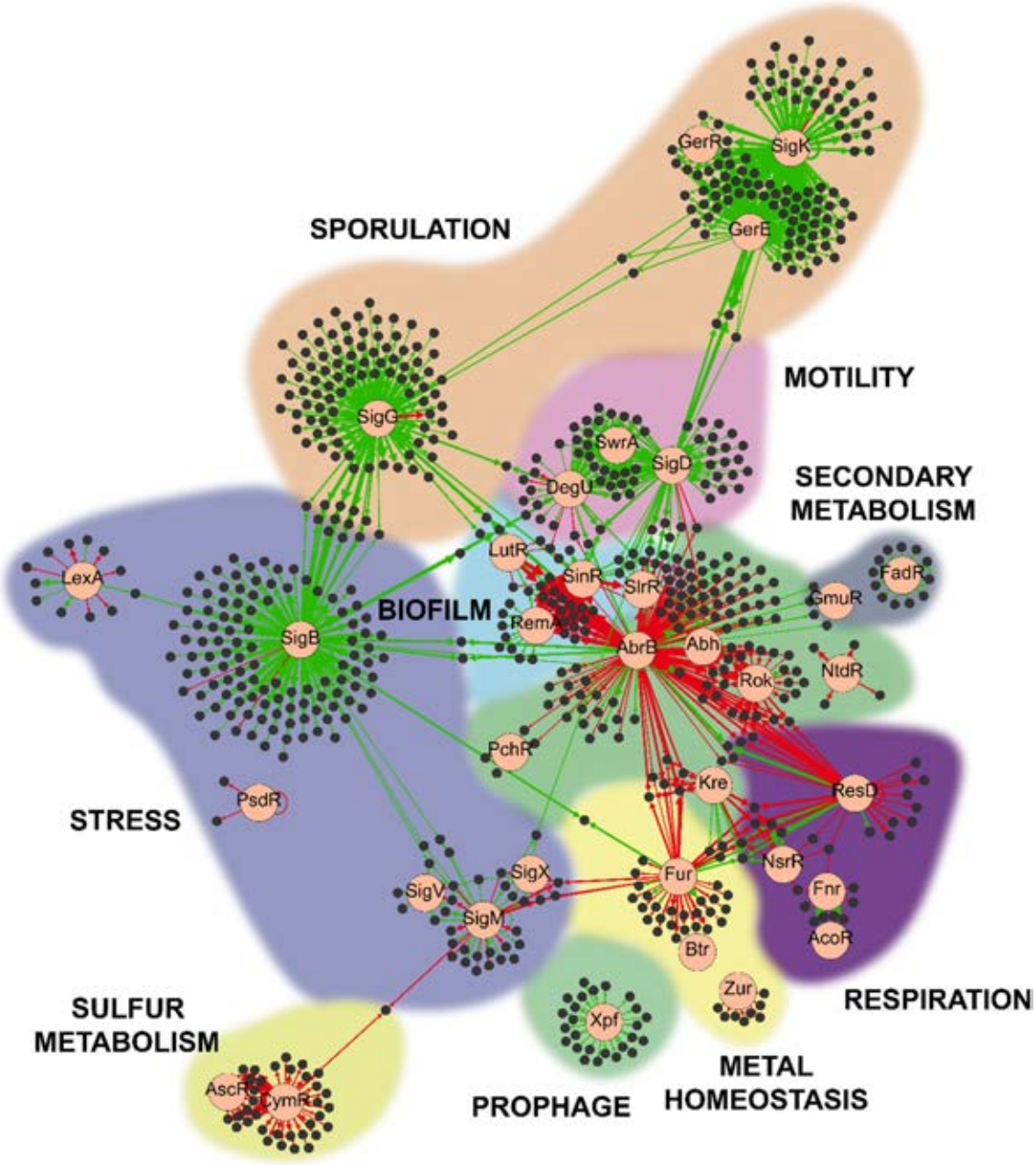

Figure S3.5. Regulation networks affected in a *tasA* mutant at 48 h. Regulation networks of the differentially expressed genes in Δ*tasA* compared to the WT at 48 h. The bigger circles indicate de main regulator of that regulon, which is surrounded by arrows pointing to smaller circles that are the differentially expressed genes. The thickness of the arrows indicates expression levels. The color in the arrows indicates induction (red) or repression (green).

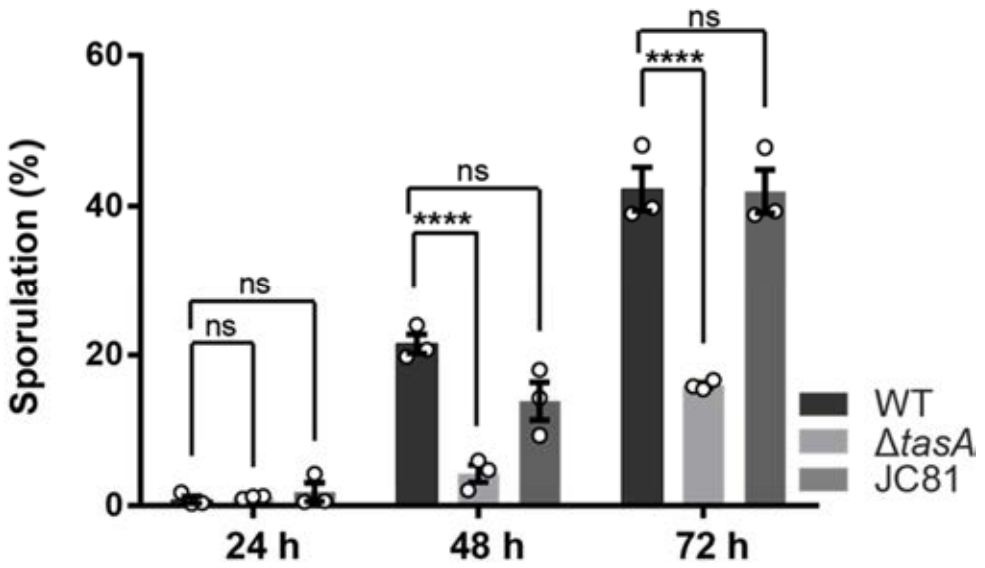

Figure S3.6. The Δ*tasA* strain shows a lower percentage of sporulation compared to those of the WT and JC81 strains. Sporulation rates of the WT, Δ*tasA* and JC81 colonies 24 h, 48 h and 72 h. The Δ*tasA* colonies showed a sporulation delay typical of ECM mutants with significant differences compared to the WT colonies at 48 h and 72 h. Mean values of three biological replicates are shown. Error bars represent the SEM. Statistical significance was assessed via two-tailed independent t-tests at the corresponding time-points (**** p<0.0001).

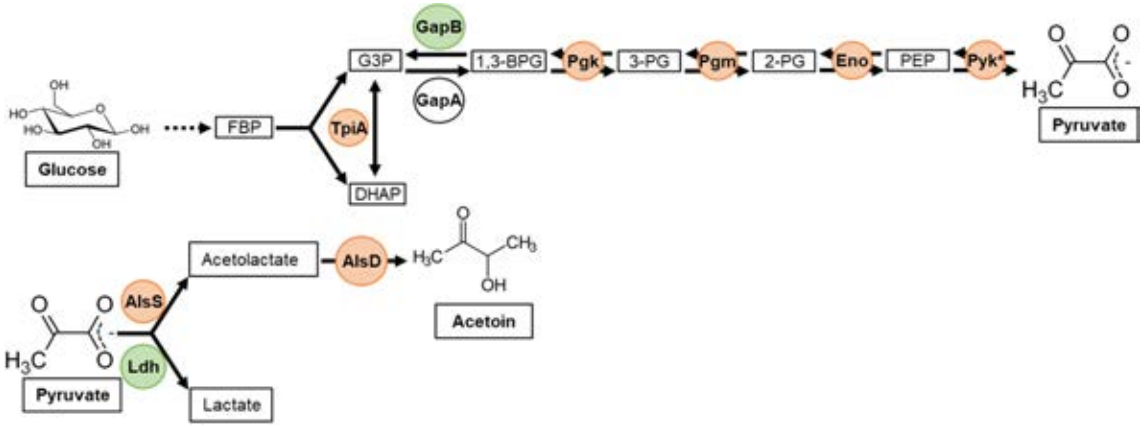

Figure S3.7. Deletion of *tasA* affects gene expression. The diagram shows the pathway that terminates in acetoin synthesis. Some steps of the glycolysis pathway (arrows to the right) are induced in the *ΔtasA* strain, whereas the divergent or gluconeogenetic steps (arrows to the left) are repressed at 72 h. Green indicates repression. Red indicates induction.

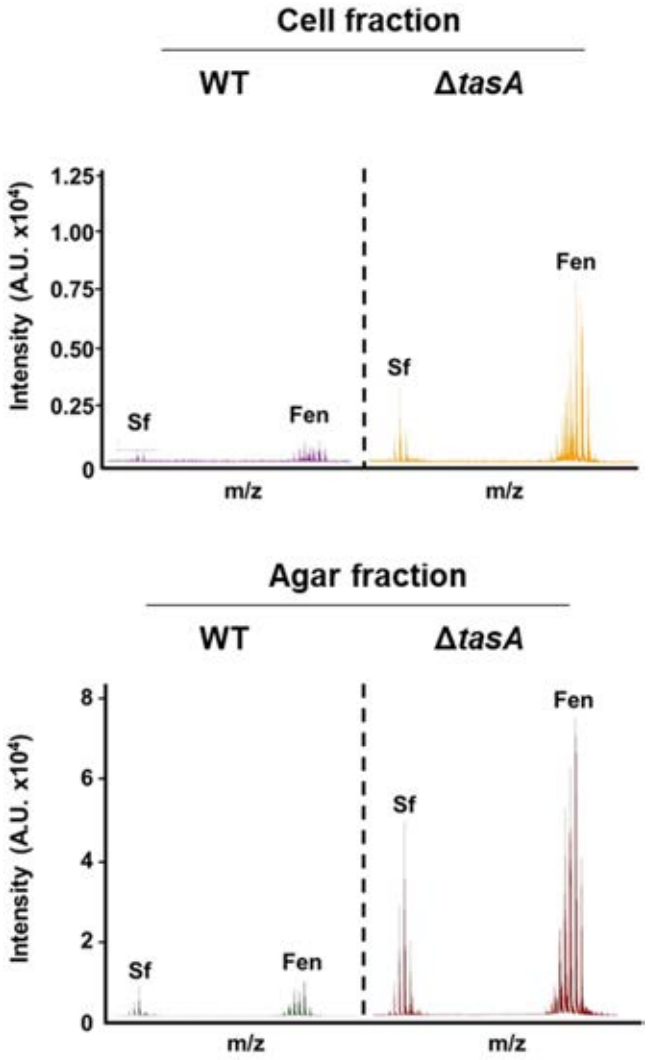

Figure S3.8. Δ*tasA* produced higher relative amounts of fengycin. Mass spectra corresponding to the cells (top) or the agar (bottom) fractions of the WT or ΔtasA colonies grown on solid MSgg for 72 h.

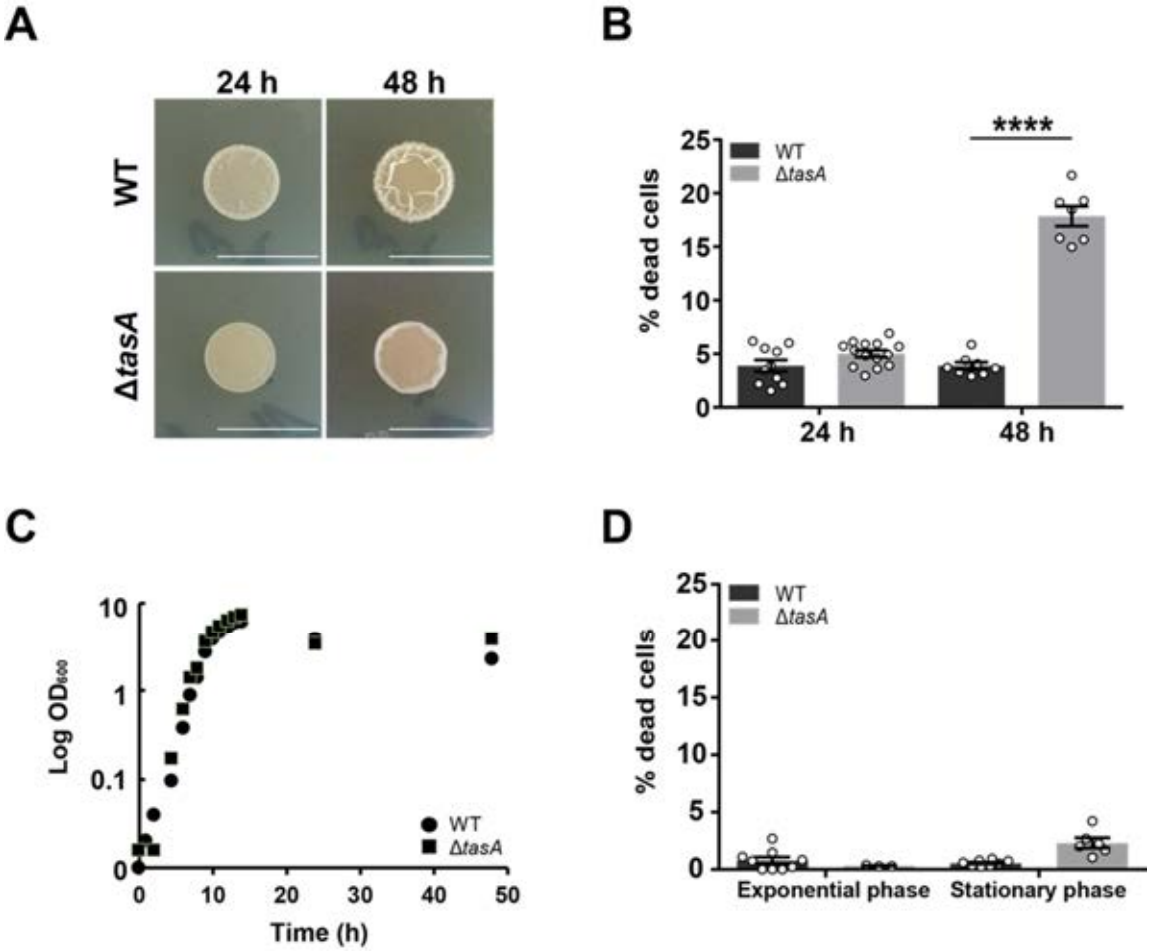

Figure S3.9. The physiological phenotypes observed in Δ*tasA* are independent of media composition. A) Colony morphologies of WT or Δ*tasA* growing in LB plates for 48 h. Scale bars = 1 cm. **B)** Quantification via CLSM of the proportions of dead cells found in the WT or Δ*tasA* colonies grown on solid LB for 24 or 48 h. The points indicate the number of colonies examined over three independent experiments. The error bars represent the SEM. Statistical significance was assessed via two-tailed independent t-test at each time-point (**** p<0.0001). For each experiment and sample, at least three fields-of-view were measured. **C)** Growth curves of the WT strain and Δ*tasA* strain in liquid MSgg. No differences were observed in the growth rates of both strains in these experimental conditions. **D)** Quantification via CLSM of the proportions of dead cells found in the WT or Δ*tasA* liquid MSgg cultures in exponential or stationary phase. All samples were measured over three independent experiments. For each experiment and sample, at least three fields-of-view were measured. Average values are shown.

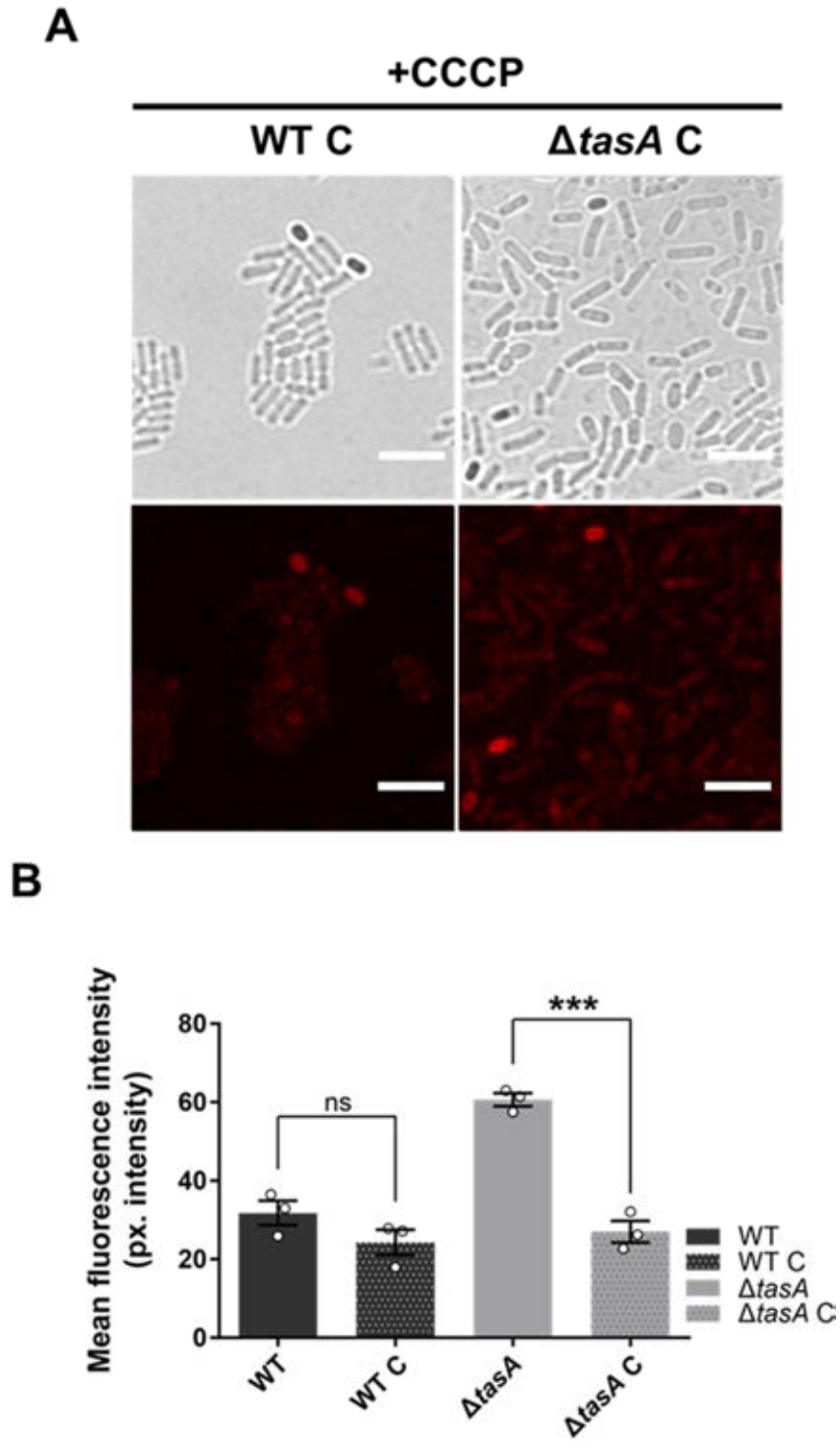

Figure S3.10. Treatment of WT and *ΔtasA* cells with CCCP caused a decrease in membrane potential. A) As a control for the TMRM experiments, CLSM analysis of 72-hour-old WT and *ΔtasA* colonies treated with CCCP, a known ionophore that causes proton gradient disruption and depolarization, was performed. The WT cells showed a natural decay in their membrane potential over time; therefore, at 72 h, CCCP had very little effect (WT C). However, in the *ΔtasA* cells, which showed hyperpolarization at 72 h, CCCP had a major effect on the membrane potential (*ΔtasA* C), as it could depolarize cells to a level comparable to that in WT C. Scale bars = 5 μm. **B)** Quantification of the TMRM signals in WT C and *ΔtasA* C showed statistically significant differences in Δ*tasA* C at 72 h compared to that of the untreated sample. The points indicate the number of colonies examined over three independent experiments. For each experiment and sample, at least three fields-of-view were measured. Average values are shown. Error bars indicate the SEM. Statistical significance was assessed via two-tailed independent t-tests between treated and untreated samples (*** p<0.001).

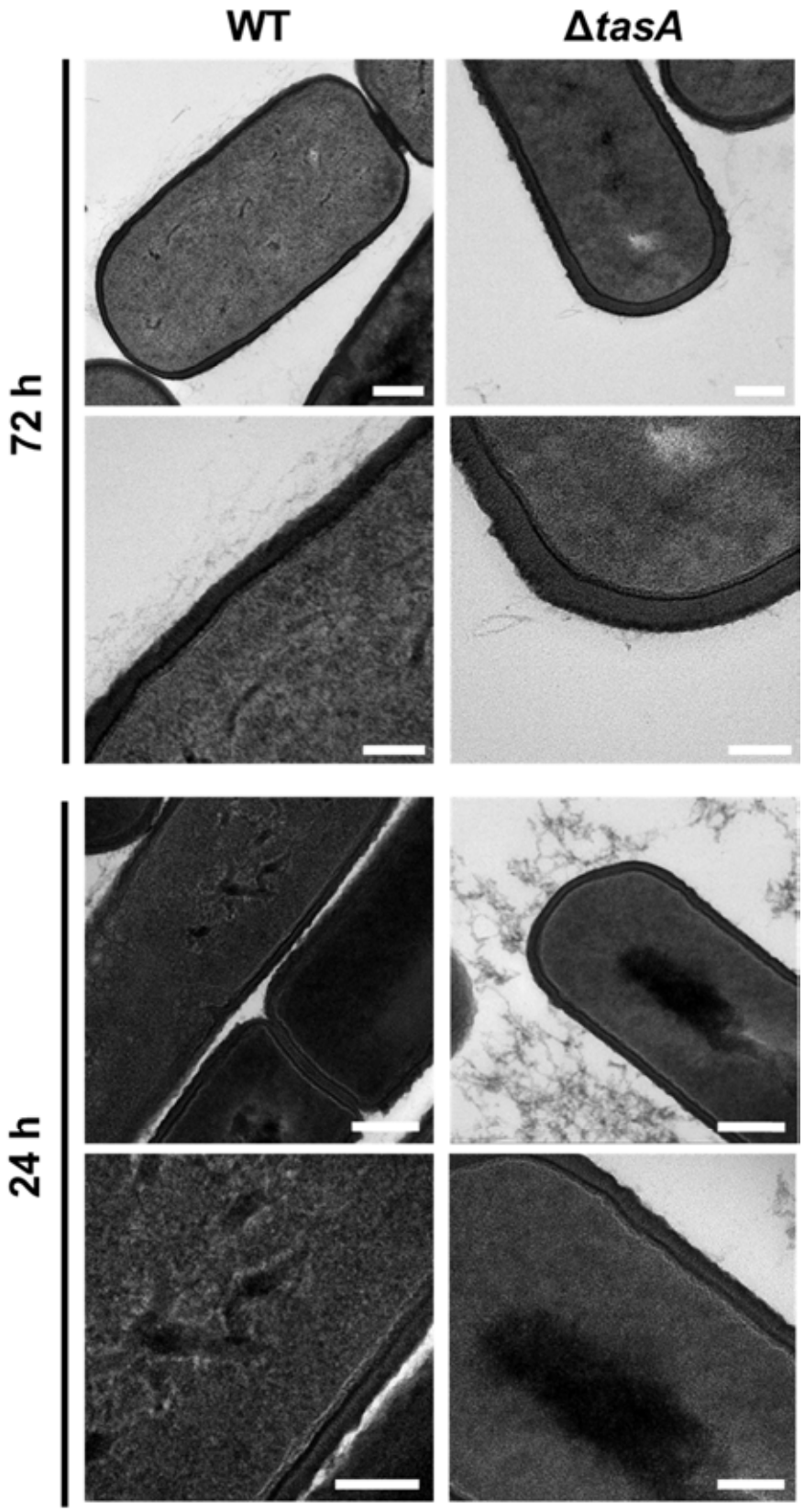

Figure S3.11. No structural alterations were found on the surfaces of Δ*tasA* cells. Transmission electron micrographs of thin sections of embedded WT and *ΔtasA* cells at 24 and 72 h. The details of the cell surfaces show no differences in shape, integrity or thickness. Scale bars = 200 nm (top images) or 100 nm (bottom images).

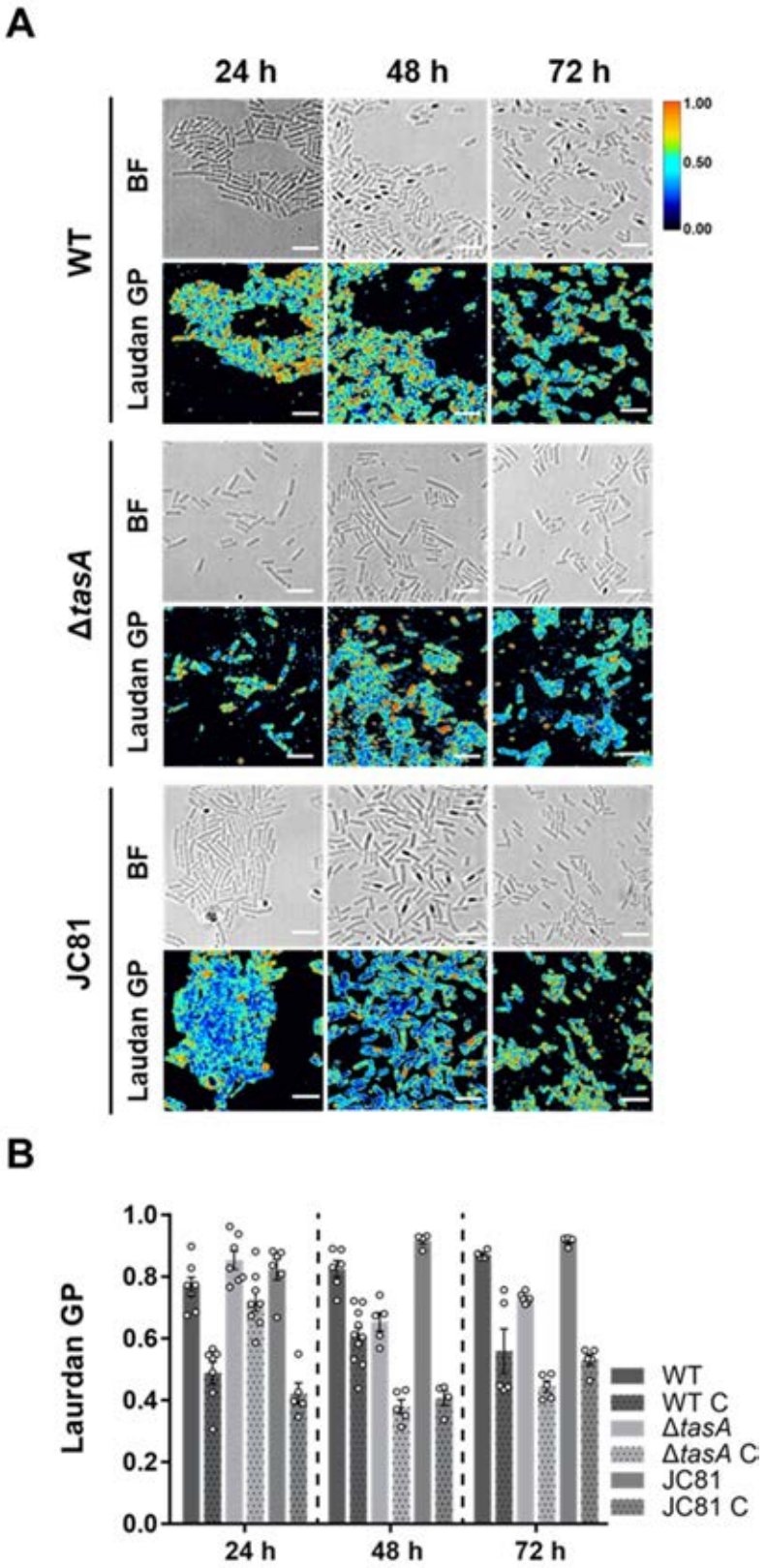

Figure S3.12. Membrane fluidity is increased upon treatment of the cells with benzyl alcohol. A) The Laurdan GP values of WT, *ΔtasA* and JC81 cells treated with 2% benzyl alcohol, a known membrane fluidifier, at 24, 48 and 72 h, were used as controls. The processed Laurdan GP images show decreased Laurdan GP values (i.e., increased membrane fluidity) at all time points in all of the strains upon treatment with benzyl alcohol compared with the values of the untreated samples. A calibration bar (from 0 to 1) is located on the right. Scale bars = 5 μm. **B)** Quantification of the Laurdan GP values in benzyl alcohol-treated samples. The points indicate the number of colonies examined over three independent experiments. For each experiment and sample, at least three fields-of-view were measured. Average values are shown, with error bars indicating the SEM.

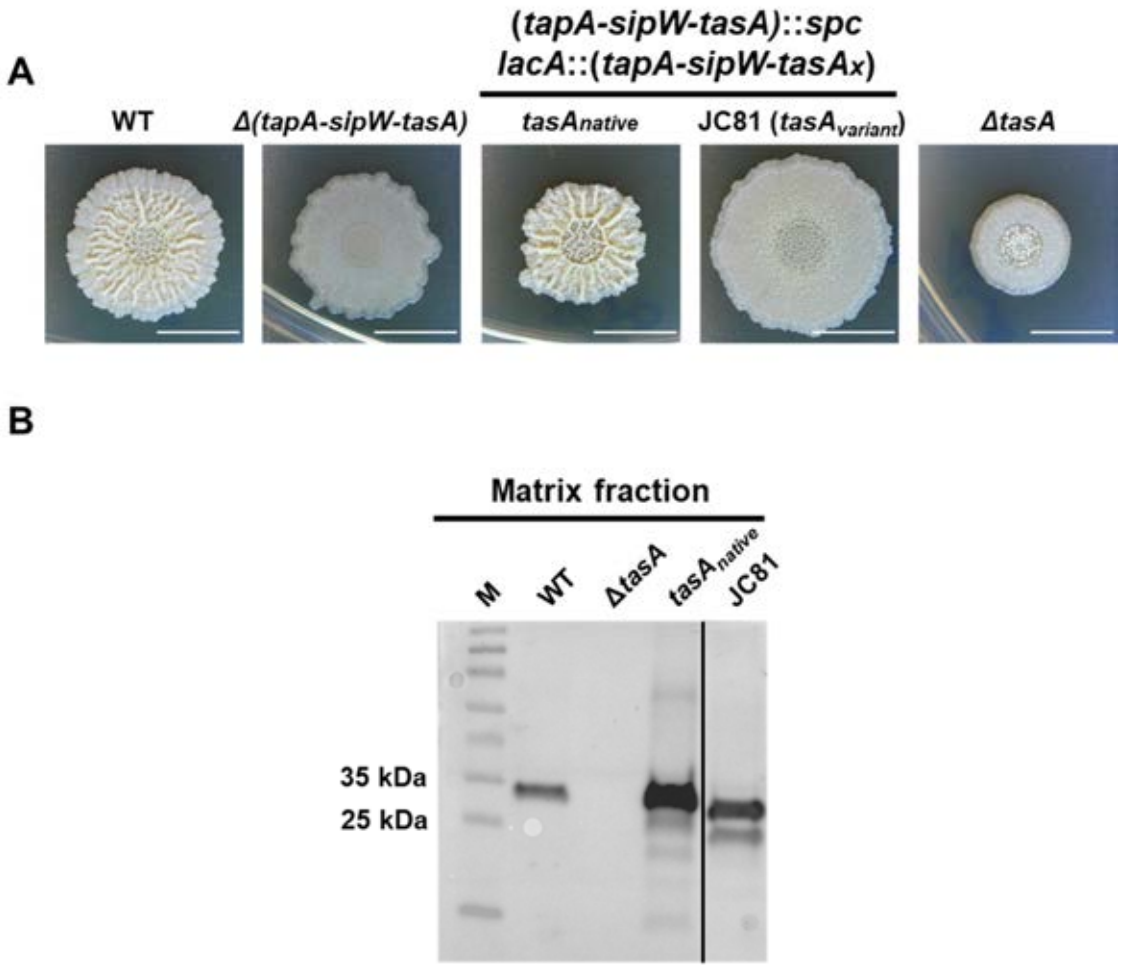

Figure S3.13. Phenotypes of the JC81 strain, which carries an allelic variant of *tasA* (Lys68Ala, Asp69Ala). A) A *Δ*(*tapA-sipW-tasA*) strain was used as the genetic background for introducing the entire operon (in *lacA*, a neutral locus) with different versions of *tasA* in which some amino acids were substituted with alanine via site-directed mutagenesis. Colony morphologies of the different *B. subtilis* mutants on MSgg agar plates. From left to right: WT, *Δ*(*tapA-sipW-tasA*), *Δ*(*tapA-sipW-tasA*)::(*tapA-sipW-tasA*$_{native}$) (containing a WT version of the gene), *Δ*(*tapA-sipW-tasA*)::(*tapA-sipW-tasA*$_{variant}$) (strain JC81, containing the Lys68Ala, Asp69Ala allele) and Δ*tasA*. Scale bars = 1 cm. **B)** Western blot of the biofilm matrix fraction analyzed with anti-TasA antibody. Immunoblot images have been cropped and spliced for illustrative purposes. Black lines over the blot images delineate boundaries of immunoblot splicing.

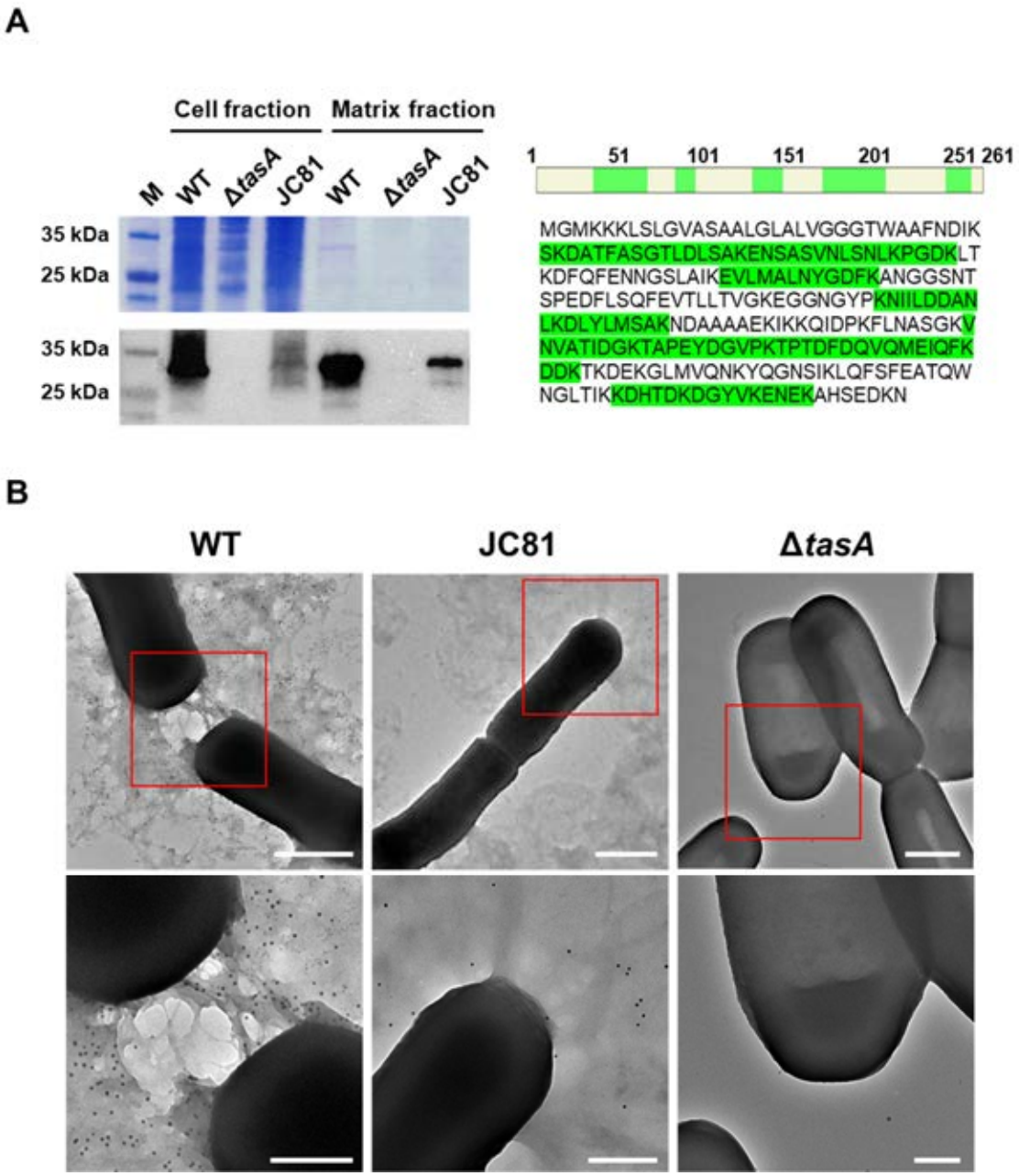

Figure S3.14. The TasA produced by JC81 strain (expressing the TasA variant Lys68Ala, Asp69Ala) corresponds to the mature form of the protein. A) Biofilm fractionation of WT, Δ*tasA* or JC81 colonies and SDS-PAGE of the different fractions followed by Coomassie Blue staining or western blot. The highest band in lane 6 was cut and analyzed via mass spectrometry analysis. The coverage obtained is shown on the right. Gel and blot images have been cropped for illustrative purposes. **B)** Transmission electron micrographs of negatively stained, anti-TasA immunogold labeled samples from cells grown for 48 h in biofilm-inducing conditions. Scale bars = 500 nm (top) and 200 nm (bottom).

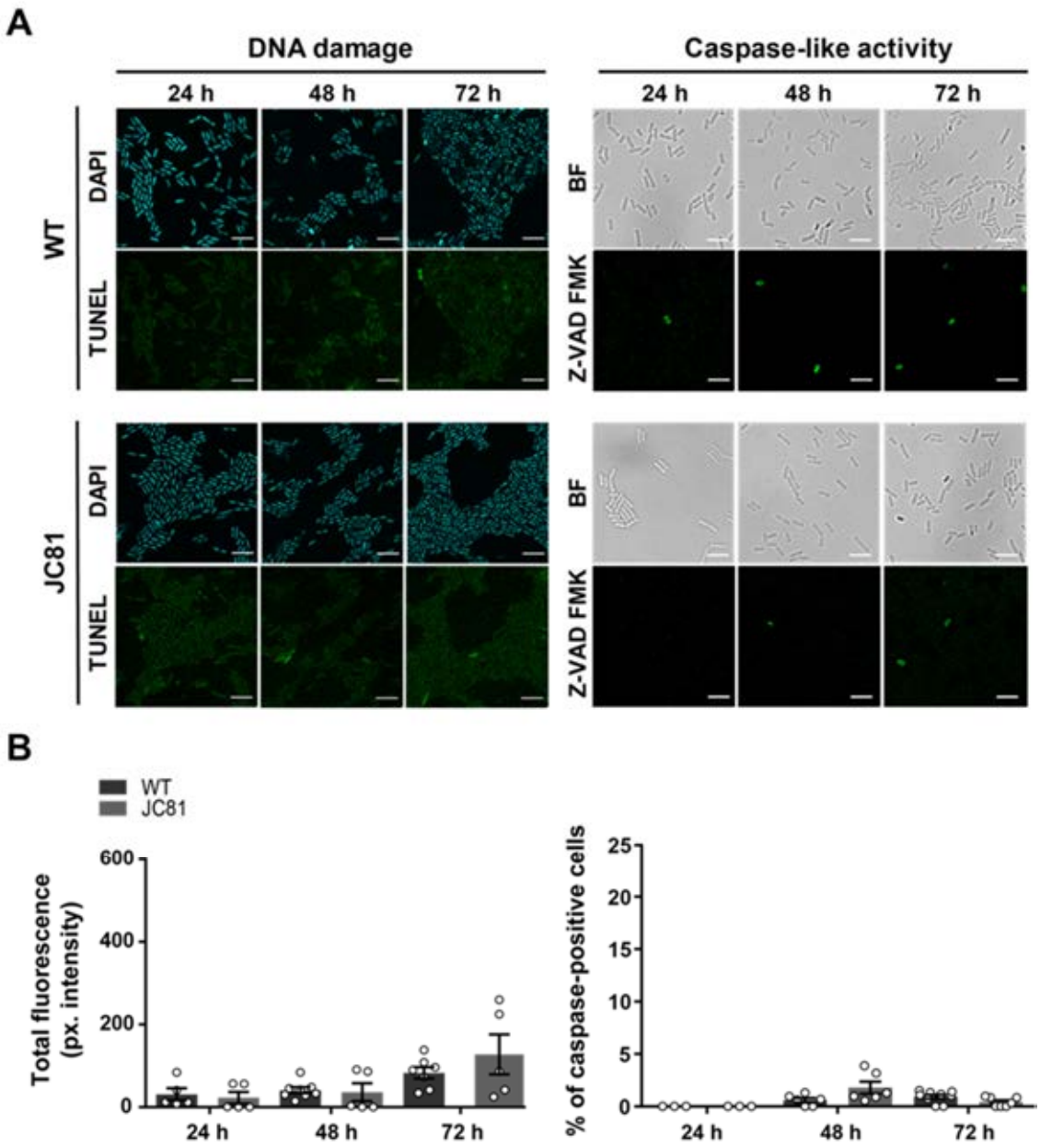

Figure S3.15. JC81 showed no difference in the levels of DNA damage or caspase-like activity compared with those of the WT strain. A) Left. TUNEL assay and CLSM analysis revealed no difference in the levels of DNA damage between JC81 colonies and WT colonies. Right. CLSM analysis of cells stained with the FITC-conjugated caspase substrate inhibitor Z-VAD-FMK indicated no significant difference in the caspase-like activity of JC81 cells (bottom panels) compared to that of the WT cells (top panels). Bright field images (top) are shown for reference. Scale bars = 5 µm. **B)** Left. Quantification of the TUNEL signals in WT and JC81 colonies showed similar values. The points indicate the number of colonies examined over three independent experiments. For each experiment and sample, at least three fields-of-view were measured. Error bars indicate the SEM. Right. Quantification of cells positive for caspase-like activity (stained with FITC-Z-VAD-FMK) in WT or JC81 colonies. No significant differences were found at the analyzed time-points. The points indicate the number of colonies examined over three independent experiments. For each experiment and sample, at least three fields-of-view were measured. Error bars indicate the SEM.

.

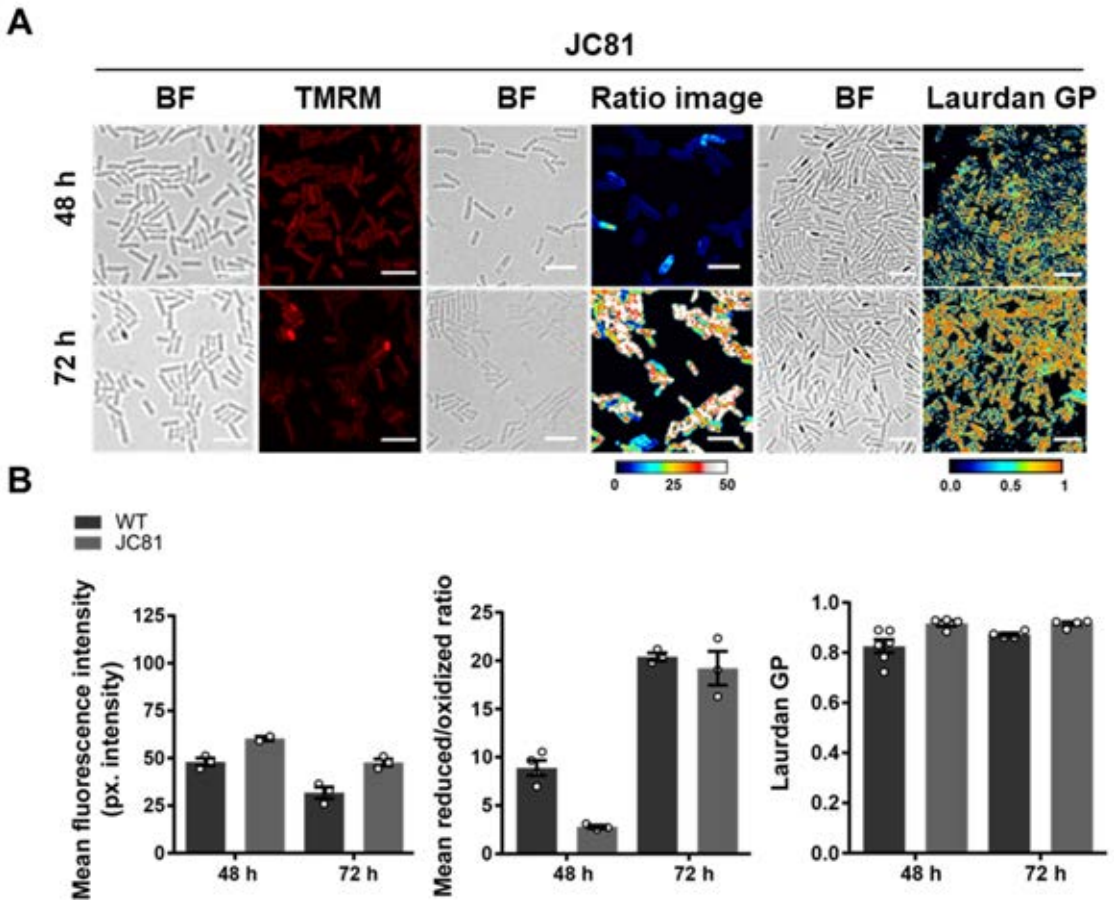

Figure S3.16. The allelic variant of *tasA* (Lys68Ala, Asp69Ala) present in JC81 strain restores the physiological status of Δ*tasA* cells. A) Left panel. A TMRM assay of JC81 cells shows similar membrane potential as WT cells. Center panel. Assessment of the lipid peroxidation levels using BODIPY 581/591 C11 reagent in JC81 cells after treatment with 5mM CuHpx and analysis by CLSM. The ratio images represent the ratio between the two states of the lipid peroxidation sensor: reduced channel (590-613 nm emission)/oxidized channel (509-561nm emission). The ratio images were pseudo-colored depending on the reduced/oxidized ratio values. A calibration bar (from 0 to 50) is located at the bottom of the panel. Confocal microscopy images show that CuHpx treatment was ineffective in the JC81 strain at 72 h. Right panel. Laurdan GP analyzed via fluorescence microscopy. The images were taken at two different emission wavelengths (gel phase, 432 to 482 nm and liquid phase, 509 to 547 nm) that correspond to the two possible states of the Laurdan reagent depending on the lipid environment. The Laurdan GP images represent the Laurdan GP value of each pixel (see Materials and methods). The Laurdan GP images were pseudo-colored depending on the laurdan GP values. A calibration bar (from 0 to 1) is located at the bottom of the set. The Laurdan GP images of JC81 cells show similar membrane fluidity as WT cells at 48 and 72 h. All scale bars are equal to 5 μm. **B)** Quantification of the TMRM signal, lipid peroxidation and laurdan GP revealed no differences between the WT and JC81 colonies at 48 and 72 h. For each assay, the points indicate the number of colonies examined over three independent experiments. Average values are shown with error bars representing the SEM. For each experiment and sample, at least three fields-of-view were measured.

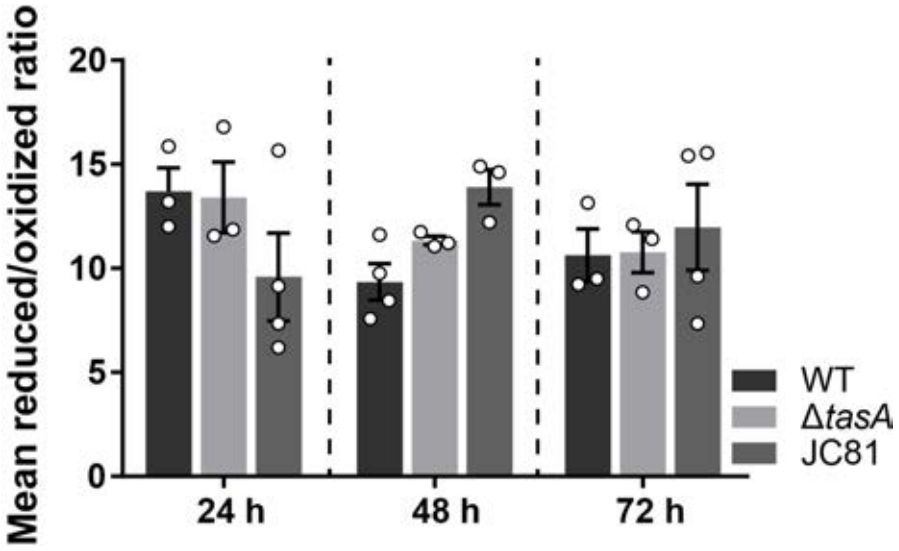

Figure S3.17. Untreated cells from the WT, Δ*tasA* and JC81 strains show no differences in the endogenous levels of lipid peroxidation. Assessment of lipid peroxidation in untreated WT, Δ*tasA* and JC81 colonies. The points indicate the number of colonies examined over three independent experiments. Quantification of the lipid peroxidation from the ratio images shows no differences in the reduced/oxidized ratio between the strains at the different time points. Average values are shown. Error bars indicate the SEM.

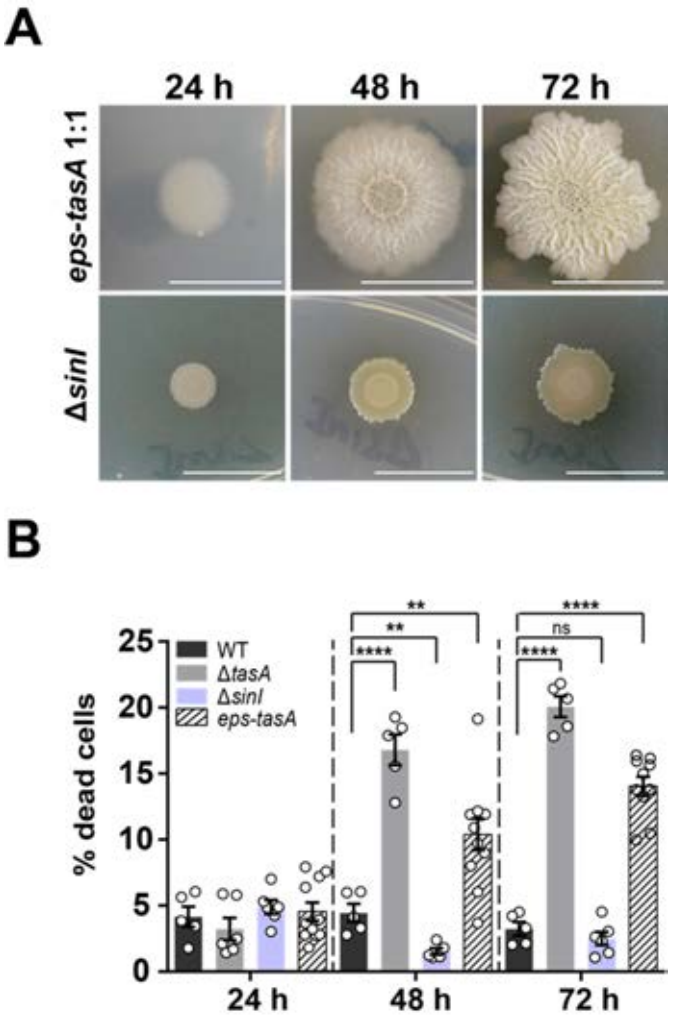

Figure S3.18. The physiological function of TasA does not rely on ECM assembly. A) Colony morphologies at 72 h of a mixture of Δ*tasA* and Δ*eps* strains co-inoculated at a 1:1 ratio and a Δ*sinI* strain. Scale bars = 1 cm. **B)** Quantification via CLSM of the proportion of dead cells found in the WT, Δ*tasA*-Δ*eps* mixture and Δ*sinI* colonies grown on solid MSgg for 24, 48, and 72 h. The points represent the number of colonies examined over three independent experiments. Average values are shown with error bars representing the SEM. Statistical significance was assessed via two-tailed independent t-tests at each time-point comparing with the WT strain (** p< 0.01 **** p<0.0001).

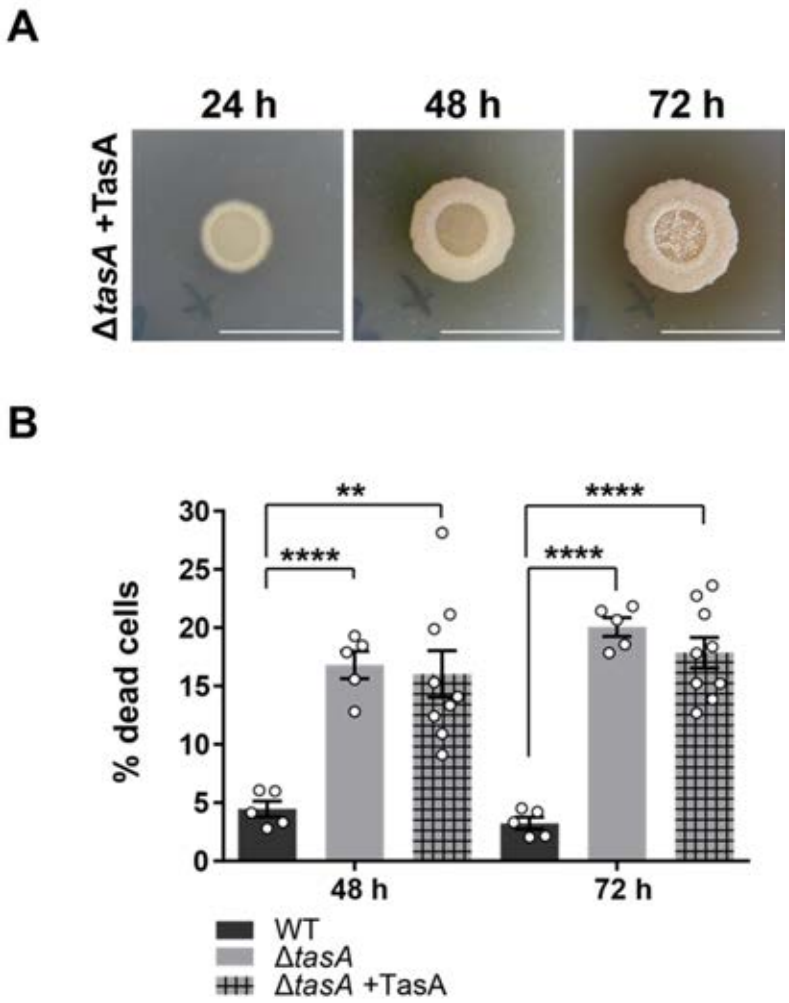

Figure S3.19. Exogenous addition of TasA to solid medium does not complement the functionality of TasA. A) Colony morphologies of a Δ*tasA* strain complemented with 80 µg of purified TasA protein on solid medium at 24, 48 and 72 h. Scale bars = 1 cm. **B)** Quantification via CLSM of the proportions of dead cells found in the WT (N = 5) and complemented Δ*tasA* colonies grown in solid MSgg for 48, and 72 h. The points represent the number of colonies examined over three independent experiments. Average values are shown with error bars representing the SEM. Statistical significance was assessed via two-tailed independent t-tests at each time-point comparing with the WT strain (**** p<0.0001, ** p<0.01).

Chapter IV

Interaction of TasA with lipid bilayers is key for membrane dynamics and cell physiology

ABSTRACT

The functional amyloid TasA is the main component of the amyloid fibers found in the extracellular matrix of *Bacillus subtilis* biofilms. In a previous study, we demonstrated the role of TasA in bacterial physiology preventing premature cell death independently from its functionality in biofilm formation. Here, we demonstrate using microscopy and biophysical approaches, that TasA exerts this newly described function by being able to interact with biological membranes. TasA is found associated to detergent-resistant fractions of the cell membrane, likely related to functional membrane microdomains, where it imposes a direct effect in membrane fluidity and localization of the flotillin-like protein FloT. Our data shows that, *in vitro*, the interaction of TasA with model membranes relies on the sequence properties of the N-terminal amyloid core and is dependent on the lipid composition. We conclude that alternatively to the ECM, TasA is a membrane-bound protein that provides stability to the cell membrane.

INTRODUCTION

The bacterial cell surface is a platform where a variety of structures and appendages participate in the interaction of microorganisms with their environment[1]. As part of the surface, the bacterial extracellular matrix (ECM) is one of the most important bacterial structures secreted by the bacterial community, that ends, in turn, embedded within this milieu as a result of biofilm formation[2]. The formation of biofilms is one of the most intriguing lifestyles of bacteria, which are defined as bacterial communities attached to any surface. These communities are formed as a result of a complex developmental program, in which diverse signaling pathways converge to synthesize and secrete the ECM[3]. In *Bacillus subtilis,* a soil dwelling bacterium, the structural elements of the ECM are very diverse: the exopolymeric substances (EPS), mainly comprised by the exopolysaccharides, are the main adhesive element within the ECM, playing a role in the cohesion of the cells and mediating the cell-to-surface interaction[4]; the hydrophobin BslA forms a thin proteinaceous layer over the surface of the ECM and confers the biofilm its hydrophobic properties[5]; and finally, the amyloid fibers, which are the main protein component of the ECM and act as a protein scaffold that provides structural integrity to the biofilm[6-8]. These fibers consist of a major protein, TasA[9], which is a functional amyloid able to polymerize into the form of filaments with formidable robustness and resistance against different physicochemical aggressions[6], and an accessory protein, TapA, that assists the polymerization of these fibers[10].

Amyloid proteins are infamously known for their role in protein misfolding and disease[11], however, in recent years, amyloid proteins have appeared involved in different functions in a broad range of organisms, which is the reason for their designation of part of this family of proteins as functional amyloids. Bacteria have exploited the exclusive features of the amyloid fold for different functions such as biofilm formation, bacterial competition or cell-host interactions[12]. Consistent with this notion of multifunctionality attributed to amyloid proteins, in a previous work, we have demonstrated that TasA, beyond its structural role as part of the amyloid fiber, participates in the stabilization of cellular physiology during colony development, preventing the premature cell death of part of the population. A Δ*tasA* strain shows transcriptional changes in more than a third of the genes at 48 h growing under biofilm inducing conditions, and exhibits an excess of cellular stress featured by DNA damage, hyperpolarization of the membrane potential or increased membrane fluidity that collectively deteriorate cellular physiology leading to decrease in cell viability. However, the mechanism by which TasA is responsible of this physiological function still remains unclear.

In every living cell, the plasma membrane acts as an interface for the interaction of the organism with its environment, controlling the trafficking of small molecules and secreted proteins, and sensing external stimuli that are transmitted to the different subsystems through signal transduction pathways[13]. Moreover, bacterial cell membranes are not as simple as initially thought, as they exhibit some of the features displayed by eukaryotic plasma membranes such as functional compartmentalization[14]. Indeed, several domains are found within the bacterial cell membrane. As eukaryotic lipid rafts, functional membrane microdomains (FMMs) in bacterial cell membranes[15] show unique lipid composition and are rich in proteins, since they organize protein complexes that are involved in signal transduction[16]. Of the many proteins present in the FMM, the bacterial flotillins play a crucial role, recruiting proteins to organize signaling networks that participate in many different biological processes such as biofilm formation or natural competence[17-20].

In this study we report the mislocalization of the flotillin protein FloT in the absence of TasA which, along with previous results, led us to hypothesize a role for TasA in the stabilization of the cell membrane. Moreover, we demonstrate that the functional amyloid TasA is present in the cell membrane, specifically, in the detergent resistant fraction (DRM) where most of the FMMs associated proteins are found. Localization studies of TasA by confocal microscopy showed that the protein is present homogeneously across the surface of the membrane except at the poles, where it forms two discrete foci. *In vitro* mechanistical analysis of the interaction of recombinant purified TasA with liposomes of different compositions by solid-state nuclear magnetic resonance spectroscopy (SSNMR) revealed that the lipid vesicles are able to accommodate the protein without suffering any structural perturbation. In addition, our data show that TasA increases the rigidity of the lipid environment and suggest a certain tendency of TasA to bind the curvature area of the cell membrane. Finally, permeabilization studies performed using fluorescence spectroscopy demonstrate that TasA shows specificity depending on the lipid composition.

Overall, we prove that TasA is located in the membrane, where it is involved in the stabilization and dynamics of cell membranes. These results concur with the cellular defects observed in the Δ*tasA* strain and provide a mechanistic insight for all the cellular and physiological alterations observed in the absence of this functional amyloid.

RESULTS

TasA associates with detergent resistant fractions of the cell membrane

In a previous work we have established the physiological defects that occur in Δ*tasA* cells including cytological changes such as: lower intracellular pH, decreased respiratory rates, increased generation of reactive oxygen species, higher levels of DNA damage, alterations in membrane potential and increased in membrane fluidity. The fact that a transcriptional response is observed as early as 24 h post-inoculation suggests that TasA is an intrinsic part of the cellular structure and therefore, its absence perturbates cell biology and physiology from the first stages of colony development.

The cytological defects observed in the absence of TasA, specially the negative effects on membrane dynamics due to changes in membrane potential and membrane fluidity, are, in bacterial cells, directly related to functional membrane microdomains (FMM). FMMs are specialized membrane domains that also regulate multiple important cellular functions[17-19,21]. The bacterial flotillins FloT and FloA are localized in FMMs and are directly involved in the regulation of membrane fluidity[21]. This line of evidence led us to propose a connection between the alterations in membrane fluidity and permeability found in Δ*tasA* cells with changes in the FMMs. We initially studied the membrane distribution of FloT as a marker for FMMs in WT and Δ*tasA* cells using a FloT-YFP translational fusion and confocal microscopy (Fig. 4.1A). The WT strain showed the typical FloT distribution pattern, in which the protein is located within the bacterial membrane in the form of discrete foci[15] (Fig. 4.1A top). However, in the Δ*tasA* cells, the fluorescent signal was visible only in a subset of the population, and the normal distribution pattern was completely lost (Fig. 4.1A bottom). In agreement with these findings, quantification of the fluorescent signal in WT and Δ*tasA* samples showed significant decreases in the signal of Δ*tasA* mutant cells at 48 and 72 h. Additionally, RNA-seq data showed fluctuations in the *floT* expression levels at all times (see chapter III, supplementary data 3.1, 3.2 and 3.3)

The loss of the normal distribution pattern of FloT in the cell membrane in the Δ*tasA* mutant cells led us to consider the presence of TasA in the cell membrane, likely, related to the FMMs. Membranes from both prokaryotes and eukaryotes can be separated into detergent-resistant (DRM) and detergent-sensitive fractions (DSM) based on their solubility in detergent solutions[15]. Although it is important to point out that the DRM and FMMs (or lipid rafts in eukaryotes) are not equivalent, the DRM fraction has a differential lipid composition and is enriched with proteins, rendering it more resistant to detergents;

furthermore, many of the proteins present in FMMs are also present in the DRM[22]. Immunodetection assays of the DRM, DSM and cytosolic fractions of each strain using an anti-TasA antibody showed the presence of anti-TasA reactive bands of the expected size primarily in the DRM fraction and in the cytosol (Fig. 4.1C top, lanes 1 and 3). As controls, the fractions from the *tasA* mutant showed no signal (Fig. 4.1C top, lanes 4, 5 and 6). Western blots of the same fractions isolated from WT and Δ*tasA* strains carrying a FloT-YFP translational fusion with an anti-YFP antibody (Fig. 4.1C bottom) confirmed that FloT was mainly present in the DRM of WT cells (Fig.4.1C bottom, lane 1). The signal was barely noticeable in the same fraction from Δ*tasA* cells (Fig. 4.1C bottom, lane 4), mirroring the reduced fluorescence levels observed via microscopy (Fig. 4.1A). We further validated the presence of TasA in the bacterial cell membrane by using a strain carrying a TasA-mCherry translational fusion (Fig. 4.1D and 4.2).

In order to validate the strain bearing the TasA-mCherry construct, we performed a biofilm assay to check whether TasA-mCherry is able to genetically complement the absence of native TasA (Fig. 4.2A). Our results show that, indeed, the strain expressing TasA-mCherry is able to recover the formation of wrinkles in a Δ*tasA* background, reflecting its proper functionality. A western blot using anti-TasA (Fig. 4.2B right) or anti-mCherry (Fig. 4.2B left) antibodies in the cells or matrix fractions of this strain grown in MSgg-agar for 48 hours, confirmed the presence of a band that, in both cases, correspond to the expected size of the TasA-mCherry fusion (Fig. 4.2B). An additional band corresponding to the size of mCherry (Fig. 4.2B left) or TasA (Fig. 4.2B right) alone is observed, most likely due to the unknown processing that naturally occurs in mature TasA (see chapter II, Fig. S2.1). All the appropriate fluorescence controls for these experiments were considered in order to ensure that the observed signals for TasA-mCherry or the membrane dye were real (Fig. 4.2C).

Confocal microscopy showed an overlap between the TasA-mCherry signal and the membrane-specific dye CellBrite Fix 488 (Fig. 4.1D, top). Interestingly, these images show that TasA is homogenously distributed across the cell membrane except for at the poles, where it frequently forms 2 small foci on each side (Fig. 4.1D, top). Second, the surfaces of protoplasted cells, i.e., cells lacking the peptidoglycan layer, were decorated with fluorescent signal corresponding to the TasA-mCherry fusion protein (Fig. 4.1D bottom). These results confirm that TasA is, indeed, associated with the DRM fraction of the cell membrane.

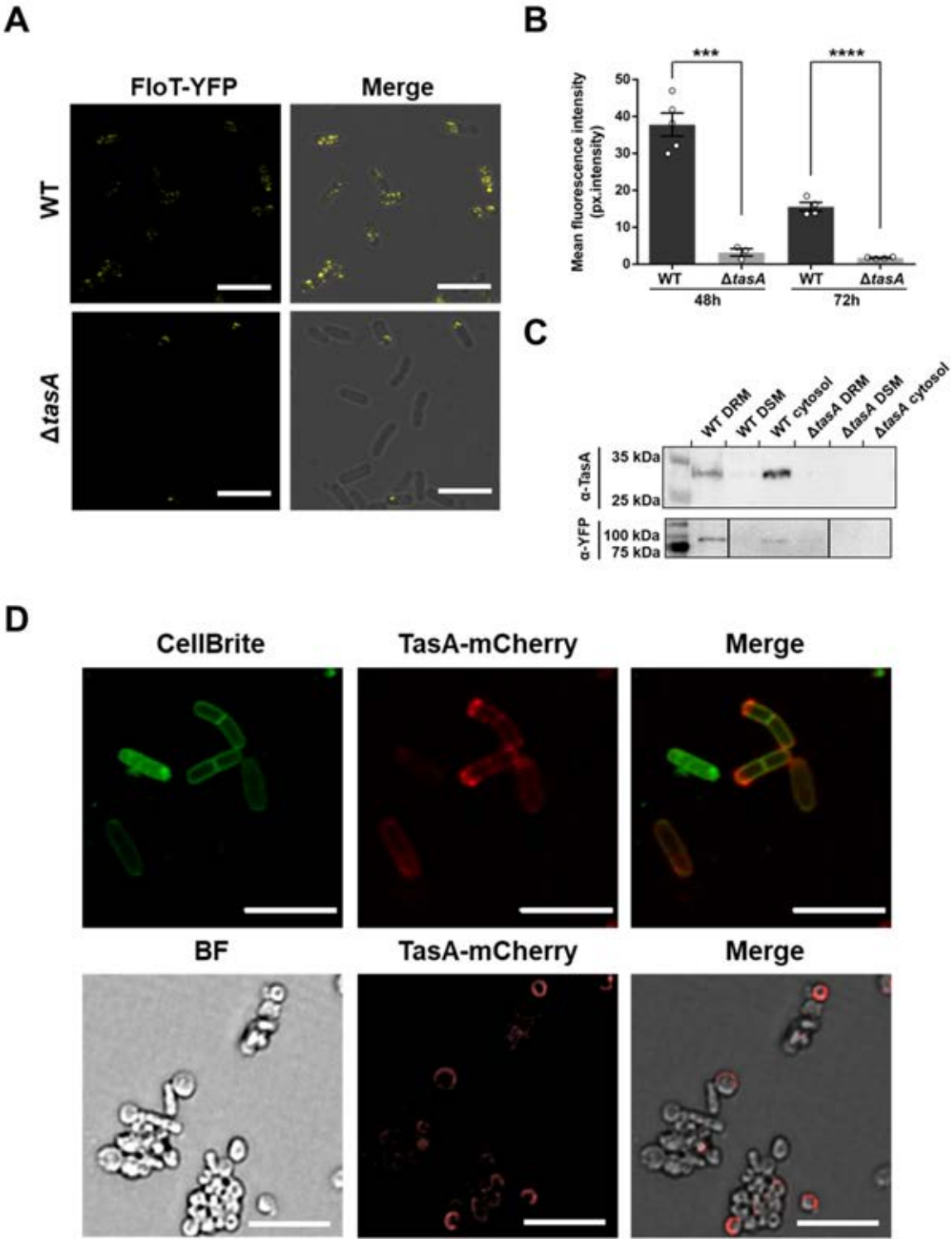

Figure 4.1. TasA is a protein from the DRM fraction of the cell membrane. A) Representative confocal microscopy images showing WT or Δ*tasA* cells expressing the *floT-yfp* construct at 72 hours. WT images show the typical punctate pattern associated to FloT. That pattern is lost in Δ*tasA* cells. **B)** Quantification of fluorescence signal in WT and Δ*tasA* samples at 48 and 72 h show significant differences between the two strains (*** p<0.001 **** p<0.0001). The points indicate the number of colonies analyzed over three independent experiments. Average values are shown with error bars representing the SEM. For each experiment and sample, at least three fields-of-view were measured. **C)** Western blot of different membrane fractions exposed to an anti-TasA or anti-YFP antibodies. Immunoblot images have been cropped and spliced for illustrative purposes. Black lines over the images indicate the boundaries of immunoblot splicing. D) Top: CLSM images of 48-h incubated cells expressing the translational fusion *tasA-mCherry* and stained with the membrane dye CellBrite Fix 488. Bottom: Fluorescence microscopy of protoplast cells expressing the *tasA-mCherry* translational fusion. The signal corresponding to TasA appears on the surface of the protoplasts. Scale bars = 5 μm.

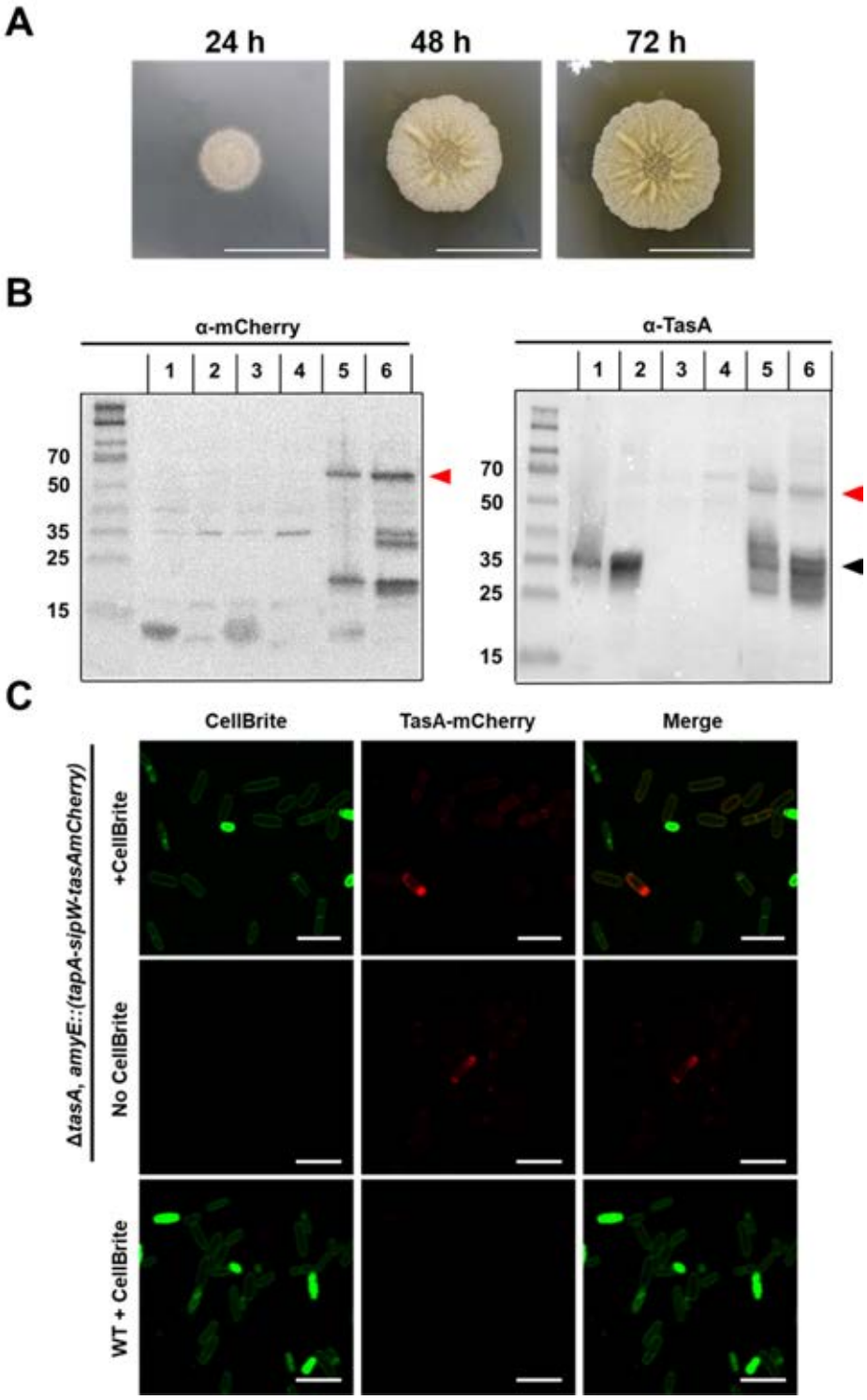

Figure 4.2. TasA-mCherry functions like the native TasA. A) Colony morphology of a Δ*tasA*, *amyE::(tapA-sipW-tasA-mCherry)* strain. Scale bar = 1 cm. **B)** Western blot of the different biofilm fractions of a Δ*tasA*, *amyE::(tapA-sipW-tasA-mCherry)* strain using anti-mCherry or anti-TasA antibodies: Lanes: 1 = WT cell fraction, 2 = WT ECM fraction, 3 = Δ*tasA* cell fraction, 4 = Δ*tasA* ECM fraction. 5 = Δ*tasA*, *amyE::(tapA-sipW-tasA-mCherry)* cell fraction, 6 = Δ*tasA*, *amyE::(tapA-sipW-tasA-mCherry)* ECM fraction. Immunoblot images have been cropped and spliced for illustrative purposes. Red arrowhead indicates the expected band size corresponding to the TasA-mCherry fusion. Black arrowhead indicates the expected size for TasA. **C)** CLSM images of the Δ*tasA*, *amyE::(tapA-sipW-tasA-mCherry)* strain in the presence (top images) or absence (center images) of the membrane stain CellBrite Fix 488, as a control for the CellBrite staining. The bottom images show the WT strain stained with CellBrite Fix 488 as a negative control for mCherry fluorescence. Scale bars = 5 μm.

Given the localization of TasA in the membrane and the alterations in FloT expression and distribution patterns in the absence of TasA, we wondered whether the putative interaction of FloT and TasA within the cell membrane could play a role in the phenotypic changes observed in the *tasA* mutant (see chapter III). To test this possibility, we used a WT strain carrying TasA-mCherry and FloT-YFP translational fusions. Considering that TasA is only expressed in a subset of the population[3] and that FloT is present in almost all cells, we analyzed 48-h colonies, in which the TasA expression is at its maximum, and we manually selected cells that exhibited expression of both proteins. The fluorescence microscopy analysis of the selected bacterial cells showed no significant colocalization of the two proteins (Fig. 4.3A), as further demonstrated by Pearson's coefficient values (0.36 ± 0.03) (Fig. 4.3B).

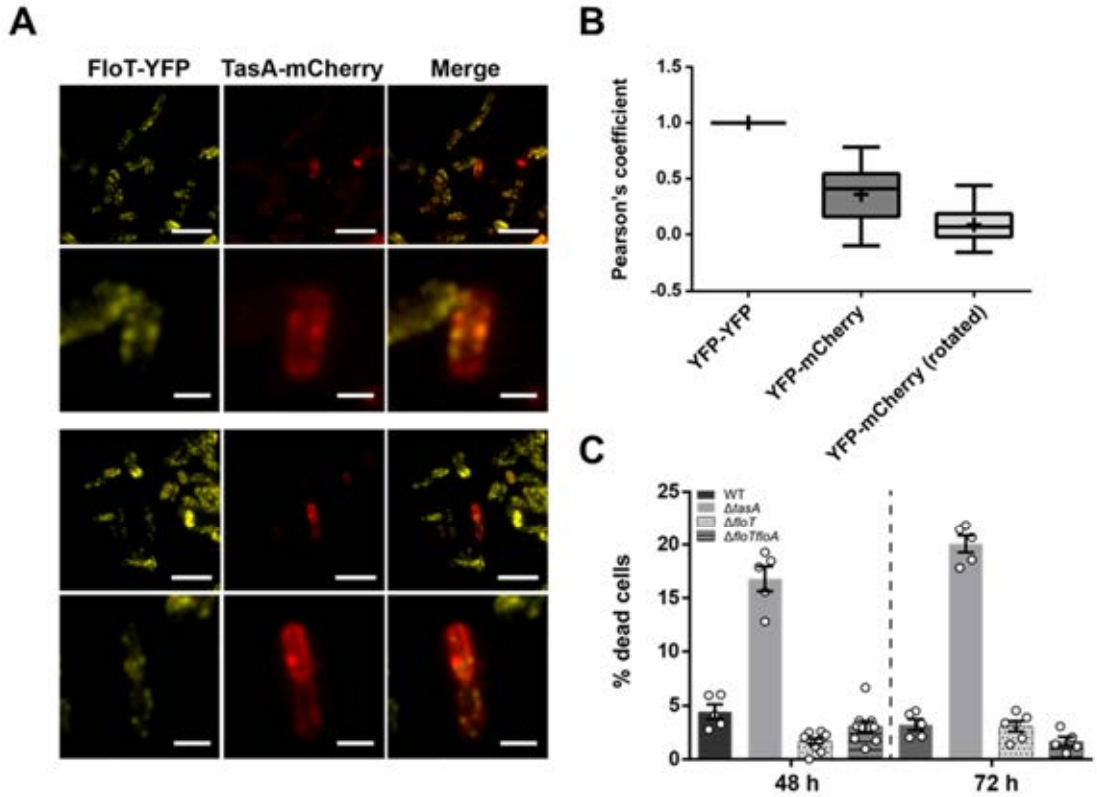

Figure 4.3. Colocalization analysis of FloT and TasA and analysis of cell death in flotillin mutants. A) Colocalization of TasA-mCherry and FloT-YFP was analyzed via fluorescence microscopy in a strain carrying the two translational fusions in a WT genetic background. The top panels are images at low magnification (scale bars = 5 μm). The bottom panels are close up views of those regions (scale bars = 1 μm). **B)** Box and whisker plots of the Pearson's coefficients. Colocalization was measured and quantified in a total of 50 individual bacteria. As a positive control, for each analyzed bacterium, the Pearson's coefficient of the YFP channel was calculated compared with the same channel. As a negative control, for each analyzed bacterium, the Pearson's coefficient was calculated comparing the YFP channel with an image of the 90-degree rotated mCherry channel. The bars of the box and whisker plot indicate the minimum (Q1 - 1.5 x Interquartile range) or maximum (Q1 + 1.5 x Interquartile range). The box represents the interquartile range. The center line represents the median and the "+" sign represents the mean. **C)** Quantification by CLSM of the proportion of dead cells found in the Δ*floT* or Δ*floTfloA* colonies grown in solid MSgg for 48 or 72 h. The points indicate the number of colonies analyzed over three independent experiments. Average values are shown with error bars representing the SEM.

Furthermore, we asked whether the loss of FloT foci was somehow related to the increased cell death observed in the absence of TasA (see chapter III). We used a LIVE/DEAD viability stain in a Δ*floT* colony and in a Δ*floTfloA* colony, a double mutant for the two flotillin-like proteins in the *B. subtilis* genome. The results showed no significant differences in the proportion of cell death compared to the WT strain at 48 h and 72 h (fig. 4.3C). In conclusion, these experiments demonstrate that the increased cell death is not caused by loss of the FloT distribution pattern that occurs in the *tasA* mutant.

Altogether, these results allow us to conclude that TasA is located in the DRM fraction of the cell membrane where it contributes directly to membrane dynamics and that its absence leads to alterations in membrane functionality, compromising membrane stability and eventually leading to cell death.

Bilayer rigidity is increased in the presence of TasA

Based on the findings described above, we next investigated the effect of TasA on lipid organization in the membrane at the local level via solid-state nuclear magnetic resonance (NMR) spectroscopy. We mixed reconstituted multi-lamellar vesicles (MLV) (Fig. 4.4A) with a lipid composition mimicking *B. subtilis* membranes (PE:PG 85:15 molar ratio, with deuterated PE lipids) with TasA at a lipid-to-protein ratio of 50:1. ^{2}H solid-state NMR was performed under static conditions to extract ^{2}H quadrupolar couplings along the acyl chain. Our results show the profile of the carbon-C-^{2}H order parameter (SCD) as a function of the labelled carbon position in the acyl chain obtained after converting the quadrupolar doublets into order parameters (Fig. 4.4B). At the ambient temperature, and without TasA, the PE:PG lipid bilayer reflects a typical behavior, with a gradient of order parameters associated with increased rigidity of the lipids near the glycerol scaffold, followed by a decrease in the order parameter towards the terminal methyl group localized at the center of the membrane[23]. In presence of TasA, we observed a similar profile, confirming that PE/PG membranes can accommodate TasA without perturbing their stability and integrity. Spectral simulations (Fig. 4.4C and D) were performed by considering a spherical distribution of bilayer normals with respect to the magnetic field to extract the c/a ratio, with c and a representing the major and minor ellipsoid semi axes, respectively. This parameter reports on the membrane deformation due to the diamagnetic susceptibility of lipids in a magnetic field[24]. We observed different ratios with c/a=1.55 for PE/PG and c/a=1 for PE/PG (Fig. 4.4C and D) in presence of TasA, indicating that the protein compensates the potential for elastic deformation of

natural PE/PG membranes. We confirmed the effect of TasA on the membrane organization by recording wide line ^{31}P NMR experiments.

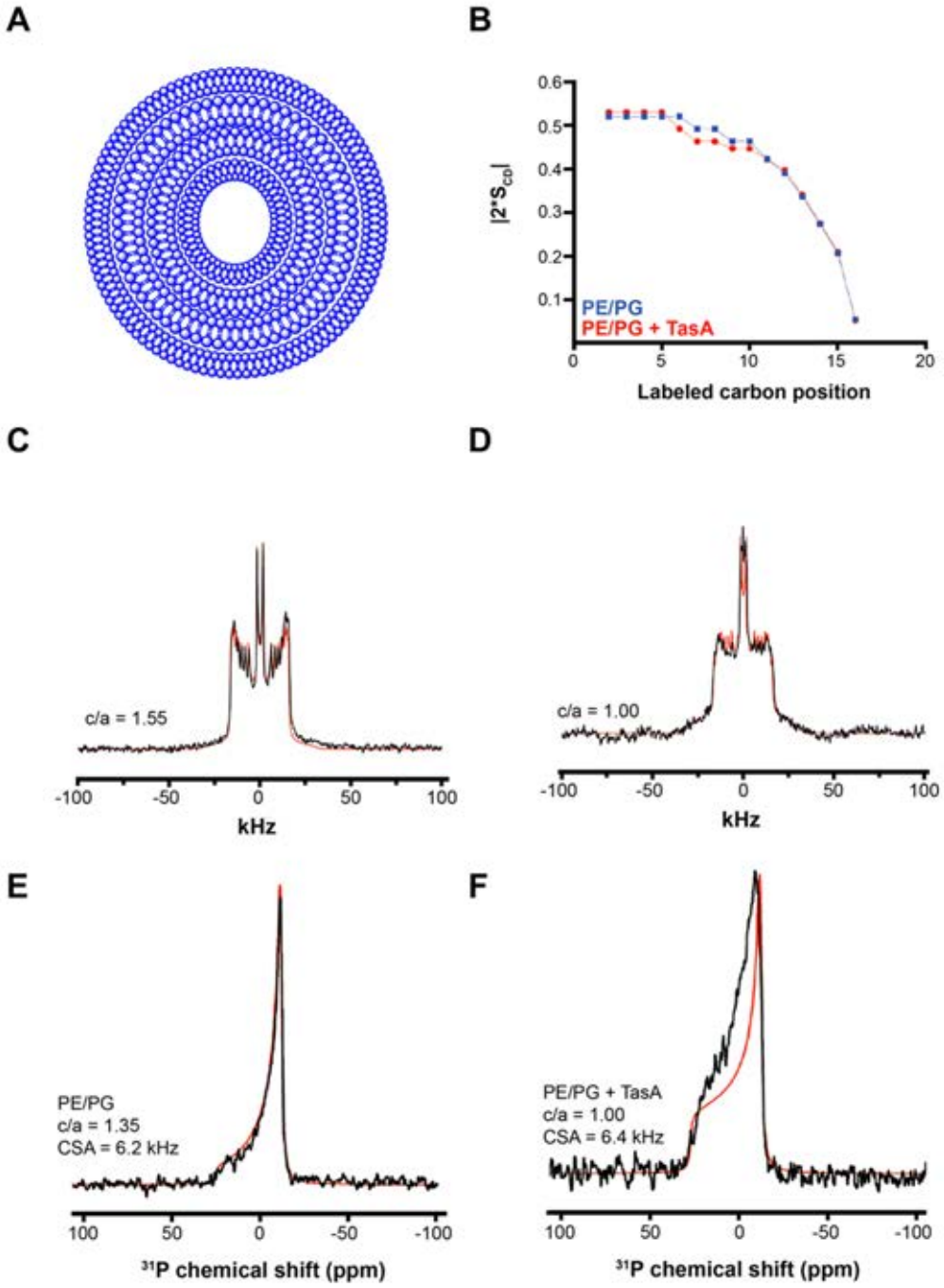

Figure 4.4 Solid-state NMR analysis on TasA effect on membranes. A) Schematic representation of MLVs **B)** Evolution of the C-^{2}H order parameters along the acyl chain for reconstituted membranes of PE:PG 85:15 (in blue) and PE:PG 85:15 with TasA (in red). **C)** Simulations of deuterium solid-state spectra, for PE/PG 85:15 membranes in the absence of TasA. **D)** Simulations of deuterium solid-state spectra, for PE/PG 85:15 membranes in the presence of TasA (protein-to-lipid ratio 1/50). Black and red lines respectively indicate experimental and simulated specta. **E)** ^{31}P solid-state NMR experiments of PE:PG in the absence of TasA. **F)** ^{31}P solid-state NMR experiments of PE:PG in the presence of TasA. Experimental data (in black) and simulation (in red) are presented. c and a are the long and short semi-axes with c being aligned with the B_0 magnetic field direction.

A powder line shape associated with a broad anisotropic signal with a pronounced peak at the high field- and a less intense shoulder at the low field-edge was observed, typical for phospholipids organized in a lamellar phase (Fig. 4.4E). TasA had an effect on the chemical shift anisotropy, which shifted from 6.2 kHz (PE:PG) to 6.4 kHz (PE:PG and TasA) (Fig. 4.4E and 4.4F, respectively), and, interestingly, the ^{31}P signal shape changed. Both of these observations reflect an effect of TasA on the phosphate group motional behavior and hence on membrane elasticity, indicating an increased rigidity of the lipids in the presence of TasA. The ^{31}P measurements, with values of c/a =1.35 and 1, respectively, for PE/PG membranes alone and PE/PG with TasA (Fig. 4.4E and 4.4F), indicate the same trend as the ^{2}H data.

Taken together, the ^{2}H and ^{31}P NMR data indicate that the lipid bilayer can accommodate TasA without drastically perturbing the membrane structural integrity, while the natural membrane elasticity observed for a PE:PG lipid composition (in the absence of TasA) is compensated by the presence of TasA, demonstrating that the addition of TasA increases the rigidity of the membrane and suggesting an affinity of TasA for the membrane curvature, consistent with the confocal microscopy results (Fig. 4.1D) and the results obtained in previous works (see chapter III).

Lipid composition determines the interaction of TasA with lipid vesicles

Amyloid proteins, in solution, have the ability to aggregate, forming an heterogenous population consisting on monomers, oligomers of different sizes, and amyloid fibers[25]. The cytotoxic effect of amyloid protein and peptides is given by their ability to interact with cellular membranes, which is, precisely, a feature of the oligomeric state of the amyloid fold, the molecular species responsible of many neurological disorders[26]. Based on the ability of TasA to interact with lipid vesicles *in vitro* when reconstituted inside MLVs, we next wonder whether purified TasA, in solution, was able to interact with membranes of different compositions when added externally. For this purpose, we studied by fluorescence spectroscopy the interaction of purified TasA with small unilamellar vesicles (SUVs) that encapsulate a fluorescent probe. This probe is only released when the protein is inserts into the bilayer, permeabilizing the vesicle. In these experiments, we prepared SUVs with lipid compositions that have been reported in the literature as the phospholipid components of the cell membranes of several microorganisms, specifically, *Staphylococcus aureus* (PG:CL, 58:42 molar ratio), *Pseudomonas aeruginosa* (PE:PG:CL, 64:24:12 molar ratio) and *Bacillus subtilis* l'A

(PG:PE:CL, 80:15:5 molar ratio) (a different strain from the *Bacillus* strains used throughout this work)[27,28].

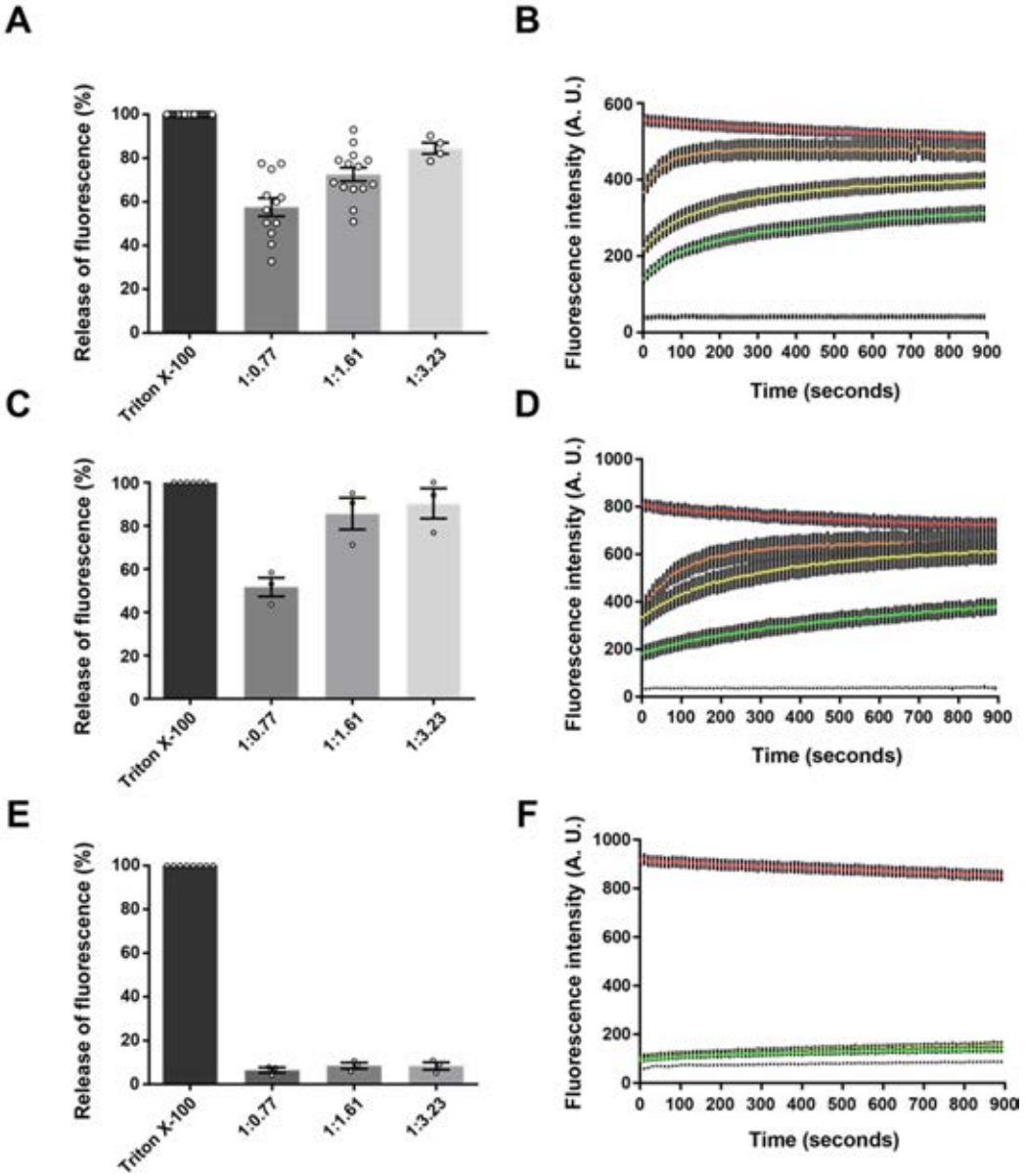

Figure 4.5. TasA shows specificity in the interaction with different lipid compositions. A) % of release of HPTS from PG:PE:CL SUVs (80:15:5) at different lipid:protein ratios. **B)** Kinetics of HPTS release from PG:PE:CL SUVs (80:15:5) at different lipid:protein ratios over the course of 900 seconds. **C)** % of release of HPTS from PG:CL SUVs (58:42) at different lipid:protein ratios. **D)** Kinetics of HPTS release from PG:CL SUVs (58:42) at different lipid:protein ratios over the course of 900 seconds. **E)** % of release of HPTS from PE:PG:CL SUVs (64:24:12) at different lipid:protein ratios. **F)** Kinetics of HPTS release from PE:PG:CL SUVs (64:24:12) at different lipid:protein ratios over the course of 900 seconds. In all cases, average values of at least three independent experiments are shown. In all cases, error bars indicate the SEM. Permeabilization caused by triton X-100 is considered as 100% leakage. Permeabilization caused by buffer is considered as 0% leakage. Colors indicate the different lipid:protein molar ratios: green 1:0.77, yellow 1:1.61 and orange 1:3.23. Red indicates the leakage caused by triton X-100.

Our results show that when mixed at different lipid:protein ratios, a release of the fluorescent probe, as indicated by the increased fluorescence over time, is observed in the presence of TasA in a concentration-dependent manner for the SUVs mimicking the lipid composition of *B. subtilis* l'A and *S. aureus* (Fig. 4.5 A and B and Fig. 4.5 C and D, respectively). However, when mixed with the SUVs mimicking *Pseudomonas aeruginosa*

membranes, no effect is observed (Fig. 4.5E and F). These results show that TasA exhibit a chemical preference in the interaction with lipid bilayers depending on lipid composition.

Next, we investigated whether TasA is able to adsorb to membranes with these lipid compositions. For this purpose, we performed experiments using a lipid monolayer and we investigated the binding of TasA to the monolayer surface by measuring the differences in surface pressure in the presence or absence of TasA using a Langmuir-Blodgett trough. This method is based on the ability of membrane-interacting peptide and proteins to increase the surface pressure (Π) in the lipid monolayer after injection in the subphase, which indicates the incorporation of the molecules into the monolayer. To explore this hypothesis, we used the same lipid composition described in the permeabilization experiments, for *S. aureus* SUVs. Using different initial values of surface pressure (Π_i), determined by the increasing concentration of the lipid monolayer, we injected TasA in the subphase at a constant concentration and measured the variations of surface pressure in order to obtain the maximal insertion pressure (i. e the surface pressure beyond which no absorption can happen) and the $d\Pi_0$ parameter, which is a measure of the affinity of the molecule for the lipids present in the monolayer. In our settings, the injection of TasA into the subphase leads to surface pressure increases dependent on the initial surface pressures (Fig. 4.6A), reflecting the ability of the protein to adsorb into the monolayer. By calculating the $\Delta\Pi$ at a given value of Π_i, we elaborated a linear regression (Fig. 4.6B) later used to calculate the above-mentioned parameters. TasA displays a maximal insertion pressure in this monolayer of 45.24 mN/m, which is above the 30-35 mN/m estimated for natural membranes, suggesting the ability of TasA to insert into membranes of this lipid composition. Moreover, a $d\Pi_0$ parameter of 1.97 indicates that this lipid composition exerts an attractive effect over TasA.

In conclusion, we have demonstrated that TasA interacts preferentially and differentially, and in some cases, by adsorption and insertion, with lipid bilayers of different compositions, establishing the ability of this protein to interact with lipids and confirming its membrane bound nature.

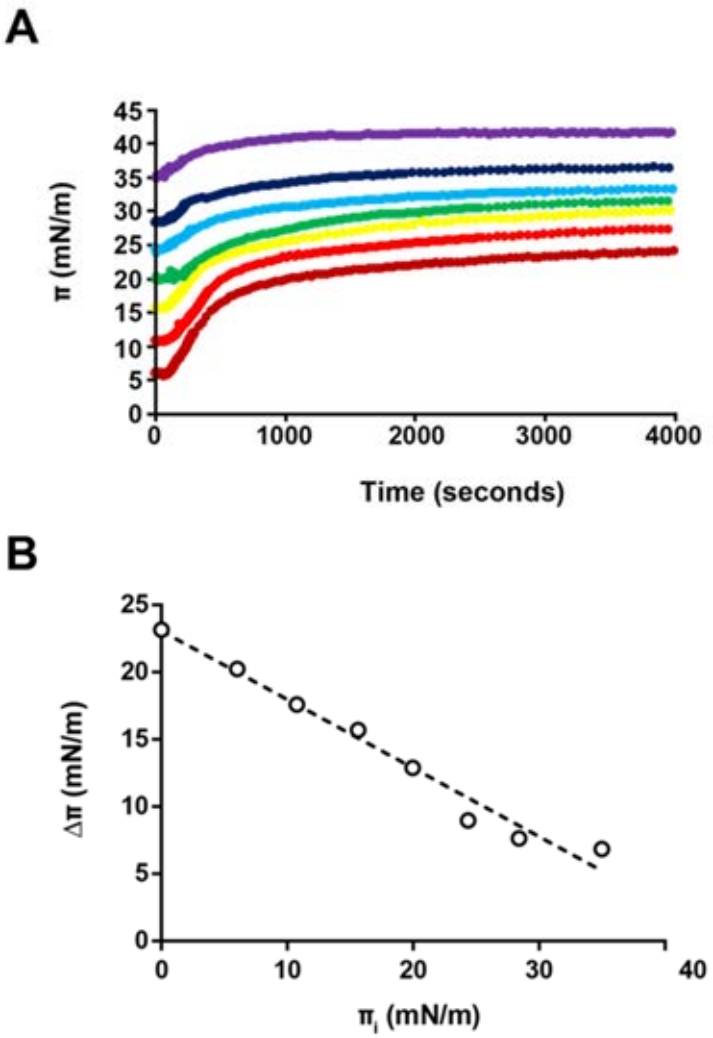

Figure 4.6. TasA is incorporated to lipid monolayers of specific composition. A) Stabilization curves of the surface pressure (Π) after injection of TasA in the subphase. Each curve is recorded using different values of initial surface pressure, determined by the lipid concentration in the interphase. **B)** Linear regression obtained comparing the surface pressure increment (ΔΠ) against the initial surface pressure value (Π_i). The linear equation y = 0.5076x + 23.018 obtained from this regression, was used to calculate the maximal insertion pressure of the protein in the monolayer (at y = 0) and the $d\Pi_0$ value (at x = 0).

Amyloidogenic regions are relevant for the interaction of TasA with biological membranes

Considering that TasA is a membrane-bound protein with the ability to interact with lipids both *in vivo* and *in vitro*, we next asked on the TasA sequence determinants responsible for this interaction. We first studied the hydrophobic properties of TasA sequence. We computed the hydrophobicity plot for TasA using the ExPasy Protscale tool[29] (Fig. 4.7A). Results show that TasA presents two hydrophobic stretches, i. e. protein regions of more than 5 amino acids with a hydrophobicity score over 0, that extend from amino acids 52 to 61 and from 81 to 90 of the mature TasA protein. Interestingly, these regions are nearly identical to the amyloidogenic regions detected within the amyloid core of TasA (see

chapter II, Fig. 2.7A and Fig. S2.2A). To study these regions in the context of protein-lipid interaction, we first opted for an *in-silico* approach. We modelled these hydrophobic-amyloidogenic regions to obtain a 3D model of both molecules (Fig. 4.7B) in order to perform molecular dynamics simulations of the interactions of these regions with model membranes. The LG-13 peptide (Fig. 4.7B left) folds into an alpha-helix, whereas the DG-13 peptide shows an unfolded conformation (Fig. 4.7B right). To simulate the interaction of these regions with biological membranes we used the IMPALA method[30]. This method simulates the insertion of a molecule into an implicit model membrane to predict the ability of the molecule to interact with the lipid bilayer. We applied this method to both peptides and found that, in general, the total energy restraints show that LG-13 (Fig. 4.7C and D) and DG-14 (Fig. 4.7E and F) find their most favorable position (where the energy restraint is minimal) in the interface between the polar phosphate heads and the hydrophobic alkyl chains while the energy restraint is maximum at the bilayer center, indicating that these molecules are, likely, not stable when positioned near the hydrophobic core of the bilayer, and therefore, are not able to cross it. In addition, the total energy restraint for DG-14 outside the bilayer is lower than the obtained for LG-13 (Fig. 4.7E and 4.7C respectively), suggesting that the interaction of DG-14 with lipids is energetically more favorable than LG-13. In contrast, LG-13 displays lower energy restraint values than those of DG-14 in several positions close to the upper limit of the alkyl chains, while in DG-14, only one discrete minimum Is observed at z = 18, suggesting that LG-13 penetrates deeper and is more stable once the contact with the lipids is established.

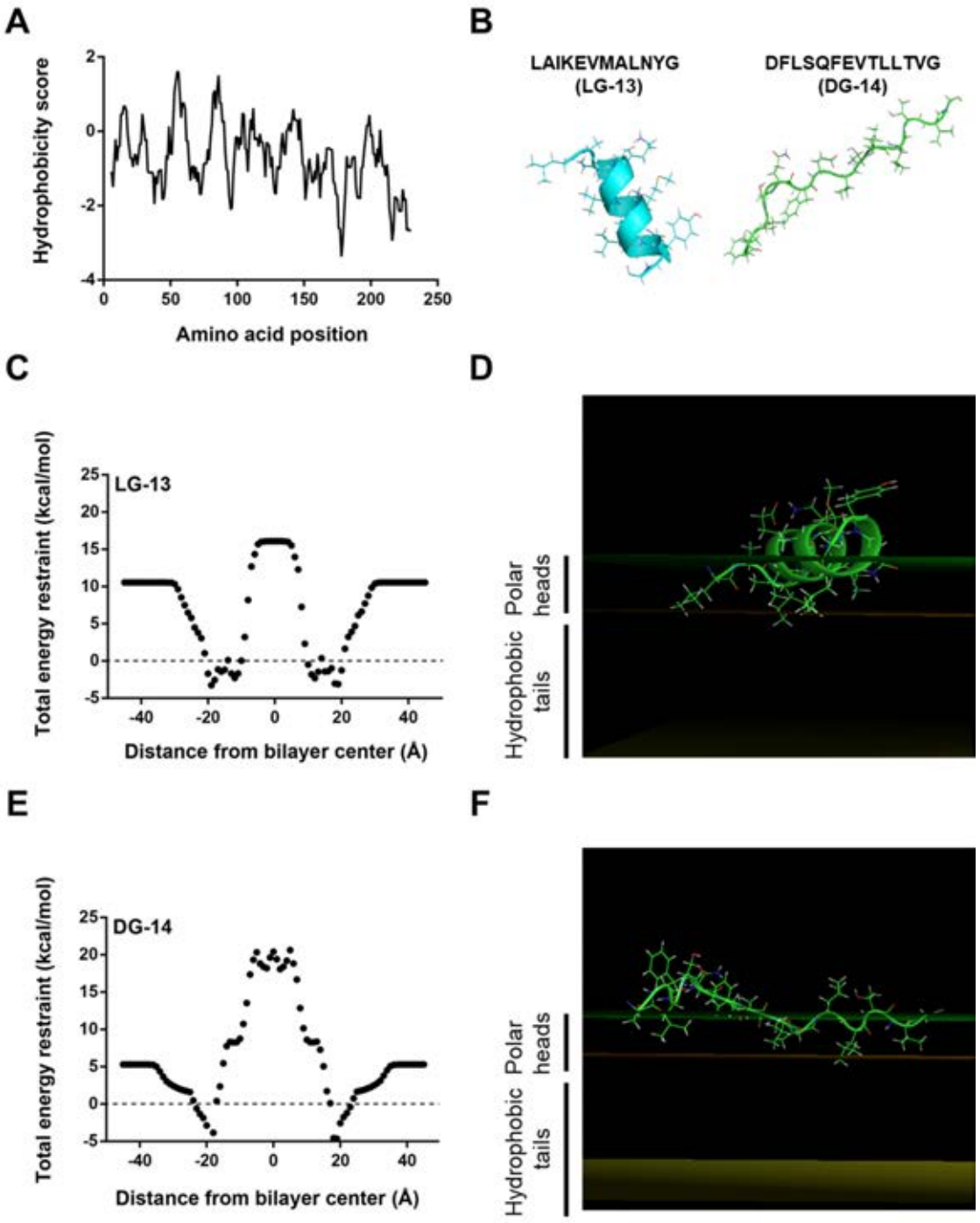

Figure 4.7. The amyloidogenic sequences from TasA amyloid core are relevant for protein-lipid interactions. A) Hydrophobicity score by residue obtained using the ProtScale tool. **B)** 3D models obtained with iTasser of the peptides corresponding to the amyloidogenic-hydrophobic sequences found within TasA amyloid core (LG-13 and DG-14). **C)** Evolution of the total energy restraint as a function of the penetration of LG-13 into an implicit bilayer obtained by IMPALA. **D)** Representation of the interaction of LG-13 with the model membrane. The image represents the most stable position of the peptide within the model bilayer. **E)** Evolution of the total energy restraint as a function of the penetration of the DG-14 peptide into an implicit bilayer obtained by IMPALA. **F)** Representation of the interaction of DG-14 with the model membrane. The image represents the most stable position of the peptide within the model bilayer. In both images (D and F) The green and orange interphases represent the upper and lower limits of the lipid polar heads. The yellow interphase represents the bilayer center, ant the space between this yellow interphase and the orange interphase represents the hydrophobic apolar tails of the phospholipids.

To experimentally study the interactions of these regions with model membranes, we performed permeabilization experiments of SUVs with a lipid composition mimicking *S. aureus* and *P. aeruginosa* membranes that were described in the above section, using the synthetic peptides corresponding to these regions that have been previously studied (see chapter II). These lipid compositions were affected or not, respectively, by the presence of TasA, therefore, we wondered how these vesicles are affected in the presence of these hydrophobic-amyloidogenic peptides.Results from these experiments show that the LG-13 peptide is unable to cause leakage from any of these SUVs (Fig. 4.8A). In contrast, peptide DG-14, did not affect *S. aureus* SUVs (Fig. 4.8B top), but, interestingly, were able to cause leakage from *P. aeruginosa* liposomes in a concentration dependent manner (Fig. 4.8B bottom). These results suggest that the energy barriers, according to the simulations, are high enough to prevent the interaction of LG-13 with the studied lipid compositions. However, the DG-14 peptide, that has lower energy restraints in proximity with the bilayer, is able to cause the leakage of *P. aeruginosa* liposomes. The fact that this peptide is able to permeabilize SUVs with this lipid composition, contrary to what occurs with the whole protein, that interacts preferentially with the *S. aureus* liposomes, reflect the difference in the hydrophobic properties of the peptide alone compared to the full-length protein.

Altogether, these results indicate the relevance of these region in the interplay of TasA with biological membranes and highlight the importance of the amyloid core of the protein, and specifically, the amyloidogenic regions, in the interaction with lipids, supporting the notion of this functional amyloid as a membrane protein involved in membrane dynamics and stabilization.

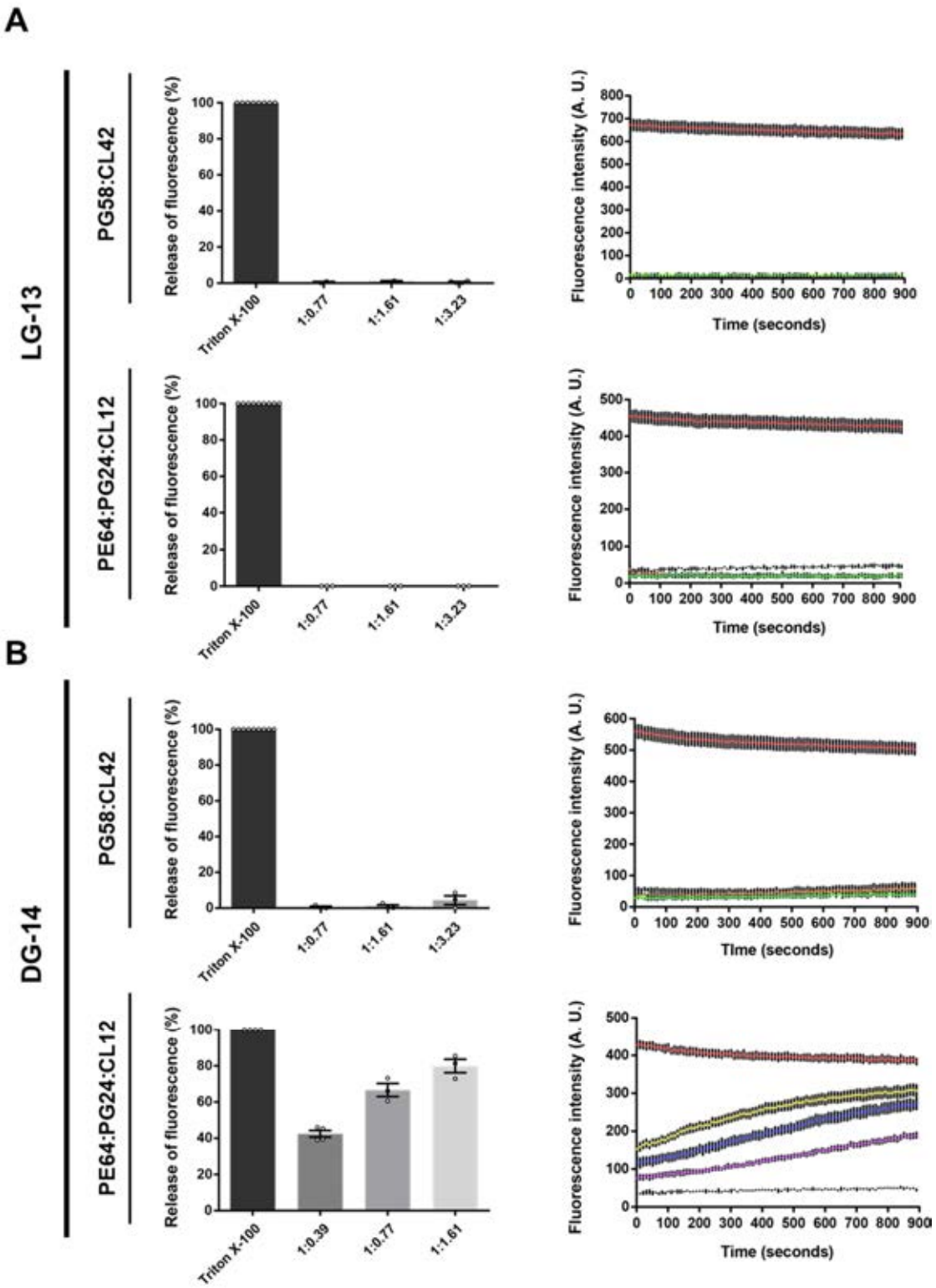

Figure 4.8. Interaction of TasA amyloidogenic-hydrophobic peptides with SUVs of different lipid compositions. A) Left. % of release of HPTS from SUVs of different lipid compositions in the presence of the LG-13 peptide at different lipid:peptide ratios. **Right.** Kinetics of HPTS release from SUVs of different lipid compositions in the presence of the LG-13 peptide at different lipid:peptide ratios over the course of 900 seconds. **B) Left.** % of release of HPTS from SUVs of different lipid compositions in the presence of the DG-14 peptide at different lipid:peptide ratios. **Right.** Kinetics of HPTS release from SUVs of different lipid compositions in the presence of the DG-14 peptide at different lipid:peptide ratios over the course of 900 seconds. In all the graphs shown, the average value of at least three independent experiments is shown. The error bars represent the SEM in all cases. Permeabilization caused by triton X-100 is considered as 100% leakage. Permeabilization caused by buffer is considered as 0% leakage. Colors indicate the different increasing lipid:peptide molar ratios.

DISCUSSION

TasA, as demonstrated in a previous work, shows a dual functionality implicated in the prevention of cell death and the normal development of the colony. In this study we have characterized TasA as a membrane protein, likely present in the FMMs of the cell membrane, involved in membrane dynamics and, as a consequence, in the maintenance of membrane stability required for the proper viability of the bacterial community. This is evidenced, as demonstrated in this work, by the *in vitro* interaction of TasA with liposomes, where TasA interacts with the lipids, increasing the rigidity of the bilayer, in agreement with the data observed *in vivo*. In addition, we have seen that this interaction is dependent on the specificity of the lipid composition. The ability of TasA to interact with lipids *in vitro* is not unprecedented. It has been previously demonstrated that this amyloid protein has the ability to interact with model membranes, influencing its morphology and structure[31]. Our results are in line with these findings and in addition, highlight the importance of the amyloidogenic capacity of the N-terminal region of TasA for this interaction, as most of the hydrophobic load of the protein coincide in the amino acids that show the highest amyloidogenic strength. Considering these novel findings, it is tempting to speculate that cells can regulate membrane dynamics by, among other processes, tuning the amount of TasA present in the membrane at a given moment, which would permit a better physiological response to different environmental cues. In particular, our results suggest that the membrane instability caused by the absence of TasA triggers a cascade of malfunctions in biological processes that eventually lead to cell death in a subset of the population.

The fact that TasA is detected in the DRM fraction of the cell membrane and that its absence lead to a mislocalization of FloT are strong evidences suggesting the functional relationship of TasA with the FMMs of the cell membrane. Considering the importance of these regions for organizing the different signal transduction pathways[19], our evidences indicate that the absence of TasA, somehow, affect these regions, independent from the role of this functional amyloid in the ECM, are causing the cellular and physiological disruption observed in a Δ*tasA* strain in previous works. It is not unprecedented that amyloid proteins interact with functional domains within the cell membrane. In eukaryotic cells, for instance, it has been reported that lipid rafts participate in the interaction between the amyloid precursor protein and the secretase required for the production of the amyloid-β peptide[32]. However, further research is needed to fully understand the role of TasA in FMMs and how interact with other hypothetical protein partners.

The ability of amyloid proteins to interact and even disrupt biological membranes is not a rare phenomenon and it is this ability, precisely, what confer pathological amyloids their cytotoxicity[33]. Many antimicrobial peptides have the ability to form pores or open channels through the lipid bilayers[33,34]. Some examples are the cysteine rich antimicrobial peptide PG-1, with a β-sheet secondary structure or the LL-37 peptide, an antimicrobial peptide from the cathelicidins family, widely expressed in eukaryotic cells. For these peptides, amyloid properties have been reported in both cases, for instance, they form β-sheet enriched aggregates and have the ability to form fibers and to bind amyloid-specific dyes such as congo red or thioflavin-T[35,36]. However, one of the most striking cases are the amyloid β-peptides Aβ1-42 and Aβ1-40, the main responsible agents of Alzheimer's disease. These peptides are generated in the neural tissue, where they form deposits that are found in the brains of patients with this condition. However, recent studies have demonstrated that these peptides exhibit a broad-spectrum antimicrobial activity, suggesting their role as part of the innate immune response[37,38]. The tendency of the amyloid fold to interact with biological membranes is given by the ability of these proteins to aggregate in β-sheet enriched tertiary and quaternary structures, which support the formation of β-barrels and other molecular intermediaries that behave as pores with a high affinity to membrane lipids[26,33]. Interestingly, TasA was initially described as a spore coat protein with antimicrobial activity[39], reflecting the ability of this protein to interact with biological membranes and, specifically, with bacterial bilayers, supporting the concept of TasA as a membrane protein and the findings obtained in this work.

In gram-negative bacteria, there are several proteins involved in the maintenance of integrity and stability of the outer membrane. These are the outer membrane proteins (OMPs), and they participate in multiple and varied functions such as transport, biosynthesis of flagella and pili, etc[40]. Most of these proteins adopt a β-barrel conformation that facilitates membrane interaction, similarly to what occurs with amyloid oligomers, suggesting a common mechanism between the two families of proteins. Among all the proteins present in this cell compartment, OmpA is one of the major outer membrane proteins, presumably involved in the anchoring of the peptidoglycan layer[41]. The ability of TasA to stabilize the cell membrane preventing cell death and its interaction with TapA, an accessory protein found in the peptidoglycan[10], suggest an analogous role, however, much deeper research is needed to understand how these two proteins contribute to the physical connection between the membrane, the cell wall and the ECM.

MATERIALS AND METHODS

Bacterial strains and culture conditions

Bacterial strains used in this study are listed in table 4.1. For plasmid replication, *Escherichia coli* DH5α was used. For protein expression and purification, *Escherichia coli* BL21(DE3) was used. All strains were grown in Luria-Bertani (LB) medium (1% tryptone, 0.5% yeast extract and 0.5% NaCl) at 37 °C prior to the corresponding experiments. Biofilm assays were performed on MSgg medium: 100 mM morpholinepropane sulphonic acid (MOPS) (pH 7), 0.5% glycerol, 0.5% glutamate, 5 mM potassium phosphate (pH 7), 50 µg/ml tryptophan, 50 µg/ml phenylalanine, 50 µg/ml threonine, 2 mM $MgCl_2$, 700 µM $CaCl_2$, 50 µM $FeCl_3$, 50 µM $MnCl_2$, 2 µM thiamine, 1 µM $ZnCl_2$. Media were solidified by addition of bacteriological agar (Oxoid) to a final concentration of 1.5%.

The antibiotics used and their final concentrations were 10 µg/ml kanamycin and 100 µg/ml spectinomycin. For MLS resistance, 1 µg/ml erythromycin and 25 µg/ml lincomycin were used.

Table 4.1. Bacterial strains used in this study.

Bacterial strain	Genotype	Source
Bacillus subtilis 168	Prototroph	Laboratory collection
Bacillus subtilis NCIB3610	Wild type. Undomesticated strain	Laboratory collection
CA017	*Bacillus subtilis* NCIB3610 *tasA::km*	(Aguilar et al., 2010)[42]
DL1207	*Bacillus subtilis* NCIB 3610 *amyE::floT-yfp* (spc)	(López and Kolter, 2010)[15]
DR40	*Bacillus subtilis* NCIB 3610 *tasA::spc* *lacA::(tapA-sipW-tasA-mCherry) (mls)*	(Kolodkin-Gal et al, 2010)[43]
DL1419	*Bacillus subtilis* NCIB 3610 *floT::km* *floA::mls*	(Yepes et al. 2012)[17]
DRBB5	*Bacillus subtilis* NCIB 3610 *tasA::km (km)* *amyE::floT-yfp (spc)*	This study
JC138	*Bacillus subtilis* NCIB3610 *floT::km*	This study
DRBB2	*Bacillus subtilis* NCIB3610 *lacA::(tapA-sipW-tasA-mCherry) (mls)* *amyE::floT-yfp (spc)*	This study

Strain construction

All of the *B. subtilis* strains were generated by transforming *B. subtilis* 168 via natural competence and then using the transformants as donors for transferring the constructs into *Bacillus subtilis* NCIB3610 via generalized SPP1 phage transduction[44].

Biofilm assays

TasA and FloT localization experiments were performed under biofilm-inducing conditions. Biofilms in solid MSgg-agar plates were generated as described elsewhere[9]. Briefly, the bacterial strains were grown on LB plates overnight at 37 °C. The resulting colonies were resuspended in sterile distilled water to an OD_{600} of 1. Next, 2-µl drops of the different bacterial suspensions were spotted on MSgg- agar plates and incubated at 30 °C for the corresponding amount of time, depending on the assay.

Biofilm fractionation

To validate the strain bearing the TasA-mCherry fusion, biofilms on solid MSgg medium were fractionated into cells and ECM as described elsewhere[9], and both fractions were analyzed separately. Briefly, 48-hour-old colonies grown under biofilm-inducing conditions were carefully lifted from the plates and resuspended in 10 ml of MS medium (MSgg broth without glycerol and glutamate, which were replaced by water) with a 25 $^{5/8}$ G needle. Next, the samples were subjected to mild sonication in a Branson 450 digital sonifier (4-5 5 seconds pulses at 20% amplitude) to ensure bacterial resuspension. The bacterial suspensions were centrifuged at 9000 g for 20 minutes to separate the cells from the extracellular matrix. The cell fraction was resuspended in 10 ml of MS medium and stored at 4 °C until further processing. The ECM fraction was filtered through a 0.22 µm filter and stored at 4 °C.

For protein precipitation, 2 ml of the cell or ECM fractions were used. The cell fraction was treated with 0.1 mg/ml lysozyme for 30 minutes at 37 °C. Next, both fractions were treated with a 10% final concentration of trichloroacetic acid and incubated in ice for 1 h. Proteins were collected by centrifugation at 13,000 g for 20 minutes, washed twice with ice-cold acetone, and dried in an Eppendorf Concentrator Plus 5305 (Eppendorf). Finally, precipitated proteins were resuspended in 2x Laemmli buffer prior to analysis by SDS-PAGE and western blot.

Cell membrane fractionation

Crude membrane extracts were purified from 50 ml MSgg liquid cultures (with shaking) of the different *B. subtilis* strains. Cultures were centrifuged at 7,000 g for 10 minutes at 4 °C and then resuspended in 10 ml of PBS. Lysozyme was added at a final concentration of 20 µg/ml and the cell suspensions were incubated at 37 °C for 30 minutes. After incubation, the lysates were sonicated on ice with a Branson 450 digital sonifier using a cell disruptor tip and 45 second pulses at 50% amplitude with pauses of 30 seconds between pulses until the lysates were clear. Next, the cell lysates were centrifuged at 10,000 g for 15 minutes to eliminate cell debris, and the supernatants were separated and passed through a 0.45 µm filter. To isolate the cell membrane, the filtered lysate was ultracentrifuged at 100,000 g for 1 hour at 4 °C. The supernatant, which contained the cytosolic proteins, was separated and kept at -20 °C. The pellet, which contained the crude membrane extract, was washed 3 times with PBS and processed using the CelLytic MEM protein extraction kit from Sigma. Briefly, the membrane fractions were resuspended in 600 µl of lysis and separation working solution (lysis and separation buffer + protease inhibitor cocktail) until a homogeneous suspension was achieved. Next, the suspension was incubated overnight at 4 °C on a stirring wheel. After incubation, the suspension is incubated at 37 °C for 30 minutes and then centrifuged at 3,000 g for 3 minutes. The DSM (upper phase) was separated and kept at -20 °C, and the DRM (lower phase) was washed three times with 400 µl of wash buffer by repeating the process from the 37 °C incubation step. Three washes were performed to ensure the removal of all hydrophilic proteins. The isolated DRM was kept at -20 °C until use. The DRM, DSM and cytosolic fractions were used directly for immunodetection.

Fluorescence microscopy

The localization of TasA in *B. subtilis* protoplasts was evaluated using a TasA-mCherry translational fusion. To generate the protoplast cells, *B. subtilis* colonies of the different strains grown on MSgg agar plates for 72 h were resuspended in protoplast buffer (20 mM potassium phosphate, pH 7.5, 15 mM $MgCl_2$, 20% sucrose), mildly sonicated as describe above and incubated for 30 min in the presence of 10 µg/ml lysozyme at 37 °C. The protoplast suspensions were mounted and visualized immediately under a Leica DM2500 LED fluorescence microscope with standard Texas Red (TX2 Ex. 560/40 Em. 645/76) filter to visualize cells expressing the *tasA-mCherry* construct. The images were taken with a Leica DFC 7000T 2.8 MP camera.

The colocalization experiments with TasA-mCherry and FloT-YFP were performed using a strain carrying *tasA-mCherry* and *floT-yfp* constructs in a WT background. Cells were

grown for 48 h on MSgg plates, and colonies were resuspended as described above. Cells were mounted and visualized using an Inverted Nikon Ti Eclipse microscope with a 100x 1.49 NA TIRF PL APO oil-immersion objective. Samples were excited using an argon-ion 488 nm laser for YFP and a yellow diode 561 nm laser for mCherry. Contrast was optimized by adjusting the angle of laser illumination to achieve HILO (Highly Inclined and Laminated Optical sheet) or full TIRF (total Internal Reflection Fluorescence) imaging depending on the distance between the coverslip and the bacteria. Images were taken with an Andor iXon3 897 EM-CCD camera.

Confocal laser scanning microscopy (CLSM)

The localization of FloT in *B. subtilis* cells was evaluated using a FloT-YFP translational fusion in a WT or Δ*tasA* genetic background. Colonies grown at 30 °C on MSgg solid medium were isolated at different time points and resuspended as described above. Samples were mounted and visualized immediately with excitation at 514 nm and emission recorded from 518 to 596 nm.

The localization of TasA was studied using a TasA-mCherry translational fusion in a Δ*tasA* genetic background. Colonies were grown at 30 °C on MSgg solid medium, isolated at 48 h and resuspended as described above. Bacterial suspensions were treated with CellBrite Fix 488 Membrane Stain (Biotium, stock solution at 1000X) at a final concentration of 1X. Images of the stained bacteria were acquired sequentially to obtain images from the membrane stain and the mCherry fluorescence. The CellBrite image was acquired by exciting the dye at 488 nm and recording the emissions from 498 to 553 nm, followed by a second acquisition corresponding to the mCherry fluorescence with excitation at 561 nm and recording of the emissions from 572 to 665 nm.

SDS-PAGE and immunodetection

Proteins were separated via SDS-PAGE in 12% acrylamide gels and then transferred onto PVDF membranes using the Trans-Blot Turbo Transfer System (BioRad) and PVDF transfer packs (BioRad). For immunodetection of TasA, the membranes were probed with anti-TasA antibody (rabbit) used at a 1:20,000 dilution in Pierce Protein-Free (TBS) blocking buffer (ThermoFisher). For immunodetection of FloT-YFP or TasA-mCherry, a commercial anti-GFP primary antibody (Clontech living colors full-length polyclonal antibody) or anti-mCherry primary antibody (Invitrogen mCherry Polyclonal Antibody) both developed in rabbit were used at a 1:1,000 or 1:2,000 dilution respectively in the buffer mentioned above. A secondary anti-rabbit IgG antibody conjugated to horseradish peroxidase (BioRad) was used at a 1:3,000 dilution in the same buffer. The membranes were developed using the Pierce ECL Western Blotting Substrate (ThermoFisher).

Protein expression and purification

Protein was expressed and purified as previously described[8] with some changes. Briefly, freshly transformed BL21(DE3) *E. coli* colonies were picked, resuspended in 10 mL of liquid LB with 100 µg/mL of ampicillin and incubated O/N at 37 °C with shaking. The next day, the pre-inoculum was used to inoculate 500 mL of LB supplemented with ampicillin, and the culture was incubated at 37 °C until an OD_{600} of 0.7-0.8 was reached. Next, the culture was induced with 1 mM isopropyl β-D-1-thiogalactopyranoside (IPTG) and incubated O/N at 30 °C with shaking to induce the formation of inclusion bodies. The next day, cells were harvested via centrifugation (5000 G, 15 minutes, 4 °C) resuspended in buffer A (Tris 50mM, 150mM NaCl, pH8), and then centrifuged again. The pellets were kept at -80 °C until purification or processed after 15 minutes. After thawing, cells were resuspended in buffer A, sonicated on ice (3x45 sec, 60% amplitude) and centrifuged (15000 G, 60 min., 4 °C). The supernatant was discarded, as proteins were mainly expressed in inclusion bodies. The pellet was resuspended in buffer A supplemented with 2 % Triton X-100, incubated at 37 °C with shaking for 20 minutes and centrifuged (15000 G, 10 min., 4 °C). The pellet was extensively washed with buffer A, centrifuged (15000 G for 10 min, 4 °C), resuspended in denaturing buffer (Tris 50 mM NaCl 500 mM, 6 M GuHCl) and incubated at 60 °C overnight until complete solubilization occured. Lysates were clarified via sonication on ice (3x45sec, 60% amplitude) and centrifugation (15000 G, 1h, 16 °C) and were then passed through a 0.45-µm filter prior to affinity chromatography. Protein was purified using an AKTA Start FPLC system (GE Healthcare). Soluble inclusion bodies were loaded into a HisTrap HP 5 mL column (GE Healthcare) previously equilibrated with binding buffer (50 mM Tris, 0.5 M NaCl, 20 mM imidazole, 8 M urea, pH 8). Protein was eluted from the column with elution buffer (50 mM Tris, 0.5 M NaCl, 500 mM imidazole, 8 M urea, pH 8). After the affinity chromatography step, the purified protein was loaded into a HiPrep 26/10 desalting column (GE Healthcare), and the buffer was exchanged to Tris 20 mM, NaCl 50 mM to perform the corresponding experiments.

Preparation of SUVs

For permeabilization experiments, L-α-Phosphatidylethanolamine from egg yolk, L-α-Phosphatidyl-DL-glycerol sodium salt from egg yolk lecithin and Cardiolipin sodium salt from bovine heart were purchased from Merck. For these experiments, small unilamellar vesicles (SUVs) were used. To prepare these vesicles, briefly, lipidic films of the corresponding lipid compositions, PE:PG:CL (64:24:12), PG:PE:CL (80:15:5) and PG:CL (58:42) (molar ratio) were prepared by dissolving the corresponding amounts of each

lipid in 2 ml of chloroform:methanol (2:1) until the mixture is homogeneous. Then, the lipidic film is formed by evaporation in a rotary evaporator at room temperature and is left overnight in a desiccator to ensure complete evaporation of the solvent. To encapsulate the fluorescent probe and the quencher, the lipidic film is resuspended at 37 °C in a solution containing 12.5 mM HPTS (8-Hydroxypyrene-1,3,6-Trisulfonic Acid), 45 mM DPX (p-Xylene-Bis-Pyridinium Bromide), which are the fluorescent probe and the quencher respectively, in 10 mM Tris, 150 mM NaCl. Next, the suspension is frozen in liquid nitrogen and then thawed in a 37 °C bath, repeating the cycle five times. To form the SUVs, the suspension is subjected to 10 2-minutes pulses of sonication at 40% amplitude in a Branson 450 digital sonifier with 1-minute pauses in ice.

To separate the liposomes containing HPTS from the free fluorescent probe, we performed size exclusion chromatography using Sephadex G-75 (Merck) and a 1 x 20 cm Econo-Column (BioRad).

The fractions containing the liposomes were quantified by colorimetrical determination of phosphorous concentration. Briefly, fractions containing the liposomes, blanks and positive or negative controls were dried at 60 °C for 30 minutes under a flow of nitrogen. Then, the content of the tubes was dissolved in perchloric acid and vortexed. The tubes were then placed in a sand bath under a temperature of 190 °C for 45 minutes. A solution containing 2.4 mM of ammonium molybdate was added to the tubes along with 100 µl of Fiske and Subbarow reducer and finally, the tubes were incubated at 100 °C in a bath for 10 minutes. To determine the concentration of the phospholipids, the absorbance of the samples was measured at 830 nm.

The size, stability and homogeneity of the produced liposomes was verified by dynamic light scattering throughout a week. Stable liposomes of ~100 nm diameter were obtained with this method.

Permeabilization experiments

For permeabilization of SUVs, different molar ratios of lipid:protein (or peptide) (1:0.77, 1:1.61 and 1.3.23, corresponding to 20, 40 or 80 µg of protein respectively) were used. Synthetic LG-13 and DG-14 peptides were purchased from Proteogenix and dissolved in 50% TFE in buffer (tris 10 mM NaCl 150 mM) or DMSO respectively. SUVs were used at a final concentration of 2.5 µM. 1% Triton X-100 was used to completely permeabilize the SUVs and was considered the “maximum” permeabilizing agent (F_{max}). Buffer was considered the “minimum” permeabilizing agent (F_{min}). The released fluorescence was measured by fluorescence spectroscopy in a Perkin Elmer LS55 spectrofluorimeter, with excitation/emission wavelengths of 450/512 nm respectively, over the course of 900

seconds. The percentage of released HPTS at a given TasA concentration (F) was calculated as follows (1):

$$\left(\frac{F-F_{min}}{F_{max}-F_{min}}\right)\times 100 \quad (1)$$

Preparation of MLVs

For the solid-state NMR spectroscopy experiments, POPE-d31 (phosphatidylethanolmine) and DMPG (phosphatidylglycerol) were purchased from Avanti Polar Lipids (Alabaster, AL). Deuterium-depleted water (2-3ppm deuterium) was obtained from Eurisotop (France). Ultrapure water with a nominal resistivity of 18.2 MΩcm (MilliQ, Millipore, France) was used for lyophilisation.

To prepare MLVs, the appropriate amounts of POPE-d31 and DMPG powders adjusted to the molar ratio (85:15, respectively) were mixed in organic solvent (chloroform/methanol, 2:1) with or without purified TasA (protein to lipid molar ratio fixed at 1:50) for co-solubilization. Solvent was evaporated under a flow of N_2 to obtain a thin lipid film. Lipids mixture were then rehydrated and lyophilised. The lipid or lipid/protein powder was hydrated with deuterium-depleted water (85% hydration) and homogenised by three cycles of shaking in a vortex mixer, freezing (liquid nitrogen, - 196 °C, 1 min) and thawing (40 °C in a water bath, 15 min). This protocol led to milky suspensions of micrometre-sized MLVs, which were packed into 4 mm-diameter solid-state NMR rotors.

Solid-state NMR spectroscopy

^{2}H NMR spectroscopy experiments were performed by using a Bruker Avance II 500 MHz WB (11.75 T) spectrometer. ^{2}H NMR spectroscopy experiments on POPE-d31 were performed at 76 MHz with a phase-cycled quadrupolar echo pulse sequence (908x-t-908y-t-acq). ^{31}P NMR spectra were acquired at 162 MHz by using a phase-cycled Hahn-echo pulse sequence (90°x-t-180°x/y-t-acq) on a Bruker Avance III HD 400 MHz spectrometer.

Spectral window of 250 kHz for ^{2}H NMR spectroscopy and 50 kHz for ^{31}P NMR were used, p/2 pulse widths ranged from 2.62 to 2.88 µs for ^{2}H and 15 µs for ^{31}P, echo delays (t) were of 40 µs, recycled delays ranged from 1.1 to 2 s for ^{2}H and 5 s for ^{31}P; 2000 to 20000 scans were used for ^{2}H NMR spectroscopy and 8000 scans were used for ^{31}P NMR spectroscopy, depending on samples.

Time domain signal were multiplied by an exponential weighting function with a line broadening of 100 to 300 Hz for ^{2}H and ^{31}P NMR spectra (before Fourier transform from the top of the echo for ^{2}H data). Samples were equilibrated for 30 min at each given temperature prior to data acquisition. All spectra were processed and analysed by using Bruker Topspin 4.0.2 software. Spectral moments were calculated for each temperature by using the NMR Depaker 1.0rc1 software [Copyright (C) 2009 Sébastien Buchoux]. Orientational order parameters (SCD) were calculated from experimental quadrupolar splittings (DnQ) according to the equation (2):

$$(2) \qquad \Delta\nu_Q(\theta) = \frac{3}{2} A_Q \left(\frac{3cos^2\theta - 1}{2}\right) S_{CD}$$

in which A_Q, the quadrupolar coupling constant for methyl moieties is 167 kHz, and q is the angle between the magnetic field and the bilayer normal. We calculated twice the value of the order parameter as a mean for structural order along the bilayer normal.

Adsorption experiments to lipid monolayer

Adsorption experiments were performed in a KSV Minitrough (Helsinki, Finland, 7.5 × 20 cm^2). The subphase was Tris 20 mM, NaCl 50mM, pH 7.4 prepared from Milli-Q water (~80 mL) with a constant temperature at 22.0 ± 1.0 °C. The subphase was continuously stirred with a magnetic stirrer. A mixture of PG:CL (58:42 molar ratio) in chloroform/methanol (2:1) solvent, was spread at the air−water interface to reach the desired initial surface pressure. After 15 min. of waiting for solvent evaporation and film stabilization, TasA, at a constant concentration of 0.5 μM, was injected underneath the preformed lipid monolayer. Their adsorption to the lipid monolayers was followed by the increase in surface pressure. As a negative control, the same volume of buffer was injected underneath the lipid monolayer, and no change in the surface pressure was observed. An independent experiment injecting 0.5 μM TasA in buffer was performed to record the surface pressure at the equilibrium in the absence of a lipid monolayer (Π_E). Maximal Insertion Pressure (MIP) corresponds to the surface pressure beyond which no absorption can happen and was obtained by linear regression of the plot $\Delta\Pi$ vs Π_i at the intersection with the x axis. The differential Π_0 ($d\Pi_0$) is the difference between $\Delta\Pi_0$, which is the y intercept of the linear regression of the $\Delta\Pi$ vs Π_i plot, and Π_E. A positive $d\Pi_0$ indicates positive effect of the tested lipid composition over the molecule adsorption. A negative value of $d\Pi_0$ suggests a negative impact of the lipid composition over the molecule insertion.

Molecular dynamics simulations by IMPALA method

For the study of the interaction of the LG-13 and DG-14 peptides with lipids, both peptides were modelled using iTasser[45] server and the IMPALA method[30] was used. The IMPALA method uses a membrane model described as a continuous medium whose properties vary along the axis perpendicular to the bilayer plane (Z axis). In addition, the method uses two energy restraints: a hydrophobic restraint and a lipid perturbation restraint, to simulate the interactions between the molecule of interest and the lipid bilayer. In this simulation, the peptides are systematically moved along the Z axis by 1 Å steps, from one side of the membrane to the other, and the restraints are calculated for each position. A profile of the energy restraints as a function of the penetration into the implicit bilayer is obtained. The sum of the two restraints is calculated to predict the most stable position within the implicit membrane.

Image analysis

Image processing was performed using Leica LAS AF (LCS Lite, Leica Microsystems), FIJI/ImageJ[46] and Imaris v7.4 (Bitplane) software.

To quantify the fluorescence of the bacteria expressing the *floT-yfp* construct, images were analyzed by subtracting a value of 5 to the YFP channel of all the images to reduce the background. The bright field channel of each image was used for thresholding a counting to calculate the mean fluorescence intensity in the YFP channel. Images were processed in batch using a custom imageJ macro.

For the colocalization analysis in the FloT-YFP and TasA-mCherry fluorescence microscopy images, 50 individual bacteria with a bright signal in both channels were manually selected and extracted from the image. Colocalization was analyzed by using the colocalization module present in Imaris, and the Pearson's coefficient value was calculated using fixed parameters for all of the analyzed bacteria. The Pearson's coefficient values corresponding to the colocalization analysis of a YFP-YFP channel from the same image were used as a positive control. The Pearson's coefficient values corresponding to the colocalization analysis of a YFP channel and 90-degree rotated images from the mCherry channel from the same image were used as a negative control.

Statistical analysis

All of the data are representative of at least three independent experiments with at least three technical replicates. The results are expressed as the mean ± standard error of the mean (SEM). Statistical significance was assessed by performing the appropriate tests (see the figure legends). All analyses were performed using GraphPad Prism version 6. P-values <0.05 were considered significant. Asterisks indicate the level of statistical significance: * = p <0.05, ** = p <0.01, *** = p <0.001, and **** = p<0.0001.

REFERENCES

1 Filloux, A. & Whitfield, C. Editorial: The many wonders of the bacterial cell surface. *FEMS Microbiol. Rev.* **40**, 161-163, (2016).

2 Vlamakis, H., Chai, Y., Beauregard, P., Losick, R. & Kolter, R. Sticking together: building a biofilm the *Bacillus subtilis* way. *Nat. Rev. Microbiol.* **11**, 157-168, (2013).

3 Vlamakis, H., Aguilar, C., Losick, R. & Kolter, R. Control of cell fate by the formation of an architecturally complex bacterial community. *Genes Dev.* **22**, 945-953, (2008).

4 Marvasi, M., Visscher, P. T. & Casillas Martinez, L. Exopolymeric substances (EPS) from *Bacillus subtilis*: polymers and genes encoding their synthesis. *FEMS Microbiol Lett.* **313**, 1-9, (2010).

5 Arnaouteli, S., MacPhee, C. E. & Stanley-Wall, N. R. Just in case it rains: building a hydrophobic biofilm the *Bacillus subtilis* way. *Curr. Opin. Microbiol.* **34**, 7-12, (2016).

6 Romero, D., Aguilar, C., Losick, R. & Kolter, R. Amyloid fibers provide structural integrity to *Bacillus subtilis* biofilms. *Proc. Natl. Acad. Sci. S A* **107**, 2230-2234, (2010).

7 Diehl, A. *et al.* Structural changes of TasA in biofilm formation of *Bacillus subtilis*. *Proc. Natl. Acad. Sci. USA* **115**, 3237-3242, (2018).

8 El Mammeri, N. *et al.* Molecular architecture of bacterial amyloids in Bacillus biofilms. *FASEB J.* **33**, 12146-12163, (2019).

9 Branda, S. S., Chu, F., Kearns, D. B., Losick, R. & Kolter, R. A major protein component of the *Bacillus subtilis* biofilm matrix. *Mol. Microbiol.* **59**, 1229-1238, (2006).

10 Romero, D., Vlamakis, H., Losick, R. & Kolter, R. An accessory protein required for anchoring and assembly of amyloid fibres in *B. subtilis* biofilms. *Mol. Microbiol.* **80**, 1155-1168, (2011).

11 Eisenberg, D. & Jucker, M. The amyloid state of proteins in human diseases. *Cell* **148**, 1188-1203, (2012).

12 Camara-Almiron, J., Caro-Astorga, J., de Vicente, A. & Romero, D. Beyond the expected: the structural and functional diversity of bacterial amyloids. *Crit. Rev. Microbiol.* **44**, 653-666, (2018).

13 Bernardino de la Serna, J., Schutz, G. J., Eggeling, C. & Cebecauer, M. There Is No Simple Model of the Plasma Membrane Organization. *Front. Cell Dev. Biol.* **4**, 106, (2016).

14 Strahl, H. & Errington, J. Bacterial Membranes: Structure, Domains, and Function. *Annu. Rev. Microbiol.* **71**, 519-538, (2017).

15 Lopez, D. & Kolter, R. Functional microdomains in bacterial membranes. *Genes Dev.* **24**, 1893-1902, (2010).

16 Wagner, R. M., Kricks, L. & Lopez, D. Functional Membrane Microdomains Organize Signaling Networks in Bacteria. *J. Membr. Biol.* **250**, 367-378, (2017).

17 Yepes, A. *et al.* The biofilm formation defect of a *Bacillus subtilis* flotillin-defective mutant involves the protease FtsH. *Mol. Microbiol.* **86**, 457-471, (2012).

18 Mielich-Suss, B., Schneider, J. & Lopez, D. Overproduction of flotillin influences cell differentiation and shape in *Bacillus subtilis*. *MBio* **4**, e00719-00713, (2013).

19 Schneider, J. *et al.* Spatio-temporal remodeling of functional membrane microdomains organizes the signaling networks of a bacterium. *PLoS Genet* **11**, e1005140, (2015).

20 Schneider, J., Mielich-Suss, B., Bohme, R. & Lopez, D. In vivo characterization of the scaffold activity of flotillin on the membrane kinase KinC of *Bacillus subtilis*. *Microbiology* **161**, 1871-1887, (2015).

21 Bach, J. N. & Bramkamp, M. Flotillins functionally organize the bacterial membrane. *Mol. Microbiol.* **88**, 1205-1217, (2013).

22 Brown, D. A. Lipid rafts, detergent-resistant membranes, and raft targeting signals. *Physiology (Bethesda)* **21**, 430-439, (2006).

23 Davis, J. H. The description of membrane lipid conformation, order and dynamics by 2H-NMR. *Biochim. Biophys. Acta* **737**, 117-171, (1983).

24 Helfrich, W. Lipid bilayer spheres: Deformation and birefringence in magnetic fields. *Physics Letters A* **43**, 409-410, (1973).

25 Knowles, T. P., Vendruscolo, M. & Dobson, C. M. The amyloid state and its association with protein misfolding diseases. *Nat. Rev. Mol. Cell Biol.* **15**, 384-396, (2014).

26 Haass, C. & Selkoe, D. J. Soluble protein oligomers in neurodegeneration: lessons from the Alzheimer's amyloid beta-peptide. *Nat. Rev. Mol. Cell Biol.* **8**, 101-112, (2007).

27 Bernat, P. *et al.* Lipid composition in a strain of *Bacillus subtilis*, a producer of iturin A lipopeptides that are active against uropathogenic bacteria. *World J. Microbiol. Biotechnol.* **32**, 157, (2016).

28 Epand, R. F., Savage, P. B. & Epand, R. M. Bacterial lipid composition and the antimicrobial efficacy of cationic steroid compounds (Ceragenins). *Biochim. Biophys. Acta* **1768**, 2500-2509, (2007).

29 Wilkins, M. R. *et al.* Protein identification and analysis tools in the ExPASy server. *Methods Mol. Biol* .**112**, 531-552, (1999).

30 Ducarme, P., Rahman, M. & Brasseur, R. IMPALA: a simple restraint field to simulate the biological membrane in molecular structure studies. *Proteins* **30**, 357-371, (1998).

31 Malishev, R., Abbasi, R., Jelinek, R. & Chai, L. Bacterial Model Membranes Reshape Fibrillation of a Functional Amyloid Protein. *Biochemistry* **57**, 5230-5238, (2018).

32 Hicks, D. A., Nalivaeva, N. N. & Turner, A. J. Lipid rafts and Alzheimer's disease: protein-lipid interactions and perturbation of signaling. *Front. Physiol.* **3**, 189, (2012).

33 Kagan, B. L. *et al.* Antimicrobial properties of amyloid peptides. *Mol. Pharm.* **9**, 708-717, (2012).

34 Brogden, K. A. Antimicrobial peptides: pore formers or metabolic inhibitors in bacteria? *Nat. Rev. Microbiol.* **3**, 238-250, (2005).

35 Jang, H. *et al.* Antimicrobial protegrin-1 forms amyloid-like fibrils with rapid kinetics suggesting a functional link. *Biophys. J.* **100**, 1775-1783, (2011).

36 Sood, R., Domanov, Y., Pietiainen, M., Kontinen, V. P. & Kinnunen, P. K. Binding of LL-37 to model biomembranes: insight into target vs host cell recognition. *Biochim. Biophys. Acta.* **1778**, 983-996, (2008).

37 Soscia, S. J. *et al.* The Alzheimer's disease-associated amyloid beta-protein is an antimicrobial peptide. *PLoS One* **5**, e9505, (2010).

38 Moir, R. D., Lathe, R. & Tanzi, R. E. The antimicrobial protection hypothesis of Alzheimer's disease. *Alzheimers Dement.* **14**, 1602-1614, (2018).

39 Stover, A. G. & Driks, A. Secretion, localization, and antibacterial activity of TasA, a *Bacillus subtilis* spore-associated protein. *J. Bacteriol.* **181**, 1664-1672, (1999).

40 Koebnik, R., Locher, K. P. & Van Gelder, P. Structure and function of bacterial outer membrane proteins: barrels in a nutshell. *Mol. Microbiol.* **37**, 239-253, (2000).

41 Samsudin, F., Ortiz-Suarez, M. L., Piggot, T. J., Bond, P. J. & Khalid, S. OmpA: A Flexible Clamp for Bacterial Cell Wall Attachment. *Structure* **24**, 2227-2235, (2016).

42 Aguilar, C., Vlamakis, H., Guzman, A., Losick, R. & Kolter, R. KinD is a checkpoint protein linking spore formation to extracellular-matrix production in *Bacillus subtilis* biofilms. *mBio* **1**, (2010).

43 Kolodkin-Gal, I. *et al.* D-amino acids trigger biofilm disassembly. *Science* **328**, 627-629, (2010).

44 Yasbin, R. E. & Young, F. E. Transduction in *Bacillus subtilis* by bacteriophage SPP1. *J. Virol.* **14**, 1343-1348, (1974).

45 Yang, J. & Zhang, Y. I-TASSER server: new development for protein structure and function predictions. *Nucleic Acids Res.* **43**, W174-181, (2015).

46 Schindelin, J. *et al.* Fiji: an open-source platform for biological-image analysis. *Nat. Methods* **9**, 676-682, (2012).

Chapter V

General discussion

Parts of the content of this chapter have been published in:

Jesús Cámara-Almirón, Joaquín Caro-Astorga, Antonio de Vicente and Diego Romero. Beyond the expected: the structural and functional diversity of bacterial amyloids. *Critical Reviews in Microbiology*. 44:6, 653-666 (2018).

Based on the results derived from this research thesis, we can establish a model that summarize our current knowledge about the contribution of TasA and TapA to ECM assembly and bacterial physiology of *B. subtilis* (Fig. 5.1).

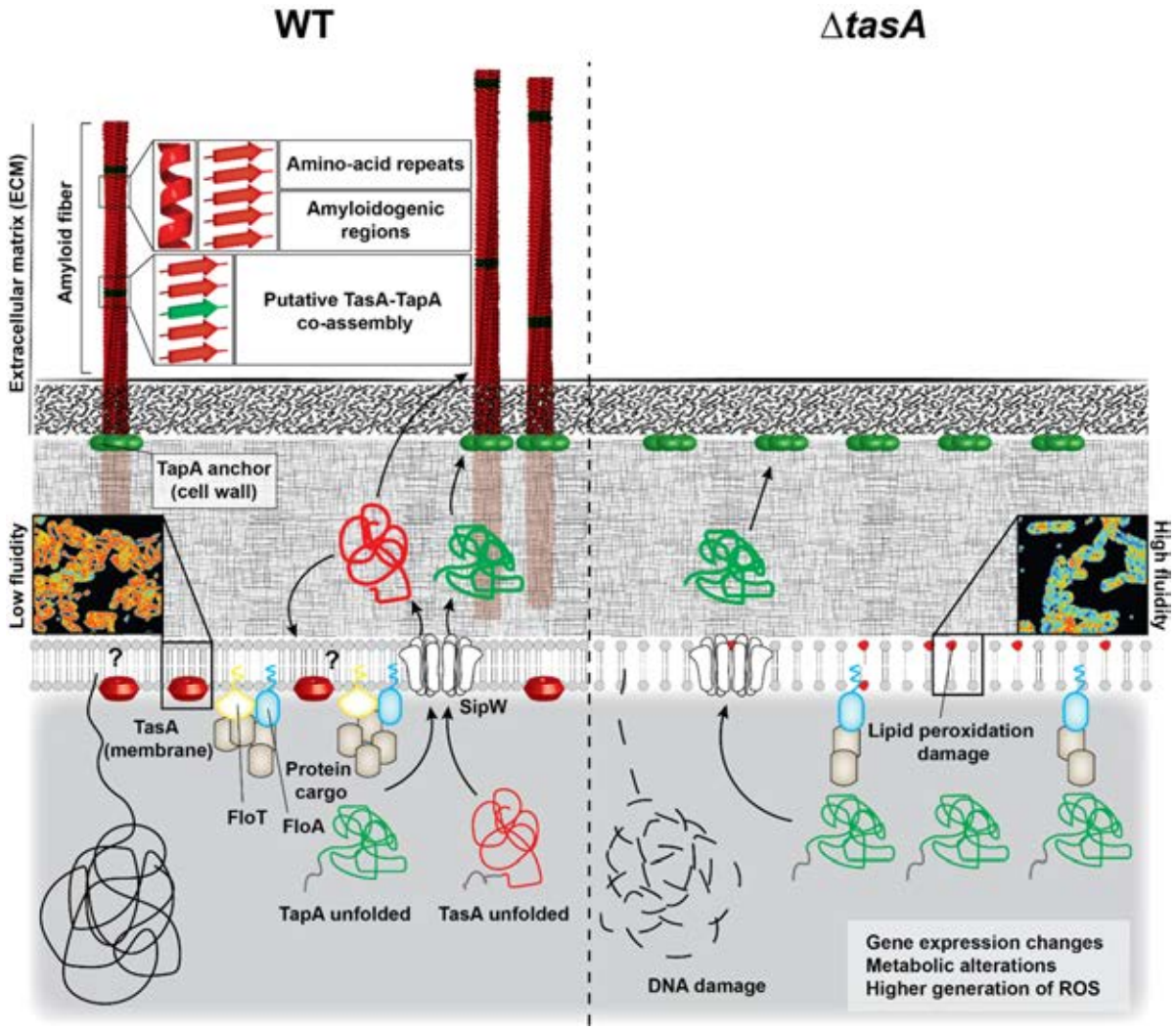

Figure 5.1. Current model of the contribution of TasA and TapA to bacterial ECM formation and cell physiology. TasA (in red) and TapA (in green) are the components of the amyloid fiber present in *B. subtilis* ECM. Both proteins are synthesized in the cytoplasm and are exported outside the cell through the SEC system, where they are processed in the membrane by the signal peptidase SipW. Mature TasA is the main component of the amyloid fiber. These fibers are enriched in β-sheet content, with an unusual proportion of α-helix. Imperfect amino-acid repeats and amyloidogenic regions within TasA sequence facilitate the amyloid fold. Mature TapA stimulates TasA polymerization and anchor the fibers to the cell surface (specifically to the cell wall). TapA also shows amyloid properties, and a putative co-assembly along with TasA is possible. Mature TasA is also present in the cell membrane, where it contributes to cell membrane dynamics and stabilization by maintaining a physiological fluidity. The flotillins (FloT and FloA) are also localized in the cell membrane, organizing functional membrane microdomains (FMM). In the absence of TasA, membrane destabilization occurs. Membrane fluidity is increased, leading to gene expression changes, FloT mislocalization, metabolic alterations, higher generation of ROS, etc, which cause an excess of stress and damage to cellular components (DNA, lipids, etc), eventually triggering cell death.

As mentioned throughout this work, TasA is the major protein component of the ECM of *B. subtilis*[1]. This protein is the main component of the amyloid fibers, that structurally support the ECM of this microorganism[2]. TapA is an accessory protein, minorly present in the fiber, that facilitates TasA polymerization into the form of fibers and, presumably,

anchor these fibers to the cell wall[3]. Therefore, both proteins are essential for biofilm formation. TasA and TapA are translocated to the cell membrane by the SEC system, where they are processed by the signal peptidase SipW[4-6], encoded in the same operon, prior to their release outside the cell, where the amyloid fibers are formed. The work shown in Chapter II allow us to establish a mechanistic picture by which this process occurs. We have demonstrated that recombinant TasA heterologously expressed in *E. coli*, *in vitro*, exhibit the hallmark features of amyloid properties: i) polymerization in fibrillar entities, ii) binding to amyloid-specific dyes i. e. ThT and iii) typical X-ray diffraction pattern. Moreover, recombinant purified TasA exogenously added to *B. subtilis* Δ*tasA* cultures restored the strain's ability to assemble a biofilm, confirming the biological functionality of the recombinant protein.

The analysis of the structural fingerprint of TasA filaments by SSNMR spectroscopy revealed that TasA filaments exhibit a high degree of structural order, comprised by well-ordered TasA subunits. The analysis of the secondary structure propensity of TasA filaments revealed that, these were enriched in β-sheet content, although an unusual proportion of α-helix is found. Furthermore, the rigid amyloid core of the filament, highly ordered with a cross-beta arrangement, does not include the whole TasA protein. Our NMR analysis revealed that only a portion, specifically, the N-terminal part of the protein contributes to the formation of this amyloid core. An in-depth analysis of the sequence corresponding to this amyloid core revealed several sequence features that contribute to the amyloid tendency of TasA and to the formation of the fiber: imperfect amino-acid repeats and two amyloidogenic regions within the N-terminal half of the protein.

Furthermore, we also studied TapA, the other protein required for the assembly of the amyloid fiber during biofilm formation, anchorage of the TasA fibers to the cell wall[3] and enhancement of TasA polymerization[7]. Interestingly, our NMR analysis show that this protein, *in vitro*, self-assemble into amyloid aggregates with a structural fold similar to that observed for TasA, exhibiting all the features typical of amyloid proteins. Further analysis by NMR spectroscopy showed that *in vitro* coassembly of the two proteins did not perturb the global TasA filament architecture, highlighting the possibility that this co-assembly also occurs *in vivo*.

The structural role of TasA amyloid system in ECM assembly and biofilm formation is long known. However, in the last years several groups have investigated the mechanistic insights by which the extracellular fibers of *B. subtilis* biofilms are formed. The model has been recently challenged, and claims were made regarding the amyloid nature of these fibers, at least, when the protein is expressed in *E. coli*[8]. Nonetheless, further structural

studies have proven the amyloidogenicity of TasA beyond any doubt. As discussed in Chapter II, the crystal structure of soluble monomeric TasA heterologously produced was recently solved, consisting in a jellyroll fold (i. e. a protein structure in which beta-strands are arranged in antiparallel β-sheets) of two antiparallel β-sheets surrounded by six α-helices. This soluble form of TasA transitions to different oligomeric forms, including amyloid fibrils with the characteristic cross-β pattern, that is the most commonly found form in biofilms[9]. The work described in Chapter II of this thesis is focused on the characterization of fibrillar assemblies formed by recombinant TasA. Indeed, when TasA transition to the fibrillar form, these assemblies are enriched in β-sheet content, show the typical tinctorial properties of amyloid proteins and display the canonical X-ray diffraction signals thus, confirming the amyloid nature of the purified protein, in agreement with previous works[10].

In this study we also engaged in the structural study of TapA, the accessory protein required for the proper assembly of the ECM *in vivo*. In contrast with its partner, what we know about TapA comes only from functional studies[3,7], and there is a lack of structural information regarding this protein, which is only present in *B. subtilis* and closely related species. In our study, we found that TapA also exhibit all the typical amyloid properties, which can explain why TapA is co-purified with TasA in *B. subtilis* fibers[3]. These findings open the possibility of a putative co-assembly *in vivo* between the two-proteins, which is, in theory, possible, as demonstrated by our NMR experiments. Regarding the biological function of this protein, very little progress has been made. We know from past studies that this protein participates in the polymerization process[7] of TasA and that, somehow, TapA maintains the filaments attached to the cell surface via the cell wall[3], however, we still miss information on how TasA and TapA interact, the amino-acids involved in this interaction, detailed structural information of TapA and the mechanism by which this protein interacts with the peptidoglycan. In fact, only a small part of TapA sequence seems to be important for the assembly of the ECM and biofilm formation, as it has been demonstrated that the C-terminal end of the protein is dispensable for this function[7]. Nonetheless, this part of the protein is completely unstructured, which suggest that this region may be involved in a different functionality yet to be discovered. The fact that TapA has been found associated to the peptidoglycan and TasA, as demonstrated in Chapter IV, has been located in the cell membrane when both proteins lack any canonical sequence to bind these cellular localizations, suggest other protein partners might be actively playing a role in this amyloid platform by interacting with either TasA or TapA. More research is needed to expand our knowledge of these two proteins in this

direction. Overall, this work has deepened our understanding of the amyloid system present in *B. subtilis*.

Orthologues to TasA are found in *Bacillus cereus* and closely related pathogenic *Bacillus* species, such as *Bacillus anthracis* or *Bacillus thuringiensis*. In these group of Bacilli, TasA (referred as $TasA_{Bc}$) is encoded in a genomic region that includes a *sipW-tasA* operon, in which TapA is absent and another orthologue of TasA, CalY, is found in a separate transcriptional unit[41]. The $TasA_{Bc}$ protein is considerably smaller than *B. subtilis* TasA (197 vs 261 amino-acids) and they share a ~35% sequence homology that is mostly located at the N-terminal half of the protein, concurring with the amyloid core region found in *B. subtilis* TasA[10]. In contrast, $TasA_{Bc}$ and CalY share much higher sequence identity, ~62%. Both TasA orthologues have the canonical signal peptide sequences that are recognized by the signal peptidase SipW and they are involved in biofilm formation in *B. cereus*. In fact, $TasA_{Bc}$ forms fibers in the cell surface similar to those observed for TasA in *B. subtilis*, suggesting an analogous role[41]. Indeed, structural studies performed in $TasA_{Bc}$ confirmed that, *in vitro*, the protein is able to polymerize into filaments faster than its homolog in *B. subtilis*, although with less structural organization. Nonetheless, $TasA_{Bc}$ fibers exhibit the typical amyloid tinctorial properties, with the canonic X-ray diffraction pattern. Solid state NMR data have shown that the filaments formed by the two proteins have the same structural fingerprint, indicating that the rigid core of both filaments share similar structural fold, however, $TasA_{Bc}$ filaments show a higher degree of structural polymorphism, i. e. structural variations among the different molecular assemblies formed by this protein[42], suggesting differences in the assembly process. Similar to TapA, CalY, seems to act as an accessory protein, favoring $TasA_{Bc}$ nucleation, catalyzing the polymerization process and adopting a typical amyloid fold, but in contrast to $TasA_{Bc}$, this protein does not assemble into filaments, and rather amorphous aggregates are observed[10]. Therefore, despite our abundant structural knowledge about the function of $TasA_{Bc}$ and CalY in biofilm formation in *B. cereus*, we lack any information regarding an analogous function of these functional amyloids to *B. subtilis* TasA in bacterial physiology and membrane interaction, which will hopefully be the subject of future studies.

Nevertheless, functional amyloids are present in a broad range of organisms and they are especially relevant in bacteria, where, in many cases, fulfill analogous roles in biofilm formation as those described for TasA and TapA. Fibrillation of functional amyloids can lead to the generation of oligomeric pre-fibrillar assemblies[11] that are toxic and can affect cell viability due to their ability to disrupt biological membranes, the main target of this molecular assemblies[12]. One way to prevent the formation of these pre-fibrillar

assemblies is to control the rate at which these species are formed. Accordingly, some functional amyloids undergo a very fast transition to the fibrillar state to minimize the proliferation of this toxic oligomeric intermediates[11]. This is achieved, in the case of bacterial amyloids, by accessory proteins that tightly control the polymerization process and, in most cases, enhance it. The curli amyloid fibers of *Escherichia coli* and *Salmonella spp.* are composed mainly of the major protein component CsgA (and its corresponding ortholog in *Salmonella spp.*)[13]. Nonetheless, the protein CsgB, encoded in the same operon *csgABC,* acts as a nucleator of curli fiber assembly, in a similar way to TapA in *B. subtilis*. CsgB facilitates polymerization of CsgA into fibers upon interaction and seems to be responsible for the attachment of the fibers to the cell surface[14,15] through the interaction with CsgF[16]. In addition to CsgB, there are 5 other proteins, CsgC-G, which are similarly important to fiber assembly even though they are not directly components of the fiber. CsgD acts as a positive transcriptional regulator of the system[17], whereas the other proteins have a more complex role. CsgG and CsgF are responsible for the formation of a channel structure in the outer membrane that allows for the secretion of CsgA, CsgB and CsgF from the periplasm to the outside of the cell[18]. CsgE interacts with CsgA by a signal-peptide dependent mechanism, conferring substrate specificity to the CsgG-mediated secretion[19] . In addition, it has been shown that CsgE blocks the polymerization of CsgA *in vitro*, and it is therefore thought to be a molecular chaperone that restricts curli fiber formation to the extracellular space, thus preventing the production of toxic amyloid oligomers inside the cell[19]. In a similar way, it has been shown that CsgC functions as a very selective and efficient amyloid inhibitor that is able to impede polymerization of CsgA and other amyloid proteins that share a common motif within their sequence[20]. Finally, CsgF works as a chaperone that facilitates CsgB localization and function (Nenninger et al. 2009) and, in addition, it has been demonstrated how this protein, when found as part of the dual CsgG-CsgF dual pore structure, participates in the specific recognition of CsgA during amyloid fiber assembly through specific amino-acids located in the N-terminal region of CsgA[16].

Accessory proteins that assist bacterial amyloid polymerization are also found in other gram-negative bacteria. The *fapABCDEF* operon is present in several members of the *Beta-*, *Delta-*, and *Gammaproteobacteria*[21] and has been well characterized in *Pseudomonas spp*. This operon is responsible for encoding the Fap amyloid fibrils found in *Pseudomonas spp.* biofilms that play a role in their hydrophobicity and robustness[22]. The protein FapC is the major protein component of the Fap fibers[23]. However, the other Fap proteins play an important role in the proper assembly and function of the FapC fibril[24]. In addition to FapC, there are two other proteins present in a lower proportion in

the fiber: FapB and FapE. FapB seems to function as a nucleator protein in a similar way as CsgB in curli and TapA in TasA filaments, whereas the role of FapE is still uncertain. Similar to curli, all the Fap proteins are secreted via Sec across the inner membrane, and once located in the periplasm, they are sorted according to their final destinations. FapA and D remain in the periplasm, while FapB, C and E are potentially secreted to the outside of the cell by FapF, which has been identified by bioinformatic methods as a probable membrane-associated pore with a β-barrel conformation. This has been recently confirmed by the determination of the complete 3D structure of FapF, which is defined as a trimer composed of three beta barrels plugged by α-helices in its closed state, resembling the classical structure of the Type V auto-transporter family[25]. In this protein, the N-terminal coiled-coil region aids the complex in forming a stable trimer and is required for the secretion of FapC outside the cell via a mechanism that probably involves a conformational change in the plugs, which have been shown to be additionally required for FapF-dependent FapC secretion. Evidence suggests that in the periplasm, FapA acts as a molecular chaperone, possibly facilitating the incorporation of FapC and B monomers to the growing fibers, whereas FapD might be a dedicated protease for the processing of other Fap proteins, which in collaboration with FapF might direct their transport to the extracellular milieu. Indeed, FapD has been characterized as a cysteine-peptidase active in the periplasm and required for FapC secretion, which most likely targets FapE since it has been demonstrated that the N-terminal region of FapE is cleaved during the secretion process[25]. It is also interesting to note that the C-terminal region of FapE contains amino acid repeats similar to the amyloid regions found in FapC and B suggesting a FapD-dependent processing of FapE prior to the formation of the amyloid fibril, which would facilitate FapC and B secretion through FapF.

Indeed, amino-acid repeats seem to be a common theme in bacterial functional amyloids that are involved in biofilm formation, but also in other amyloid proteins[26,27] as they seem to be important for amyloidogenesis. Consistently, amino-acid repeats found in TasA are relevant for ECM assembly and biofilm formation in *B. subtilis*, and substitution of one amino-acid from this region completely alter colony morphology and affect the stability of the protein when it reaches the ECM, indicating a malfunction in the assembly of the amyloid filament. However, more work is needed to fully characterize the importance of these regions in the functionality of TasA during biofilm formation.

Nonetheless, in other gram-positive organisms the assembly of amyloid protein scaffolds required for ECM formation is not mediated by accessory proteins and rather, a combination of the intrinsic properties of the protein sequence along with specific environmental conditions trigger the amyloidogenic process in some biofilm-related

proteins. That is the case of Bap (biofilm associated protein), a surface anchor protein involved in bacteria-bacteria and bacteria-surface interactions present in *Staphylococcus aureus* and other coagulase-negative Staphylococci[28,29]. This protein has the ability to aggregate when the medium es acidified, indicative of its role in biofilm formation during stationary phase-related processes. Moreover, Bap is processed during development via an unknown mechanism and is the N-terminal half of the protein the one that is found in Bap aggregates, required for the multicellular behavior of this bacterium. *In vitro*, the Bap aggregates show an amyloid fold at acidic pH, exhibiting the typical biochemical properties of amyloid proteins, and adopt a fibrillar quaternary structure. Interestingly, Bap behavior is affected by minimal concentrations of calcium, that are able to suppress amyloid aggregation, consistent with the inhibition of bacterial aggregation observed in the presence of this ion[30,31]. Similar behavior has been found for other Bap orthologues, such as the Esp amyloid fibers found in *Enterococcus faecalis*[32].

The importance of TasA in the assembly of the amyloid fiber and ECM formation is supported by the contribution of this structure to the fitness of *B. subtilis* on plant leaves. Previous studies demonstrated the importance of surfactin, a lipopeptide produced by *B. subtilis* that is involved in quorum sensing signaling during the formation of multicellular communities[33], in the persistence and biofilm formation of this bacterium over the phylloplane, contributing to its antagonistic capacity against plant pathogens[34]. Thus, we asked whether the different structural components of the ECM played a relevant role in the interaction of *B. subtilis* with plant leaves. Over the plant, the ECM, and the presence of TasA in particular, demonstrated to be important for the survival and persistence of *B. subtilis* cells. Moreover, Δ*tasA* cells produced larger amounts of fengycin than the WT strain, therefore, despite the inability of the *tasA* mutant to form a biofilm and efficiently persist over plant leaves, both strains display comparable antagonistic activity against a plant phytopathogenic fungus. This finding led us to investigate a more intriguing role of TasA, beyond its structural functionality during ECM assembly, in preserving bacterial physiology. As seen in Chapter III, deletion of TasA has a pleiotropic effect, leading to gene expression changes of nearly one third of the genome at some time points. We saw that all the transcriptomic changes occurring in the *tasA* mutant point toward complete metabolic rearrangement and an excess of cellular stress in Δ*tasA* cells, with differential expression of genes related to: synthesis of secondary metabolites, anaerobic respiration and fermentation, general stress and DNA damage among other functions.

Indeed, *tasA* mutant cells exhibited a broad range of cellular alterations and damage. First, cells lacking TasA show altered respiration rates and a higher generation of ROS.

This is probably the cause of different cytological alterations found in Δ*tasA* cells, such as lower tolerance to lipid peroxidation or presence of DNA strand breaks. In addition, the metabolic alterations translate into a higher production of fengycin in Δ*tasA* cells, and a decrease in the intracellular pH. The absence of TasA, in addition, causes an increase in the membrane fluidity and alterations in the membrane potential, which could be the source of all the changes mentioned above as a consequence of cell membrane destabilization. These changes, eventually, lead to an increase of cell death within the Δ*tasA* that is, on average, around 20% higher than in WT colonies. This role of TasA in preventing premature cell death is independent from the role of this protein in biofilm formation. We demonstrated that mutant strains impaired in biofilm formation, e. g. a *tapA* or a *sinI* mutant, were unaffected in their cell death levels when compared to the WT strain. To further confirm this, we used a strain bearing a mutated version of TasA, that was unable to fully assemble the ECM, but in which TasA was stable and present in the ECM in similar amounts as those found in the WT strain. This mutated TasA protein is, presumably, affected in its amyloid capacity. However, this mutated protein was able to restore to normality all the physiological phenotypes that were altered in a *tasA* null mutant. Thus, we can assign TasA a new function in the prevention of premature cell death during colony growth.

The molecular mechanism by which this new function occurs has been addressed in Chapter IV of this thesis. The absence of TasA altered functions related to the cell membrane, such as membrane potential and membrane fluidity. Alterations in a critical cellular structure, such as the cell membrane, are consistent with the extent of the changes observed in the *tasA* mutant. The increase of membrane fluidity compared to the WT strain, pointed toward specific changes related to the flotillins. These proteins organize signaling complexes in the membrane that regulate diverse biological processes by acting as scaffolds[35-38]. They are localized in specific domains within the cell membrane, designated as functional membrane microdomains (FMM)[36], that are characterized for being enriched in proteins and having a different lipid composition[38,39]. These proteins present a typical distribution pattern in the form of foci that are heterogeneously distributed across the cell membrane[36,37]. By studying the localization of the flotillin FloT in Δ*tasA* cells, we found that this protein was delocalized in the mutant, which lost the typical focal localization of FloT within the cell membrane. In addition, we checked the localization of TasA by several methods. First, we performed a chemical fractionation of purified membrane fractions based on detergent solubility. This treatment partitions the membrane in detergent-resistant and sensitive fractions (DRM or DSM, respectively)[36,40]. The DRM fraction contains most of the membrane proteins that are

present in the FMMs, hence its higher resistance to solubility by detergents. The analysis of this fractions by western blot, localized TasA mostly in the DRM fraction of the membrane and in the cytosol. Second, the analysis of TasA localization by confocal microscopy, revealed that this protein was homogeneously distributed in the cell surface, and, in occasions, we could see two small foci formed at the cell poles. Interestingly, this was also observed when protoplasted cells were analyzed. Overall, these results indicate that TasA is a membrane bound protein.

To further confirm the presence of TasA in the cell membrane, we studied *in vitro* the interaction of this protein with lipids of different nature. We used the purified TasA protein encapsulated inside multilamellar vesicles and studied the lipid structure in the presence of TasA by solid-state NMR spectroscopy. Our results demonstrate that the lipid bilayers can accommodate TasA without perturbing their integrity or structure and in fact, TasA increases the global rigidity of the lipid structure. Further experiments demonstrated that the interaction of TasA with lipids is determined by the lipid composition and that in these interactions, an amyloidogenic sequence in the N-terminal region of the protein, that interestingly, exhibit a high degree of hydrophobicity, seems to be the contributor. In conclusion, we have demonstrated that TasA is bound to the cell membrane and this maintains the cell membrane stability and dynamics necessary for preventing the premature cell death that is observed in Δ*tasA* cells.

As seen in Chapters III and IV, the presence of TasA in the cell membrane stabilizes cell membrane dynamics, preventing the excess of cellular stress that leads to cell death in Δ*tasA* colonies. Our findings are consistent with previous work that describe how the heterogeneity in cell death, spatially compartmentalized within the *B. subtilis* colony, affects 3D patterning during biofilm formation. Interestingly, this study found that cell death is specifically localized in the wrinkles that appear when *B. subtilis* biofilms are formed on solid media and this pattern of cell death is lost when some genes related to the ECM assembly, such as *tasA* or *epsH*, are deleted[43]. In these strains, cell death seems to be homogeneously distributed in the center of the colony, where most of the wrinkles are generated in the WT strain. Indeed, we saw that when *tasA* is deleted, cell death is not only spatially altered but also increased, as we found an increment of nearly 15% more dead cells in the Δ*tasA* colony compared to the WT colony, consistent with the lower CFU counts found in the Δ*tasA* colony. We observed that TapA plays no part in this biological function exerted by TasA, as this is completely independent from the role of TasA in ECM assembly. Indeed, Δ*tapA* cells show levels of cell death comparable to those of the WT strain. This result implies that the interaction between these two proteins is not necessary to direct or stabilize TasA in the cell membrane. In fact, a *sinI*

deletion strain, unable to repress sinR and therefore, producing the lowest amount of TasA[44,45], exhibited levels of cell death similar to those found in the WT strain. These results suggest that most of the synthesized TasA is needed for the assembly of the amyloid fiber and biofilm formation and only a small fraction of the protein is required in the cell membrane to regulate cell membrane dynamics.

The data shown in Chapter III suggest that the decreased cell viability observed in Δ*tasA* colony might be the consequence of a process of programmed or regulated cell death (PCD or RCD). For the purpose of this discussion, both terms will be used interchangeably (See reference number 49 for more information). In eukaryotic cells, cell death is the final outcome of apoptosis, a well-established process whose existence in bacterial communities has been of interest in the recent years[46-48]. Indeed, the membrane instability caused by the absence of TasA is itself a trigger responsible for the alterations in the expression levels of almost one third of the genome at some time-points, which fits consistently with the definition of a controlled process rather than something accidental. Accidental cell death (ACD) is defined as a "virtually instantaneous and uncontrollable form of cell death corresponding to the physical disassembly of the plasma membrane caused by extreme physical, chemical, or mechanical cues"[49]. ACD could be triggered, for instance, when cells are abruptly and extremely heated above physiological temperatures; therefore, this process does not rely on any cellular regulation as it occurs suddenly and rapidly. The cell death observed in the *tasA* mutant occurs increasingly over time, concomitant with progressive and major changes in gene expression. Therefore, all of the related alterations observed in the absence of TasA might be more consistent with the definition of RCD, which is a general term used to describe any "form of cell death that results from the activation of one or more signal transduction modules"[49]. In fact, many of the physiological and cytological defects exhibited by the *tasA* mutant have been previously described to be associated with processes of PCD, such as the generation of reactive oxygen species[50], DNA fragmentation[51], hyperpolarization of the membrane potential[52], caspase-like activity[53] or lipid peroxidation[54]. However, the cell death pathway activated in the absence of TasA is yet unknown. The overexpression in Δ*tasA* cells of endolysins and holins from the bacteriophage PBSX, a prophage encoded within the *B. subtilis* genome and fully activated in the *tasA* mutant (see Supplementary Data 3.1, 3.2 and 3.3), could be a possible mechanism by which Δ*tasA* cells are able to trigger a process of PCD, but this remains to be investigated in detail.

Considering that the lower cell viability found within the Δ*tasA* colony is the consequence of processes of PCD arising in *tasA* mutant cells, it is tempting to suggest an accelerated

aging as a global explanation for the pleiotropic changes that occur in the absence of this protein. In eukaryotes and prokaryotes, senescence involves a global change in cell physiology that, in microorganisms, begins with their entry into stationary phase[55-57]. At this stage, cell division occurs at a slower rate[57], the molecular machinery adapts to increase cellular resistance and respiration, and the primary metabolism shifts to fermentative pathways and to the production of secondary metabolites[58]. During bacterial growth, the cells divide in a semi-asymmetrical fashion such that the daughter cells receive the newly synthesized cellular elements, while the mother cells receive an old cell pole that contains flawed components, such as damaged DNA, compromised cell envelopes and oxidized proteins, which must be repaired or replaced. This uneven partitioning of cellular components comes with a fitness cost for the microorganism[59,60]. This process triggers a response typified by molecular mechanisms designed to overcome these adversities and to ensure survival: activation of general stress response genes[61,62], a shift to anaerobic respiration[58], enhanced DNA repair[63], and induction of pathways to metabolize alternative nutrient sources or sub-products of primary metabolism[64]. All the above described phenotypes and changes are reminiscent of the alterations found in Δ*tasA* cells and are compatible with a process of senescence, but this is a question that has to be thoroughly studied.

Apart from our work in the *tasA* mutant, we also investigated if deletions of other ECM structural components were able to cause a similar phenotype as that observed in Δ*tasA* cells. For that purpose, we performed experiments with Δ*eps* mutant strain, lacking the whole *eps* operon (data not shown). The Δ*eps* colony exhibited higher levels of cell death than those of the WT colony and comparable to those found in the Δ*tasA* colony. However, a preliminary analysis of RNA-seq data from this mutant revealed that the causes underlying this excess of cell death are different from those acting in the Δ*tasA* strain. The comparison of Δ*tasA* or Δ*eps* strains with the WT strain at every time-point, revealed similarities among the two mutants in their transcriptional responses. However, the number of differentially expressed genes in the Δ*tasA* strain, when adding the Δ*eps* strain into consideration, is considerably lower, highlighting the alterations dependent on the absence of a structured ECM. Nonetheless, the comparison between the Δ*tasA* and Δ*eps* strains revealed that the Δ*tasA* strain specifically shows differential expression of functional categories related to the cell membrane and induction of stress pathways, including *sigB*, which appear to be induced at all times, and many SigB-related general stress genes, i.e., genes involved in the detoxification of ROS, DNA repair and all of the genes related to the bacteriophage PBSX. These changes lead to specific phenotypic changes in the Δ*tasA* compared to the Δ*eps* strain, such as the loss of the normal

distribution pattern of FloT, which in the Δ*eps* strain, in contrast, occurs normally, indicating that the membrane destabilization that occurs in Δ*tasA* cells is not happening in the Δ*eps* strain and therefore, the increase of cell death observed in the Δ*eps* strain is due to other factors.

It has been established, as previously mentioned, that the presence of TasA in the membrane maintains membrane stabilization and participates in the regulation of cell membrane dynamics, however, in contrast to the already existing amount of structural information regarding the role of TasA in the ECM, very little is known about the conformation adopted by TasA at this cellular localization. In Chapter IV, we focused on how TasA affect the local structure of the lipid environment and how this protein interact with different lipid structures and compositions. Another study[65] confirmed the interaction of TasA with two types of lipid vesicles and studied the secondary structure of the protein in the presence of lipids, however, it does not reveal neither insightful structural information nor any information regarding the aggregation state of TasA when it is in contact with these vesicles. The influence of biological membranes in the folding of amyloid proteins has been extensively investigated, especially in the disease related amyloids that affect human health[66-68]. Indeed, the interaction of a native protein with lipids can cause or exacerbate protein unfolding, as some molecular interactions governing protein native folding can be loosened when facing a hydrophobic surface. There are several ways by which the lipid environment can affect amyloid aggregation: i) actively recruiting a protein and thus, increasing its local concentration, favoring the aggregation process; ii) inducing a conformational change in the target protein to a partially folded state; iii) triggering an aggregation-prone conformational change or iv) modulating the insertion depth of the polypeptide into the bilayer, which it is related to the nucleation propensity[69]. Normally, the oligomeric state of amyloid proteins is the preferred form in the interaction with biological membranes and lipids and in fact, this ability of prefibrillar oligomers to directly interact with cell membranes is what confers amyloid proteins part of their toxicity[70-72] (Fig. 5.2).

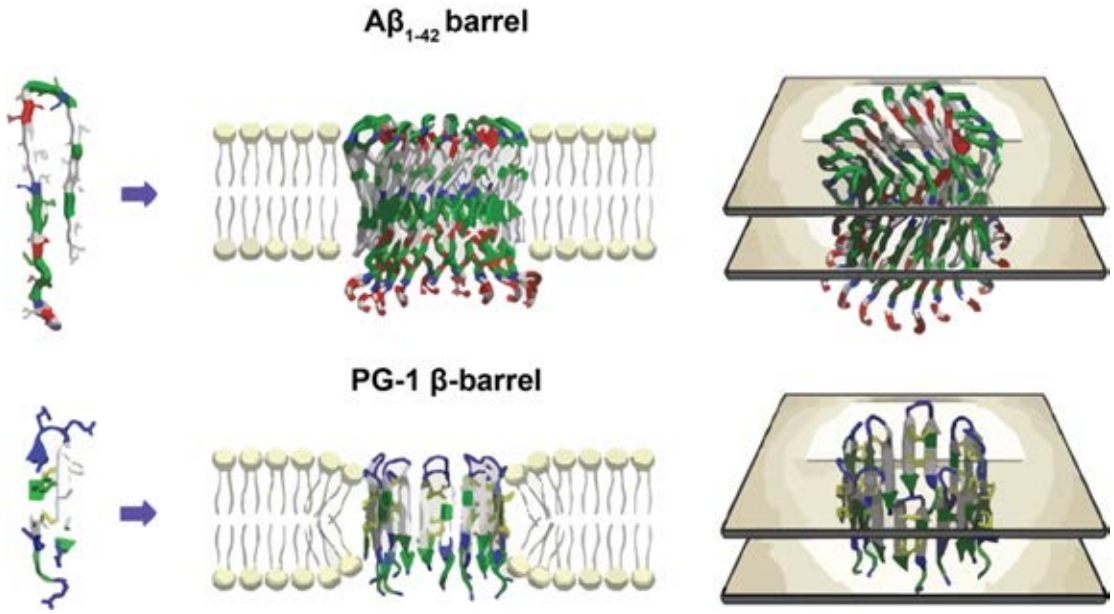

Figure 5.2. Schematic representation of membrane channels formed by amyloid peptides. $A\beta_{1-42}$ is the main peptide found in the brain deposits of patients suffering from Alzheimer's disease. Protegrin-1 (PG-1) is a broad-spectrum antimicrobial peptide produced as part of the immune response. Antimicrobial peptides and some amyloid peptides and proteins share similarities in their quaternary structure, adopting a β-barrel oligomeric conformation that is able to disrupt lipid bilayers by permeabilizing them, leading to increased cytotoxicity. Reprinted with permission from Kagan, B. L. *et al.* (2012)[71]**.**

The alternative role of TasA in functions other than ECM assembly has also been described elsewhere. In a recent work, it has been observed that a Δ*tasA* mutant is impaired in motility, and transcriptomics analysis of Δ*tasA* colonies, similar to that mentioned in Chapter III, evidence that indeed, TasA is necessary for the expression of flagellar genes and further experiments confirmed the TasA-dependent flagellar motility[73]. Interestingly, the presence of TasA seems to activate the switching of the cells from biofilm to a motile state. This switch, as previously seen, is governed by the regulators SinI. SlrR and DegU (through a different pathway)[74-77]. The deletion of TasA in a mutant genetic background for each of the regulators mentioned above had no effect in the number of motile cells, which increased independently on *tasA* deletion (in the case of the *sinI* or *slrR* mutant backgrounds). However, in a *degU* mutant background, deletion of *tasA* further decreased the already diminished population of motile cells, indicating that TasA is involved in the biofilm-motility switch in a manner completely independent from these regulators. The isolation of a suppressor mutant in the motility defect observed in a Δ*tasA* colony revealed that the CssR/CssS two-component system, only known to be involved in stress response[78], regulates motility and the expression of ECM-related genes. Moreover, this system seems to counteract the switch back to motility promoted by TasA, suggesting that biofilms need to maintain a certain degree of motility to face unpredictable and changing environmental conditions. Overall, these

results confirm the multifunctional role of this functional amyloid and adds another function beyond the formation of the amyloid fiber.

Up to this date, TasA is the only known functional amyloid that exert part of its functionality associated to the cell membrane and is the first functional amyloid directly found associated to this cell compartment. Considering the biological functions of TasA beyond its structural role in biofilm formation, it is interesting to suggest that different amyloid conformations could be involved in distinct biological functions executed at specific cellular localizations, consistent with the notion of functional amyloid. For instance, the ability of TasA to selectively interact with different types of lipid vesicles *in vitro* containing different lipid compositions (see Chapter IV), suggest that, as mentioned above, an oligomeric state of TasA might be responsible of maintaining the cell membrane stability. If this is the case, how is cell viability preserved in the presence of, potentially toxic, oligomeric species in the membrane? First, it is tempting to speculate that the interaction of TasA with other proteins might be stabilizing these oligomers in the membrane at the same time that these proteins somehow lead TasA monomers to the ECM to assemble the amyloid fiber. Second, another way to minimize the toxicity of these kind of amyloid assemblies is to limit their numbers[11]. As previously seen, experiments performed in a *sinI* mutant suggest that membrane stabilization by TasA requires minimal amounts of the protein, minimizing the potential toxicity of these putative oligomers. However, the biologically active conformation of TasA within the cell membrane is still a question that remains to be answered in future works.

The fact that TasA is involved in the regulation of cell membrane stability and membrane dynamics and the mislocalization of FloT that occurs in Δ*tasA* cells arise the question about the interplay between TasA, the flotillins and the FMMs. The alterations mentioned above, and the localization of TasA in the DRM fraction of the cell membrane are evidences of this putative relationship, that will place TasA in proximity to these membrane regions. However, the evidence suggest that TasA is not part of these FMMs directly. FMMs are determined by the flotillins (Fig. 5.3A), which are dynamic structures that diffuse across the cell membrane[36,40,79]. In contrast, TasA has been found homogenously distributed in the cell membrane and, more importantly, seems to be static within this structure. Deletion of either FloT or FloT and FloA had no effect in cell viability, therefore, it seems that the loss of FloT distribution pattern is just a consequence of the alteration of membrane stability triggered by the absence of TasA.

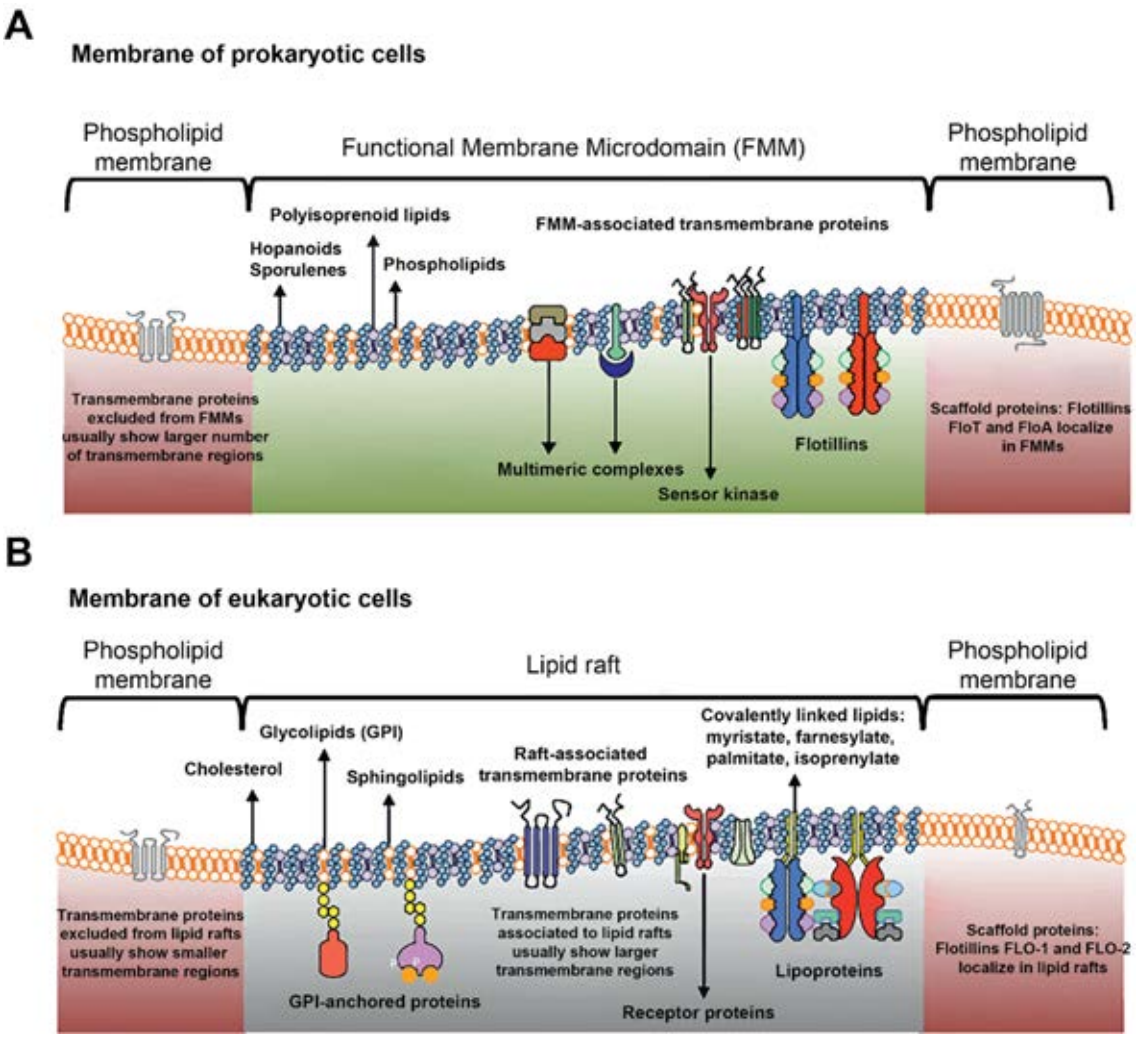

Figure 5.3. Schematic representation of functional membrane microdomains (FMM) found in prokaryotic cells (A) and comparison with lipid rafts from eukaryotic cell membranes (B). Both kind of lipid domains are enriched in proteins and display a differential lipid composition compared to rest of the membrane. However, the binding mechanisms of proteins to these domains are different. In addition, lipid rafts can contain monomeric protein, whereas FMMs contain protein complexes of several partners. Reprinted from López, D. and Koch, G. (2017)[39] with permission from Elsevier.

The mechanism by which these flotillins are bound to the cell membrane is by interaction with certain phospholipids, which is possible in eukaryotes thanks to the presence of a prohibitin homology domain (PHB) that contain acylation targets that, along with hydrophobic regions within the protein sequence, stimulate the binding of these proteins to the cell membrane and their oligomerization[80]. In the case of bacterial flotillins, the PHB domain does not seem to be involved in the binding of these proteins to the membrane, which is achieved by a small hydrophobic N-terminal hairpin loop, whereas the PHB domain is dedicated to protein oligomerization[81]. Therefore, the mislocalization of FloT that occurs in Δ*tasA* cells must be related, somehow, to changes in the lipid composition of the cell membrane. Farnesol, a polyisoprenoid cholesterol-like lipid found in *B. subtilis* cell membrane (Fig. 5.3A), seems to be characteristically present in FMMs,

inhibitors of YisP, the enzyme required for the synthesis of this compound, are able to disassemble FMMs causing an alteration in the distribution pattern of FloT[36]. This suggests that the levels of farnesol could be somehow altered in Δ*tasA* cells. Farnesol has a similar behavior in membranes as cholesterol in eukaryotic cell membranes (Fig. 5.3B), it has affinity for liquid phases of the cell membrane and induces the gel-fluid coexistence, increasing the heterogeneity of the cell membrane[82]. At the same time, TasA has a direct influence in membrane fluidity upon interaction with lipids, as demonstrated in Chapter IV, therefore, a combination of both events i) the absence of TasA from the cell membrane and ii) alteration in the levels of farnesol or polyisoprenoid lipids could be the underlying cause for the mislocalization of FloT observed in the absence of TasA. These changes suggest a disruption of FMMs in Δ*tasA* cells, evidenced by the mislocalization of FloT.

Flotillins are also involved in the control of membrane fluidity[35], which is a cellular parameter essential for the maintenance of homeostasis[83]. For instance, physiological membrane fluidity is required for proper membrane protein folding, catalytic activity or diffusion of membrane proteins[84,85], however, an excess of membrane fluidity affects membrane permeability of small molecules or protons[86,87]. Evidence suggest that this increased membrane fluidity is directly or indirectly related to many of the changes observed in Δ*tasA* cells, such as the higher amounts of fengycin released, the changes in membrane polarization, the lower intracellular pH, the altered respiration rates, etc. Indeed, recent works support this notion by analyzing how membrane fluidity affects basic cellular functions. It has been shown how the loss of both flotillins affects peptidoglycan synthesis by altering the dynamics of the bacterial cytoskeleton protein MreB. In fact, it was observed that the flotillins directly influence membrane dynamics by increasing *in vitro* the membrane fluidity of lipid vesicles[88]. Consistently, previous studies demonstrated that the absence of flotillins reduce membrane fluidity[35], having exactly the opposite effect to TasA. More importantly, it was shown that treatment of cells with a fluidifying agent restore the WT phenotype in the absence of flotillins[88]. Recently, another study has further demonstrated the cellular alterations that occur when membrane fluidity is altered. Indeed, lower membrane fluidity was engineered in *B. subtilis* by interfering with the synthesis of branched chain fatty acids. This strain exhibited alterations in membrane potential, complete disassembly of the MreB cytoskeleton and complete phase separation of the plasma membrane[89]. Interestingly, Δ*tasA* cells also show defects in many of the described phenotypes, including membrane potential and cell size or morphology.

In summary, these results indicate that alterations of membrane fluidity might be the underlying cause for the loss of viability observed in Δ*tasA* cells, that show some of the alterations mentioned above. Moreover, the role of flotillins in organizing the FMMs and facilitating the interactions between different protein partners involved in signal transduction complexes, and their direct involvement in the control of membrane fluidity, antagonizing the role of TasA in this function, is suggestive of a connection between TasA and the FMMs. This would not be surprising, as previous works have brought to light the existence of a connection between eukaryotic lipid rafts and neurodegenerative disorders, in which these membrane domains directly interact with amyloid proteins or influence their aggregation process[90-92]. However, the mechanism by which this connection occurs still remains elusive and will be the subject of future research.

REFERENCES

1 Branda, S. S., Chu, F., Kearns, D. B., Losick, R. & Kolter, R. A major protein component of the *Bacillus subtilis* biofilm matrix. *Mol. Microbiol.* **59**, 1229-1238, (2006).

2 Romero, D., Aguilar, C., Losick, R. & Kolter, R. Amyloid fibers provide structural integrity to *Bacillus subtilis* biofilms. *Proc. Natl. Acad. Sci. USA* **107**, 2230-2234, (2010).

3 Romero, D., Vlamakis, H., Losick, R. & Kolter, R. An accessory protein required for anchoring and assembly of amyloid fibres in *B. subtilis* biofilms. *Mol. Microbiol.* **80**, 1155-1168, (2011).

4 Tjalsma, H. *et al.* Conserved serine and histidine residues are critical for activity of the ER-type signal peptidase SipW of *Bacillus subtilis*. *J. Biol. Chem.* **275**, 25102-25108, (2000).

5 Stover, A. G. & Driks, A. Secretion, localization, and antibacterial activity of TasA, a *Bacillus subtilis* spore-associated protein. *J. Bacteriol.* **181**, 1664-1672, (1999).

6 Stover, A. G. & Driks, A. Control of synthesis and secretion of the *Bacillus subtilis* protein YqxM. *J. Bacteriol.* **181**, 7065-7069, (1999).

7 Romero, D., Vlamakis, H., Losick, R. & Kolter, R. Functional analysis of the accessory protein TapA in *Bacillus subtilis* amyloid fiber assembly. *J. Bacteriol.* **196**, 1505-1513, (2014).

8 Erskine, E. *et al.* Formation of functional, non-amyloidogenic fibres by recombinant *Bacillus subtilis* TasA. *Mol. Microbiol.* **110**, 897-913, (2018).

9 Diehl, A. *et al.* Structural changes of TasA in biofilm formation of *Bacillus subtilis*. *Proc. Natl. Acad. Sci. USA* **115**, 3237-3242, (2018).

10 El Mammeri, N. *et al.* Molecular architecture of bacterial amyloids in Bacillus biofilms. *FASEB J.* **33**, 12146-12163, (2019).

11 Jackson, M. P. & Hewitt, E. W. Why are Functional Amyloids Non-Toxic in Humans? *Biomolecules* **7**, (2017).

12 Stefani, M. Biochemical and biophysical features of both oligomer/fibril and cell membrane in amyloid cytotoxicity. *FEBS J* **277**, 4602-4613, (2010).

13 Chapman, M. R. *et al.* Role of *Escherichia coli* curli operons in directing amyloid fiber formation. *Science* **295**, 851-855, (2002).

14 Hammer, N. D., Schmidt, J. C. & Chapman, M. R. The curli nucleator protein, CsgB, contains an amyloidogenic domain that directs CsgA polymerization. *Proc. Natl. Acad. Sci. USA* **104**, 12494-12499, (2007).

15 Shu, Q. *et al.* The E. coli CsgB nucleator of curli assembles to beta-sheet oligomers that alter the CsgA fibrillization mechanism. *Proc. Natl. Acad. Sci. USA* **109**, 6502-6507, (2012).

16 Yan, Z., Yin, M., Chen, J. & Li, X. Assembly and substrate recognition of curli biogenesis system. *Nat. Commun.* **11**, 241, (2020).

17 Hammar, M., Arnqvist, A., Bian, Z., Olsen, A. & Normark, S. Expression of two csg operons is required for production of fibronectin- and congo red-binding curli polymers in *Escherichia coli* K-12. *Mol. Microbiol.* **18**, 661-670, (1995).

18 Robinson, L. S., Ashman, E. M., Hultgren, S. J. & Chapman, M. R. Secretion of curli fibre subunits is mediated by the outer membrane-localized CsgG protein. *Mol. Microbiol.* **59**, 870-881, (2006).

19 Nenninger, A. A. *et al.* CsgE is a curli secretion specificity factor that prevents amyloid fibre aggregation. *Mol. Microbiol.* **81**, 486-499, (2011).

20 Evans, M. L. *et al.* The bacterial curli system possesses a potent and selective inhibitor of amyloid formation. *Mol. Cell* **57**, 445-455, (2015).

21 Dueholm, M. S., Otzen, D. & Nielsen, P. H. Evolutionary insight into the functional amyloids of the pseudomonads. *PLoS One* **8**, e76630, (2013).

22 Zeng, G. *et al.* Functional bacterial amyloid increases *Pseudomonas* biofilm hydrophobicity and stiffness. *Front Microbiol* **6**, 1099, (2015).

23 Dueholm, M. S. *et al.* Functional amyloid in *Pseudomonas*. *Mol. Microbiol.* **77**, 1009-1020, (2010).

24 Dueholm, M. S. *et al.* Expression of Fap amyloids in *Pseudomonas aeruginosa*, *P. fluorescens*, and *P. putida* results in aggregation and increased biofilm formation. *Microbiology open* **2**, 365-382, (2013).

25 Rouse, S. L. *et al.* A new class of hybrid secretion system is employed in Pseudomonas amyloid biogenesis. *Nat. Commun.* **8**, 263, (2017).

26 Daskalov, A., Dyrka, W. & Saupe, S. J. Theme and variations: evolutionary diversification of the HET-s functional amyloid motif. *Sci. Rep.* **5**, 12494, (2015).

27 Harada, R. *et al.* The effect of amino acid substitution in the imperfect repeat sequences of alpha-synuclein on fibrillation. *Biochim. Biophys. Acta* **1792**, 998-1003, (2009).

28 Lasa, I. & Penades, J. R. Bap: a family of surface proteins involved in biofilm formation. *Res. Microbiol.* **157**, 99-107, (2006).

29 Tormo, M. A., Knecht, E., Gotz, F., Lasa, I. & Penades, J. R. Bap-dependent biofilm formation by pathogenic species of Staphylococcus: evidence of horizontal gene transfer? *Microbiology* **151**, 2465-2475, (2005).

30 Taglialegna, A. *et al.* Staphylococcal Bap Proteins Build Amyloid Scaffold Biofilm Matrices in Response to Environmental Signals. *PLoS Pathog.* **12**, e1005711, (2016).

31 Arrizubieta, M. J., Toledo-Arana, A., Amorena, B., Penades, J. R. & Lasa, I. Calcium inhibits bap-dependent multicellular behavior in *Staphylococcus aureus*. *J. Bacteriol.* **186**, 7490-7498, (2004).

32 Taglialegna, A. *et al.* The biofilm-associated surface protein Esp of *Enterococcus faecalis* forms amyloid-like fibers. *NPJ Biofilms Microbiomes* **6**, 15, (2020).

33 Lopez, D., Vlamakis, H., Losick, R. & Kolter, R. Paracrine signaling in a bacterium. *Genes Dev.* **23**, 1631-1638, (2009).

34 Zeriouh, H., de Vicente, A., Perez-Garcia, A. & Romero, D. Surfactin triggers biofilm formation of *Bacillus subtilis* in melon phylloplane and contributes to the biocontrol activity. *Environ. Microbiol.* **16**, 2196-2211, (2014).

35 Bach, J. N. & Bramkamp, M. Flotillins functionally organize the bacterial membrane. *Mol. Microbiol.* **88**, 1205-1217, (2013).

36 Lopez, D. & Kolter, R. Functional microdomains in bacterial membranes. *Genes Dev.* **24**, 1893-1902, (2010).

37 Schneider, J. *et al.* Spatio-temporal remodeling of functional membrane microdomains organizes the signaling networks of a bacterium. *PLoS Genet.* **11**, e1005140, (2015).

38 Bramkamp, M. & Lopez, D. Exploring the existence of lipid rafts in bacteria. *Microbiol. Mol. Biol. Rev.* **79**, 81-100, (2015).

39 Lopez, D. & Koch, G. Exploring functional membrane microdomains in bacteria: an overview. *Curr. Opin. Microbiol.* **36**, 76-84, (2017).

40 Donovan, C. & Bramkamp, M. Characterization and subcellular localization of a bacterial flotillin homologue. *Microbiology* **155**, 1786-1799, (2009).

41 Caro-Astorga, J., Perez-Garcia, A., de Vicente, A. & Romero, D. A genomic region involved in the formation of adhesin fibers in *Bacillus cereus* biofilms. *Front Microbiol* **5**, 745, (2014).

42 Close, W. *et al.* Physical basis of amyloid fibril polymorphism. *Nat. Commun.* **9**, 699, (2018).

43 Asally, M. *et al.* Localized cell death focuses mechanical forces during 3D patterning in a biofilm. *Proc. Natl. Acad. Sci. USA* **109**, 18891-18896, (2012).

44 Kearns, D. B., Chu, F., Branda, S. S., Kolter, R. & Losick, R. A master regulator for biofilm formation by *Bacillus subtilis*. *Mol. Microbiol.* **55**, 739-749, (2005).

45 Chai, Y., Chu, F., Kolter, R. & Losick, R. Bistability and biofilm formation in *Bacillus subtilis*. *Mol. Microbiol.* **67**, 254-263, (2008).

46 Lewis, K. Programmed death in bacteria. *Microbiol. Mol. Biol. Rev.* **64**, 503-514, (2000).

47 Bayles, K. W. Bacterial programmed cell death: making sense of a paradox. *Nat. Rev. Microbiol.* **12**, 63-69, (2014).

48 Peeters, S. H. & de Jonge, M. I. For the greater good: Programmed cell death in bacterial communities. *Microbiol. Res.* **207**, 161-169, (2018).

49 Galluzzi, L. *et al.* Molecular mechanisms of cell death: recommendations of the Nomenclature Committee on Cell Death 2018. *Cell Death Differ.* **25**, 486-541, (2018).

50 Redza-Dutordoir, M. & Averill-Bates, D. A. Activation of apoptosis signalling pathways by reactive oxygen species. *Biochim. Biophys. Acta* **1863**, 2977-2992, (2016).

51 Collins, J. A., Schandi, C. A., Young, K. K., Vesely, J. & Willingham, M. C. Major DNA fragmentation is a late event in apoptosis. *J. Histochem. Cytochem.* **45**, 923-934, (1997).

52 Perry, S. W. *et al.* HIV-1 transactivator of transcription protein induces mitochondrial hyperpolarization and synaptic stress leading to apoptosis. *J. Immunol.* **174**, 4333-4344, (2005).

53 Dwyer, D. J., Camacho, D. M., Kohanski, M. A., Callura, J. M. & Collins, J. J. Antibiotic-induced bacterial cell death exhibits physiological and biochemical hallmarks of apoptosis. *Mol. Cell* **46**, 561-572, (2012).

54 Gaschler, M. M. & Stockwell, B. R. Lipid peroxidation in cell death. *Biochem. Biophys. Res. Commun.* **482**, 419-425, (2017).

55 Gonidakis, S. & Longo, V. D. Assessing chronological aging in bacteria. *Methods Mol Biol* **965**, 421-437, (2013).

56 Kolter, R., Siegele, D. A. & Tormo, A. The stationary phase of the bacterial life cycle. *Annu. Rev. Microbiol.* **47**, 855-874, (1993).

57 Dukan, S. & Nystrom, T. Bacterial senescence: stasis results in increased and differential oxidation of cytoplasmic proteins leading to developmental induction of the heat shock regulon. *Genes Dev.* **12**, 3431-3441, (1998).

58 Navarro Llorens, J. M., Tormo, A. & Martinez-Garcia, E. Stationary phase in gram-negative bacteria. *FEMS Microbiol. Rev.* **34**, 476-495, (2010).

59 Stewart, E. J., Madden, R., Paul, G. & Taddei, F. Aging and death in an organism that reproduces by morphologically symmetric division. *PLoS Biol.* **3**, e45, (2005).

60 Lindner, A. B., Madden, R., Demarez, A., Stewart, E. J. & Taddei, F. Asymmetric segregation of protein aggregates is associated with cellular aging and rejuvenation. *Proc. Natl. Acad. Sci. USA* **105**, 3076-3081, (2008).

61 Hecker, M., Pane-Farre, J. & Volker, U. SigB-dependent general stress response in *Bacillus subtilis* and related gram-positive bacteria. *Annu. Rev. Microbiol.* **61**, 215-236, (2007).

62 Reder, A., Hoper, D., Gerth, U. & Hecker, M. Contributions of individual sigmaB-dependent general stress genes to oxidative stress resistance of *Bacillus subtilis*. *J. Bacteriol.* **194**, 3601-3610, (2012).

63 Gomez-Marroquin, M. *et al.* Role of *Bacillus subtilis* DNA Glycosylase MutM in Counteracting Oxidatively Induced DNA Damage and in Stationary-Phase-Associated Mutagenesis. *J. Bacteriol.* **197**, 1963-1971, (2015).

64 Chan, C. M., Danchin, A., Marliere, P. & Sekowska, A. Paralogous metabolism: S-alkyl-cysteine degradation in *Bacillus subtilis*. *Environ. Microbiol.* **16**, 101-117, (2014).

65 Malishev, R., Abbasi, R., Jelinek, R. & Chai, L. Bacterial Model Membranes Reshape Fibrillation of a Functional Amyloid Protein. *Biochemistry* **57**, 5230-5238, (2018).

66 Bucciantini, M., Rigacci, S. & Stefani, M. Amyloid Aggregation: Role of Biological Membranes and the Aggregate-Membrane System. *J Phys Chem Lett* **5**, 517-527, (2014).

67 Khondker, A., Alsop, R. J. & Rheinstadter, M. C. Membrane-Accelerated Amyloid-beta Aggregation and Formation of Cross-beta Sheets. *Membranes (Basel)* **7**, (2017).

68 Rawat, A., Langen, R. & Varkey, J. Membranes as modulators of amyloid protein misfolding and target of toxicity. *Biochim. Biophys. Acta. Biomembr*. (2018).

69 Gorbenko, G. P. & Kinnunen, P. K. The role of lipid-protein interactions in amyloid-type protein fibril formation. *Chem. Phys. Lipids* **141**, 72-82, (2006).

70 Bucciantini, M. *et al.* Inherent toxicity of aggregates implies a common mechanism for protein misfolding diseases. *Nature* **416**, 507-511, (2002).

71 Kagan, B. L. *et al.* Antimicrobial properties of amyloid peptides. *Mol. Pharm.* **9**, 708-717, (2012).

72 Haass, C. & Selkoe, D. J. Soluble protein oligomers in neurodegeneration: lessons from the Alzheimer's amyloid beta-peptide. *Nat. Rev. Mol. Cell Biol.* **8**, 101-112, (2007).

73 Steinberg, N. *et al.* The extracellular matrix protein TasA is a developmental cue that maintains a motile subpopulation within *Bacillus subtilis* biofilms. *Science Signalling*, (2020).

74 Chai, Y., Kolter, R. & Losick, R. Paralogous antirepressors acting on the master regulator for biofilm formation in *Bacillus subtilis*. *Mol. Microbiol.* **74**, 876-887, (2009).

75 Chai, Y., Kolter, R. & Losick, R. Reversal of an epigenetic switch governing cell chaining in *Bacillus subtilis* by protein instability. *Mol. Microbiol.* **78**, 218-229, (2010).

76 Chai, Y., Norman, T., Kolter, R. & Losick, R. An epigenetic switch governing daughter cell separation in *Bacillus subtilis*. *Genes Dev.* **24**, 754-765, (2010).

77 Mordini, S. *et al.* The role of SwrA, DegU and P(D3) in *fla/che* expression in *B. subtilis*. *PLoS One* **8**, e85065, (2013).

78 Noone, D. *et al.* Signal perception by the secretion stress-responsive CssRS two-component system in *Bacillus subtilis*. *J. Bacteriol.* **194**, 1800-1814, (2012).

79 Dempwolff, F. *et al.* Super Resolution Fluorescence Microscopy and Tracking of Bacterial Flotillin (Reggie) Paralogs Provide Evidence for Defined-Sized Protein Microdomains within the Bacterial Membrane but Absence of Clusters Containing Detergent-Resistant Proteins. *PLoS Genet.* **12**, e1006116, (2016).

80 Otto, G. P. & Nichols, B. J. The roles of flotillin microdomains--endocytosis and beyond. *J. Cell Sci.* **124**, 3933-3940, (2011).

81 Bach, J. N. & Bramkamp, M. Dissecting the molecular properties of prokaryotic flotillins. *PLoS One* **10**, e0116750, (2015).

82 Feng, X. *et al.* Structural and functional analysis of *Bacillus subtilis* YisP reveals a role of its product in biofilm production. *Chem. Biol.* **21**, 1557-1563, (2014).

83 Ernst, R., Ejsing, C. S. & Antonny, B. Homeoviscous Adaptation and the Regulation of Membrane Lipids. *J. Mol. Biol*. **428**, 4776-4791, (2016).

84 Andersen, O. S. & Koeppe, R. E., 2nd. Bilayer thickness and membrane protein function: an energetic perspective. *Annu. Rev. Biophys. Biomol. Struct.* **36**, 107-130, (2007).

85 Lee, A. G. How lipids affect the activities of integral membrane proteins. *Biochim. Biophys. Acta* **1666**, 62-87, (2004).

86 van de Vossenberg, J. L., Driessen, A. J., da Costa, M. S. & Konings, W. N. Homeostasis of the membrane proton permeability in *Bacillus subtilis* grown at different temperatures. *Biochim. Biophys. Acta* **1419**, 97-104, (1999).

87 Rossignol, M., Thomas, P. & Grignon, C. Proton permeability of liposomes from natural phospholipid mixtures. *Biochim. Biophys. Acta* **684**, 195-199, (1982).

88 Zielińska, A. *et al.* Flotillin mediated membrane fluidity controls peptidoglycan synthesis and MreB movement. *bioRxiv*, 736819, (2020).

89 Gohrbandt, M. *et al.* Low membrane fluidity triggers lipid phase separation and protein segregation *in vivo*. *bioRxiv*, 852160, (2019).

90 Kim, S. I., Yi, J. S. & Ko, Y. G. Amyloid beta oligomerization is induced by brain lipid rafts. *J. Cell Biochem.* **99**, 878-889, (2006).

91 Hicks, D. A., Nalivaeva, N. N. & Turner, A. J. Lipid rafts and Alzheimer's disease: protein-lipid interactions and perturbation of signaling. *Front. Physiol.* **3**, 189, (2012).

92 Angelopoulou, E., Paudel, Y. N., Shaikh, M. F. & Piperi, C. Flotillin: A Promising Biomarker for Alzheimer's Disease. *J. Pers. Med.* **10**, (2020).

Conclusions

The main conclusions derived from this thesis are listed below:

1. Heterologous expression in *E. coli* has been shown to be an efficient system for the production of biologically active TasA, capable of self-assembling, *in vitro*, into filaments that exhibit the distinctive properties of amyloid proteins, similar to the native fibers purified directly from *B. subtilis*. The possibility of obtaining high amounts of TasA as monomers and without contamination by the TapA accessory protein, has allowed for the molecular and structural characterization of TasA, revealing its unquestionable intrinsic amyloid nature.

2. TasA fibers show a rigid core resistant to protease degradation and enrichment in β-sheet content, with an unusual proportion of α-helix, as well as imperfect amino acid repeats and two amyloidogenic segments that are relevant to the amyloid behavior of TasA and biofilm formation in *B. subtilis*.

3. Heterologous expression of TapA in *E. coli* has allowed for the structural and biochemical characterization that has demonstrated the amyloid nature of this protein. Despite certain differences with TasA at the morphological level, the two proteins share a similar structural fold. Our studies reinforce the catalytic role of TapA in TasA fibrillation and support a co-assembly of the two proteins in the context of biofilm formation.

4. Deletion of *tasA* has a pleiotropic effect, featured by changes in the expression of hundreds of genes and a battery of cytological defects and physiological alterations that compromise cell viability. The in-depth study of the *tasA* mutant has allowed for the assignment of a new and essential function to TasA beyond its involvement in the assembly of the extracellular matrix, which is the stabilization of cell membrane dynamics when cells enter the stationary phase of growth.

5. Microscopy, biophysical, and biochemical studies demonstrate that TasA is a membrane-bound protein, found in detergent-resistant fractions of the cell membrane, that plays its stabilizing role by directly affecting membrane fluidity, both *in vivo* and *in vitro*. The data suggest that this function relies on the selective interaction of TasA with different membrane lipids.

6. Microbial ecology studies have shown that TasA is relevant for the survival and the antagonistic activity of *B. subtilis* on melon leaves. This is based on two complementary functions exerted by this protein: i) its structural role in the formation of amyloid fibers and therefore the construction of the extracellular matrix and the assembly of a biofilm, and ii) the new assigned role in membrane stabilization and maintenance of cell viability that allows proper adaptative response to the changing environment that is found on the plant surface.

Conclusiones

Las principales conclusiones derivadas de esta tesis doctoral se enumeran a continuación:

1. La expresión heteróloga en *E. coli* ha demostrado ser un sistema eficiente para la purificación de TasA biológicamente activa y capaz de autoensamblarse, *in vitro*, en filamentos que exhiben las propiedades típicas de las proteínas amiloides, de forma similar a las fibras nativas purificadas directamente de *B. subtilis*. La posibilidad de obtener altas cantidades de TasA en forma monomérica y sin contaminación de la proteína accesoria TapA, ha permitido llevar a cabo la caracterización molecular y estructural de TasA, revelando su indudable naturaleza amiloide.

2. Las fibras de TasA muestran un núcleo rígido resistente a la degradación por proteasas y enriquecido en estructura secundaria de láminas-β, con una proporción inusual de hélice-α, así como repeticiones aminoacídicas imperfectas y dos segmentos amiloidogénicos que son relevantes para el comportamiento amiloide de TasA y la formación de biofilm en *B. subtilis*.

3. La expresión heteróloga de TapA en *E. coli* ha permitido la caracterización estructural y bioquímica que ha demostrado la naturaleza amiloide de esta proteína. A pesar de ciertas diferencias con TasA a nivel morfológico, las dos proteínas comparten un pliegue estructural similar. Nuestros estudios refuerzan el papel catalítico de TapA en la fibrilación de TasA y apoyan un co-ensamblaje de las dos proteínas en el contexto de la formación de biofilm.

4. La deleción de *tasA* tiene un efecto pleiotrópico, caracterizado por cambios en la expresión de cientos de genes y una batería de defectos citológicos y alteraciones fisiológicas que comprometen la viabilidad celular. El estudio en profundidad del mutante en *tasA* ha permitido asignar una nueva y esencial función a TasA más allá de su participación en el ensamblaje de la matriz extracelular, que es la estabilización de la dinámica de la membrana celular cuando las células entran en fase estacionaria.

5. Los datos obtenidos mediante técnicas bioquímicas, biofísicas, y microscopía demuestran que TasA es una proteína unida a la membrana, detectada en fracciones de la membrana resistentes a los detergentes y que desempeña su papel estabilizador en esta localización al tener un efecto directo sobre la fluidez de la membrana, tanto *in vivo* como *in vitro*. Los datos sugieren que esta función se basa en la interacción selectiva de TasA con diferentes lípidos de membrana.

6. Estudios de ecología microbiana han demostrado que TasA es relevante para la supervivencia y la actividad antagonista de *B. subtilis* en las hojas de melón. Esto se basa en las dos funciones complementarias ejercidas por esta proteína: i) su papel estructural en la formación de las fibras amiloides y, por lo tanto, en la construcción de la matriz extracelular y el ensamblaje del biofilm, y ii) su nueva función en la estabilización y mantenimiento de la membrana y la viabilidad celular, lo cual permite una respuesta adaptativa adecuada al entorno cambiante que se encuentra en la superficie de la planta.

Appendix

CRITICAL REVIEWS IN MICROBIOLOGY
2018, VOL. 44, NO. 6, 653–666
https://doi.org/10.1080/1040841X.2018.1491527

Taylor & Francis
Taylor & Francis Group

REVIEW ARTICLE

OPEN ACCESS Check for updates

Beyond the expected: the structural and functional diversity of bacterial amyloids

Jesús Cámara-Almirón*, Joaquin Caro-Astorga*, Antonio de Vicente and Diego Romero

Instituto de Hortofruticultura Subtropical y Mediterránea "La Mayora" – Departamento de Microbiología, Universidad de Málaga, Málaga, Spain

ABSTRACT

Intense research has confirmed the formerly theoretical distribution of amyloids in nature, and studies on different systems have illustrated the role of these proteins in microbial adaptation and in interactions with the environment. Two lines of research are expanding our knowledge on functional amyloids: (i) structural studies providing insights into the molecular machineries responsible for the transition from monomer to fibers and (ii) studies showing the way in which these proteins might participate in the microbial fitness in natural settings. Much is known about how amyloids play a role in the social behavior of bacteria, or biofilm formation, and in the adhesion of bacteria to surfaces; however, we are still in the initial stages of understanding a complementary involvement of amyloids in bacteria–host interactions. This review will cover the following two topics: first, the key aspects of the microbial platforms dedicated to the assembly of the fibers, and second, the mechanisms by which bacteria utilize the morphological and biochemical variability of amyloids to modulate the immunological response of the host, plants and humans, contributing to (i) infection, in the case of pathogenic bacteria or (ii) promotion of the health of the host, in the case of beneficial bacteria.

ARTICLE HISTORY
Received 26 October 2017
Revised 22 May 2018
Accepted 18 June 2018
Published online 14 September 2018

KEYWORDS
Functional amyloids; bacteria; immunological response; microbe–host interactions

Introduction

Functional amyloids are a very heterogeneous class of proteins that are widely distributed in nature from humans to bacteria and that have a variety of functions that are fundamentally different from the pathological features of their relatives "traditional" amyloids. In bacteria, some physiological processes known to be associated with functional amyloids are as follows: (i) bacterial cell attachment and biofilm formation (Chapman et al. 2002; Dueholm et al. 2010; Romero et al. 2010), (ii) reproduction (Claessen et al. 2003), (iii) control of plasmid replication (Molina-García et al. 2016), (iv) cytotoxicity (Hetz et al. 2002) and virulence (Oh et al. 2007). In eukaryotes, functional amyloids have been found to be dedicated to the following: (i) cell adhesion in yeasts (Ramsook et al. 2010), (ii) hyphae compatibility in filamentous fungi (Coustou-Linares et al. 2001), (iii) antimicrobial activity (Jang et al. 2011), iv) structural functions (Iconomidou et al. 2000; Kenney et al. 2002), and (v) detoxification in certain physiological processes (Fowler et al. 2005) and hormone storage (Maji et al. 2009). These examples are indicative of the versatility of the amyloid state in their contributions to multiple aspects of the biology of living organisms. In addition to differences in their biological significance, the idea that the polymerization process of functional amyloids is tightly controlled in comparison to their pathogenic siblings is widely supported; functional amyloids partner with themselves and with several other proteins in the system for localization and stabilization. Some functional amyloids are secreted to the outside of the cell, where they polymerize into long fibers that are used for attachment to surfaces or biofilm formation; others remain inside the cell, occupying optimal subcellular localizations and developing their functionality in normal cell physiological processes. Such is the case of Hfq, an RNA chaperone in *Escherichia coli*. The C-terminus of this protein displays typical amyloid features and the capacity to self-assemble into fibrils. This protein appears to be localized in patterns within the cell cytoplasm (Fortas et al. 2015).

CONTACT Romero Diego diego_romero@uma.es Instituto de Hortofruticultura Subtropical y Mediterránea "La Mayora" – Departamento de Microbiología, Universidad de Málaga, Bulevar Louis Pasteur 31 (Campus Universitario de Teatinos), Málaga, Spain
*These authors contributed equally to this work.

THE FASEB JOURNAL • RESEARCH • www.fasebj.org

Molecular architecture of bacterial amyloids in *Bacillus* biofilms

Nadia El Mammeri,[*,1] Jesus Hierrezuelo,[†,1] James Tolchard,[*] Jesús Cámara-Almirón,[†] Joaquín Caro-Astorga,[†] Ana Álvarez-Mena,[†] Antoine Dutour,[*] Mélanie Berbon,[*] Jayakrishna Shenoy,[*] Estelle Morvan,[‡] Axelle Grélard,[*] Brice Kauffmann,[‡] Sophie Lecomte,[*] Antonio de Vicente,[†] Birgit Habenstein,[*] Diego Romero,[†,2] and Antoine Loquet[*,3]

[*]L'Institut de Chimie et Biologie des Membranes et des Nano-Objets (CBMN), Unité Mixte de Recherche (UMR) 5248, and [‡]Institut Européen de Chimie et Biologie (IECB), Unité Mixte de Service (UMS) 3033 Unité de Soutien (US) 001, Centre National de la Recherche (CNRS), University of Bordeaux, Pessac, France; and [†]Departamento de Microbiología, Universidad de Málaga, Málaga, Spain

ABSTRACT: The formation of biofilms provides structural and adaptive bacterial response to the environment. In *Bacillus* species, the biofilm extracellular matrix is composed of exopolysaccharides, hydrophobins, and several functional amyloid proteins. We report, using multiscale approaches such as solid-state NMR (SSNMR), electron microscopy, X-ray diffraction, dynamic light scattering, attenuated total reflection Fourier transform infrared (FTIR), and immune-gold labeling, the molecular architecture of *B. subtilis* and pathogenic *B. cereus* functional amyloids. SSNMR data reveal that the major amyloid component TasA in its fibrillar amyloid form contain β-sheet and α-helical secondary structure, suggesting a nontypical amyloid architecture in *B. subtilis*. Proteinase K digestion experiments indicate the amyloid moiety is ∼100 aa long, and subsequent SSNMR and FTIR signatures for *B. subtilis* and *B. cereus* TasA filaments highlight a conserved amyloid fold, albeit with substantial differences in structural polymorphism and secondary structure composition. Structural analysis and coassembly data on the accessory protein TapA in *B. subtilis* and its counterpart camelysin in *B. cereus* reveal a catalyzing effect between the functional amyloid proteins and a common structural architecture, suggesting a coassembly in the context of biofilm formation. Our findings highlight nontypical amyloid behavior of these bacterial functional amyloids, underlining structural variations between biofilms even in closely related bacterial species.—El Mammeri, N., Hierrezuelo, J., Tolchard, J., Cámara-Almirón, J., Caro-Astorga, J., Álvarez-Mena, A., Dutour, A., Berbon, M., Shenoy, J., Morvan, E., Grélard, A., Kauffmann, B., Lecomte, S., de Vicente, A., Habenstein, B., Romero, D., Loquet, A. Molecular architecture of bacterial amyloids in *Bacillus* biofilms. FASEB J. 33, 12146–12163 (2019). www.fasebj.org

KEY WORDS: functional amyloids · extracellular matrix · solid-state NMR

Functional amyloids (1) are protein aggregates that have emerged as 1 of the most outstanding contributors to bacterial physiology and behavior (2–4). Amyloid functions (5) can range from purely structural (6) to supporting multicellular bacterial communities (7), mediating interaction with surfaces (8), driving assembly of the extracellular matrix (9, 10), and, more recently, a putative role in neurodegeneration (11). This broad functional versatility and their remarkable ability to form filamentous self-assemblies, robust and resistant to most denaturing or environmental conditions (12–14), contribute to functional amyloids being considered as a molecular Swiss-army knife in the bacterial kingdom.

A fascinating step in the bacterial life cycle is the assembly of bacterial communities called biofilms. Biofilms are composed of an insoluble, noncrystalline supramolecular matrix mostly made up of water, proteins, lipids, and polysaccharides. The coordinated expression of a pool of structural elements permits the building of the extracellular matrix, a sort of bacterial tissue that provides physical support to the biofilm, protects the cells, mediates interactions with the environment, and regulates the flow

ABBREVIATIONS: 1D, 1-dimensional; 2D, 2-dimensional; 3D, 3-dimensional; ATR, attenuated total reflection; CalY, camelysin; DLS, dynamic light scattering; DSS, 4,4-dimethyl-4-silapentane-1-sulfonic acid; FA, formic acid; FTIR, Fourier transform infrared; IB, inclusion body; INEPT, insensitive nuclei enhanced polarization transfer; MS, mass spectrometry; n.a., natural abundance; PBST, PBS with 0.1% Tween20; PDSD, proton-driven spin-diffusion; SSNMR, solid-state NMR; SSP, secondary structure propensity; TasA-bs, *Bacillus subtilis* TasA; TasA-bc, *Bacillus cereus* TasA; TEM, transmission electron microscopy; ThT, thioflavin T

[1] These authors contributed equally to this work.

[2] Correspondence: Departamento de Microbiología, Universidad de Málaga, Málaga, Spain. E-mail: diego_romero@uma.es.

[3] Correspondence: CBMN, IECB, CNRS, University of Bordeaux, Pessac, 33607, France. E-mail: a.loquet@iecb.u-bordeaux.fr

doi: 10.1096/fj.201900831R

This article includes supplemental data. Please visit *http://www.fasebj.org* to obtain this information.

0892-6638/19/0033-12146 © FASEB

nature COMMUNICATIONS

ARTICLE

https://doi.org/10.1038/s41467-020-15758-z OPEN

Dual functionality of the amyloid protein TasA in *Bacillus* physiology and fitness on the phylloplane

Jesús Cámara-Almirón[1,3], Yurena Navarro[1,3], Luis Díaz-Martínez[1], María Concepción Magno-Pérez-Bryan[1], Carlos Molina-Santiago[1], John R. Pearson[2], Antonio de Vicente[1], Alejandro Pérez-García[1] & Diego Romero[1✉]

Bacteria can form biofilms that consist of multicellular communities embedded in an extracellular matrix (ECM). In *Bacillus subtilis*, the main protein component of the ECM is the functional amyloid TasA. Here, we study further the roles played by TasA in *B. subtilis* physiology and biofilm formation on plant leaves and in vitro. We show that Δ*tasA* cells exhibit a range of cytological symptoms indicative of excessive cellular stress leading to increased cell death. TasA associates to the detergent-resistant fraction of the cell membrane, and the distribution of the flotillin-like protein FloT is altered in Δ*tasA* cells. We propose that, in addition to a structural function during ECM assembly and interactions with plants, TasA contributes to the stabilization of membrane dynamics as cells enter stationary phase.

[1] Instituto de Hortofruticultura Subtropical y Mediterránea "La Mayora" – Departamento de Microbiología, Universidad de Málaga, Bulevar Louis Pasteur 31 (Campus Universitario de Teatinos), 29071 Málaga, Spain. [2] Nano-imaging Unit, Andalusian Centre for Nanomedicine and Biotechnology, BIONAND, Málaga, Spain. [3] These authors contributed equally: Jesús Cámara-Almirón, Yurena Navarro. ✉email: diego_romero@uma.es

SCIENCE SIGNALING | RESEARCH ARTICLE

BIOFILMS

The extracellular matrix protein TasA is a developmental cue that maintains a motile subpopulation within *Bacillus subtilis* biofilms

Nitai Steinberg[1,2]*, Alona Keren-Paz[1]*, Qihui Hou[1], Shany Doron[1], Keren Yanuka-Golub[1], Tsviya Olender[1], Rotem Hadar[1†], Gili Rosenberg[1], Rakeshkumar Jain[1], Jesus Cámara-Almirón[2], Diego Romero[2], Sven van Teeffelen[3], Ilana Kolodkin-Gal[1‡]

In nature, bacteria form biofilms—differentiated multicellular communities attached to surfaces. Within these generally sessile biofilms, a subset of cells continues to express motility genes. We found that this subpopulation enabled *Bacillus subtilis* biofilms to expand on high-friction surfaces. The extracellular matrix (ECM) protein TasA was required for the expression of flagellar genes. In addition to its structural role as an adhesive fiber for cell attachment, TasA acted as a developmental signal stimulating a subset of biofilm cells to revert to a motile phenotype. Transcriptomic analysis revealed that TasA stimulated the expression of a specific subset of genes whose products promote motility and repress ECM production. Spontaneous suppressor mutations that restored motility in the absence of TasA revealed that activation of the biofilm-motility switch by the two-component system CssR/CssS antagonized the TasA-mediated reversion to motility in biofilm cells. Our results suggest that although mostly sessile, biofilms retain a degree of motility by actively maintaining a motile subpopulation.

INTRODUCTION

Bacteria in nature most often reside in multicellular differentiated communities of cells commonly referred to as biofilms (*1*). Compared to the planktonic (free-living) state, bacteria in biofilms are more protected from external insults, such as antibiotics and the host immune system, attach more firmly to their hosts, and have improved access to nutrients (*2*–*9*). Whereas biofilms formed by pathogenic bacteria are deleterious to the host (*3*, *10*), biofilms formed by other bacteria can be beneficial to the host (*11*–*15*).

Bacterial biofilms follow a robust and complex pattern of differentiation. One main property defining biofilms is the production of an extracellular matrix (ECM) that surrounds, connects, and protects the cells and allows them to adhere to each other or to a surface (*16*–*18*). The main components of the bacterial ECM are exopolysaccharides, proteins, nucleic acids (*19*), and biogenic minerals (*20*–*22*). Exopolysaccharides play a fundamental structural role in biofilms of different bacterial species (*23*–*28*). Biofilms of *Bacillus subtilis* produce several exopolysaccharide polymers (*29*, *30*) through the combined actions of enzymes encoded in the *epsA-O* operon. Mutants for this operon, and specifically the glycosyltransferase-encoding gene *epsH*, lack the exopolysaccharide component of the ECM and form colonies that are featureless, in contrast to the wrinkled colonies of wild-type cells (*31*). The major proteinaceous component of *B. subtilis* ECM is the protein TasA, encoded by the *tapA-sipW-tasA* operon (*32*, *33*). TasA forms amyloidal fibers (*32*, *34*, *35*) that are attached to the cell wall and, in conjunction with other extracellular components, promote cell-cell adhesion (*32*, *36*). Colonies formed by *tasA* deletion mutants are smaller and less structurally complex than those of wild-type strains (*34*).

Being energetically costly, ECM production is under tight regulation and activated only under appropriate conditions, such as when neighboring cells already produce ECM. In *B. subtilis*, two positive feedback mechanisms lead to increased ECM production: (i) the tyrosine kinase EpsAB, which is specifically activated by *B. subtilis* exopolysaccharides (*37*); and (ii) the disruption of flagellar rotation, which has been proposed to activate ECM production through a mechanosensory mechanism (*38*, *39*). Motility is also energetically costly, involving the production of multiple protein components and energy investment in flagellar rotation. Thus, the expression of genes necessary for flagella structures, assembly, and rotation is all coordinated (*40*–*42*). Only a subpopulation of cells expresses flagellar genes, which are activated by the alternative sigma factor D (σ^D) (*41*). Similarly to other bacterial species, *B. subtilis* was long thought to shut down flagellar motility when grown on high-friction surfaces (*43*, *44*).

In an individual *B. subtilis* cell, a regulatory switch couples the activation of ECM production with the repression of motility (*38*, *39*, *45*–*60*). This regulatory switch depends mainly on two master regulators that together control both motility and biofilm development—the homologous proteins SinR and SlrR (*54*–*59*). During planktonic growth, SinR represses the expression of the ECM production operons *epsA-O* and *tapA-sipW-tasA*, as well as the expression of *slrR* (*61*, *62*). Once the biofilm state is induced, SinI inhibits SinR activity by binding to it and preventing SinR from binding DNA, resulting in derepression of the ECM operons and *slrR* (*61*, *63*, *64*). In turn, SlrR binds to SinR, creating a heterodimer that represses the *fla/che* operon, which encodes key components of motility (*59*) and gene encoding autolysins, which are important for breaking down the cell wall so that cells can separate from one another (*56*). Thus, the same regulator, SinR, represses either the ECM operons or motility but not both simultaneously in the same cell, and therefore, the two transcriptional programs are mutually exclusive at the single-cell level.

[1]Department of Molecular Genetics, Weizmann Institute of Science, Rehovot, Israel. [2]Instituto de Hortofruticultura Subtropical y Mediterránea "La Mayora", Departamento de Microbiología, Universidad de Málaga, Málaga, Spain. [3]Department of Microbiology, Institute Pasteur, Paris, France.
*These authors contributed equally to this work.
†Present address: Chaim Sheba Medical Center, Tel-Hashomer, Ramat-Gan, Israel.
‡Corresponding author. Email: ilana.kolodkin-gal@weizmann.ac.il

TESIS DOCTORAL

Structural and functional study of bacterial amyloids in *Bacillus subtilis*

Jesús Cámara Almirón

Málaga 2020

Director: Diego Romero Hinojosa

UNIVERSIDAD DE MÁLAGA

Facultad de Ciencias.
Departamento de Microbiología
Programa de Doctorado en
Biología Celular y Molecular